Universitat Autònoma de Barcelona

Calibration of the ATLAS central hadronic Tile Calorimeter in LHC Run-2 and beyond

Ammara Ahmad

Calibration of the ATLAS central hadronic Tile Calorimeter in LHC Run-2 and beyond

Ph.D. dissertation

Ammara Ahmad

Institut de Física d'Altes Energies
Universitat Autònoma de Barcelona
Departament de Física
Facultat de Ciències
Edifici Cn E-08193 Bellaterra (Barcelona)

Thesis director
Dr. Henric George Wilkens
CERN EP-ADE
Dr. Ilya Korolkov
Departament de Fìsica
Universitat Autònoma de Barcelona

Thesis tutor
Dr. Maria Pilar Casado Lechuga
Departament de Fìsica
Universitat Autònoma de Barcelona

Acknowledgements

First and foremost, I would like to express my sincere gratitude to my PhD supervisor **Henric Wilkens** who is the best supervisor I could have ever asked for. Thank you Henric for giving me the opportunity to work at the best research facility i.e, CERN. Thank you for offering insightful scientific guidance and elegant advice, providing relentless support whenever I needed it, and most importantly thank you for understanding my family situation and giving me your full support through thick and thin. I also appreciated that you always found the time to help me, and is mostly you that I need to thank for concluding this work and therefore having had very joyful PhD years.

I also would like to acknowledge **Pawel Klimek** and **Rute Pedro** for providing me with technical guidance throughout my PhD journey. You both always proved to be the trustworthy advisor and taught me a lot of what I know about the subject.

A special word of gratitude is owed to **Ilya Korolkov** for your kind support in a lot of matters, especially in helping with administrative issues since the very start of my PhD.

I wish to thank **Giulia de Gregoria** and **Beatriz Pereira** for their time and technical support. I extend my gratitude to all the members of the ATLAS TileCal group, for welcoming me and being available to discuss and share ideas and follow my progress. This thesis would not have been possible without the work of all its members.

Finally, I would like to thank my loving family, mother **Kausar**, father **Ahmad**, my brother **Abdur Rafay**, and sister **Javeria** for always encouraging me and making me believe that nothing is impossible. My most sincere gratitude goes to my loving husband, **Mehmood**, for your unending support and encouragement throughout the years. You always believed in me and inspired me. I would also like to applaud my daughters, **Bareerah** and **Aairah**, for their patience and understanding during these years.

It was an amazing journey, and would not have been possible without the backing of the above-mentioned people. You are all remarkable, and I hope to work with you again in the future, on one project or another.

Abstract

The Tile Calorimeter is a sampling hadronic calorimeter covering the central region of the ATLAS experiment, with steel as the absorber and plastic scintillators as an active medium. The scintillators are read out by wavelength shifting fibres to 9852 photomultiplier tubes. The analogue signals from the photomultiplier tubes are amplified, shaped, and digitised on the detector every 25 ns. The data are then read out to the off-detector systems for further processing. The Tile Calorimeter employs several calibration systems that, together with the collected collision data, provide the basis for response equalisation and monitoring at each stage of the readout path, from scintillation light production to energy and time reconstruction. A Laser system is used to monitor the stability and to perform a calibration of the Tile Calorimeter, from the photomultipliers to the read-out electronics. This dissertation provides a detailed description of the calculation of the energy calibration factors from Laser data. These calibration factors, produced weekly, have been applied to calorimeter channels in order to reduce the channel-to-channel spread and to recover the global calorimeter response disturbed by the photomultiplier tube drifts during the LHC Run-2. The observed PMT response evolution as a function of time over the entire Run-2 period is also shown.

The response of the PMTs depends on their past operation, the amount of light collected, and the current delivered in hours, days, and weeks prior to its current use. The TileCal PMTs were already operating for about 14 years and are expected to function for about that long more. This dissertation discusses quantitative models to quantify the evolution of the PMT response as a function of luminosity during LHC Run-2 and to forecast how this response will change over time during Run-3 and Run-4.

For the Long Shutdown III, it has been decided to replace about 1000 PMTs with new ones with better properties. In this thesis, a brief overview of the test bench built at CERN is given. Using this test bench, the responses of a set of PMTs will be studied in controlled conditions.

Table of Contents

List of Tables

List of Figures

Chapter 1

Introduction

Particle physics is the branch of science that studies the interaction and characteristics of matter's tiniest building blocks. Particle accelerators are designed and built by physicists with the purpose of studying fundamental particles. In high-energy physics experiments, calorimeters are essential for identifying particles and determining their energy and direction. Calorimeters were initially made as a basic, simple tool for a few particular uses in particle physics studies. However, in recent years, their function has significantly changed, and calorimetry has emerged as a crucial experimental technique, particularly in studies that employ the increasingly potent accelerators and storage rings that have been developed and used during this time. In terms of luminosity and collision energy, the **L**arge **H**adron **C**ollider (LHC) is the world's largest and most powerful particle accelerator, located at the European Organisation for Nuclear Research (CERN). ATLAS is one of the two general-purpose experiments at the Large Hadron Collider (LHC) which uses calorimeter technology to measure the energy of a particle as it passes through the detector. The ATLAS experiment calorimeter systems operated successfully during Run-1 and Run-2 of the LHC data-taking period. A more detailed discussion about LHC and ATLAS experiments is given in Chapter 4.

Chapter 2 and Chapter 3 of this dissertation are dedicated to the general introduction to calorimeters and calorimetry. Chapter 2 gives an introduction to hadronic and electromagnetic calorimetry. A brief overview of the various approaches being studied for future calorimetry in the post-LHC period is also included in the same chapter. While the energy response of homogeneous and sampling calorimeters to various particles is briefly covered in Chapter 3 along with a discussion of the calorimeters' performance.

This dissertation work focuses on the analysis of the Run-2 calibration data collected with the ATLAS hadronic Tile Calorimeter. The Tile hadronic Calorimeter (TileCal),

described in detail in Chapter 5, is one of the two components of the ATLAS calorimetry system which measures the energy of the hadronic particles and is the heaviest part of the ATLAS experiment. The Tile Calorimeter uses four main dedicated calibration systems to track the performance of the various detector components at each stage of the TileCal signal reconstruction. A more detailed discussion on calibration systems is given in Chapter 6. The laser Calibration system is one of the four systems which calibrate and monitors the 9852 photomultiplier tubes (PMTs) and detector readout electronics. The determination of the PMT response variation with the Laser system and the data analysis methods are detailed in Chapter 7. Finally, the description of the calibration procedure and the observed PMT response drifts during LHC Run-2 using laser calibration data are also discussed. During the development of this dissertation, all the results shown in this chapter were discussed and approved by the TileCal group as ATLAS TileCal public results Ref [24]. The results presented here are also a part of the TileCal internal note that is an input for a publication "Laser calibration of the ATLAS Tile Calorimeter during LHC Run-2" to be submitted to JINST. The results on the response of TileCal's PMTs are also included in "Operation and performance of the ATLAS Tile Calorimeter during LHC Run 2", to be submitted to EPJC. Both of the above-mentioned papers are in the final review stage in ATLAS Collaboration. A part of this work was also shown in a poster at LHCC 2020 poster session which was held on 19th Feb 2020. The conference proceedings are published in Moscow University Physics Bulletin Ref [25].

Chapter 8 of this dissertation is divided into three main sections highlighting the results of the modeling of PMT response evolution. The response of the photomultiplier tubes depends on its past operation, the amount of light collected, and the current delivered in hours, days, and weeks prior to its current use. The first section discusses the different approaches that were made during this dissertation work to quantify the response recovery of the PMTs during each **Y**ear **E**nd **T**echnical **S**tops (YETS) period of Run-2. The second section focuses on the different models studied to better understand the PMT response evolution including the response recovery as well as response loss as a function of machine Luminosity convoluted function. In the final and last section, the results of the model of Run-2 PMT response evolution as a luminosity convoluted function are used to predict the future PMT response evolution in Run-3 and Run-4 when the LHC will deliver higher luminosities, leading to even more significant trends in the photomultipliers responses. All the results shown in this chapter were shown and discussed in several internal TileCal meetings as well as in TileCal Calibration, Data Preparation, and Performance session

during Tile Week.

In the future, the Tile calorimeter will be equipped with 1000 new PMTs, so three test benches, one of them at CERN, have been developed in order to fully qualify all these PMTs. Besides this, the CERN test bench will also be used for the re-qualification of the old TileCal PMTs. The performances of this test bench are inspected for each type of measurement (amplification, quantum efficiency, photocathode efficiency, gain, dark current, linearity, and stability). The technical design and initial test results of some PMTs obtained with the CERN test bench are summarized in chapter 9.

Finally, the conclusion is drawn in Chapter 10.

Chapter 2

Calorimetry

Calorimetry is a powerful, versatile, and well-understood measurement method. Calorimetry in general is the science associated with the determination of the changes in energy of a system by measuring the heat exchanged with the surroundings. The term "Calorimetry" originates from thermodynamics, in which the calorimeters are thermally isolated boxes containing the substance of study. However, calorimetry in nuclear and particle physics refers to the detection and measurement of the properties of particles mainly energy but also position, direction, and time.

2.1 Calorimetry in particle physics

Particle detection is an important experimental tool in high-energy physics. Due to development in the energy resolution methods and properties of the calorimeters, calorimeters play a major role in particle detection. Initially, calorimetry was used in cosmic-ray studies, this method was then developed and excelled for accelerated-based particle physics experimentation.

Most particle physics detectors are equipped with calorimeters. Conceptually, calorimeters are the blocks of matter which are used to detect and measure particle properties. The interaction of incident particles with a sufficiently thick calorimeter is the core working principle of a calorimeter. These incident particles deposit all of their energy in a subsequent cascade of lower energy_particles, eventually dissipating most of the incident energy as heat. The incident particle interacts with the detector either only through electromagnetic processes or through electromagnetic and strong processes. Calorimetry can be broadly classified into two categories based on the nature of fundamental particle interactions.

2.1.1 Electromagnetic calorimetry

Charged particles and photons lose energy when they pass through dense materials due to electromagnetic (em) interactions (e.g. pair formation, bremsstrahlung). As a result of em interactions, the charged particles and photons generate more electrons and photons as the shower progresses. Electromagnetic forces are the best-known and well-understood forces that result in the energy-loss mechanisms inside the electromagnetic calorimeter. There are different processes through which em interactions manifest themselves, such as:

- Ionization: In this process, the incident particles of sufficient energy, knock out the atomic electrons of the medium by overcoming the Coulomb fields generated by the atomic nuclei.
- Excitation: In some cases, the incoming charged particle instead of ionizing, excite the atoms or molecules of the medium to lose their energy. When the atoms de-excite from these metastable states, they may release scintillation light which can be used as a signal in calorimeters.
- Cerenkov light: Cerenkov light is emitted by the medium if the incoming particles travel faster than the speed of light.
- Nuclear reactions: At very high energies, electromagnetic interactions will also induce nuclear reactions.
- Bremsstrahlung: At high energies, charged particles may lose their energy through bremsstrahlung.

In this section, the physics of electromagnetic calorimetry is discussed.

Electromagnetic cascade

For a charged particle traversing matter at considerably high energies ($\approx$ 10 MeV) usually, the bremsstrahlung process dominates the other electromagnetic interactions. As a result of Coulomb interaction with electric fields generated by the atomic nuclei, the traversing electrons and positrons emit photons. The emitted photons' energy spectrum decreases as 1/E. Figure. 2.1 shows the fractional energy loss in lead by positrons and electrons as a function of the energy.

As seen in Fig 2.1 the processes of average energy loss can be classified into two main energy regimes. For incident particles having energy $\geq$ 10 MeV, bremsstrahlung is the main

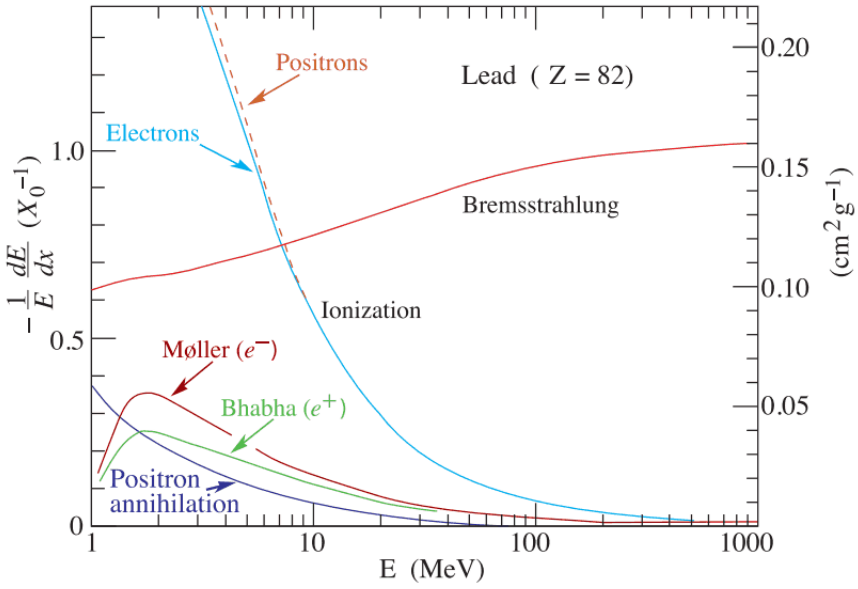

Figure 2.1: Fractional energy loss in lead as a function of positron or electron energy per radiation length Ref [1].

source of electron energy loss. On the other hand, in incident particles having lower energy, the electrons collide with the atoms and molecules of the material and as a result, lose their energy through ionization and thermal excitation. While at high energies of $\geq$ 1GeV these processes become approximately independent of energies. Hence electrons and photons striking a medium at very high energy ($\geq$1 GeV) produces secondary electrons and positrons through the process of pair production and secondary photons through bremsstrahlung. The secondary particles produce more particles following the same mechanism, thus creating a shower (cascade) of particles with progressively decreasing energies. The number of particles in the em shower continues to increase until the electron component of the shower reaches below certain energy called critical energy. Below the critical energy the particles of the shower instead of generating other particles, start losing their energy by excitation and ionization processes.
The lateral and longitudinal dimensions are basic features of electromagnetic showers and play a significant role when designing the electromagnetic calorimeter. The main features of em showers can be explained in terms of radiation length (X_0) and the Moliere radius ρ_M.

- Radiation length: The radiation length (X_0) is defined as the average distance (x) over which a sufficiently high energy ($\gg$ 1 GeV) positron or electron, on average loses

$\frac{1}{e}$ of its original energy (E_0) through bremsstrahlung mechanism. It is related to the mean path length of an electron in a material, as follows :

$$X_0(\frac{g}{cm^2}) = (\frac{716\ g\ cm^{-2}\ \mathrm{A}}{\mathrm{Z(Z+1)}\ ln(\frac{287}{\sqrt{\mathrm{Z}}})}) \tag{2.1}$$

where in Equation 2.1, A and Z are the atomic weight and an atomic number of the material and X_0 depends on the characteristics of the material.

- Moliere radius: The Moliere radius is used to describe the transverse development of electromagnetic showers. It can be defined as a ratio of radiation length X_0 and critical energy ϵ_c as Equation 2.2:

$$\rho_M = E_s \frac{X_0}{\epsilon_c} \tag{2.2}$$

where E_s is the scale energy which is defined as Equation 2.3:

$$E_s = m_e c^2 \sqrt{\frac{4\pi}{\alpha}} \tag{2.3}$$

The numerical value of E_s from Equation 2.3 is equal to 21.2 MeV (Ref. [26]). On average, a cylinder of radius $\approx 1\rho_M$ contains 90% of the shower energy.

The rate at which electrons lose energy due to bremsstrahlung is determined by the radiation length as Equation 2.4:

$$\langle E(x) \rangle = E_0 e^{-\frac{x}{X_0}} \tag{2.4}$$

where E_0 is the original energy of an electron while x represents the average distance traveled by an electron in material to lose its energy to $1/e$ of its E_0.
Similarly, the rate at which photon beams traversing a medium loses $1/e$ of its original intensity I_0 at a distance of $x = \frac{9}{7}X_0$ (Ref. [27]) through pair production mechanism can be written in terms of radiation length as Equation 2.5:

$$\langle I(x) \rangle = I_0 e^{-\frac{7}{9}\frac{x}{X_0}} \tag{2.5}$$

The above Equations 2.4 and 2.5 indicate that the development of em shower for incident electrons and photons defined in terms of radiation length (X_0) are similar to each other regardless of the nature of the material. Hence, the basic features of the em showers can be

described by a simple radiation length function.

Electromagnetic calorimeters energy resolution

An electromagnetic calorimeter measures energy on a basic principle i.e. the energy of the incident particle is proportional to the energy released in the detector material through excitation or ionization by the charged particles in the shower.
Besides radiation length and Moliere radius, critical energy ϵ_c is also an important parameter to describe the structure and dimensions of em showers. The critical energy (ϵ_c) is defined in two ways which are slightly different from each other. According to one definition (ϵ_c) is the energy at which the two main energy loss processes i.e., ionization and bremsstrahlung become equal to each other. This energy depends only on the characteristics of the material and is written for solids (gases) as Equation 2.6 Ref [27]:

$$\epsilon_c = \frac{610(710)\ \text{MeV}}{\text{Z} + 1.24(0.92)} \tag{2.6}$$

According to the other definition Ref [28], critical energy (ϵ_c) is the energy at which the ionization loss per radiation length (X_0) is equal to the energy of an electron written as Equation 2.7:

$$\frac{dE}{dx}(ionization) = \frac{E}{X_0} \tag{2.7}$$

Both definitions would be equivalent at higher energies when the ionization loss becomes negligible i.e.,

$$\frac{dE}{dx}(bremsstrahlung) \approx \frac{E}{X_0} \tag{2.8}$$

The basic principle of energy measurement with an electromagnetic calorimeter is that the energy released by the charged particles of the shower through ionization and excitation is proportional to the energy of the incident particle. The sum of all ionization tracks created by the charged particles in the cascade is defined as the total track length T_0 of the shower. The track length is proportional to the number of particles in the shower and the energy of the original particles 2.9. To measure the internal energy resolution of an em calorimeter, track length (T_0) is an important parameter.

$$T_0(\frac{g}{cm^2}) \propto X_0 \frac{E_0}{\epsilon_c} \tag{2.9}$$

where $\frac{E_0}{\epsilon_c}$ is the total number of particles in the shower.
For an ideal calorimeter, the intrinsic energy resolution is mainly dominated by the track length (T_0) fluctuations. Since (T_0) and the shower track segments number are proportional to each other, the internal energy resolution based entirely on statistics is given by Equation 2.10:

$$\sigma(E) \propto \sqrt{T_0} \tag{2.10}$$

From above Equation 2.10, the actual energy resolution for a non-ideal calorimeter (Realistic) generally can be written as Equation 2.11:

$$\frac{\sigma}{E} = \frac{a}{\sqrt{E}} \oplus \frac{b}{E} \oplus c \tag{2.11}$$

where the symbol $'\oplus'$ stands for a quadratic sum. The different terms in the above Equation 2.11 are explained below:

- **Stochastic term**: The first term $\frac{a}{\sqrt{E}}$ is called the 'stochastic term' which is introduced due to the shower intrinsic fluctuations. These intrinsic fluctuations are small in homogeneous calorimeters because the energy deposited in the active volume of the detector by an incident homogeneous beam of particles does not fluctuate event by event. However in sampling calorimeters, as the active layers are interleaved with absorber layers, the deposited energy in the active medium of sampling calorimeters fluctuates event by event. Hence the intrinsic fluctuations in sampling calorimeters are large and are called *sampling fluctuations*.
- **Noise term**: The second term $\frac{b}{E}$ on the right hand is the noise term. Depending on the techniques used by the detector and the characteristics of the readout circuits, an electronic noise may be introduced in the readout chains, adding up to the noise term. In sampling calorimeters, the sample fraction can be increased to reduce the noise because the larger the sampling fraction, the larger the signal from the active medium and hence the higher the signal-to-noise ratio.
- **Constant term**: The last term in the Equation 2.11 is the constant term which includes all the contributions which are independent of particle energy. The constant term contributes more and more to the energy resolution of electromagnetic calorimeters as the energy of accelerators increases. With the advancement of the calorimeters, this term is becoming the most dominant contribution to the electromagnetic calorimeters' energy resolution.

- **Additional factors**: There are also some additional factors contributing to the energy resolution of electromagnetic calorimeters, namely longitudinal and lateral leakages, upstream energy losses, and non-hermetic coverage. All these contributions are introduced mainly due to the limitations to which a calorimeter is subjected when installed in a big experiment which leads to non-uniformity and imperfection in construction.

In the ATLAS experiment at CERN, the intermediate energy resolution technique is prioritised to gain a uniform response leading to the powerful capability of particle identification and angular measurement, while the CMS experiment although motivated by the same physics goal focused on the excellent internal energy resolution.

2.1.2 Hadronic calorimetry

Calorimeters dedicated to the measurements of hadrons (mostly protons, neutrons, and pions) are known as "hadronic calorimeters". Hadronic calorimetry is more complicated than electromagnetic (EM) calorimetry mainly due to the involvement of "strong forces" in the energy deposition process of hadrons. In this section nature of hadronic showers and the energy resolution in hadronic calorimetry have been discussed.

Hadronic cascade

When a hadron traverses through a dense medium it loses its energy (mostly) through strong interactions with the calorimeter material. Due to the nature of strong interactions, a certain fraction of energy produced is *fundamentally undetectable* referred to as "invisible energy". As a consequence hadronic showers are far more complicated than electromagnetic showers.
The strong interaction between a high energy hadron and a block of matter of the medium produces a combination of two phenomena, one at the particle level and the other at the nuclear level.

- **Particle level**: When a charged hadron traverses the medium, it ionizes the atoms of the medium thus producing a continuous chain of events leading to the production of hadronic shower particles. The majority of these particles are pions. The neutral pions decay in $2\gamma's$ producing a particle shower that is very similar to an em shower.

- **Nuclear level**: When a sufficiently high energy hadron penetrates a dense material, it knocks out the neutrons and protons from the atomic nuclei. The fraction of the

shower energy used to break the nuclear binding energy of these nucleons is termed is *invisible-energy*, as it does not contribute to the calorimetric signal. The invisible energy can also come from muons, neutrinos, or neutrinos escaping. For neutral hadrons, the only option to lose their energy is through nuclear reactions as they do not ionize the medium. The particles produced in first-generation nuclear reactions (mesons, $\gamma's$, nucleons) either lose their energy through ionisation or initialize second generation nuclear reactions thus generating a hadronic particle shower.

At first the number of hadronic shower particles and the energy deposited by them in a block of matter of given thickness increases as a result of the multiplication process. But, after a certain depth, the multiplication and the absorption of shower particles balance each other resulting in the gradual decrease of the number of shower particles and their deposited energy in given the block of matter.

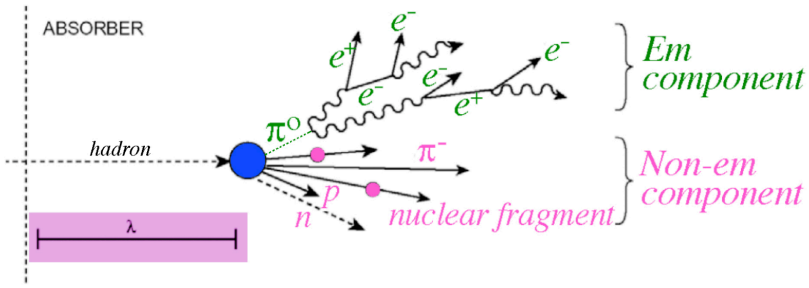

Figure 2.2: Schematic depiction of the Physics of Hadron Shower Development. The figure is taken from Ref [2].

As seen in Fig 2.2 the energy of the hadron is typically divided into two main components, both of which are responsible for the fluctuation in hadronic showers:

- **Electromagnetic component**: The electromagnetic component which includes electrons (e), photons (γ) and neutral pions (π^0) of the hadronic shower decays

through electromagnetic interactions. EM component is responsible for large and non-Gaussian fluctuations in the hadronic shower.

- **Hadronic (non-em) component**: The non-em component includes charged hadrons (π^{+-}, K^{+-}), nuclear fragments, neutrons, soft $\gamma's$ and break-up of nuclei ("invisible"). The *invisible energy* does not take part in signals detected by the calorimeter.

In reality, the energy dependence of both components in a hadronic shower is complicated, due to the involvement of certain other factors. According to a study Ref [29], the energy dependence of electromagnetic components of hadronic showers is governed by a power law:

$$f_{em} = 1 - (\frac{\mathrm{E}}{\mathrm{E_0}})^{\mathrm{k}-1} \tag{2.12}$$

where in Equation 2.12, E_0 is a scale factor, which is defined as the average energy required to produce a pion (π^0) while k in the exponent can be defined as the energy dependence of the em shower fraction. It is determined by two parameters: the average fraction of π^0 production (f_{π^0}) and the average multiplicity $\langle m \rangle$ per nuclear interaction. Hence the k can be expressed as Equation 2.13:

$$1 - f_{\pi^0} = \langle m \rangle^{(k-1)} \rightarrow k = 1 + \frac{\ln\left(1 - f_{\pi^0}\right)}{\ln \langle m \rangle} \tag{2.13}$$

In general, Equation 2.12 can also be written as Equation 2.14 provided that $\frac{\mathrm{E}}{\mathrm{E_0}}$ corresponds to the total number of pions that would be produced by a shower initiated by a hadron of energy E in the absence of an electromagnetic component of the shower.

$$f_{em} = 1 - \langle m \rangle^{\mathrm{n(k-1)}} \tag{2.14}$$

where n is the number of generations which depends on the energy E of the particle that initiated the shower.

Thus generally the dependence of em shower component is measured by the number of pions (π_0) produced in the shower development per unit of energy, i.e., the value of parameter $\frac{1}{E_0}$. In general, a good agreement could be brought between Equation 2.12 and the energy dependence of the average em fraction of hadron showers, in a given absorber material by choosing suitable values of k and E_0 parameters. The shape of a hadronic shower is different from the one in an electromagnetic shower due to the em component

fluctuations and strong interaction characteristics. The development of a hadronic shower depends significantly on nuclear interaction, and thus the shower dimensions are governed by the average distance covered by a high-energy hadron inside an absorber medium before a nuclear interaction occurs. This distance is termed as nuclear interaction length λ_{int} of an absorber medium The probability of a particle traveling through a medium that covers a distance z without having nuclear interactions is given by:

$$P = \exp\left(-\frac{z}{\lambda_{int}}\right) \tag{2.15}$$

Nuclear interaction length (λ_{int}) is inversely proportional to the total nuclear interactions cross-section :

$$\sigma_{tot} = \frac{A}{N_A \lambda_{int}} \tag{2.16}$$

where N_A is the Avogadro's number, A is the mass number of absorber material, and σ_{tot} mentioned in the Equation 2.16 is measured by the size of target nuclei and projectiles. Nuclear interaction length λ_{int} is the average distance covered by a high energy hadron till its energy has been lessened to $\frac{1}{E}$ of its original energy. According to a numerical approximation, nuclear interaction length is related to the density of absorber material as:

$$\lambda_{int}[gcm^{-2}] \approx 35A^{\frac{1}{3}} \tag{2.17}$$

Hence the properties of hadron showers depend critically on the details of the absorber. Typically the thickness of hadronic calorimeters at LHC experiments is 10 nuclear interaction lengths.

Hadronic calorimeters energy resolution

The characteristics of the electromagnetic component of the hadron shower also have some important consequences on the energy resolution of hadronic calorimeters along with their signal linearity and the response function. Because of the *invisible energy* and the large fluctuations in the cascade, the resolution of the hadronic calorimeter is significantly worse than that of the electromagnetic calorimeter. Hence with equal incident energy, the response of the signal to hadrons is lower than the signal response to electrons i.e., $\frac{e}{h} > 1$. The condition where $\frac{e}{h} \neq 1$ is termed as non-compensation and the corresponding calorimeter is called as non-compensating calorimeter. Event by event, the visible energy of the hadron-induced cascade usually varies between fully electromagnetic and fully hadronic

energy (with a maximum of invisible energy) deposit. For non-compensating calorimeters with $\frac{e}{\pi} \neq 1$ following conclusions can be drawn :

- Fluctuations in the fractions of average pions π^0 production (f_{π^0}) are the major part of energy resolution in hadronic calorimetry.
- Since the electromagnetic fraction (f_{em}) of a hadronic shower is energy dependent therefore the response of the calorimeter is non-linear for hadron detection.
- The fluctuations in the fractions of π^0 production (f_{π^0}) are non-gaussian and thus the energy resolution scales for hadron calorimeters is weaker than $\frac{1}{\sqrt{E}}$.

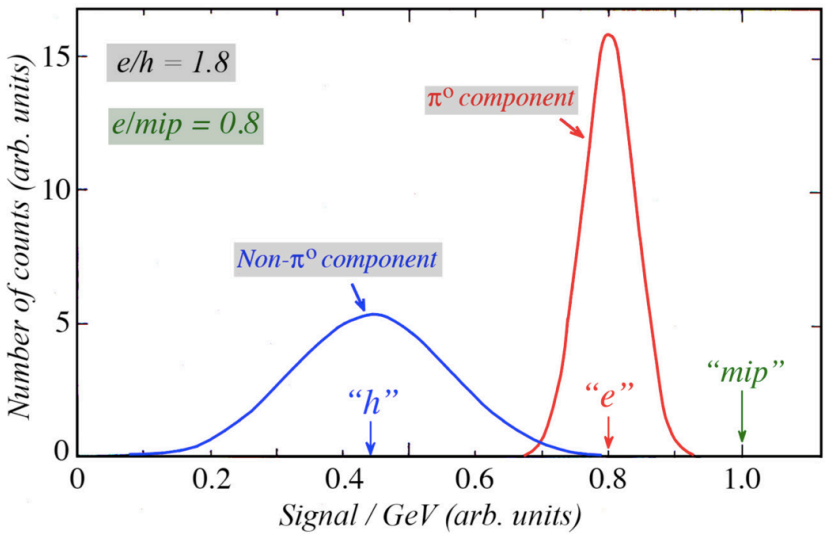

Figure 2.3: The calorimeter response to the em and non-em components of hadron showers for a non-compensating calorimeter Ref [2].

The Figure 2.3 illustrates the schematic representation of the response of the signal per unit deposited energy separately for the electromagnetic and hadronic components of hadron showers, where "e" stands for em response, "h" for hadronic (non-em) response and "mip" is the response of minimum ionizing particles in a hadronic shower. These distributions are normalized to the mip response. The ratio of the em and hadronic responses is called as e/h value of the calorimeter. In the Figure 2.3, for a shower induced by a high energy pion the ratio $e/h = 1.8$. This indicates that the response function of the calorimeters

containing both em (e) and non-em (h) components centers around a mean value in between them. This mean value is determined by the average energy ($\langle f_{em} \rangle$) shared between em and non-em components of the shower. Since with the increase in energy the $\langle f_{em} \rangle$ also increases, the calorimeter is hence non-linear for pion detection.
The value of ratio e/h cannot be determined directly. Instead, it can be derived from the relationship between e/π and e/h, i.e.:

$$\frac{e}{\pi} = \frac{\frac{e}{h}}{1 - \langle f_{em} \rangle (1 - \frac{e}{h})} \tag{2.18}$$

Those calorimeters which pull off the compensation for the loss of invisible energy are called "compensated" calorimeters and they have $e/\pi = 1$. To optimise the performance, it is possible to 'tune' the e/π response of a certain calorimeter to attain $e/\pi = 1$. But this is a very remarkable and rare property to achieve. Most practical used calorimeters are under-compensating, with e/h values typically varying between 1.5 and 2.0. Ref.[26].

A non-trivial method to determine the hadronic calorimeter signal response is with respect to minimum-ionizing particles (mip) signals. For instance, in a hadronic shower, $\frac{h}{mip}$ can be defined as the signal produced by a hadron to that of a mip, the relative response of purely hadronic component $\frac{\eta_h F_h E}{mip}$ can be written as:

$$\frac{h}{mip} = (\frac{f_{ion} ion}{mip} + \frac{f_n n}{mip} + \frac{f_\gamma \gamma}{mip}) \tag{2.19}$$

where $\frac{h}{mip} = \frac{\eta_h F_h E}{mip}$ and f_{ion}, f_n, f_γ represents the average fractions of ionising hadrons, neutrons and photons respectively. Typically energetic hadrons lose comparatively less energy ($< 10\%$) through the ionization process before going to such low energies where other nuclear processes begin to dominate. Thus, in the absorber and in the active materials energy resolution of the calorimeter is more affected by $\frac{\gamma}{mip}$ and $\frac{n}{mip}$ values.
The response of the hadron calorimeter to the full shower including both components can be written as follows:

$$R = \epsilon_h E_h + \epsilon_{em} E_{em} \tag{2.20}$$

where fractions of the average hadronic and em shower component are shown in Equation 2.21 and Equation 2.12 respectively.

$$F_h = (\frac{E}{E_0})^k \tag{2.21}$$

while ϵ_h and ϵ_{em} stands for the efficiency of calorimeter to detect hadronic and electromagnetic components of shower with E_h and E_{em} energies respectively. The ratio $\frac{E_{em}}{E_h}$ is dependent on the fluctuations in a particular event which can be measured by the variation of the event by event production of total pions π^0. For a hadronic calorimeter the response of the ratio between electrons and pions of the same energy in terms of efficiencies is written as:

$$(\frac{e}{\pi})^{-1} = 1 - (1 - \frac{\epsilon_{em}}{\epsilon_h})F_h \tag{2.22}$$

For a compensating calorimeter the ratio $\frac{\epsilon_{em}}{\epsilon_h}$ is equalized to 1, otherwise, it would be a "non-compensating calorimeter". Thus the major parameter controlling the overall performance of a hadron calorimeter is $\frac{\epsilon_{em}}{\epsilon_h} = 1$, which promise linearity, energy resolution of $\frac{1}{\sqrt{E}}$ scaling and best resolution. Practically hadron calorimeters are always built as sampling devices in which the energy is sampled in the active layers which is essentially a very small percent of the total incident energy. The response can be adjusted to acquire $\frac{\epsilon_{em}}{\epsilon_h} \approx 1$ by choosing the appropriate thickness and kind of active and passive materials.

2.2 Future calorimetry

In the past few years, post-LHC era discussions have mainly concentrated on a high-energy electron-positron collider with a center of mass energy that would allow the machine to produce $t\bar{t}$ and Higgs boson in sufficient amounts. In this regard, both linear and circular colliders are being considered. Different approaches developed to the calorimeter systems for this task are discussed in this section.

2.2.1 Calorimetry in TeV regime

Advancement in the understanding of matter and its characteristic properties has led to the construction of ever more powerful particle accelerators. The best possible precise measurements of four vectors (i.e., energy and momentum) of the scattered particles could be achieved by detectors at these powerful colliders. At the TeV regime, these scattered particles are either leptons, photons, gluons, di-quarks, or fragmenting quarks (normally referred to as jets). One of the goals of the future electron-positron collider calorimeters is to differentiate between hadronically decaying W and Z bosons. The condition that the di-jet masses of hadronically decaying W and Z bosons are separable by at least one Rayleigh

criterion indicates that jets of 80-90 GeV should be detectable with a resolution of 3-3.5 GeV. For single hadrons this condition has been achieved with compensating calorimeters, but not for jets. However, in the em shower development, the signals generated by the neutrons would require large volumes and time to achieve em energy resolution. But, practically in compensating calorimeter sampling fraction is relatively small. Due to this sometimes it is not possible to achieve this resolution goal in practice.
The calorimetric energy resolution is sometimes expressed as $\frac{1}{\sqrt{E}}$ which is incorrect in the TeV domain due to the dominance of non-Poissonian fluctuations at high energies. Often it is assumed that the effect of non-compensation on energy resolution is a "constant term" (energy independent), which is incorrect. At high energies, the effects of Poisson statistics become very small and thus the fluctuations in the em shower component start dominating the calorimetric resolution. Therefore energy dependence becomes the dominant characteristic for this resolution. The fluctuations in f_{em} can be described more appropriately by a term "l" which accounts for Poissonian fluctuations:

$$\frac{\sigma}{E} = \frac{a_1}{\sqrt{E}} \oplus a_2[(\frac{E}{E_0})^{l-1}] \tag{2.23}$$

Where E_0 is a constant which depends on the material. In hadronic interactions E_0 is related to the average multiplicity. For high Z-absorber materials, E_0 value is a factor of two larger than other materials Ref [26]. The parameter a_2 is a measure of the non-compensation in a calorimeter. Its value varies between $0 \rightarrow 1$ where 0 and 1 are for extremely compensating and non-compensating calorimeters respectively. In between these values a_2 can be expressed as linearly dependent on $\frac{h}{e}$ Ref [30].

$$a_2 = |1 - \frac{h}{e}| \tag{2.24}$$

In the current energy regime (up to 400 GeV) the hadronic energy resolution can be written as a linear sum of a constant and stochastic term Ref [31]:

$$\frac{\sigma}{E} = \frac{c_1}{\sqrt{E}} + c_2 \tag{2.25}$$

In current (GeV) energy scale $c_1 > a_1$, where c_1 and a_1 are stochastic parameters in Equation 2.25 and Eq 2.23 respectively. However, in the TeV scale, the similarity between these two expressions vanishes due to the effects of fluctuations in f_{em} in the hadronic energy resolution.

To summarise at TeV regime, precise measurements of four vectors are an important aspect of accelerator-based experiments. In the future with a better understanding of hadronic components of matter at high energies, one can expect to measure the energy and momentum of all the elementary particles within a precision of $\pm 1\%$ or more.

2.2.2 Dual-Readout calorimetry

Besides compensation, dual-readout calorimetry is also an approach to improve the energy resolution of the hadronic calorimeter. However in compensating calorimeters the requirement to use high-Z absorber material e.g., uranium or lead makes it less efficient. The main drawback of using high Z-absorber materials in compensating calorimeters is the difficulty to acquire compensating conditions i.e, $e/h = 1.0$ due to the following reasons:

- They produce a large number of neutrons.
- They decrease the response of electromagnetic shower by removing the contribution of fluctuations of em shower fraction f_{em}.

An alternative approach to getting rid of the effects of the fluctuations introduced by the em shower fraction (which becomes dominant in hadronic energy resolution for non-compensating calorimeters) is to calculate f_{em} for every individual event. This approach can be achieved by the Cerenkov mechanism which is the basis of the "Dual-REAdout method" or DREAM. Calorimeters that use Cerenkov light as a source of signal, only respond to the em fraction of hadronic showers.
In the Dual-Readout calorimetry approach the em shower fraction f_{em} can be measured by comparing the relative strengths of the detectable deposited energy signals (dE/dx) and the Cerenkov light produced in the shower absorption process. The total shower energy in this case can be reconstructed using the known value(s) of e/h of the calorimeter. Thus the calorimeter following dual-readout calorimetry deals with two types of signals in the production of showers namely a scintillation signal (S) and a Cherenkov signal (C). Calibration of these signals can be done with electrons of energy E. For a certain event, the hadronic response of such calorimeters is given by:

$$\begin{aligned} R_S &= f_{em} + \frac{1}{(\frac{e}{h})_S}(1 - f_{em}) \\ R_C &= f_{em} + \frac{1}{(\frac{e}{h})_C}(1 - f_{em}) \end{aligned} \tag{2.26}$$

for em showers the signals are calibrated such that $\langle S\rangle = \langle C\rangle = E$ and the calorimeter response is $R_{em} = \frac{\langle S\rangle}{E} = \frac{\langle C\rangle}{E}$. Equation 2.26 states that the hadronic response of dual-readout calorimetry can be expressed as a sum of an electromagnetic (f_{em})and hadronic component $(1 - f_{em})$ of the shower. The reconstructed energy of calorimeter if $f_{em} < 1$ and $e/h \neq 1$ will be smaller than E:

$$\begin{aligned} S &= E[f_{em} + \frac{1}{(\frac{e}{h})_S}(1 - f_{em})] \\ C &= E[f_{em} + \frac{1}{(\frac{e}{h})_C}(1 - f_{em})] \end{aligned} \tag{2.27}$$

The dual-readout method works only because $(e/h)_S \neq (e/h)_C$ and it is better if the difference between these values is larger. Thus the drawbacks of the compensating calorimeters can be eliminated by the Dual-Readout Method or DREAM due to the following reasons:

- Excellent em energy resolution could be achieved provided the fact that the sampling fraction of the calorimeter can be selected as desired using this method.
- The dual-readout method does not depends on the detection of neutrons, hence there is no need to integrate signals over large times and calorimeter size.
- There is no requirement to use high-Z absorber materials for this method resulting in less massive detectors and better energy resolution.

Until now, the DREAM project has been successful as it gives maximum flexibility in detector composition as well as eliminates the drawbacks of compensating calorimetry. Therefore, dual-readout calorimeters provide better-quality calorimetry for all kinds of particles.

2.2.3 Particle flow analysis

In order to recognize, reconstruct and separate the hadronically decaying W and Z bosons in high-energy experiments, an entirely different approach has been proposed which is known as "Particle Flow Analysis" or PFA. The basic idea of this technique revolves around a precision tracker and calorimeter of high granularity, in which the precision tracker can be used to precisely measure the charged jet particles while with the calorimeter the energy

of the neutral particles is measured. This principle has been successfully used to improve the performance of experiments with hadronic calorimetry, however, the improvements are fundamentally limited.
The major drawback of this technique is that it is unable to distinguish whether the absorbed particles in the calorimeter are electrically charged or not. Therefore for the contributions of charged jet particles, correction should be applied to the detected calorimeter signals.
There is a number of different algorithms designed to investigate the maximum extent to which the hadronically decaying W and Z bosons can be separated using particle flow-based detector systems. All these algorithms conclude that the performance of particle flow analysis is dependent on reconstruction software and a detector with fine granularity.

Chapter 3

Calorimeters Energy Response

Calorimeters are blocks of instrumented material in which particles to be measured are fully absorbed and their energy transformed into a measurable quantity. The interaction of the incident particle with the detector (through electromagnetic or strong processes) produces a shower of secondary particles with progressively degraded energy. The energy deposited by the charged particles of the shower in the active part of the calorimeter, which can be detected in the form of charge or light, serves as a measurement of the energy of the incident particle.

In this chapter, the calorimeter response is emphasized. The term "calorimeter response" is defined as the average calorimeter signal per unit of deposited energy of the incident particle. Thus depending on the signal-generating mechanism, the calorimeter response is expressed in terms of units such as photoelectrons per GeV or pico-coulombs per MeV, etc. If the calorimeter response is constant to the incident particles then it is said to be linear for the detection of those particles.
Every calorimeter is characterized by its two constants, both of which are independent of energy.

- $\frac{e}{h}$: It is related to the electromagnetic and non-electromagnetic components of hadron showers. In general, the e/h ratio cannot be determined directly, but instead, it can be deduced using the known energy dependence of average em shower fraction $\langle f_{em} \rangle$.
- $\frac{e}{mip}$: This constant is related to the calorimeter responses to electrons and minimum ionizing particles. Similar to e/h, this ratio also cannot be determined directly, but it has to be deduced from e/μ signal ratios measured at different energies.

In the following, the calorimeter response of different types of calorimeters is discussed.

3.1 Homogeneous calorimeters

In a homogeneous calorimeter, the signal generating and the particle absorbing phenomena are done by a single medium, and thus the entire detector volume contributes to the generated signal. Due to the fact that the entire energy of an incident particle is absorbed in the active medium, these calorimeters provide excellent energy resolution. Homogeneous calorimeters cannot be easily segmented laterally and longitudinally, hence they are less suitable for position measurements and particle identification. These calorimeters are almost entirely used for electromagnetic calorimetry.
Homogeneous calorimeters can be broadly classified into four classes:

- **Scintillator calorimeters**: In scintillator calorimeters, the signal is collected in the form of light which is produced by the ionization tracks of the medium material.
- **Semiconductor calorimeters**: In these calorimeters, an electric signal is generated by the electron-hole pairs produced in the conduction and valence bands of the material. These calorimeters give an excellent energy resolution.
- **Cherenkov calorimeters**: In these calorimeters, a transparent material is used as the medium. The Cherenkov photons are produced by relativistic $e^{\pm}$ in the shower. Therefore the signal is collected in the form of light.
- **Noble liquid calorimeters**: In a noble liquid calorimeter the medium is a noble gas (e.g. Argon, krypton, and xenon). These gases operate at cryogenic temperatures. In these calorimeters both scintillation and ionization, signals can be collected. The liquid krypton electromagnetic calorimeter present at the NA48 experiment at the CERN SPS is an example of a homogeneous noble liquid calorimeter.

As mentioned earlier in homogeneous calorimeters the entire detector volume contributes to signal generation. The response of homogeneous calorimeters to different particles is given in the following subsections.

3.1.1 Response to electrons and photons

In homogeneous calorimeters, the entire kinetic energy of the absorbed electrons and photons is used to excite the atoms and molecules of the calorimeter medium. When returning to the ground state, these atoms and molecules emit some of the excitation energy in the form of scintillation light which constitutes the calorimeter signals.

3.1.2 Response to muons

In homogeneous calorimeters, the muons, similar to shower particles in em shower development, also lose their kinetic energy through the excitation of the atoms and molecules of the calorimeter medium. Due to the same behavior of muons and em shower particles, the response of homogeneous calorimeters to both is also the same. Thus the average signal produced by a muon traversing the homogeneous calorimeter is equal to the average signal generated by an absorbed electron or photon during the shower development. Thus for homogeneous calorimeters, we can also say that:

$$\frac{e}{mip} = 1 \tag{3.1}$$

where mip and e represent the response of homogeneous calorimeters for minimum ionizing particles and em showers respectively.

3.1.3 Response to hadrons

For hadrons and jets, only a part of their energy is used to excite atoms and molecules of the calorimeter medium which contribute to the signals. The other part of the energy is used to dissociate atomic nuclei known as *"invisible energy"* and does not contribute to the calorimeter signals. Thus the response of homogeneous calorimeters to hadron-induced showers is smaller as well as energy dependent. For the detection of hadrons and jets, the homogeneous calorimeters are *intrinsically non-linear*. This is due to the presence of the em component in the hadronic shower, which is energy-dependent. Thus the calorimeter response to the em component of the hadrons-induced showers increases with the increase in energy. Therefore, the signal ratio h/e also increases with energy.

3.1.4 Response to jets

A jet is defined as a cluster of particles, generated by the fragmentation of a hard gluon, quark, or di-quark during collisions. The response of jets is almost similar to that of an individual hadron. Similar to an individual hadron, the energy of jets is also deposited in the form of both em showers and non-em showers during their absorption in the calorimeter medium. However, there are two minor differences in the components.

- Due to the difference in the fragmentation process the average em shower fraction $< f_{em} >$ is different for jets and individual hadrons of the same energy.

- In hadron-induced showers the em component is due to the result of $\pi^0 s$ production inside the calorimeter, while jets upon entering the calorimeter usually contains a number if γs or $\pi^0 s$ from their decay.

However, the response of homogeneous calorimeters to jets and individual hadrons is very similar and energy-dependent.

3.2 Sampling calorimeters

In a sampling calorimeter, the signal generating and the particle absorbing phenomena are done by two different media, known as passive and active medium respectively. In contrast with homogenous calorimeters, sampling calorimeters results in lower energy resolution due to the fluctuations introduced by the absorber layers interleaved with the active layers. However, they provide better position measurements and particle identifications owing to the fact that they are easy to segment laterally and longitudinally. Sampling calorimeters are used for both electromagnetic and hadronic calorimetry.

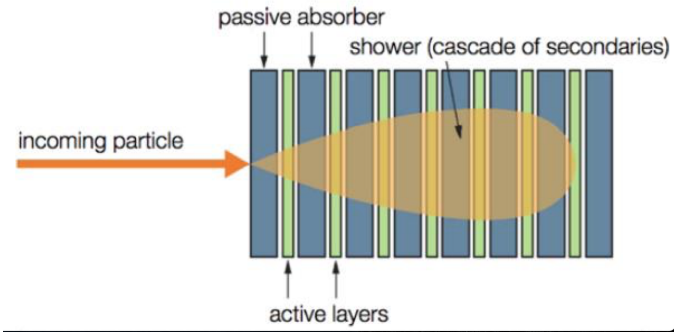

Figure 3.1: Scheme of a sandwich/sampling calorimeter

On the basis of the type of active medium, sampling calorimeters can be broadly classified into four types:

- **Scintillation calorimeters**: A scintillation sampling calorimeter uses plastic scintillators arranged in plates or fibers. The output signal is collected in the form of light. These detectors have a fast response and can be made compensating by properly tuning the ratio between the amount of scintillator and absorber material.

- **Gas calorimeters**: In gas sampling calorimeters gases are used as an active medium. When a charged particle passes through a gas-filled volume under a high-voltage

field, a discontinued number of ionizing collisions takes place. This process creates electron-ion pairs producing secondary electron-ion pairs. Thus the internal amplification of the charge produced by the ionizing particle in the gas facilitates signal processing. However due to several factors such as Landau fluctuations and active layers path length variation, the electromagnetic energy resolution is not very good i.e., ($\leq 20\%\sqrt{\mathrm{E(GeV)}}$) in gas sampling calorimeters. The sampling fraction of these calorimeters are also small ($<< 1\%$) due to the low density of the active medium. Thus to obtain an acceptable signal-to-noise ratio, a large voltage is applied on the wires in the active medium which produces avalanche multiplication of electrons and yields signal gains of $10^3 - 10^5$. However, the gain in gas calorimeters is sensitive to several factors and thus the uniformity and the stability of the detector response are moderate.

- **Liquid calorimeters**: In liquid calorimeters, liquified noble gases such as krypton, argon, or xenon are used as active medium. All the liquid-based calorimeters operate in the ionization-chamber mode, in which a signal is formed by electrons produced during the ionization process.
  In noble-liquid calorimeters, two parallel metal plates define a basic active element. A potential difference ΔV is applied and a liquid sampling medium is filled between the gap of two parallel plates. The atoms in the liquid ionize when a charged shower particle passes through this gap. The produced ions and electrons move toward the respective electrodes forming the calorimeter signal.

- **Solid-state calorimeters**: In solid-state sampling calorimeters semiconductors such as silicon are used as an active medium. The basic charge carriers in these calorimeters are electron-hole pairs generated along the path of the ionizing particle. These calorimeters provide a higher signal-to-noise ratio as compared to gas calorimeters due to the higher density of active layers. Whereas a comparable signal-to-noise ratio with respect to liquid argon (LAr) calorimeters can be achieved with smaller sampling fractions. Thus silicon-based calorimeters are very compact in construction.

In sampling calorimeters, the *sampling fraction* is an important parameter. The sampling fraction of a calorimeter is defined as the energy deposited by mip in the active calorimeter layers, measured relative to the total energy deposited by these particles in the calorimeter. However the calorimeter response to mip cannot be measured directly, but it is usually determined indirectly from the signal distributions for different energies of muons. In this

Section, the response of sampling calorimeters to different particles is discussed in detail.

3.2.1 Response to electrons and photons

The electrons or photons passing through the active layers of the sampling calorimeter either excite or ionizes these layers which form the basis of calorimeter signals. However, this signal is different from the signal generated by the minimum ionizing particles (mip) passing through the calorimeter with the same energy. This difference is due to the dependence of the em signal on the Z values of the absorber and active material. In the sampling calorimeter, the response of the em showers highly depends on the atomic number "Z" of the active and absorber materials. Experiments have shown that if the difference between the Z values of the absorber and active medium is larger, the value of e/mip becomes smaller i.e. $e/mip < 1$. The term *transition effect* was introduced by Pinkau Ref [32] for the decrease of the response of em shower in sampling calorimeters with higher values of Z absorber material. According to Pinkau this apparent suppression in the signal response of em shower in sampling calorimeters is due to the effects taking place at the boundaries of the active and absorber materials having different Z values. Additionally, there are other factors involved in the signals generated by electrons, photons, and muons in sampling calorimeters as follows:

- Spatial dependence of the em response,
- Sampling frequency and em response.

3.2.2 Response to muons

The sampling calorimeter response to muons is a complex topic as a number of different processes are involved in the signal generation of muons. When a high energy muon passes through a calorimeter medium, it can radiate an energetic bremsstrahlung photon (E > 1 GeV), bremsstrahlung photons of lower energy as well energetic knock-on electrons ($\delta - rays$). Each of these events has its own specific response. The high energy bremsstrahlung photon develops an em shower which is sampled in a similar way as other em showers. For the low-energy bremsstrahlung photons, the response of the calorimeter is energy-dependent. While for the energetic knock-on electron $\delta - rays$, the energy deposited as primary ionization as well as the energy carried by these electrons depends on the Z-value of the absorber and active material. It is impossible to disentangle event by event the various responses to the calorimeter signals therefore, this problem can only be solved by using statistics.

3.2.3 Response to hadrons

During the absorption of hadrons in a sampling calorimeter medium various shower particles are produced, which can be divided into four different classes:

- **Relativistic hadrons** consisting of second or higher-order pions,
- **Non-relativistic hadrons** consisting of spallation protons,
- **Evaporation neutrons** produced with few MeV energies,
- **Electrons and positrons** through which em shower component energy is deposited.

The response of the sampling calorimeter to the above-mentioned classes of shower particles is used to determine the e/h ratio. Once the ratio of e/h is known, the response of the calorimeter to hadrons can be deduced from the energy dependence of $< f_{em} >$ in the hadronic shower development.

3.2.4 Response to jets

In sampling calorimeters, the calorimeter response to jets is equal to the responses of all the particles which constitute jets. Jets are composed of a mixture of γs and hadrons. Similar to homogenous calorimeters the jets' response are same as the response of individual hadrons. However, for jets, the average electromagnetic shower fraction $< f_{em} >$ is different from that of the individual hadrons. Therefore, the response of the jet is different from the response of individual hadrons in non-compensating calorimeters. In compensating calorimeters, their response is the same as the em and non-em energy responses are same.

3.3 Linearity

A linear calorimeter is one in which the deposited energy of the detected particle is *proportional* to the average signal produced by the calorimeter.

Linearity is a very important parameter of calorimeters since it gives precision in the energy measurement of an unknown object which produces signals in the calorimeters.

Signal linearity for hadronic showers is fundamentally different from the electromagnetic showers. In general electromagnetic calorimeters are linear as almost all the energy deposited in them is either through ionization or excitation of the detector medium. However hadronic

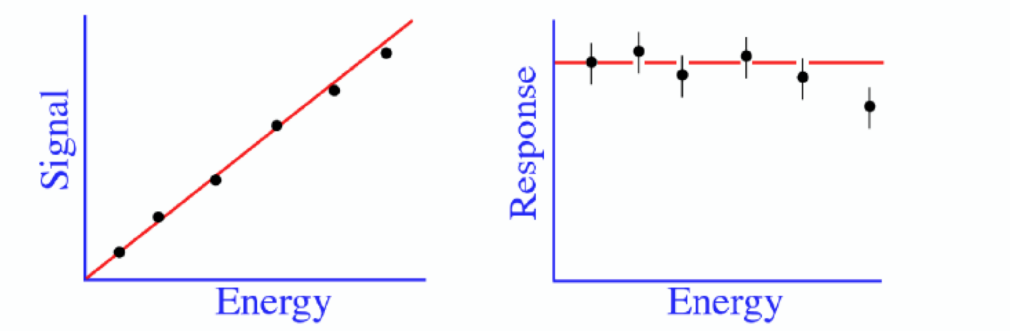

Figure 3.2: Examples showing signal linearity of a calorimeter. A calorimeter is linear if its response (average signal per unit of deposited energy) is constant. The figure is taken from Ref [3].

calorimeters are intrinsically non-linear. In hadronic showers, signals non-linearities occurs due to non-compensation ($e/h \neq 1$).

3.3.1 Sources of non-linearity

Signal non-linearity occurs due to a number of factors. Depending upon the original factor, the deviation from signal linearity may either lead to a decreasing response at higher energies or vice versa. Some of the factors are listed below:

- **Instrumental effects**: Instrumental effects occur due to a number of reasons such as saturation effects in PMTs, scintillators, or electronics. Saturation occurs when the signal-generating device reaches its intrinsic limits.

- **Leakage**: The shower leakage effect also introduces signal non-linearity. Due to this effect, the response of a calorimeter decreases with increasing energy. This occurs as the energy increases, the volume of the detector containing the shower also increases. But if the signals are collected from a particular detector volume, then the fraction of the shower contained in the detector volume outside does not contribute to the calorimeter signals. Thus decreasing the response with increasing energy.

- **Miscalibration**: Another important factor causing signal non-linearity mainly in the longitudinally segmented calorimeters is miscalibration. For the inter-calibration of the signals in multiple segments, different calibration methods are used which increases the signal non-linearity.

- **Signals from external sources**: Signals from external sources such as the particles that are not supposed to take part in the signals cause non-linearity. Such particles are usually not part of events under study. These kinds of problems are reduced by replacing the readout with one which is less sensitive to these effects.

3.4 Compensation

For compensating calorimeters, as mentioned before in subsection 2.1.2, the electron/hadron signal ration (e/h) should be equal or close to one. Thus, the e/h ratio is a parameter defining the degree of compensation in calorimeters. For devices that are overcompensating and under-compensating, the e/h values are smaller and larger than 1, respectively. One caveat is that this ratio cannot be measured directly, instead, it can be derived from other experimental measurements. A calorimeter's e/h value in terms of it's em and non-em signal components may be defined as Eq 3.2:

$$\frac{e}{h} = \frac{e/mip}{f_{rel}.rel/mip + f_p.p/mip + f_n.n/mip} \tag{3.2}$$

where f_n, f_p, f_{rel} indicate average energy fractions carried by evaporation neutrons, spallation protons and relativistic charged particles, respectively in the non-em shower component. While in the denominator, the normalized response of evaporation neutrons, spallation protons, and relativistic charged particles to mip is written as n/mip, p/mip, rel/mip respectively.
In the case of homogenous calorimeters, the response of the em shower components is at *best equal* to the response of the non-em shower components. Due to the presence of invisible energy in hadronic showers, the compensation can *never* be achieved in homogenous calorimeters. Thus all homogenous calorimeters are *undercompensating*, with $f_{rel}+f_p+f_n < 1$ and $e/h > 1$.
However, in sampling calorimeters, compensation can be achieved by tuning the parameters in Eq 3.2, such as the values of n/mip, p/mip, rel/mip.

3.4.1 Techniques to achieve compensation

After a lot of research and development in the understanding of the underlying mechanism of hadron calorimetry, several ways are identified to achieve compensation. Some of the

methods are listed below:

- **Building a sampling calorimeter**: Since compensation can never be achieved with a homogenous calorimeter, thus building a sampling calorimeter could be emphasized. Various facts in both active and passive layers of a sampling calorimeter can be put to use to achieve compensation.

- **Boosting the non-em response**: A powerful method to achieve compensation in a calorimeter is by boosting the non-em response i.e. through its response to neutrons. However, this method works only if the active layers contain hydrogen. One of the ways to amplify the neutron and soft photons component is by using U^{238} plates as absorbers due to their fission property for slow neutrons. Other ways are to optimize the sampling fractions etc.

- **Suppressing the em response**: The most efficient way to suppress the em response of a calorimeter is to use high-Z absorber materials such as Pb, Ur, and low-Z active materials. By using lead or uranium as active materials photo-electric effect dominates ($\sigma_{photo-e} \propto Z^5$) reducing the em response. Another way to reduce the em response is to shield the active layers with thin sheets of low Z passive material.

3.4.2 Effects of compensation

There are several advantages and a few disadvantages of a compensating calorimeter. It is important to mention that the different methods to achieve compensation i.e. $e/h = 1$, may also affect different ways the hadronic energy resolution. If the compensation is achieved by properly boosting the response to shower neutrons, an excellent hadronic energy resolution can be achieved. An example of such a compensating calorimeter is SPACAL whose hadronic energy resolution is $30\%/\sqrt{\mathrm{E}}$. Compensation is also an important parameter of linear calorimeters. However, due to the small sampling fraction in compensating calorimeter, the em energy resolution is limited. Since compensation also relies on detecting neutrons, compensating calorimeters usually have a large integration volume and time.

3.5 Cherenkov calorimeters

When a charged particle moves faster than the speed of light in a given medium ($\mathrm{v} > \mathrm{c/n}$, where n the index of refraction of the media), it emits Cherenkov radiation in the process

of energy loss. This radiation is emitted at a specific angle, the Cherenkov angle $\theta_C = \cos^{-1}(n\beta)^{-1}$, with the particle's direction. Cherenkov radiation detectors are commonly thought of as particle identification (PID) detectors, but they are also used in a much wider range of applications, including fast particle counters, hadronic PID, electromagnetic calorimeters (EMC), and tracking detectors that perform complete event reconstruction.
Cherenkov detectors have three main components, **Radiator** for the production of the Cherenkov photons, **Mirror or lens** for the collection and transportation of the photons and **Photodetector** for detection of the photons. The radiator is selected on the basis of its refractive index. Some astroparticle physics experiments use air, seawater, or ice as radiators.
Depending on whether or not Cherenkov counters use Cherenkov angle (θ_C) information, they can be categorized into two types:

- **Threshold counters**: The threshold Cherenkov detectors in their most basic form determine if a particle is above or below the Cherenkov threshold velocity ($\beta = 1/n$). These counters separate the particles with the same momentum but with different masses only if the Cherenkov radiations velocity is above threshold $\beta > 1/n$. With some enhancement in their basic form, threshold counters use the number of recorded photoelectrons (or a calibrated pulse height) to differentiate between particle types. They can be used over a large area e.g in a fixed target or collider experiments for secondary particles. Examples of this kind of counters include HARP@CERN (2000-2002) to measure the production of hadrons on different targets and the BELLE experiment in electron-positron collider to observe CP violation.

- **Differential counters**: The differential counters can only accept light from a specific range of angles in a specific velocity interval. Thus they have a very small acceptance in β and the direction of the charged particle. They are mostly utilized to identify particles in the beamlines.

- **Imaging counters**: The Cherenkov angle as well as the number of observed photons can be measured using image counters. Thus they can be used to both track and identify particles. They are also known as Multi-track Ring-Imaging Cherenkov detectors (generically called RICH counters). DELPHI at LEP is an example of an imaging counter. Imaging counters are better in terms of resolution with respect to equivalent differential and threshold counters.

3.6 Performance of calorimeters

Different types of calorimeters are used for various experiments based on the requirements from the physics aims of the research of the corresponding experiments. As a result, the performance of various types of calorimeters employed in different experiments varies greatly. The following are the factors that influence and limit multiple aspects of this performance.

- **Particle identification:** Much physics research relies heavily on particle identification. Calorimeter signals can be utilized to identify the particles that created the signals due to variations in the characteristic energy deposit profiles and other aspects of shower development. Various methods are used for the purpose of particle identification such as the information from longitudinal or lateral showers, the time structure of the signals, or a comparison between the momentum and energy of the particle.

- **Energy measurement:** The most essential performance attribute of a calorimeter is typically its energy resolution. In particle physics experiments, the calorimeter's energy resolution may be the limiting element in determining the mass of new particles with precision (e.g., the top quark). It could prevent particles with identical masses from separating (for example, in the jet–jet decay of the intermediate vector bosons W and Z). It also calculates the signal-to-background ratio in event samples of nearly every experiment. Sampling calorimeters provide by far the best performance for calorimetric hadron detection.

- **Particle position resolution:** The components of the four-vector such as the position and angular momentum of a particle also play an important role in the performance of a calorimeter. The most commonly used approach to estimate the position of a particle that showers in a calorimeter are by reconstructing the center of gravity ($\bar{x}$,$\bar{y}$) of the energy deposited in the different detector cells (with coordinates x_i,y_i) which contribute to the signal as follows:

$$\bar{x} = \frac{\sum_i x_i E_i}{\sum_i E_i} \tag{3.3}$$

  However, in practical calorimeters, nearly half of the shower energy is usually deposited in a single calorimeter cell and the exact percentage is only slightly dependent on the location of the impact point. So for the instances in which the impact point is near the

boundary between different calorimeter cells the shower energy was only fully shared between cells. In these circumstances, the particle's position was measured with the greatest precision and accuracy. While in other cases one cell receives the majority of the energy share with the remaining amount distributed among the surrounding cells. Besides energy resolution, the position can also be determined by the cell size. If the size of cells is small (in terms of the units of the Molière radius), more cells contribute to the signals, and more precisely the shower's center of gravity can be calculated.

Besides the aspects mentioned above the e/h ratio has a significant impact on the hadronic performance of calorimeters. Also, the timing characteristics of the calorimeter signals are very crucial especially when event rates are high, for instance in hadron colliders where event rates are measured in MHz.

Calorimeter operation in modern experiments imposes a number of constraints both in technical design (such as rapid response, low noise, and dynamic range) as well as physics performance (such as good energy, space, time resolution, and particle identification). Limitations come from environmental conditions such as radiation levels, as well as the integration with the rest of the experiment, such as the presence of a magnetic field, etc. As a result, selecting the best detector technique and design is a multi-dimensional challenge that considers all of the above factors as well as cost.

Chapter 4

CERN, LHC, and the ATLAS experiment

CERN commonly referred to as the European Laboratory for Particle Physics was established in 1954 by 12 countries and is located at the Franco-Swiss border near Geneva. Physicists and engineers from around the world use the most complex scientific instruments to study the basic building blocks of matter. This chapter sheds light on the experimental setup of the Large Hadron Collider (LHC), followed by a detailed explanation of the ATLAS experiment.

4.1 Accelerator chain at the LHC

The Large Hadron Collider, the forerunner of the European Laboratory for nuclear research, is the world's biggest and most powerful particle accelerator. Designed to accelerate protons while they circulate in two beams moving in opposite directions, LHC comprises a 26.7 km circumference of superconducting magnets with a number of accelerating cavities to boost the energy of the particles along the way. Different experiments have been set up along the ring to detect the scattered and newly produced particles produced as a result of the collisions of two beams. In addition to proton collisions, the LHC also performs Pb-Pb collisions. The technical layout of the accelerator chain, along with the experiments is shown in Figure 4.1

4.1.1 LINAC-2

The Linear Accelerator 2 (LINAC-2) replaced LINAC-1 in 1978 and was originally designed to allow higher intensity beams to be used by the accelerators that precede it in CERN's accelerator complex. A hydrogen gas cylinder is the primary source of protons, which will eventually be utilized in collisions. The hydrogen atoms from the cylinder are injected at

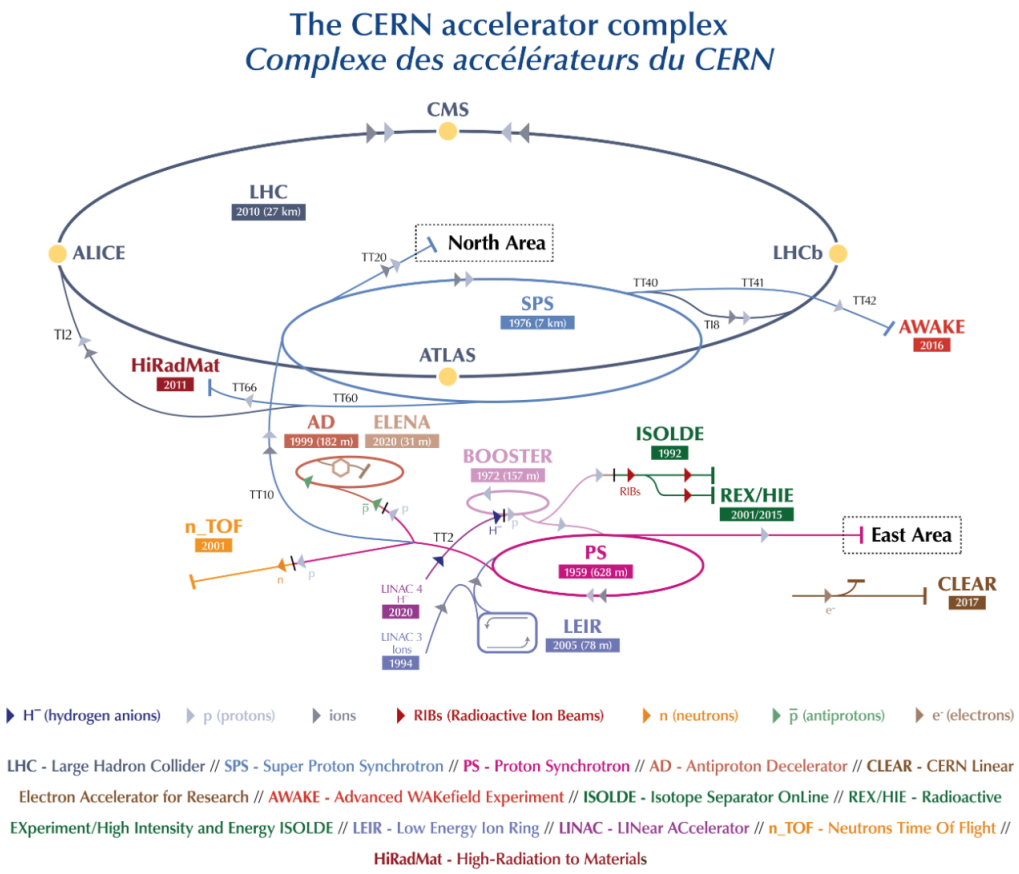

Figure 4.1: Schematic showing the CERN accelerator complex and different experiments set up at various points, with the largest ring being LHC. This figure is taken from Ref [4].

a precisely controlled rate into the linear accelerator, the LINAC-2 Ref [33]. Hydrogen atoms are then ionized in the LINAC-2 producing protons to generate new particles. These protons are accelerated by radio-frequency (RF) cavities. When the protons leave LINAC-2, they are already traveling at one-third the speed of light with an energy of about 50 MeV. For 40 years, the linear accelerator 2 (LINAC-2) provided the source of protons utilized in CERN experiments. It was switched off in 2018 and was replaced by LINAC-4.

4.1.2 LINAC-4

LINAC-4 was inaugurated in 2017 and during CERN's long shutdown-2 in 2020 it was connected to the PS Booster. The length of LINAC-4 is about 86 meters and is located 12 meters underground. Linear accelerator 4 is designed to accelerate negative hydrogen ions

to high energies (about 160 MeV) in order to prepare them for insertion into the LHC's proton synchrotron booster. The Linac4 is an important component of the endeavor to boost the LHC's luminosity during the next decade of data-taking periods.

4.1.3 Booster

The protons produced in the LINAC-2 are then injected into the Booster Ref [34], which is circular in shape having four rings with a circumference of 157 meters. Each ring in the Booster accelerates one-fourth of the packet of protons by a pulsating electric field eventually increasing the beam intensity. Inside the Booster rings, powerful magnets are placed, which keep the protons bending inside the ring. Finally, the Booster accelerates the protons to 92% of the speed of light. Each proton leaving the Booster has an energy of 1.4 GeV and is upgraded to 2 GeV for Run-3.

4.1.4 The Proton Synchrotron (PS)

The next destination of the protons is the Proton Synchrotron (PS) Ref [35], which has a 628 m circumference. The protons leave the Booster ring to circulate in the PS for 1.2 seconds. Proton Synchrotron has 100 dipole magnets to keep the beam in a circular path. The protons leaving the PS reach 99.9% of the speed of light, and from now on the increase in energy manifests in the form of an increase in mass only. The energy of the protons now reaches 25 GeV.

4.1.5 The Super Proton Synchrotron (SPS)

Proton beams from the PS are injected into the Super Proton Synchrotron (SPS) Ref [36]. The SPS has 744 dipole magnets and a circumference of 7 km. The SPS further increases the energy of the protons to 450 GeV. The SPS also reserves the CERN fixed target program.

4.1.6 The main LHC ring

After leaving the SPS, protons are fed into the main large hadron collider (LHC) ring of 26.7 km circumference with the help of kicker magnets. This ring is situated partly in France and partly in Switzerland. The LHC ring consists of two beam cavities, each for the protons traveling in opposite directions. The energy of the protons increases in the ring until it reaches the final energy i.e, for Run 2 it was 6.5 TeV per beam.

LHC contains about 16 radio-frequency (RF) cavities along its length to accelerate the protons. The speed of the protons is very close to the speed of light and in one second the beam orbit around 11000 times inside the LHC ring. Strong magnetic fields are applied through the superconducting magnets made of niobium-titanium (Ni-Ti) wires to keep the beam orbiting inside the LHC ring. There are 1232 such superconducting bending dipoles along the LHC tunnel which generate a magnetic field of 8.34 T. In order to produce superconducting conditions, superconducting magnets must be cooled which is done by superfluid liquid helium at a temperature of 1.9 K. Some of the main components of the 15 m long LHC dipole magnet is shown in Figure 4.2.

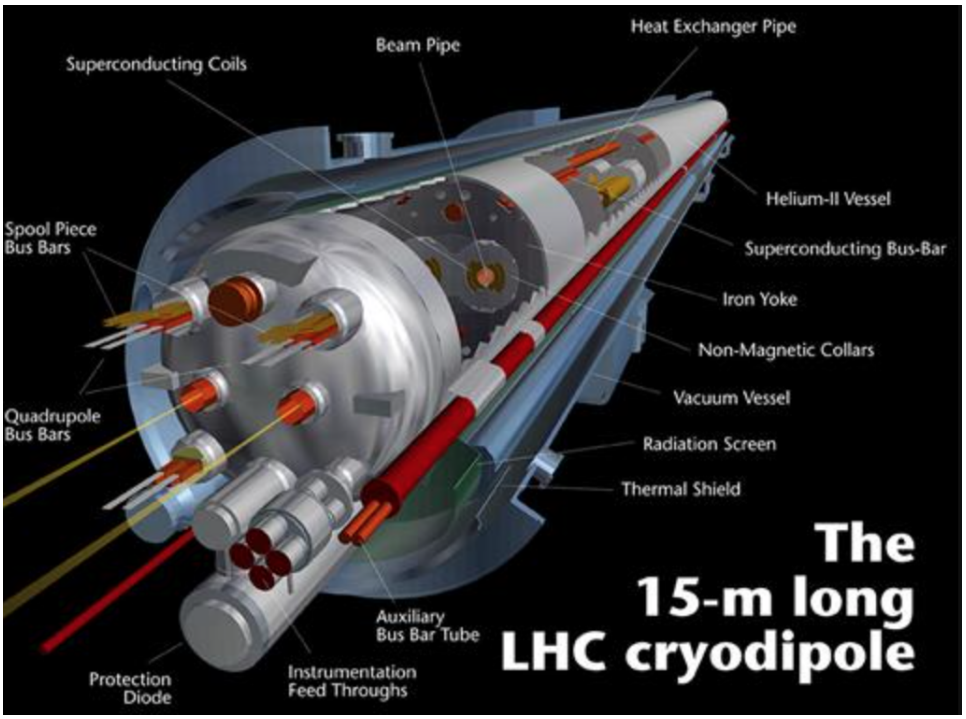

Figure 4.2: Cross section of an LHC dipole magnet showing the beam pipe, superconducting coils to bend the proton beams, along with the other necessary components. In order to avoid unnecessary collisions between the beam and other particles, the vacuum must be maintained between the two beam cavities. The figure is taken from Ref [5].

4.2 Luminosity and beam dynamics

The geometry of the LHC is not perfectly circular. As shown in Figure 4.3, it is composed of eight arcs and eight insertions. Each arc is 2.45 km long and each straight insertion is 545 m

long. In order to overcome the differences in initial conditions and the electrostatic repulsion between protons within a bunch, the protons beam must be focused on the designed orbit consisting of arcs and insertions. This focus is done by 392 quadrupole magnets along the LHC. A quadrupole magnet focuses protons in the vertical direction defocuses them in the horizontal direction, and vice versa. This combination of main dipole magnets, quadrupole magnets, and some other multipole magnets are collectively called as FODO structure. Each FODO structure is called an arc cell and in total LHC contains 23 of these arc cells.

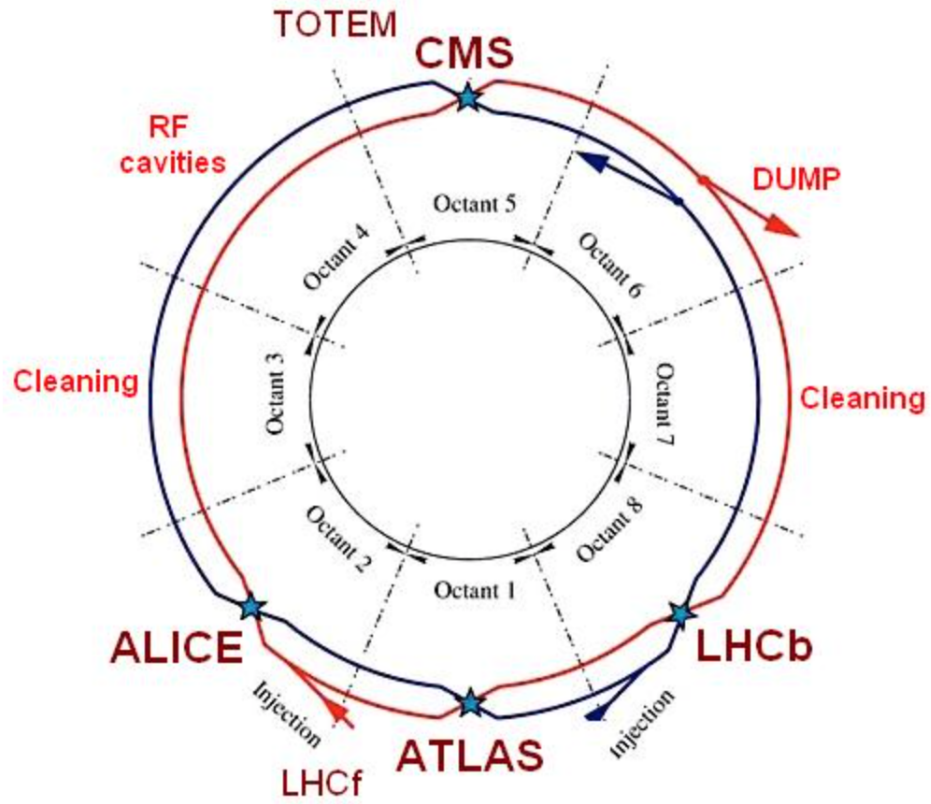

Figure 4.3: Layout of the LHC illustrating its main installations and experiments. This figure is taken from Ref [6].

A quantity can be defined now, by which the interaction rate at the points where the proton beams cross, can be measured. This quantity is called instantaneous luminosity and is written as:

$$L = f n_b \frac{n_1 n_2}{4\pi\sigma_x\sigma_y} F \tag{4.1}$$

where f is the bunch crossing frequency, n_1, n_2 are the numbers of protons in the colliding bunches, and n_b is the number of bunches per beam. σ_x and σ_y represent the beam sizes at the collision point in horizontal and vertical planes, respectively, and can be written in terms of beta function (β) and emittance of the beam as shown in Eq 4.2:

$$\sigma_x = \sqrt{\epsilon\beta_x} \tag{4.2}$$

F in Eq 4.1 is the geometric reduction factor of the luminosity coming from the crossing angle at the beam interaction point (IP). The expected number of events of a specific process can be calculated as the product of time-integrated luminosity and cross-section of the process:

$$N = \sigma \times \mathcal{L} \tag{4.3}$$

where $\mathcal{L}$ is the integrated luminosity and is defined as:

$$\mathcal{L} = \int L dt \tag{4.4}$$

and has a unit of fb^{-1}, the inverse of the cross-section.
The LHC overall delivered about 156 fb^{-1} integrated luminosity during proton-proton collisions during Run-2 as shown in Figure 4.4:

According to the updated schedule, it is expected that during Run-3, the LHC will deliver $\approx 275\text{fb}^{-1}$ over the span of four years from 2022 to 2025. In Run-4, the LHC is aimed to record data of $\approx 750\text{fb}^{-1}$ from 2029-2030 covering four years. With the upgrade of LHC to High Luminosity LHC (HL-LHC), the aim is to achieve 3000 fb^{-1} of data.

4.3 Experiments at the LHC

There are several different experiments set up at the different intersection points in the LHC ring. Four out of them are the major experiments where the clockwise and anticlockwise traveling beam cross and collide with each other. In these four experiments, ATLAS and CMS are general-purpose experiments, while the other two, ALICE and LHCb are designed for more specific purposes.

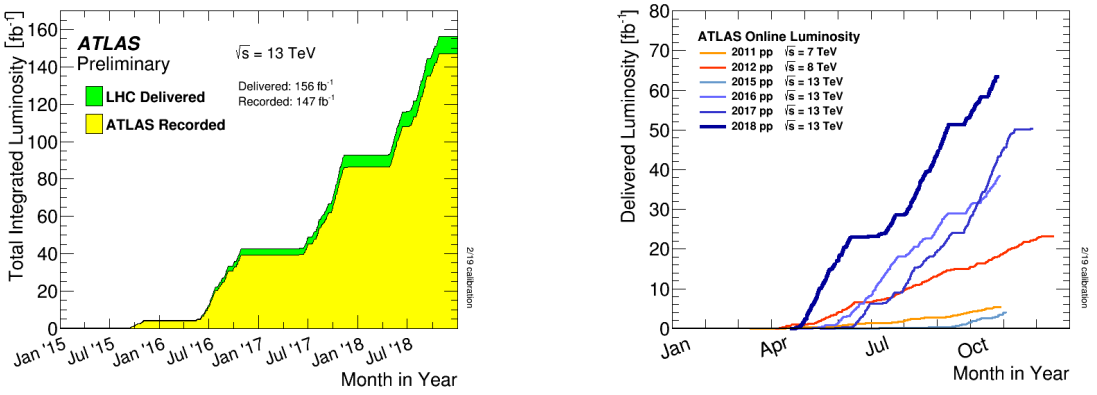

Figure 4.4: Integrated luminosity versus time delivered by the LHC, and recorded by the ATLAS experiment during Run2. The delivered luminosity to ATLAS experiment during stable beams (p-p data only) for different years in Run2 is shown on the left, whilst on the right cumulative luminosity versus time delivered to ATLAS is shown in green and recorded by ATLAS experiment is shown in yellow. These figures are taken from Ref [7].

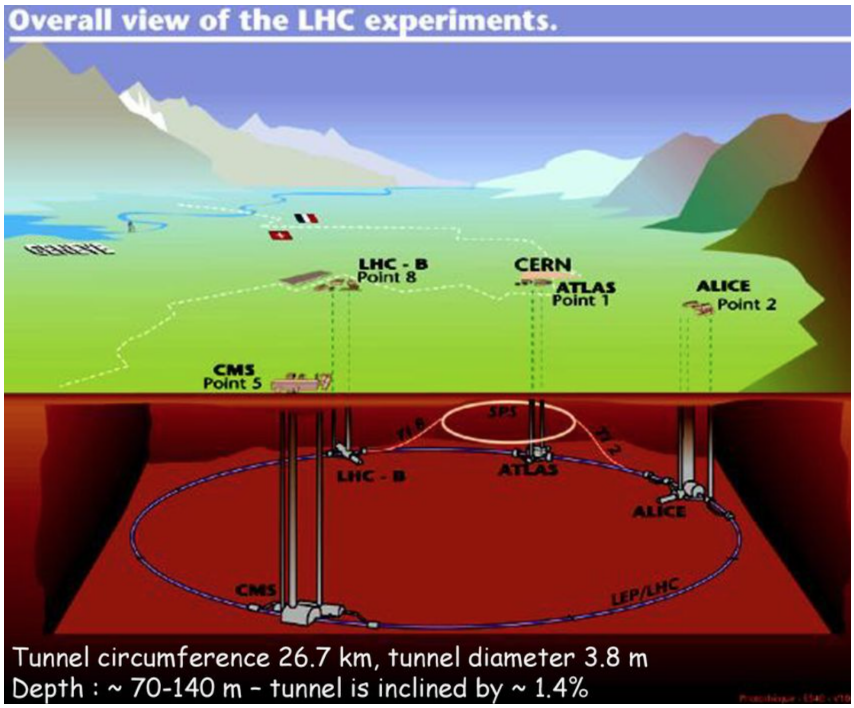

Figure 4.5: Overview of the Large Hadron Collider (LHC) showing its four major experiments. This figure is taken from Ref [8].

- **ATLAS (A Toroidal LHC ApparatuS)** is the largest detector by volume, which covers a broad field of experimental studies. The aim of the ATLAS experiment is to

look over a huge range of physics, from observing the properties of Standard Model (SM) particles, including the Higgs boson, to searching the new phenomena which involve heavy particles and very rare processes. A detailed explanation of the ATLAS experiment is given in Section 4.4.

- **CMS (Compact Muon Solenoid)** is the heaviest experiment at the LHC with a weight of about 14000 tonnes. CMS investigates almost the same physics goals as the ATLAS experiment using different technical solutions. CMS experiment optimized for muon tracking has the largest solenoid which produces about 4 T strength of the magnetic field. The main purpose of building two separate experiments with the same physics goals is so that these experiments work independently to produce similar results which reduce systematic and statistical errors.

- **ALICE (A Large Ion Collider Experiment)** is 26 m long and 16 m in diameter, designed to study heavy ions and quark-gluon plasma interactions. ALICE uses a number of detectors designed to differentiate the particles coming from the quark-gluon plasma, such as silicon tracker detectors, a Time Projection Chamber (TPC), a Transition Radiation Detector (TRD), a Time Of Flight (TOF) detector, a High Momentum Particle Identification Detector (HMPID) and calorimeters.

- **LHCb (Large Hadron Collider beauty) Experiment** is an asymmetric forward spectrometer, having 10-100 mrad and 250 mrad coverage in the horizontal and vertical directions respectively. designed to investigate the properties and decays of bottom (b) hadrons. It also looks into CP violation which occurs in the b quark sector and in D meson decays.

In addition to the above-mentioned major experiments, there are a number of minor experiments sharing the location with the major experiments in the LHC ring. These experiments include LHCf (Large Hadron Collider forward), the TOTEM (ToTal elastic and diffractive cross section measurements), and The MoEDAL (Monopole and Exotics Detector At the LHC). Moreover, after LS2, Run-3 includes the operation of two new experiments, FASER (Forward Search Experiment) and SND@LHC (Scattering and Neutrino Detector at the LHC). Both of these experiments are designed to look for physics which is not suited to study by the four main LHC experiments. FASER experiment mainly includes a search for physics beyond the Standard Model, while SND@LHC is designed to detect and study neutrinos and low-mass particles with no electric charge.

4.4 The ATLAS experiment

One of the four experiments operating at the Large Hadron Collider at CERN, The ATLAS (A Toroidal LHC Apparatus), is the largest experiment having a length of 46 meters and a diameter of 25 meters. It weighs about 7000 tonnes with 3000 km of cable. In order to provide the best spherical coverage required for the fiducial measurements, the detector is designed in a cylindrical shape with different layers around the collision interaction point. This experiment is designed to cover a broad range of research including studies of the Higgs boson beyond the Standard Model searches. In order to study a number of various production and decay channels, the ATLAS experiment is designed to provide high energy and momentum resolution with an excellent ability for particle identification. In this section, the ATLAS detector is explained in detail in terms of highlights of the technology, main characteristics, and geometry of the experiment. Furthermore, the ATLAS trigger system and the data acquisition and preparation chains are also discussed.

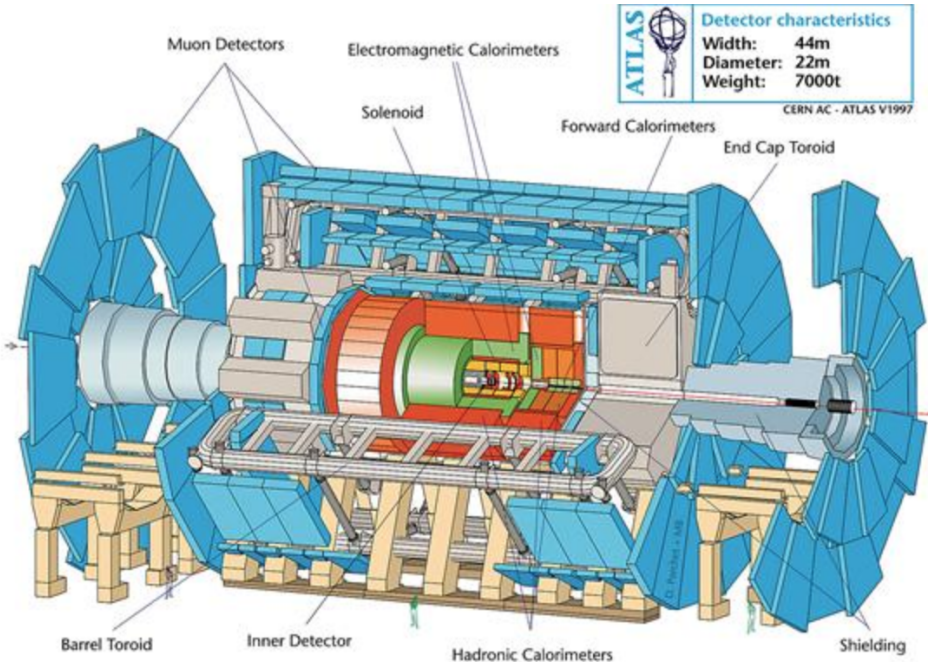

Figure 4.6: Overview of the ATLAS experiment showing its various sub-detectors. This figure is taken from Ref [9].

The ATLAS detector is further subdivided into four major sub-detectors as shown in Figure 4.6 designed to perform different goals:

- **Inner Detector (ID)**: It is the innermost sub-detector of the ATLAS experiment. It tracks the particles with precisions by measuring the transverse momentum, charges as well as directions of charged particles. To perform its tasks, the inner detector consists of the pixel detector, Semiconductor Tracker (SCT), and Transition Radiation Tracker (TRT).

- **Calorimeters**: The inner detector is followed by Hadronic and Electromagnetic calorimeters (EM). The goal of calorimeters is to identify hadrons, electrons, and photons and measure their energy and momentum. It further consists of liquid argon electromagnetic barrel and end-cap calorimeters, hadronic end-cap and forward calorimeters, and tile calorimeters.

- **The Muon Spectrometer (MS)**: The Muon Spectrometer consists of toroid magnets and muon chambers to measure and identify the highly penetrating muons transverse momentum and direction.

- **The Magnet Systems**: In the ATLAS experiment there are two magnet systems that are used to bend the charged particles in the inner detector as well as in the Muon Spectrometer resulting in the measurement of their momentum.

Figure 4.7 shows how the sub-detectors of the ATLAS experiment detect different particles in a direction perpendicular to the beam axis.

4.4.1 Coordinate system and pseudorapidity

The ATLAS detector encompasses a cylindrical form around the beam pipe. The coordinate system accustomed to describing the position and direction of particles within the detector is implicit in the geometry of the detector. Depending upon the geometry, ATLAS collaborators use two types of coordinate system conventions namely cylindrical convention system and right-handed cartesian convention system.

In the right-handed cartesian convention system, the origin lies in the center of the detector and nominal interaction point, the x-axis points along the radius of LHC towards the center of the LHC ring in the horizontal plane, the y-axis points upwards, and the z-axis points along the beam axis. While in the cylindrical coordinate system, the azimuthal angle ϕ is defined in the x-y plane transverse to the z-axis while the polar angle θ is measured along the positive z-axis with respect to the beam axis.

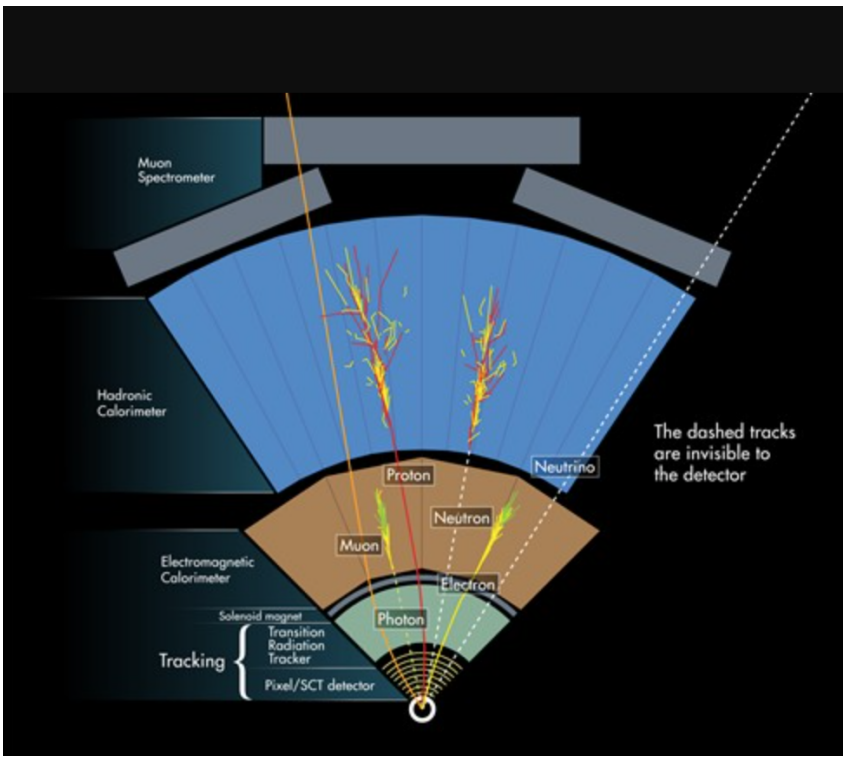

Figure 4.7: Illustration of the path of different particles in the sub-detectors of the ATLAS experiment in a plane perpendicular to the direction of the beam. This figure is taken from Ref [10].

In a detector having two particles or points with coordinates (η_1, ϕ_1) and (η_2, ϕ_2), the angular distance between them can be defined as:

$$\Delta R = \sqrt{\Delta\eta^2 + \Delta\phi^2} \tag{4.5}$$

where in Eq 4.5, η is the pseudorapidity, which is defined as a function of polar angle θ by Eq 4.7:

$$\begin{aligned} \Delta\eta &= (\eta_1 - \eta_2) \\ \Delta\phi &= (\phi_1 - \phi_2) \end{aligned} \tag{4.6}$$

$$\eta = -\ln\tan(\frac{\theta}{2}) \tag{4.7}$$

Pseudorapidity and rapidity (defined in eq 4.8) are two important quantities commonly

used in accelerator particle physics.

$$y = -\frac{1}{2}\ln(\frac{E + p_L}{E - p_L}) \tag{4.8}$$

where rapidity y is a function of longitudinal momentum p_L and the particle energy E. In hadron colliders, the rate of collision products is approximately constant over rapidity and pseudorapidity. Also, the initial momentum of the interacting particles in the x and y-direction is zero while it is unknown in the z-direction. Hence to overcome this situation other transverse quantities in z-direction such as transverse momentum p_T are used.

ATLAS experiment was designed to achieve a large number of pre-defined performance goals. The multiple sub-detectors of the ATLAS experiment make sure to achieve these pre-defined goals by using the best efficiency in tracking, momentum, and energy resolution, b-tagging, jet reconstruction as well as in particle identification using the latest and best technology. In the ATLAS detector, in the region where $|\eta| < 2.5$, the detector is dedicated to achieving the best possible precision measurements. Below these sub-detectors of the experiment are discussed in detail:

4.4.2 Inner Detector

The Inner detector (ID) is the innermost sub-detector of the ATLAS experiment. Closest to the interaction point, it is designed to provide the best possible momentum resolution and track measurements of the charged particles. It further provides information on the direction and charge of the particles as they interact with the detector material. Being nearest to the interaction point, the ID is highly exposed to radiation and thus many of its components are replaced during the long shutdown (LS) periods to ensure its highest possible performance stability with time.
Figure 4.8 shows the sketch of the ATLAS inner detector. The geometry of the ID is cylindrical with a length of 7 meters and around 2.3 meters of radius. In order to achieve its goals, the ID consists of different sub-parts as shown in Figure 4.9. The first component is made up of silicon pixel layers, known as the Pixel detector, followed by the SemiConductor Tracker and Transition radiation tracker simultaneously. A detailed explanation of these components is given below.

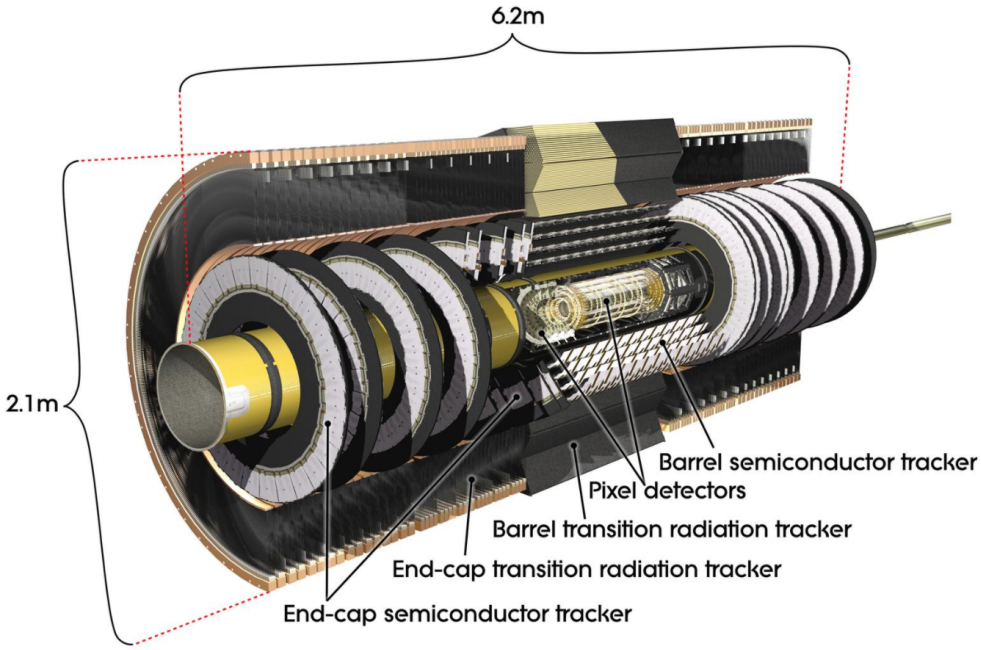

Figure 4.8: Cutaway view of the ATLAS inner detector (ID) illustrating its dimensions and different parts. This figure is taken from Ref [11].

Insertable B-Layer (IBL)

In the first long shutdown (LS1), a new pixel layer IBL has been inserted in ID with the goal of further amplifying the precision in vertex reconstruction used especially in B-tagging. The IBL is about 33.5 mm away from the beam interaction point and gives a coverage of $|\eta| < 3.0$ pseudorapidity.

Pixel Detector (PD)

The Pixel detector is located only 5cm away from the interaction point of the beam. It is made up of 3 cylindrical barrel layers and two end-cap regions in a direction perpendicular to the z-axis. It consists of about 80 million silicon pixel diodes with a total of 46080 readout pixels and 1744 pixel sensor modules. Each pixel has a thickness of 250 μm with an area of 40 x 500 μm^2. The Pixel detector is further subdivided into three layers, covering $|\eta| \leq 1.7$ in the barrel region and five end-cap disks on each side of the barrel covering a total of $|\eta| \leq 2.5$. In the pixel layers, a charged particle leads to three hits which is reconstructed and then used in full-track reconstruction algorithms.

SemiConductor Tracker (SCT)

Following the PD, SCT is composed of 80 μm wide silicon microstrips layers with silicon acting as an active material. 6.4 million read-out channels are located inside the SCT. A total of 15912 sensors are present with each barrel module having 4 sensors and a high voltage supply through an electrically conductive baseboard. SCT is composed of 4 cylindrical layers arranged in the barrel region covering up to $|\eta| \leq 1.4$. On each end-cap region, it contains nine disks providing total coverage of $|\eta| \leq 2.5$. Two planes of strips are present in each layer, which are rotated with respect to each other to allow to determine the position of the hit within the strip.

Transition Radiation Tracker (TRT)

The TRT is located next to the SCT and gives total coverage of $|\eta| \leq 2.0$. It is composed of thin drift straws filled with a gas mixture having a diameter of 4 mm. Similar to PD and SCT, the Transition Radiation Tracker is also divided into a barrel and two end-cap regions. The barrel part of the tracker covers a total of $|\eta| \leq 0.7$ with about 50,000 drift straws placed parallel to the beam pipe, while the end-cap region provides coverage of $|\eta| \leq 2.0$ with 320,000 beam straws. TRT contributes significantly to the track momentum measurements by observing approximately 36 hits in its regions. Further, it contributes to electron identification by detecting the transition radiation photons in the Xe-mixture.

4.4.3 Calorimeters

The ATLAS calorimeter system consists of an ElectroMagnetic (EM) and Hadronic CALorimeter (HCAL) with the goal to determine the energy as well as directions of the particles. Calorimeters serve a number of purposes from determining the missing transverse energy (MIT) to identifying photons, hadrons, tau leptons, and electrons in energy ranging from few GeV to few TeV. Trigger systems also use the information from calorimeters. To ensure the best possible efficiency, the ATLAS calorimeters cover a range of $|\eta| < 4.9$ pseudorapidity.

Based on different functions and technologies, the calorimeter system consists of several calorimeters positioned outside the solenoid magnet which encompasses the inner detector. The ATLAS calorimeters are sampling calorimeters explained in sec 3.2. The layout of the calorimeter systems is shown in Figure 4.10, illustrating the LAr electromagnetic and LAr

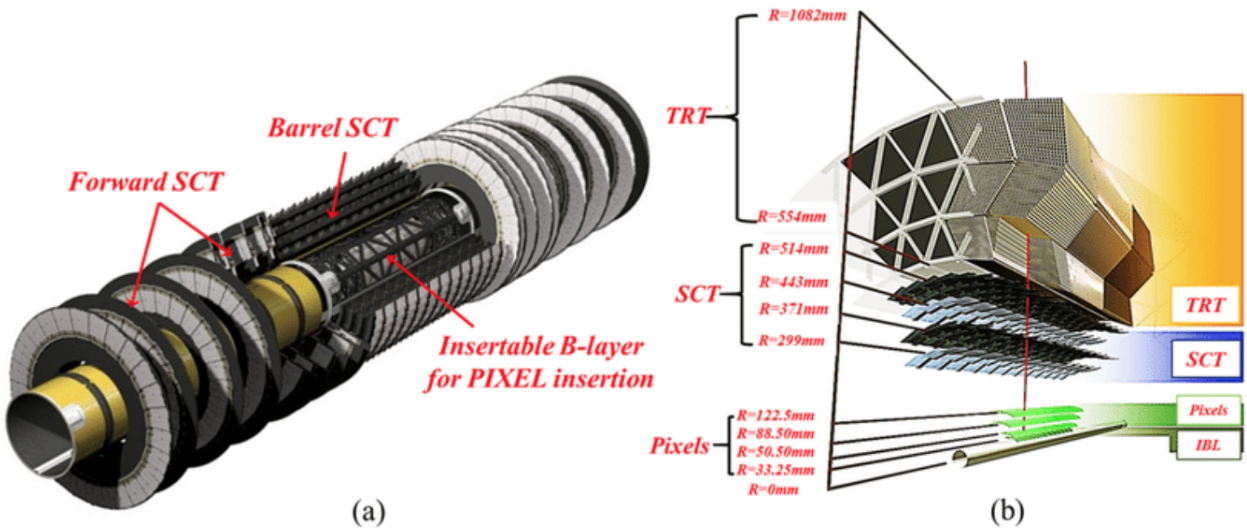

Figure 4.9: Illustration ATLAS experiment inner detector with its sub-detectors (a) and cut-away view of the ID along z-axis (b). This figure is taken from Ref [12].

hadronic end-cap, the forward and Tile calorimeter. A brief description of each type of calorimeter is discussed below:

Liquid Argon (LAr) electromagnetic calorimeter

The Liquid Argon EM calorimeter is sub-divided into a 3-layer + pre-sampler barrel region and two end-caps covering a pseudorapidity of $|\eta| < 1.475$ and $1.375 < |\eta| < 3.2$, respectively. The geometry of the LAr calorimeter ensures the full ϕ coverage with sufficient granularity to meet the resolution needs of the electromagnetic and hadronic cascade measurements. The ATLAS liquid argon calorimeter is composed of lead plates of high atomic number (Z) as absorbers and liquid argon as an active material. The main task of the EM calorimeter is to measure the energy and momentum of electrons and photons precisely.

Hadronic End-Cap (HEC) and Forward Calorimeters (FCal)

The LAr hadronic End-Cap (HEC) and Forward Calorimeter (FCal) use liquid argon as an active material. The pseudorapidity range covered by the LAr HEC is $1.5 < |\eta| < 3.2$ while for FCal it is $3.1 < |\eta| < 4.9$. The FCal is divided into three longitudinal layers, with the first layer optimized to measure the electromagnetic components with copper as

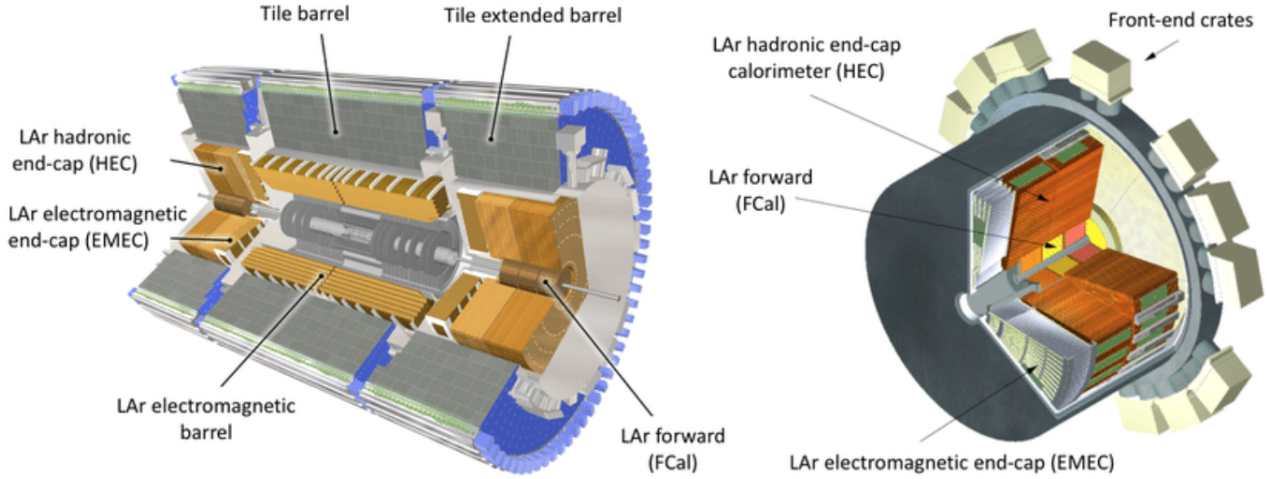

Figure 4.10: Illustration of the calorimeter subsystems (left) in ATLAS experiment and zoomed cutaway view of the end-cap calorimeters (right). This figure is taken from Ref [13].

an absorber material and the other two layers are dedicated to measuring the hadronic component using tungsten as an absorber.

The Tile hadronic Calorimeter (TileCal)

The outermost calorimeter system of the ATLAS experiment central region is the Tile Calorimeter (TileCal). It is specifically designed to fully contain the hadronic cascades and to efficiently perform the jet measurements. The Tile Calorimeter covers a pseudorapidity range of $|\eta| < 1.7$. The work presented in this thesis mainly focuses on a study on the Tile Calorimeter, hence a complete Chapter 5 is dedicated to giving a more detailed explanation of this calorimeter.

4.4.4 Muon Spectrometer

The Muon Spectrometer (MS) is the largest component of the ATLAS experiment, installed outside the calorimeter system. Its purpose is to identify and precisely measure the direction and momentum of muons. Muons with an energy of more than 3 GeV pass through the calorimeter systems and are only detected by the Muon Spectrometer with the help of its four sub-detectors. Figure 4.11 illustrates the layout of the Muon Spectrometer. It shows the sub-parts of the spectrometer i.e., monitored drift tubes (MDTs), Thin Gap Chambers (TGCs), Resistive Plate Chambers (RPCs), and Cathode Strip Chambers (CSCs).

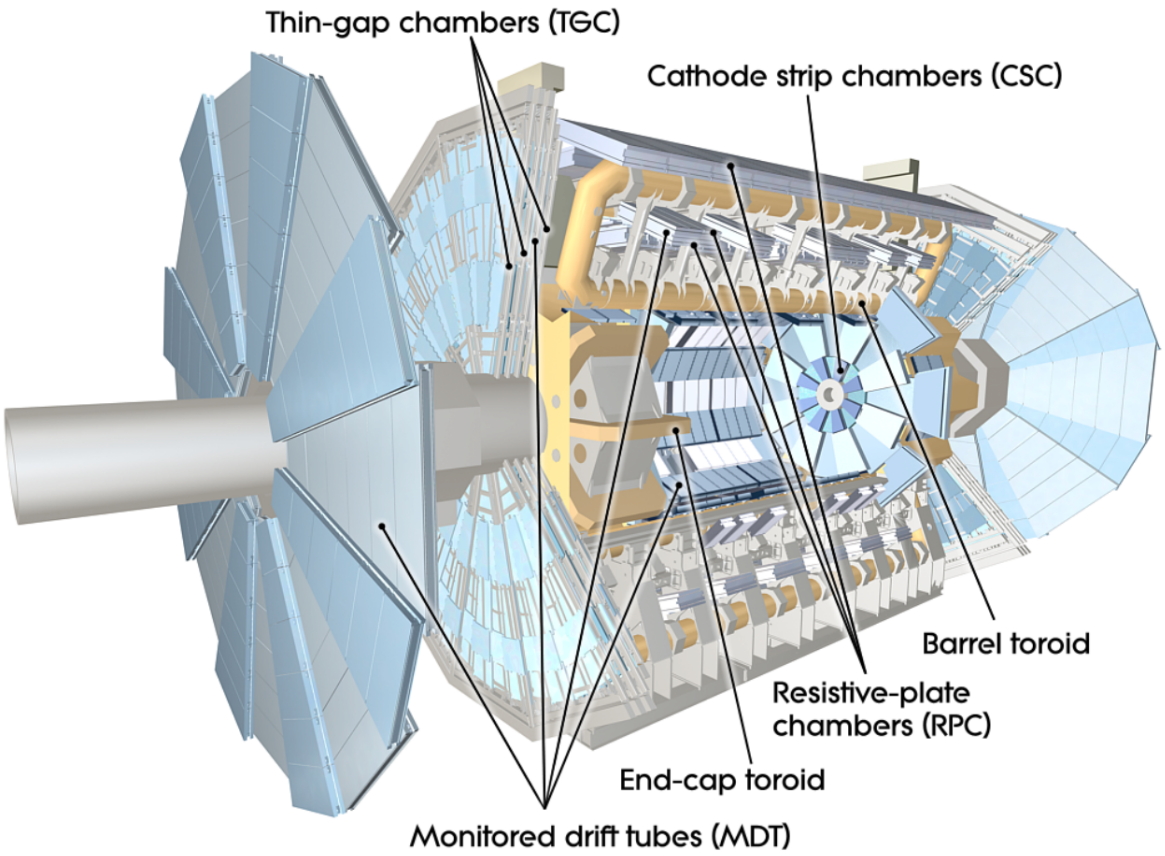

Figure 4.11: Cutaway view of ATLAS Muon Spectrometer. This figure is taken from Ref [14].

- **MDT**: Monitored Drift Tube chambers covers a pseudorapidity range of $|\eta| < 2.7$ in total with $\eta < 2.0$ for the innermost end-cap layer. Their main purpose is to precisely measure the muon tracks in the bending directions in respective pseudorapidity ranges.

- **CSC**: Cathode Strip Chambers lie in a pseudorapidity range of $2.0 < |\eta| < 2.7$, where they are used for the precision measurements in the bending directions of the muon tracks.

- **RPC**: Resistive Plate Chambers provide inputs to the muon trigger in the pseudorapidity range of $|\eta| < 1.05$ and measure the muon track position in the non-bending direction.

- **TGC**: Thin Gap Chambers provide inputs to the muon trigger in the pseudorapidity range of $1.05 < |\eta| < 2.4$ and measure the muon track position in the non-bending direction.

Precision tracking chambers

The measurements taken in MS strongly depend on the geometry and alignment precision of the MDT and CSC chambers. The optical precision alignment of these chambers must ensure to fulfill their measurement requirements. In order to fulfill the criteria, the Monitored Drift Tubes are configured in ϕ layers in the barrel region, while in the end-caps they are placed orthogonal to the beam pipe. The basic detector unit is composed of a cathode tube of approximately 15 mm radius. This cathode tube is filled with Ar and CO_2 gas and tungsten-rhenium readout wire which acts as an anode. With this configuration, 80 μm resolution per tube is achieved. The innermost layer of the Muon Spectrometer also includes Cathode Strip Chambers. The layout of the CS chambers provides approximately 40 μm resolution in the bending direction of the track while 5 mm in the track transverse plane.

Trigger chambers

In the barrel region of MS, the Resistive Plate Chambers (RPCs) act as triggering chambers, while in the end-cap region the circular-shaped Thin Gap Chambers (TGCs) is the triggering chambers. The TGC provides a spatial resolution of 1.8 mm and is made up of multiple wires, while the RP chamber is made up of a gaseous electrode plate detector. Both of these chambers provide enough time resolution, space, and rate-counting capability.

4.4.5 Magnets

In order to keep the trajectory of the charged particles bending along the way, a strong magnetic field is required. For this, the ATLAS experiment contains an ATLAS Magnet system consisting of two magnetic regions, one in the central region which uses a solenoid, and another in the barrel and end-cap region which are three toroids.

Solenoid magnet

Surrounding the inner detector, the central solenoid generates a uniform longitudinal magnetic field of 2 Tesla. The generated magnetic field bends the trajectory of the charged

particles in ϕ-direction inside the inner detector, resulting in the measurement of the momentum and electric charge from the curvature. Relatively small in size, the central solenoid magnet system is composed of a superconducting NbTi single-layer coil that works at 4.5 K temperature. A cryostat is used to provide such a low temperature. Overall, the solenoid magnet system has a length and diameter of 5.6 m and 2.5 m respectively.

Toroid magnets

In the barrel and end-cap regions, a magnetic field varying from 0.5 T to 1 T depending on location is provided by the Toroid magnet system. The magnet system covers a pseudorapidity range of $|\eta| = 2.7$. Symmetrically constructed in ϕ direction, the toroid magnet system is composed of a toroid consisting of eight superconducting coils in the barrel region and two toroids of eight coils each in both the end-cap regions. The toroid coils are composed of NbTiCu wires and to minimize the effects of multiple scattering of muons they are surrounded by air. The dimensions of the toroid magnet system are 25.3 m in length along the z-axis and the outer diameter is about 20.1 m in the barrel region making it the largest ever constructed toroidal magnet. In the end-cap region, the axial length of the toroid is about 5 m with an outer diameter of 10.7 m.

4.4.6 Trigger and Data Acquisition systems

At nominal LHC operation, the proton bunches cross each other with a frequency of 40 MHz, i.e, every 25 ns. A master clock uses this frequency to synchronize all operating LHC experiments with the LHC beam. The recorded data size of a single collision event is around 1.5 MB. For offline analysis, it is unfeasible to send 1.5 MB of data with a 40 MHz frequency. Therefore, the ATLAS Trigger and Data Acquisition (DAQ) systems were designed to sort out and record only important events for physics studies.

Most of the features of the trigger are configured based on the presence of high transverse momentum photons, electrons, muons, jets, and hadronically decaying tau leptons. Figure 4.12 shows an overview of the ATLAS DAQ system during LHC Run-2. The ATLAS trigger system consists of two levels that refine the event selection eventually reducing the event rate. The events are initially evaluated by a hardware-based Level 1 (L1) trigger system, followed by the software-based High Level Trigger (HLT) system. To reach a final decision, a specific time is required by each trigger level called the latency is an important

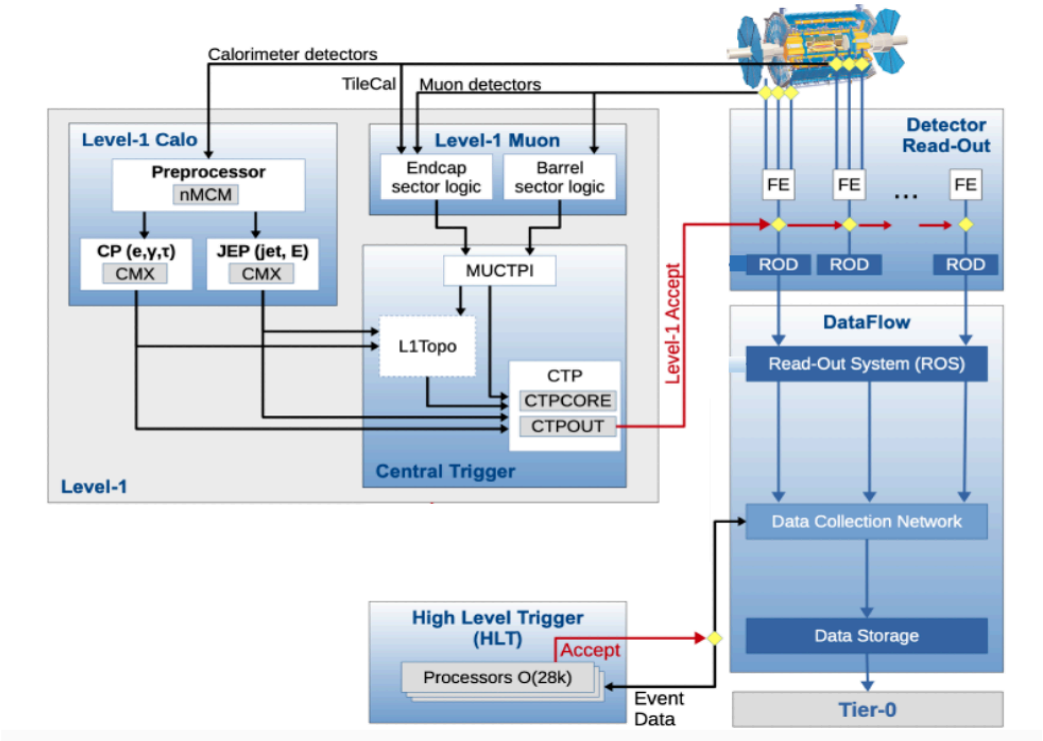

Figure 4.12: Schematic diagram of the ATLAS Trigger and Data Acquisition System used during LHC Run-2. This figure is taken from Ref [15].

requirement of the trigger system.

Level-1 trigger

Level 1 trigger is the first step of the DAQ system to record or discard events. It receives information from different subdetectors and is divided into three main parts: A level 1 Muon trigger (L1 Muon), a Level 1 calorimeter-based trigger (L1 Calo), and a Central Trigger Processor (CTP). Each L1 trigger system is operated by the respective algorithm. The L1 Muon algorithm tracks the muon path from the interaction point. The L1 Calo is dedicated to the selection of electrons, photons, jets, and hadronically decaying taus (τ_{had}) through L1 Calo e/γ, L1 Calo jet/energy and τ_{had} algorithms respectively. Besides these other systems such as Minimum Bias Trigger Scintillators (MBTS) from Tile hadronic calorimeter, Zero-Degree Calorimeter (ZDC) and the LUCID Cherenkov counter also contributes to the input fed to the Central Trigger Processor (CTP).
After selecting the relevant event information, both L1 Calo and L1 Muon processors report

to the L1 CTP. The information is based on the multiplicity of all the triggered object types, such as electrons/photons, jets, muons, and τ_{had}. The CTP receives information about thresholds passed by the total and missing transverse energy. Besides this, the CTP also counts the lumiblock and performs the timing task, giving the whole detector a clock synchronous to the LHC proton bunch-crossing. The signals accepted by the L1 then become the logical OR operation of all trigger items. The signals are then passed to the front-end electronics and Readout System (ROS) of the detector. Following the L1 trigger system decision, the readout rate is reduced from 40 MHz to around 100 kHz.

High-Level trigger

Once an event is accepted by the L1 trigger, the associated recorded data is buffered in the Read-Out System (ROS) and sent to the High-Level Trigger (HLT). The HLT then utilizes more computationally intensive reconstruction techniques on higher-granularity information from the calorimeters and tracking information from the MS and ID to subject an event to specified criteria. If an event meets (a given combination of) the trigger menu's criteria, it is locally saved at CERN and exported to the computing center for full offline reconstruction. These criteria are based on the multiplicity, momentum, and relative direction of specific trigger physics entities, such as jets, muons, and missing transverse momentum, which are all members of a particular trigger group. Finally, the HLT lowers the reading rate from 100 kHz to around 1 kHz.

Data Quality

Once events pass the triggers and are stored locally, they are subjected to additional quality tests to ensure that they will be fit for use in physics simulations. On fully rebuilt events, an offline data quality monitoring system conducts automated tests. These tests are run on histograms to find any problems or inconsistencies, and flags are applied based on the results. These flags are saved in a database for use in physics simulations. The histograms and verification results are also saved for future use.

Chapter 5

ATLAS Tile Calorimeter

The TileCalorimeter (TileCal) is a sampling calorimeter covering the most central region of the ATLAS hadronic calorimeter at the Large Hadron Collider. TileCal provides coverage of $|\eta| < 1.7$*, using plastic scintillator tiles as an active and iron plates as an absorber medium. The ATLAS TileCal gives useful information for energy and tracks the reconstruction of jets and hadrons.*

This chapter presents a detailed discussion of the TileCal architecture and the readout schemes. Since this thesis is focused on the studies of PMT response and its stability over time, a brief description of the TileCal PMTs will be discussed in Section 5.2.

5.1 TileCal architecture

The Tile Calorimeter is the central hadronic calorimeter of the ATLAS experiment, surrounding the Liquid Argon (LAr) electromagnetic calorimeter. The TileCal is a 5.8 m long cylinder with an outer and inner radius of 4.25 m and 2.28 m, respectively.
Along the z-axis, the TileCal is divided into four partitions for data acquisition and power distribution, two central long barrels called LBA and LBC and two extended barrels called EBA and EBC. The LBA and LBC collectively covers the region of $|\eta| < 1$ and EB covers two regions of $0.8 < |\eta| < 1.7$. For routing of the Inner Detector and Liquid Argon cables and electronics, a gap of 600 mm is present between the LB and EB cylinders. A part of the gap constitutes an extension of the EB called Intermediate Tile Calorimeter (ITC) designed to maximize the volume of active material in this region.

5.1.1 TileCal mechanics and optical readout

The basic task of the TileCal is to identify hadronic jets and measure their energy and direction. When a charged particle passes through the scintillation tiles, ultraviolet light is produced and collected by wavelength-shifting fibers at both edges of each tile. This light is shifted to the green spectrum and then transported by these fibers to the photomultiplier tubes (PMTs) located in the outer radius steel girder that also houses the front-end electronics. The outputs from the PMTs are amplified, shaped, and digitized by ADCs and finally stored in the front-end pipeline memory. The scintillator tiles are grouped together into cells. The alternating layers of plastic scintillating tiles and iron plates together with wavelength shifting fibers (WLS) and PMTs are shown in Fig 5.1.

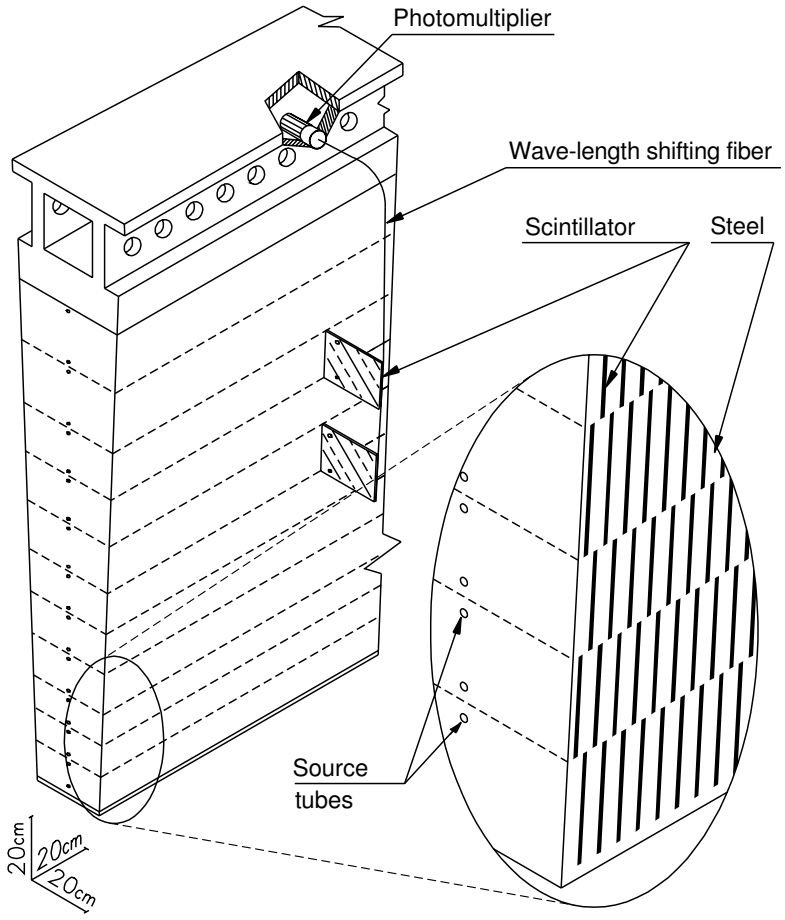

Figure 5.1: An illustration of the optical read-out and mechanical assembly of a TileCal module corresponding to a ϕ wedge. Each TileCal barrel is divided into 64 wedged modules of width $\Delta\phi \approx 0.1$ in the azimuthal direction. This figure is taken from Ref [16].

TileCal barrels are radially segmented into three longitudinal sampling layers to sample the shower at three different depths. These layers are denoted by A, B (layer BC in LB) and D with a granularity $\Delta\eta \times \Delta\phi = 0.1 \times 0.1$ in the innermost layer and $\Delta\eta \times \Delta\phi = 0.2 \times 0.1$ in the outermost layer as shown in figure 5.2. The lengths of the three layers are approximately 1.5, 2.6, and 3.3 interaction lengths (λ) for the EB region and 1.5, 4.1, 1.8 λ for the LB region, respectively. To cover the gap between the long and extended barrel region special E-cells called crack and gap scintillators (with no absorber material) are inserted. These special cells provide necessary readings for corrections for energy losses in dead material in the crack regions.

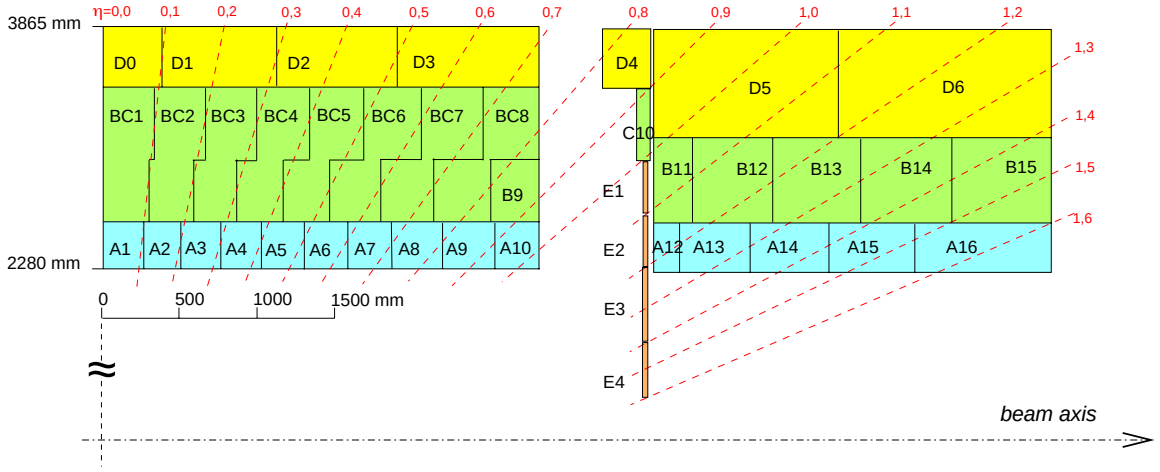

Figure 5.2: Segmentation in-depth and in η of the Tile Calorimeter modules in the central (left) and extended (right) barrels. This figure is taken from Ref [16].

The TileCal cells are formed by a grouping of fibers sending light to a PMT. A typical Tile Calorimeter cell is read out by two PMTs, corresponding to two electronic read-out channels. TileCal has a total of 9855 PMTs corresponding to about 5182 cells. The output of the PMT signals is shaped and amplified in two gains, low and high gain with a relative ratio of 1:64 for high and low signals respectively. The amplitude of the output current pulse of the PMT is proportional to the energy deposited in the associated cell. The shaping and amplification of the output pulse are done by the electronics mounted on the PMT. The analog pulse is digitized with 7 samples every 25 ns by a 10-bit analog-to-digital converter (ADC).

The Tile Calorimeter provides a three-dimensional measurement of the energy deposited by the hadronic shower. TileCal is designed to provide standalone energy resolution for jets of

energy E as:

$$\frac{\sigma}{E} = \frac{50\%}{\sqrt{E}} \oplus 3\% \tag{5.1}$$

The resolution becomes better with the increasing energy of the incoming hadrons. The 3% term in the Eq 5.1 represents the contributions that do not depend on particle energy, such as radiation damage and other instrumental effects. While the term 50% includes the stochastic fluctuations of energy deposited in the absorbers and fluctuations in the amount of visible energy. These terms are more prominent at high energies.

5.1.2 TileCal readout electronics

The TileCal readout electronics perform the amplification, shaping, and digital conversion of the PMT analog signals. Fig 5.3 shows the read-out scheme of the TileCal.

PMT block

TileCal front-end electronics are lodged in drawers at the outer radius of each module along with the PMTs. Each drawer contains a maximum of 24 channels, two of which makes a super-drawer. Each channel is made up of a PMT block. The PMT block converts light signals from the TileCal cells into electronic signals using its different components. The different components of a PMT block are the following:

- **Photomultiplier tube**
  A photomultiplier tube converts the light into electric signals. A more detailed discussion on a PMT can be found in section 5.2.

- **Light mixer**
  A light mixer serves as the interface between the fiber bundle and the PMT. The purpose of the light mixer is to couple the fibers with the PMT ensuring uniform illumination of the PMT photocathode.

- **High voltage divider**
  High voltage dividers are located at the end of PMTS. The HV dividers divide the input HV and provide voltages to the PMT dynodes.

- **3-in-1 card**
  A 3-in-1 card plugged into the anode of each PMT is named for its multiple function-

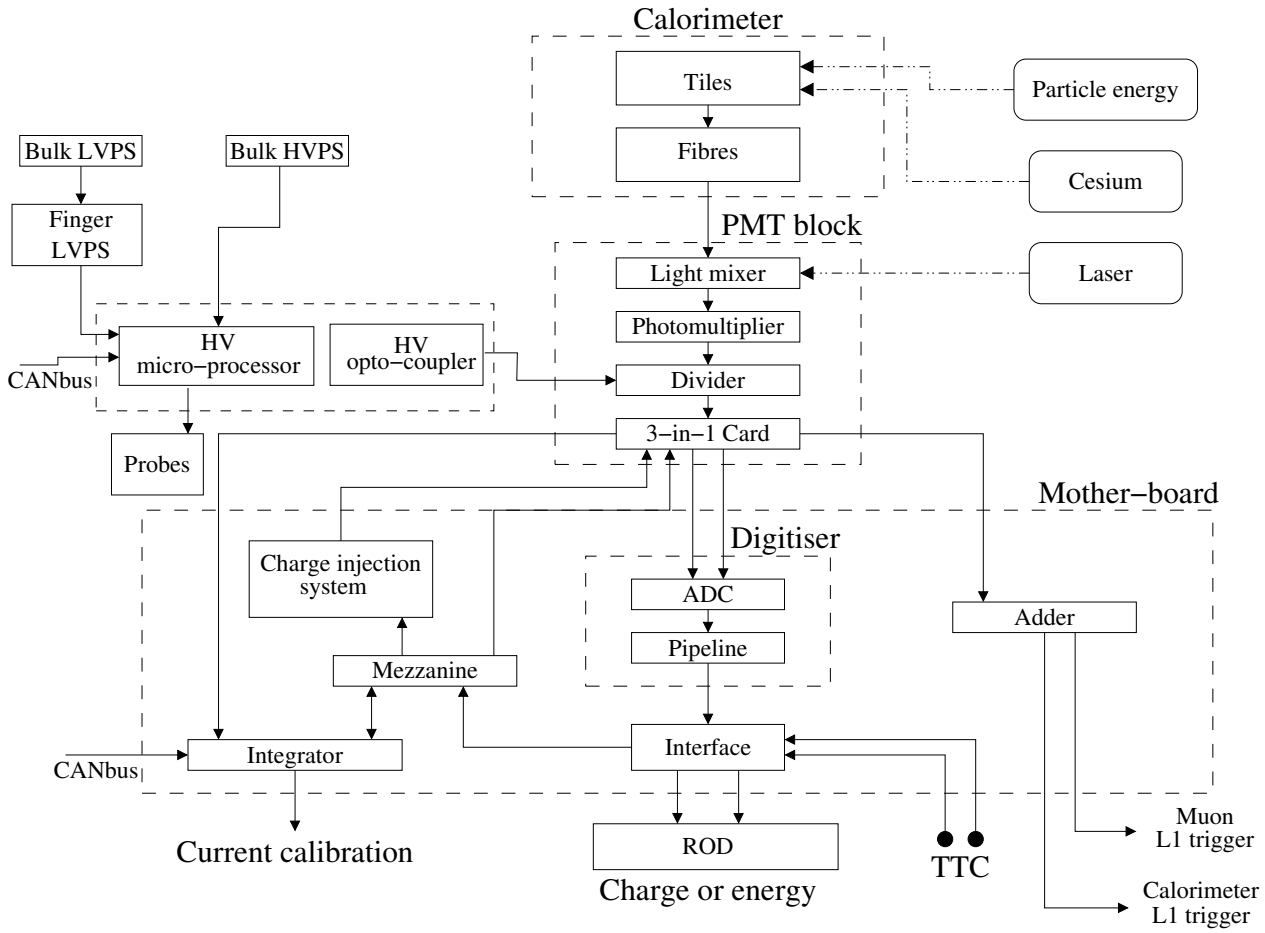

Figure 5.3: Block diagram of the TileCal readout electronics. This figure is taken from Ref [16].

alities. The schematics of the TileCal 3-in-1 card is shown in figure 5.4. It performs the following main functions:

- One of the functions of a 3-in-1 card is shaping the PMT signal to digitizers. The resulting PMT signal is split into two signals each going to two independent amplification chains. The output is bi-gain with a ratio of 1:64. These two chains are called Low Gain (LG) and High Gain (HG) branches. The advantage of the bi-gain structure is that it allows to measurement of signals from a few MeV up to TeV with high resolution throughout the energy range. The LG branch is used to feed the analog trigger system.
- 3-in-1 card is also involved in controlling and injecting a known signal of pro-

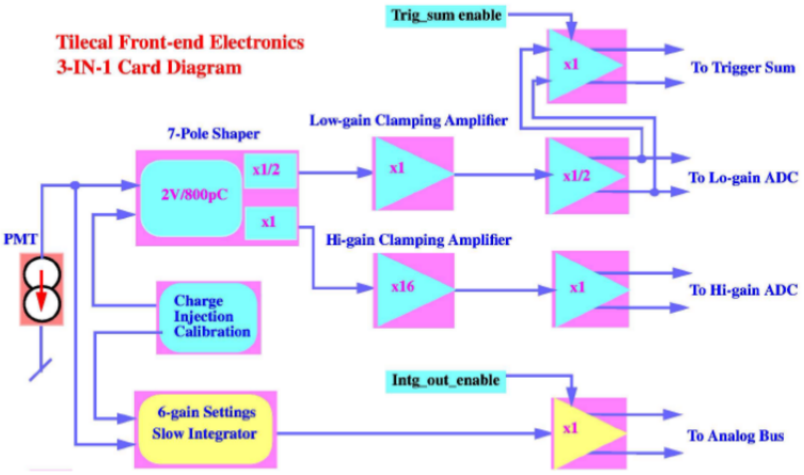

Figure 5.4: TileCal 3-in-1 card schematic.

grammable amplitude at the input stage which provides an input for the TileCal Charge Injection System (CIS) used to calibrate the ADCs.

– Another function of the 3-in-1 card is implemented with the slow integrator. The integrator signal is used to process the information from the signals produced with the cesium system which is one of the TileCal calibration systems. The integrated signal is also used to measure the average anode current produced by Minimum Bias events in TileCal.

Motherboard

The motherboard is the first layer located below the PMT block. The basic function of the motherboard is to carry the low-voltage power and digital control signals for the 3-in-1 card.

Digitizer board

The Digitizer board is the middle layer that digitizes the output analog signals received from the 3-in-1 card in the PMT block. The DMU located on the digitizer board digitizes the shaped and amplified signals every 25 ns by 10-bit ADCs. Two ADCs are required for each channel due to the two gain (high and low gain) branches. The high Gain branch is

the default data sample. When the charge goes above 12.5 pC, the High Gain branch gets saturated. The Low Gain LG samples are passed only when a threshold is met in the HG data samples. The Low Gain region ends for input above 800 pC. In energy terms, the maximum energy read out by HG and LG is about 13 GeV and 850 GeV respectively.

Interface board

The interface board is the third and outer layer which is responsible for the sampled signals transmission to the back-end electronics and reception and dispatching of the TTC signals.

5.2 TileCal photomultiplier tubes

Photomultiplier tubes (PMTs) are photodetectors or light sensors that use the external photoelectric effect phenomena to detect the light signals. In the phenomena of the external photoelectric effect when light strikes a semiconductor or metal placed in a vacuum, electrons are emitted. These PMTs are widely used in multiple fields.
As mentioned already, each cell in TileCal is read out by two PMTs, making a total of 38 PMTs in Extended Barrel and 45 PMTs in the Long Barrel region. Based on the requirements mentioned in Ref [37], after carefully analyzing and testing the TileCal collaboration chose the photomultipliers from Hamamatsu model R7877 Ref [38]. A brief description of the basic principles and characteristics of PMTs is discussed in this section.

5.2.1 Basic principles of photomultiplier tubes

When light enters a photomultiplier tube an output signal is produced through the following processes:

- Light enters the PMT through an input window. The entered light excites the electrons in the *photocathode* which led to the emission of photoelectrons known as electron flux into the vacuum.

- The emitted photoelectrons are accelerated and focused by the focusing electrode as shown in the fig 5.5. The focusing electrode is also known as *electron optical input system.* In order to efficiently collect primary and secondary photoelectrons on a dynode, the design of the electrode is optimized on the basis of electron trajectory.

- These photoelectrons pass through multiple electrodes known as *electron multiplier or dynodes* where their number is multiplied by means of secondary emission. The electrode structure of a photomultiplier tube is designed in such a way as to provide maximum performance. Emitted photoelectrons from the photocathode are incident on the first dynode and re-emitted and multiplied as secondary to the next dynodes up to the last dynode (up to 19 dynodes), with current amplification ranging from 10 to 108 times.

- The *anode* of a photomultiplier is an electrode that collects the cascade of secondary electrons or electron flux through multi-stage dynodes and transmits the electron current to an external circuit.

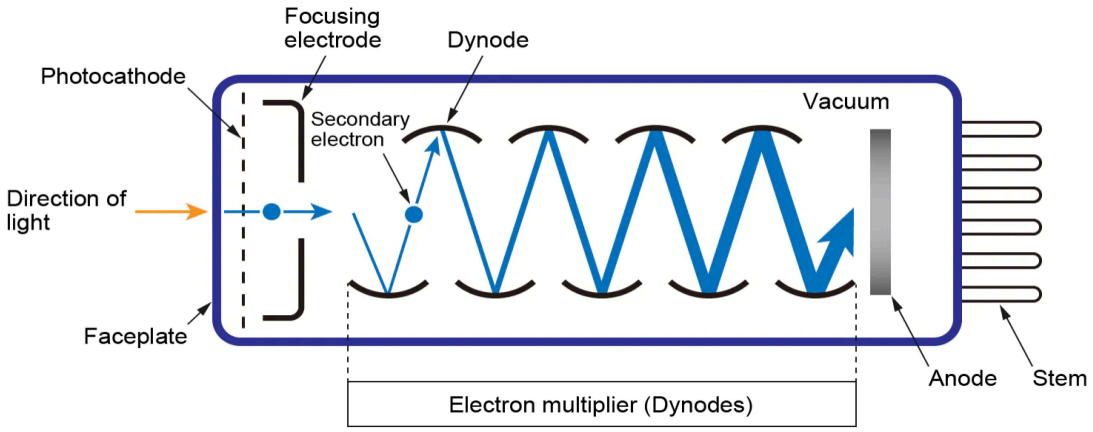

Figure 5.5: Schematic construction of a photomultiplier tube. The figure is taken from Ref [17].

5.2.2 Characteristics of TileCal photomultiplier tubes

The TileCal PMTs were chosen on the basis of certain requirements. A brief overview of the characteristics of the PMTs on the basis of their requirements is given below:

- The TileCal PMTs are located in a small space inside drawers with other electronics. Hence the first characteristic of the PMT is limited dimensions in order to be able to fit inside the drawer. The length of the TileCal PMT should not be more than 50 mm with the photocathode surface bigger than the bundle of the fiber surface. Small dimensions of a PMT provide better immunity to the effects of the transport of electron cascade from the residual magnetic field in the dynode volume.

- The second characteristic of the TileCal PMT is the linearity response in a huge interval of incident light intensity. PMTs are hit by light pulses of different energy ranges (from 350 MeV to 1.5 TeV). But the PMT response should be linear in an interval of 4 orders of magnitude. In order to detect small pulses, the gain of the photomultiplier tube should be fairly high, but not too high to not have a saturated signal. By changing the supply voltage, the correct gain value can be set by from the PMT power supply which is usually in the range from 600 V to 700 V. With this power supply setting the correct gain value (10^5) for all the PMTs can be achieved.

- Another characteristic of the TileCal PMT is the PMT rise time which should be small in order to use a calorimeter signal as a trigger. Typical PMT rise time values are less than 2.5 ns.

In the currently operating Tile Calorimeter, the PMT model R7877 from Hamamatsu is used fulfilling all the above-mentioned requirements. This model is specifically made for TileCal from the R5900 model after several iterations. In 2000-2002 a total of 10140 PMTs were produced by Hamamatsu from which 9852 were installed in the detector. The rest of the spare PMTs are present at different test sites.

Chapter 6

Calibration of the TileCal

6.1 Introduction

When a hadron passes in a hadronic calorimeter, it creates a hadronic shower. On average, around 30% of the total energy of jets from quark and gluon fragmentation is deposited in the TileCal. Therefore it plays a crucial role in the precise reconstruction of the kinematics of the physics events. The control of its stability within 1% and of its resolution is important for a correct jet and missing transverse energy reconstruction in ATLAS. In order to obtain a precise and stable measurement of the deposited energy in the calorimeter, it is important to precisely monitor any variation in the response of the PMTs and, if needed, correct for these variations. For this purpose, several complementary hardware calibration systems have been included in the TileCal design. The detailed description of these calibration systems is discussed in Section 6.2.

6.1.1 Signal reconstruction

When a charged particle passes through the plastic scintillators, the emitted light is converted by the PMTs into an analog electrical signal. In each TileCal channel, these signals are sampled with seven samples with a spacing of 25 ns synchronized with the LHC master clock. These samples are referred to as S_i, where $1 \leq \mathrm{i} \leq 7$, and are in units of ADC counts. Depending on the pulse amplitude, either a High Gain (HG) or Low Gain (LG) readout is used to maximize the signal-to-noise ratio. TileCal employs the optimal filtering (OF) algorithm Ref [39, 40] to reconstruct the amplitude and time of the channel's signal. The method uses the linear weighted sum of the samples S_i to calculate the pedestal p, and the amplitude A of the pulse.

$$A = \sum_{i=7}^{n=7} a_i S_i, \qquad A_\tau = \sum_{i=7}^{n=7} b_i S_i, \qquad p = \sum_{i=7}^{n=7} c_i S_i \tag{6.1}$$

where the OF weights a_i, b_i, and c_i are linear coefficients optimized to minimize the bias on the reconstructed quantities introduced by the electronic noise. The reference pulse shapes for both gains were extracted from the test beam data and are used to determine the coefficients. For each gain, the pulse shape is defined and stored in a dedicated database for calibration constants. Figure 6.1 shows the reference pulse shapes for high- and low-gain modes.

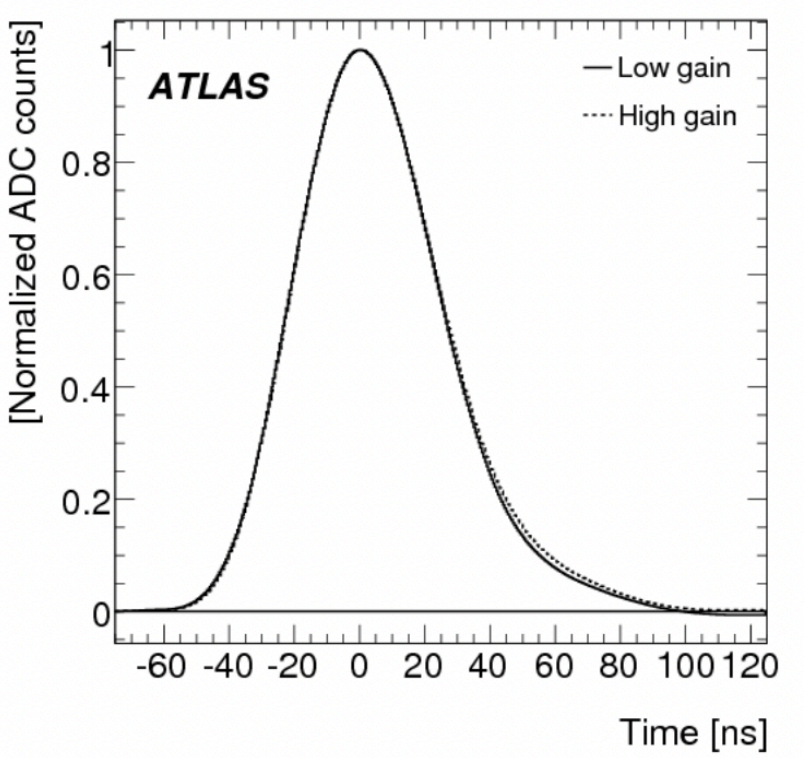

Figure 6.1: The reference pulse shape for high and low gain from test beam data, is shown in arbitrary units.

6.1.2 Energy reconstruction

To ensure the stability and monitor the behaviour of each component of the detector, there are three dedicated calibration systems at each level of the TileCal signal reconstruction.

These calibration systems maintain a time-independent electromagnetic (EM) energy scale and account for changes in the electronics and hardware framework. The reconstructed energy of each TileCal channel, E[GeV], is derived from ADC raw response and can be expressed as:

$$E\ [\text{GeV}] = \frac{A\ [\text{ADC}]}{f_{\text{pC}\to\text{GeV}} \cdot f_{\text{Cs}} \cdot f_{\text{Las}} \cdot f_{\text{ADC}\to\text{pC}}} \tag{6.2}$$

where $\boldsymbol{A}$ **[ADC]** is the signal amplitude determined by the Optimal Filtering algorithm as shown in Eq 6.1. The different f_i factors in the Eq 6.2 are the correction factors or calibration constants deduced by the different calibration systems.

- the factor $\boldsymbol{f_{\text{pC}\to\text{GeV}}}$ is the electromagnetic calibration constant and provides the conversion of the calorimeter signals measured as the electric charge in pC to the energy deposited by the electrons which produce the signals. This factor was fixed during dedicated test beam campaigns Ref [41] in which particles with known energy cross the calorimeter.

- $\boldsymbol{f_{\text{Cs}}}$ is the absolute calibration factor for the optics and the PMTs, provided by the cesium calibration system. The cesium calibration system is discussed in detail in Section 6.2.1.

- the calibration factor $\boldsymbol{f_{\text{Las}}}$ is determined with the laser system. More discussion about the laser calibration system can be found in Section 6.2.2.

- $\boldsymbol{f_{\text{ADC}\to\text{pC}}}$ is the calibration constant calculated for each channel by the Charge Injection System (CIS) that calibrated the front-end electronics. A more thorough detailed discussion of this system is in Section 6.2.3.

All of these calibration factors can evolve with time due to several factors such as the variations in PMT high-Voltage, induced stress by high light flux, or due to the aging of the scintillators because of radiation damage. The calibration systems are used to monitor the stability of these factors and provide corrections for each channel. Additionally, the minimum-bias currents in Fig 6.2) validates the changes in the response of the different detector components observed by cesium calibration system. A more detailed description of the calibration systems can be found in the following Section 6.2.

6.2 Calibration systems

Dedicated calibration systems are in place to calibrate and monitor the behaviour of the different detector components at each level of the TileCal signal reconstruction. These calibration systems ensure the stability of each element of the readout chain and provide calibration constants for each channel. There are three main calibration systems in TileCal:

- Cesium calibration
- Laser calibration
- Charge Injection System (CIS)

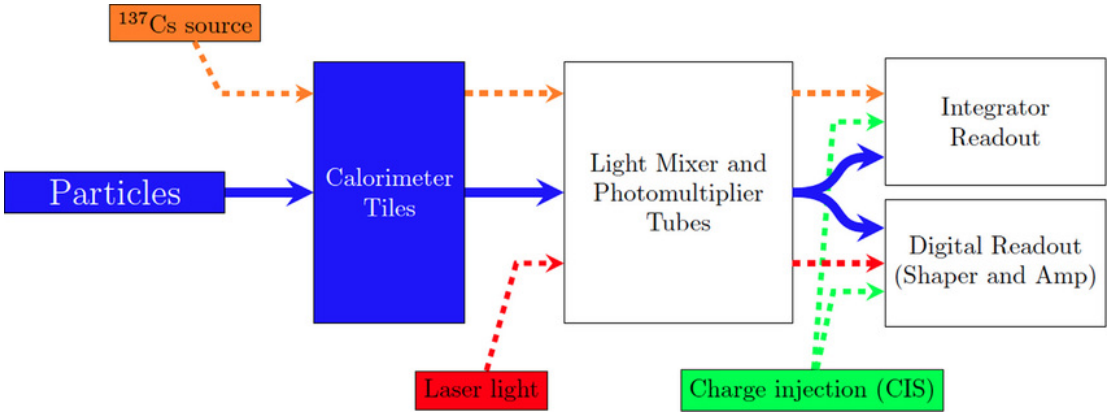

Figure 6.2: Flow diagram of the readout signal path of different TileCal calibration systems.

TileCal is calibration schema is shown in Fig 6.2. The cesium system is the main tool to equalize the response of the calorimeter cells. In the cesium system, the ^{137}Cs source is responsible for calibrating the overall response of the calorimeter including fibres, tiles, and photomultiplier tubes. The laser system calibrates the photomultiplier response between

two Cs-source calibrations. While the Charge injection system calibrates the front-end electronics. The path of these three calibration systems partially overlaps in the readout chain to identify potential failures and to do cross-checks. In addition to these systems, Minimum Bias (MB) events are used to provide an independent cross-check of cesium calibration.

These calibration systems are explained in detail in the following subsections.

6.2.1 Cesium calibration system

The cesium calibration as the name indicates, uses moveable ^{137}Cs γ-sources all over the detector volume, a few times a year. The ^{137}Cs radioactive source moves through the calorimeter in a hydraulic system with liquid flowing inside, using steel tubes that pass through the holes in each scintillator tile as shown in Fig 5.1. The ^{137}Cs γ-source produces a metastable Barium (^{137}Ba) with a beta decay. This metastable decay isotope decaying a photon with an energy of 0.662 MeV. The activity of the source is about 10^6 Bq. The released photon produces scintillation light in each tile. The mechanical concept of the cesium source system is shown in Fig 6.3.

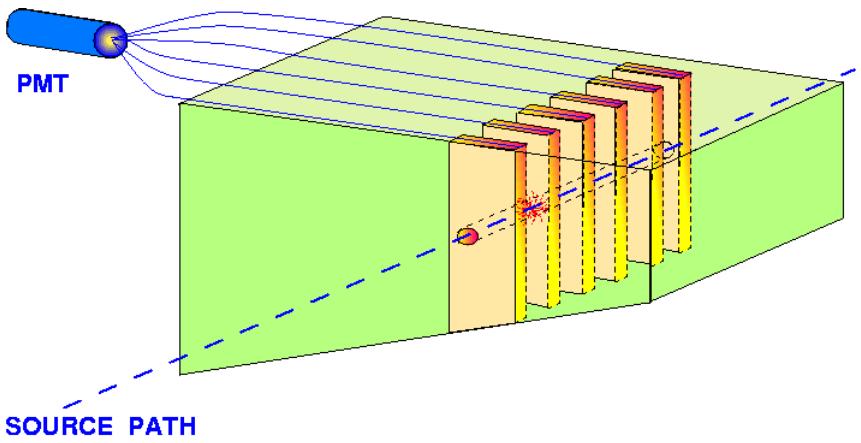

Figure 6.3: Mechanical concept of the cesium calibration system Ref [16].

A full cesium scan lasts approximately six hours through all TileCal tiles, so it needs at least six hours of pause during $p-p$ collisions fills to perform a cesium calibration. Due to this reason, cesium scans cannot be done frequently. For the three barrel regions, three separate Cs sources are used one for each partition. The velocity of the radioactive source is of the order of about 35 cm/s, which takes about 5 hours to scan Long Barrel (LB) modules and 3 hours for Extended Barrel (EB) modules. Since the hydraulic tube system in LB is larger than EB, during one scan, LB is scanned in one direction only while EB is scanned in both directions Ref [42].

The analysis of Run-1 and Run-2 cesium scans shows that there is a difference between the measured and expected response of all the cells within each barrel region. Fig 6.4 shows the average response evolution to the cesium source of the Tile calorimeter as a function of time in three longitudinal layers. The response of all layers was equalized at the beginning of Run-1 in June 2009 and at the beginning of Run-2 in February 2015. The points are the measured response while the solid black line represents the expected response indicating the loss of the response of the three sources (-2.3%/ year). The systematic uncertainty of the cesium system is about 0.3% Ref [43].

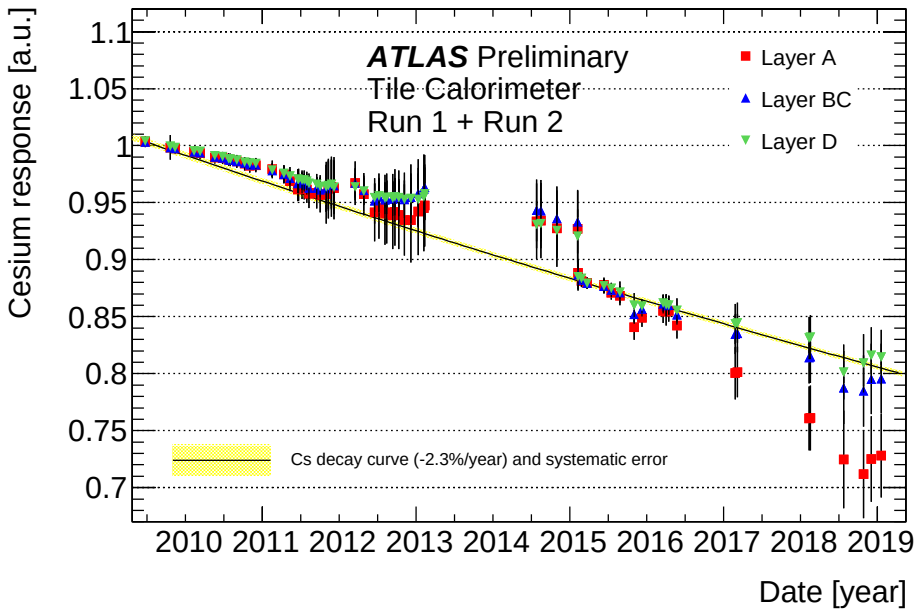

Figure 6.4: Evolution of the average response to cesium source in Run-1 and Run-2 of the three longitudinal layers as a function of time as seen by the cesium system Ref [18].

Since the cesium calibration is not so frequent, it's not sufficient to track fast drifts of

the PMT's response. The laser calibration system is thus used to track the PMTs' response between two cesium scans.

6.2.2 Laser calibration system

The laser system is one of the calibration systems used to monitor the response variations of the PMTs and the digital readout electronics. Laser calibration is also used to monitor the channel timing during data taking.

The Laser-II system shown in Fig 6.5 was installed during Long Shutdown I (LS1) in the

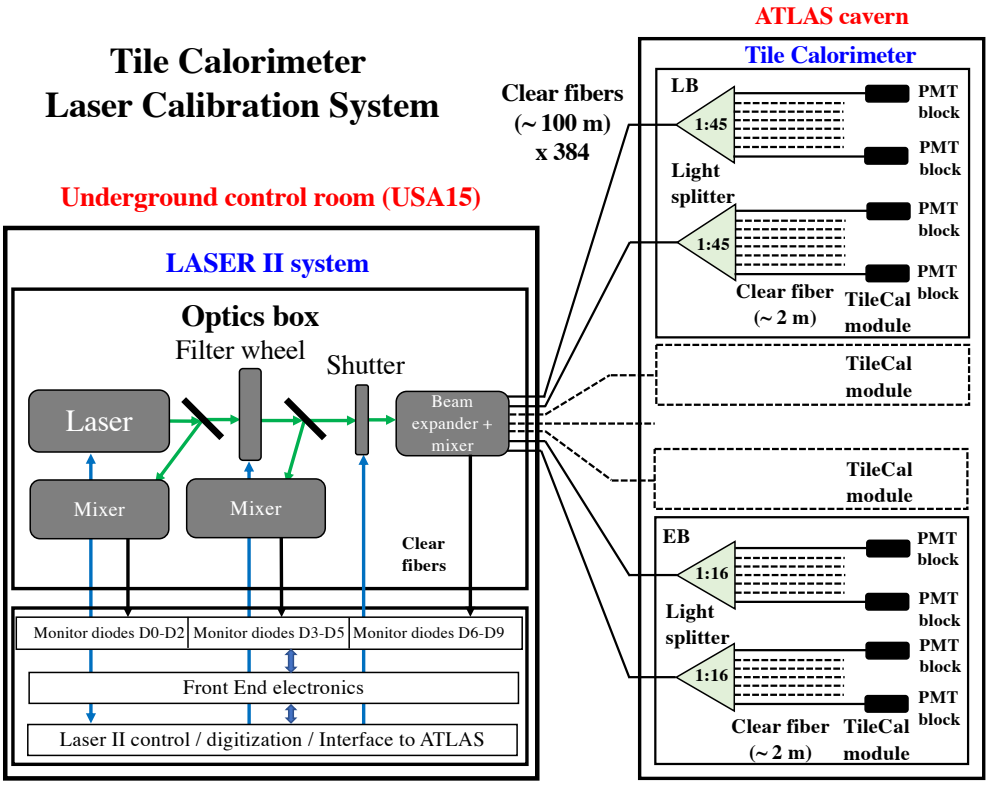

Figure 6.5: Schematic diagram of the Laser-II calibration system used during Run-2.

ATLAS main service cavern. The Laser-II system was installed in order to improve the system reliability and to correct the shortcomings in electronics and light monitoring of the laser-I system used during Run-1 Ref [44]. The new laser-II system has been used since the beginning of Run-2 in 2015. As this thesis work mainly focuses on the laser calibration

system and its procedures, a more detailed description of the Laser-II system is given below in subsection 6.2.2.1 and about laser calibration procedures is given in dedicated chapter 7.

6.2.2.1 Laser-II system apparatus

The laser-II system consists of a laser source able to send controlled short laser light pulses of about $10ns$ pulsed width and wavelength $\lambda = 532nm$ (green light)through dedicated optical fibres to photocathode of all 9852 PMTs. The entire laser-II apparatus is located off the detector in the counting room USA15. This system ensures the stability and linearity of the PMTs' response. The main components of the Laser-II apparatus are divided into six main functional blocks as shown in Fig 6.6 and explained below:

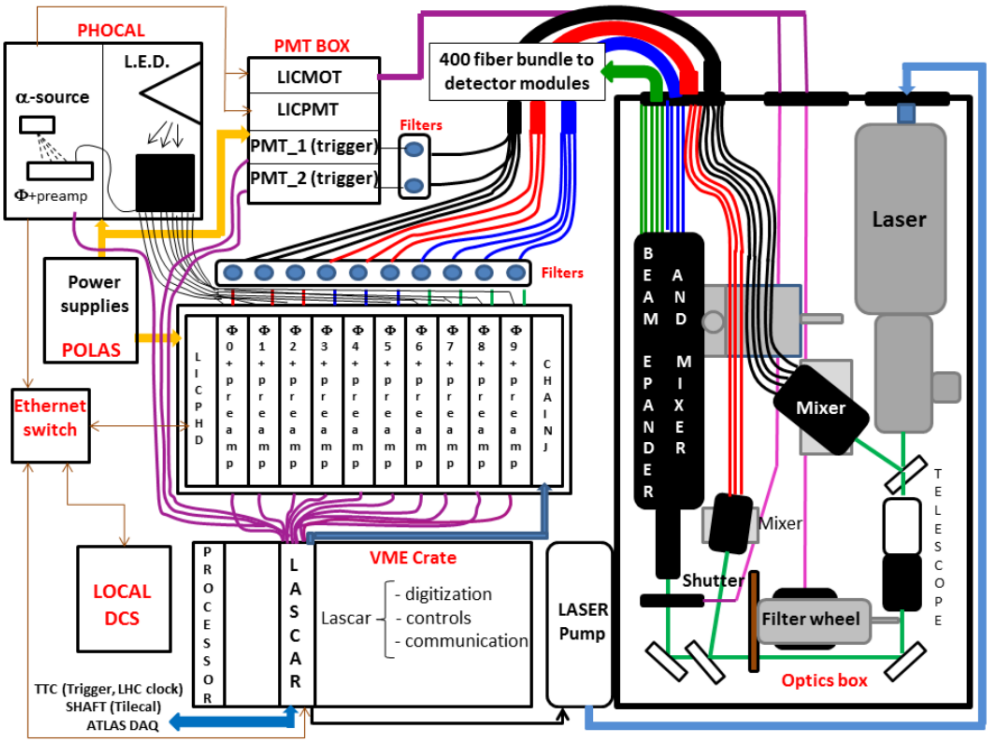

Figure 6.6: The scheme of the Laser-II system with its components.

Optics box

The optics box houses the main optical components which include a laser light source, filter wheel, beam splitter, beam expander, and mixers. The laser light source, manufactured by SPECTRA-PHYSICS Ref [45], is a commercial Q-switched diode-pumped solid-state laser. The optics box undergoes major updates in the Laser-II system with respect to the previous Laser-I system to allow a better estimation of injected laser light in the calorimeter through redundant monitoring of the transmitted light in the entire optical path with 10 photodiodes.
The laser source sends a pulsed laser light of wavelength $\lambda = 532$nm (green light) and a pulse width of about 10 ns. The characteristics of this light are very close to the light coming from detector WLS fibres, peaked at 480nm.
The beam splitter located at the output of the laser head, split the light into two beams, redirecting a small portion (about 10%) of the light towards the light mixer and then to the monitoring photodiodes. While the other portion of the light is transmitted through a beam expander to a filter wheel. The light which exits the light mixer is collected by five clear fibres. Two of the clear fibres are coupled with the two PMTs located inside the PMT box which are used to generate the trigger signal for the Laser-II data acquisition (DAQ) system. The remaining three clear fibres are connected to the monitoring photodiodes (D0-D2) located inside the photodiode box.
In the beam expander, the beam spot is expanded from 700 μm to 2 mm to reduce the light power density to the forthcoming optical elements. The reflected light then passes through a motorized filter wheel containing eight neutral-density filters with different optical densities. These different optical filters offer transmissions ranging between 100% (without filter) and 0.3%. The combination of these transmission adjustments, and the range of intensities where the laser operation is stable, allows calibrating the TileCal PMTs in an equivalent cell energy range of 500 MeV to 1 TeV.
The light from the filter is fed into a light mixer through a beam splitter. The light is then collected by the monitoring diodes (D3-D5) inside the photodiode box by three clear fibres. Another mirror at an angle of 45^0 reflects the light into the final beam expander through a shutter. From here the laser light is dispatched to the detector through 400 clear fibres. These 400 long clear fibres are grouped together and transfer the light coming from the optics box to the TileCal modules. Inside each TileCal module, the light is dispatched to each PMT through an optical system consisting of a light mixer. Some of the expander output light is routed to the monitoring photodiodes (D6-D9) by four fibres.

Optical filters

A patch panel consisting of ten optical filters with filter density ranging from 0.5 to 2.5 is set up to adjust the intensity of the light readout by each monitoring photodiode inside the photodiode box.

Photodiode box

The photodiode box is a rack containing ten modules, while each module has a photodiode coupled to a preamplifier, a control card, and a charge injection card. The charge injection card injects an electrical charge into each pre-amplifier inside the photodiode box. A pair of fibres are connected to the back end of the box. One of the two fibres is connected to the patch panel with optical filters and transfers the laser light for monitoring, while the other fibre is connected to the PHOCAL module, where LED light is injected to monitor the photodiodes' stability.

PMT box

The PMT box contains two photomultiplier tubes (Hamamatsu type R5900 Ref [38]) which reads the two optical fibres inside the optical box. The main purpose of these two PMTs is to provide the trigger signal to the Laser-II acquisition system when the laser flashes.

LASCAR electronics

LASCAR is the electronics board that contains two cards: a VME processor to communicate with ATLAS, and a special board "LASCAR" to control the Laser-II system and DAQ. The LASCAR board also provides an interface with ATLAS Data AcQuisition (DAQ).

PHOCAL system

A PHOtodiode CALibration (PHOCAL) system contains a reference photodiode, an LED, and an α-source. The blue LED checks the stability of responses of the ten monitoring photodiodes of the Laser-II system. The α-source (^{241}Am) of the PHOCAL system releases α-particles of 5.6MeV which ensures the monitoring of the reference photodiodes. The PHOCAL system did not exist in the Laser-I system.

Patch panel

The patch panel connects the 400 fibre bundle to the long fibres going to the detector. It also has a mechanical adjustment system that allows tuning the light injected in each long fibre by turning a screw on the connector.

As compared with other calibration systems the laser calibration runs are very fast, data is typically taken every 2-3 days during LHC data taking. Laser pulses are also sent during empty bunch crossings of the LHC. Using this data, the evolution of the time calibration is monitored.

6.2.2.2 Laser-II system operating modes

The Laser-II system can be in two modes:

- independently as a stand-alone system,
- integrated into the ATLAS detector data acquisition (DAQ) system with other calibration systems.

A brief detail of the two operating modes is given below:

Stand-alone operating mode

The stand-alone operating system verifies the stability of the Laser-II system and performs its internal calibration. In this mode the laser pulses are not sent to the TileCal PMTs and Laser-II components are controlled by the LASCAR. There are five running modes in stand-alone operation:

- **Pedestal mode:** This mode is used to measure the maximum number of events without any input signal from the laser, LED, or radioactive source.
- **Alpha source mode:** This mode is used to measure the response of reference photodiode to the α-source (^{241}Am) of the PHOCAL system.
- **LED mode:** This mode is used to probe the monitoring of photodiodes stability. In this mode, LED signals are sent through optical fibres to all the photodiodes, including the reference photodiode in PHOCAL module.

- **Linearity mode:** This mode assists in injecting a known electrical charge to the preamplifiers of the photodiodes to assess the stability of the readout electronics.
- **Laser mode** This mode is used to assess the stability of the TileCal PMTs by sending the laser pulses of adjustable intensity if the shutter inside the optics box is open.

A typical stand-alone calibration run combines all the above-mentioned five running modes.

ATLAS DAQ operating mode

The ATLAS DAQ mode is the main operating mode of the Laser-II system. Its main purpose is to calibrate TileCal PMTs with laser light of known wavelength. The mode is operated in two running modes:

- **Laser mode:** This is the main operating mode in which laser pulses are sent to the TileCal PMTs at the request of ATLAS DAQ through SHare Few Trigger (SHAFT) interface. The output signals produced by the PMTs and photodiodes are sent back to the ATLAS readout by LASCAR system.
- **Laser-in-gap mode:** In this mode the laser pulses in the abort gap of LHC orbit are sent only in exclusive periods of the beam when there is no collision. The SHAFT board is responsible for sending a request signal to LASCAR at a fixed time in the orbit to synchronize the laser pulses with the pre-defined orbits. After laser pulse emission, the SHAFT interface sends a laser calibration request to the ATLAS central trigger processor through the TTC system.

The majority of data shown in this thesis is taken from ATLAS DAQ operated under laser mode.

6.2.3 Charge Injection System (CIS)

The Charge Injection System (CIS) calibrates the electronics and readout components of the detector by injecting a known charge from a capacitor into the shaper circuit. This system is controlled by the *3-in-1* cards. The *3-in-1* cards Ref [37] perform three main functions:

- provides low and high gain-shaped output pulses to the digitizer board,
- provides a slow integrator output used in cesium calibration and MB monitoring,

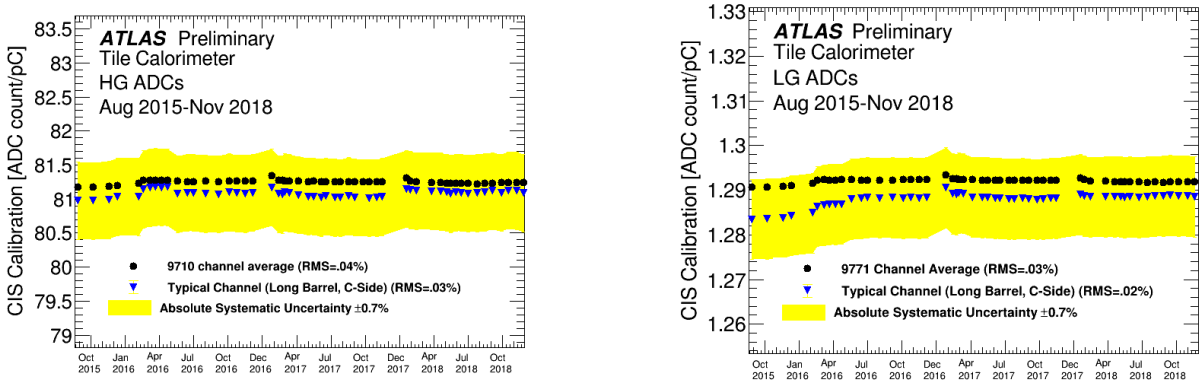

(a) (b)

Figure 6.7: CIS calibration constants averages of all (a) high-gain and (b) low-gain ADCs for selected CIS calibration runs during entire Run-2. Blue triangles represent the CIS constants of a typical channel (LBC20 - ch35 for HG and LBC20 - ch33 for LG), whereas the black circles show the averages of all ADCs. The yellow band in the plots shows the 0.7% systematic uncertainty in individual calibrations. These figures are taken from Ref [19].

- and provide analog trigger output to tower trigger sum boards mounted on mother-boards.

The CIS calibration is performed by injecting an input signal to the electronics of a given module, comparable to what is expected in normal running. The CIS constant of a given readout channel is determined by taking the ratio of the input injected signal to the peak response of the electronics. CIS calibrations are performed approximately two times a week during data taking and calibration constants are applied for each channel. An accuracy of about 1% precision in the calibration is chosen to align with the design goal of the electronics.

Fig 6.7 shows the percent change in the average of detector-wide CIS calibration constants for high gain (left) and low gain (right) ADCs between August 2015 and October 2018. As seen by the Figure the CIS constant is very stable over time.

6.2.4 Minimum bias currents

Minimum bias currents are a result of the inelastic proton-proton interactions at the LHC. These particles produce signals in all PMTs, which are used to monitor the response variation of the calorimeter over time using the integrator readout (the same system used

by the Cs calibration system). The minimum-bias rate is proportional to the instantaneous luminosity and produces signals in all the subdetectors which are uniformly distributed around the interaction point. MB events are therefore useful for luminosity measurements and monitoring of the beam background. Additionally MB events can be used to monitor the response of the TileCal readout chain during all physics runs.
In TileCal the minimum bias signals are readout in the integrator circuit as an increased PMT current I, where the PMT current is given by equation 6.3:

$$I\ [\text{nA}] = \frac{\text{ADC}\ [\text{mV}] - \text{ped}\ [\text{mV}]}{\text{Int. gain}\ [\text{M}\Omega]} \tag{6.3}$$

where ped is the pedestal value from physics runs before collisions and it accounts for the background rate, ADC voltage is measured by the integrator and the integrated gain (Int. gain) is the integrator gain constant calculated using the input from CIS calibration. Due to the distribution of the TileCal upstream material and the distance of cells from the interaction point, the minimum bias currents are not uniform. Figure 6.8 shows measured PMT current as a function of cell η (averaged over all modules) for a fixed instantaneous luminosity 1.7 x $10^{33}\text{cm}^{-2}\text{s}^{-1}$. As expected, the largest PMT current is seen in the PMT's reading the cells of the outermost layer A which are closer to the interaction point, with cell A13 ($|\eta| = 1.3$) located in the EB.

The currents induced in the PMTs by the minimum-bias activity are also used to validate the response changes observed by the cesium calibration system.

6.3 Combination of calibration methods

The cell response of TileCal varies over time and varying LHC luminosity conditions. The overlap between the different calibration systems as shown in Fig 6.2 allows the detector's entire hardware and electronics changes to be monitored and calibrated. These systems additionally give corrections for the response changes with fine granularity caused by changing luminosity conditions. This overlap also allows the identification of sources of response variation, and corrections of these variations during data taking to maintain the global EM scale throughout the data taking period.

Figure 6.9(b) shows the response variation of A13 cell with cesium and laser systems during entire Run-2. The response to the cesium and minimum bias systems are sensitive to both the PMT gain changes and scintillator degradation due to irradiation. Hence the

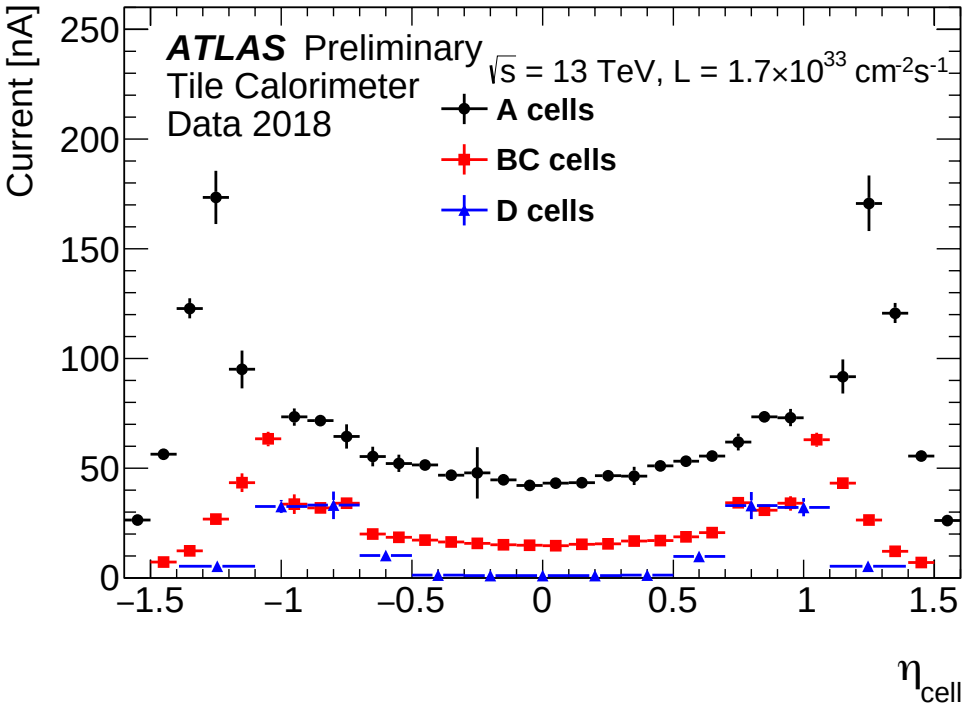

Figure 6.8: PMT current produced by MB data (collected in 2018) measured by the integrator readout as a function of cell η and averaged over all modules for the four cell types in LB and EB. The figure is taken from Ref [20].

difference between laser and cesium (or minimum-bias) response variations can be explained as an effect of scintillator's and fibres radiation damage and natural ageing. While it can be seen in Figure 6.9(a) that the response of cesium or minimum bias and laser systems indicates no effects of scintillator's irradiation in 2015. Whereas as we go towards the end of LHC Run-2 the radiation effects becomes more and more evident and can be seen in figure 6.9(b). The rate and amount of scintillator damage and recovery are complicated combinations of factors, such as particle energies, exposure rates and duration, temperatures and are difficult to quantify.

As seen in figure 6.9, the down-drift of the PMT response variation is correlated with the collision periods. Thus the cell response variation is dependent on the integrated luminosity. This relation between the PMT drift and the integrated luminosity motivates many studies of this thesis work.

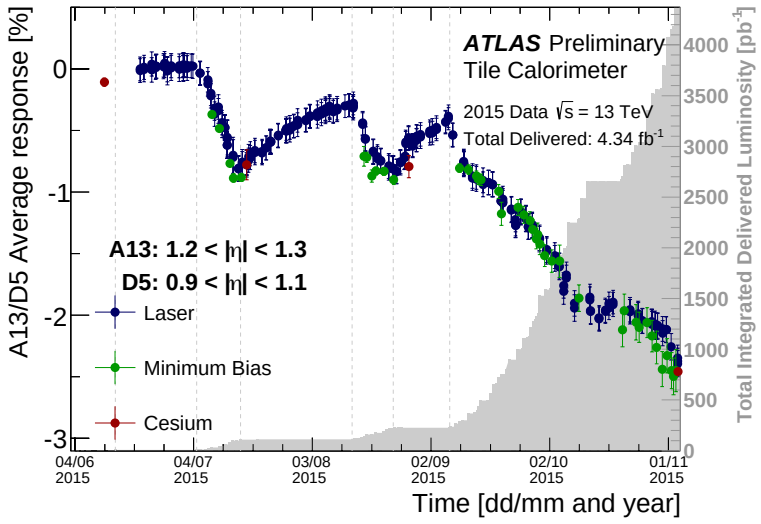

(a) The average response variation seen by laser pulses (blue points), MB events (green points) and Cs scan (red points) of A13 cell response with respect to a reference cell D5 during 2015.

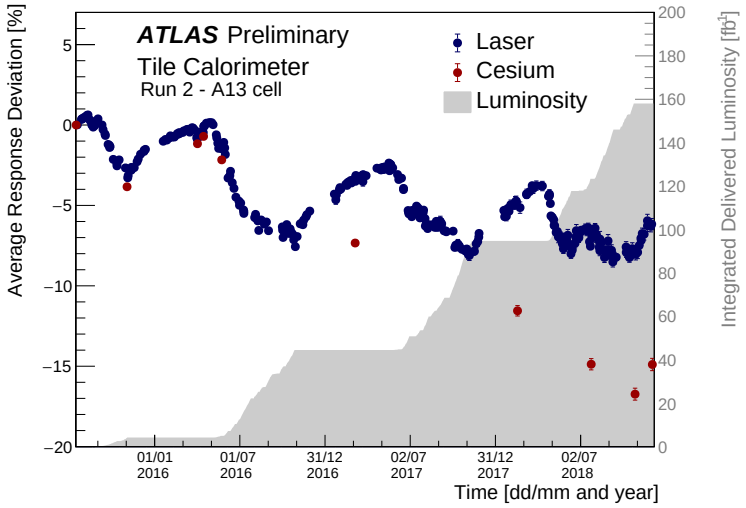

(b) The average response variation seen by laser pulses (blue points) and Cs scans (red points) of A13 cell during entire Run-2 covering the period from June 17, 2015 to December 3, 2018.

Figure 6.9: The mean response variation of the A13 cells in the inner layer of Extended barrel as seen by the three calibration systems of the TileCal. The Integrated luminosity is the total delivered luminosity during the given proton-proton collision periods, is shown for comparison in the background.

Chapter 7

Laser calibration of the calorimeter

In this chapter the description of the laser calibration procedures used to determine the laser calibration constants (f_{Laser}) is described in detail. This chapter also summarizes the results of the observed PMT response drifts during LHC Run-2 using laser calibration data.

7.1 PMT response calibration

Photomultiplier tubes and readout electronics are calibrated with the laser calibration system as shown in Figure 6.2. For each PMT channel i, the laser system data allows to calculate laser calibration constants f^i_{laser} mentioned in Eq 6.2. The laser calibration constants f^i_{Laser} are computed twice a week with the laser calibration runs. The details of the laser data and laser calibration procedures used to compute the laser constants in Run-2 are described in the following sections.

7.1.1 Laser data

The Laser runs are constituted by a set of laser pulses and corresponding signal records of each individual PMT channel. The pedestal is subtracted per channel on a pulse-by-pulse basis. For each pulse, the TileCal PMTs signal responses and the diode's response are recorded. The normalised response of each PMT channel i, the ratio $R_{i,p}$ is defined as:

$$R_{i,p} = \frac{S_{i,p}}{S_{\text{D6},p}} \tag{7.1}$$

where p stands for the laser pulse, S_i is the reconstructed signal amplitude of a given TileCal PMT readout channel i and $S_{\text{D6},p}$ is the signal amplitude measured by the photodiode

6 (D6) inside the laser box. The D6 is one of four photodiodes (D6-D9) installed in the laser box, measuring the laser light after the beam expander thus intended to probe the light beam close to the TileCal PMTs. Among the other photodiodes (D7-D9), this photodiode has the most optimal gain to measure the light intensity used during the standard laser calibration runs. The D6 response stability was found to be within 1% during the Laser II system commissioning in 2015 Ref [46]. The average and RMS value of the ratio from Eq. 7.1 for all pulses of the laser calibration run ($R_i \equiv \langle R_{i,p} \rangle$ and ΔR_i is the RMS of $\{R_{i,p}\}$) is taken into account for each PMT. During Run-2, the so-called `h3000` ntuples are used for laser analyses and calculation of laser calibration constants. Those ntuples are stored under a dedicated TileCal directory.

7.1.2 Laser data analysis

The absolute calibration of the TileCal energy scale is maintained using the cesium system. However, since the cesium system needs a pause in the proton-proton collisions of at least six hours, this procedure cannot be performed very often. Therefore, the laser system is regularly used between two cesium scans to calibrate the response of the PMTs and electronics readout. Since 2016, potential leakage problems in the cesium hydraulic system have reduced the frequency of the Cs scans even more and laser-based calibration has become more important than before. The laser calibration is done relative to a laser reference run taken close to the last cesium scan used to set the Tile Calorimeter energy scale. The relative response of the PMT channel i is defined in terms of the laser calibration factor as follows:

$$x_i = \frac{R_i}{R_i^{\text{ref}}} \tag{7.2}$$

where R_i^{ref} is the normalized response of the PMT channel i during the laser reference run. Commonly the relative response variation is defined in terms of percentage as Eq 7.3:

$$\Delta x_i = \frac{R_i - R_i^{\text{ref}}}{R_i^{\text{ref}}} \times 100\% \tag{7.3}$$

Besides the evolution of the individual PMT channel response, two other main contributions affect the measurement of x_i:

- Global effects: A global and coherent drift of all channels is possible. It could come from an instability of the reference diode, from the variation of light received by

TileCal PMTs and reference diode, or common ageing of the long fibres. The global shift is corrected by a *global correction* (δx_{G}), which denotes a measured drift on the response of all the channels.

- Fibre effects: The light transmission may vary with time from fibre to fibre. *Fibre corrections* (δx_{f}) measured as a shift affecting all the channels illuminated by the same fibre, are employed to disentangle this effect.

To take account of the above-mentioned effects, two corrections (global and fibre corrections) are applied, collectively called as optics corrections. The laser calibration constant f^{i}_{Laser}, as defined in Equation 6.2 of the channel energy reconstruction, is calculated in terms of x_i and optics corrections as:

$$f^{i}_{\mathrm{Laser}} = \frac{R^{\mathrm{ref}}_{i}}{R_i} \times \delta x_{\mathrm{G}} \delta x_{\mathrm{f}(i)} = \frac{\delta x_{\mathrm{G}} \delta x_{\mathrm{f}(i)}}{x_i} \tag{7.4}$$

and the respective PMT channel response variation, corrected from spurious optics effects, Δx_i, is:

$$\Delta x_i = \frac{R_i - R^{\mathrm{ref}}_{i}}{R^{\mathrm{ref}}_{i}} \times \frac{1}{\delta x_{\mathrm{G}} \delta x_{\mathrm{f}(i)}} \times 100\% \tag{7.5}$$

The Δx_i is the typical quantity shown in plots exhibiting the evolution of the PMTs response over time, such as those presented in Section 7.6.

Three main approaches were developed to calculate the laser calibration constants, i.e. the Direct method, the Statistical method, and the Combined method. The differences between the various approaches lay on the way they address the global and fibre effects from the optics of the Laser II system. Two of them, the Direct and the Combined methods, were effectively used during the Run-2 calibration operations. The Direct method was used to produce the laser calibration constants for the prompt processing of data from 2015–2017. Moreover, it was used for data from 2015–2016 reprocessing. The Combined method was used to produce the laser calibration constants for the prompt processing of data in 2018. Moreover, it was used for data from 2017–2018 reprocessing. The details of the calibration procedure using those methods are given in Section 7.5.1.

7.2 PMT calibration with the Direct method

The Direct method starts from Equation 7.4 and determines the global and fibre corrections as follows. The global correction is evaluated using the relative response of all PMTs reading cells in the D-layer:

$$\delta x_{\mathrm{G}} = \langle x_{\mathrm{D-cells}} \rangle \tag{7.6}$$

where $\langle x_{\mathrm{D-cells}} \rangle$ is the geometric weighted average of the relative response of all PMTs that read D cells. The weights are given by $(N \times R_i/\Delta R_i)^2$, where N is the number of pulses of the laser run. Saturated channels, channels with bad status in the TileCal data quality database, and channels for which the absolute difference between the $\mathrm{HV_{set}}$ and the actual PMT HV is above 10V ($|\Delta\mathrm{HV}| > 10\mathrm{V}$) are excluded from the computation of the global correction. Moreover, an iterative procedure rejects outlier channels laying more than 2σ apart from the $\langle x_{\mathrm{D-cells}} \rangle$ distribution. The number of iterations is three.

The fibre corrections ($\delta x_{\mathrm{f}(i)}$) in the Direct method are evaluated using information from PMTs of the D layer and PMTs reading the B13, B14, and B15 cells. This quantity is evaluated for each long clear fibre $\mathrm{f}(i) \equiv f$ as:

$$\delta x_f = \langle \frac{x_{\mathrm{D,B-cells}}}{\delta x_{\mathrm{G}}} \rangle_f \tag{7.7}$$

where $\langle\rangle$ represents a geometric weighted average. The weights are the same as the ones used for determining the global correction. The average runs over all PMTs reading D, B13, B14, and B15 cells connected to the same long clear fibre. Concretely, this means that:

- The correction associated with each of the 128 fibres in the Long Barrel is determined from the PMTs reading the cells D0 to D3 of the corresponding module.
- The correction associated with each of the 256 fibres in the Extended Barrels is determined from the even/odd PMTs reading the D4 to D6 and B13 to B15 cells of the corresponding module.

The following quality criteria used to select the channels contributing to the global correction are applied here: saturated channels, with bad status or $|\Delta\mathrm{HV}| > 10\mathrm{V}$ are excluded. The outlier rejection is also done similarly. It uses 3 iterations with a tighter rejection threshold of 1.5σ.

After applying the global and fibre corrections, the corrected relative response of the PMT channel i is:

$$x_i \to x_i' = \frac{x_i}{\delta x_{\mathrm{G}} \times \delta x_{\mathrm{f}(i)}} \tag{7.8}$$

After these corrections, the relative scale between the barrels is lost. To compensate it, a re-scaling of the response of the PMTs in the extended barrel (EB) is performed. A global correction in the extended barrel is applied assuming cells A10 and A14 (LB and EB, respectively) have similar variations. The correction C_{EB} is obtained as follows:

$$C_{\mathrm{EB}} = \langle x^{'} \rangle_{\mathrm{A10}} - \langle x^{'} \rangle_{\mathrm{A14}} \tag{7.9}$$

where $\langle x^{'} \rangle_{\mathrm{A10}}$ and $\langle x^{'} \rangle_{\mathrm{A14}}$ are the average response variations in A10 and A14 cells, respectively. The corrected relative response of the PMT channel i in extended barrel is:

$$x_i^{\mathrm{EB}} \to x_i^{\mathrm{EB}} - C_{\mathrm{EB}} \tag{7.10}$$

7.3 PMT calibration with the Statistical method

In the statistical method, the actual PMT gain is measured. The method is based on the statistical nature of photoelectron production and multiplication inside the PMT. It assumes that the effects of the electronic noise can be neglected: the noise assumes an important role at low light intensity but the typical signals in calibration runs are characterized by more than a thousand photoelectrons. The second assumption of the method is that the laser light has a temporal coherence. Under these conditions, the two main contributions to the PMT signal fluctuations are Ref [47]:

- Poissonian fluctuations in the photoelectron emission spectrum and multiplication
- Variation of the intensity of the light source

This gives:

$$\frac{\mathrm{Var}[q]}{\langle q \rangle^2} = f \cdot \frac{\mathrm{Var}[N]}{\langle N \rangle^2} + \frac{\mathrm{Var}[I]}{\langle I \rangle^2} \tag{7.11}$$

where $\langle q \rangle$ ($\mathrm{Var}[q]$) is the average (variance) anode charge q, $\langle N \rangle$ ($\mathrm{Var}[N]$) is the average (variance) number of photoelectrons N, $\langle I \rangle$ ($\mathrm{Var}[I]$) is the average (variance) light intensity I of a pulsed source on the cathode and f is the excess noise factor.

The excess noise factor f is a measurement of the deviation of the observed PMT resolution from the expected resolution based on Poisson photostatistics. In the case of a

PMT, the excess noise factor f can be expressed as Ref [48]:

$$f = 1 + \frac{1}{\delta_1} + \frac{1}{\delta_1 \cdot \delta_2} + ... + \frac{1}{\delta_1 \cdot \delta_2 \cdots \delta_n} \tag{7.12}$$

where δ_d is the gain of the dynode d.

The average anode charge $\langle q \rangle$ and the average number of photoelectrons $\langle N \rangle$ are related by:

$$\langle q \rangle = e \cdot G \cdot \langle N \rangle \tag{7.13}$$

where e is the electron charge and G is the PMT gain. Using this formula and remembering that the quantity N follows Poisson statistics, one has:

$$\frac{\mathrm{Var}[q]}{\langle q \rangle} = f \cdot e \cdot G + k \cdot \langle q \rangle \tag{7.14}$$

where $k = \frac{\mathrm{Var}[I]}{\langle I \rangle^2}$ is the coherence factor which depends only on the characteristics of the light source itself.

The k value is unknown but it is expected to be small ($\ll 1$) in the case of a real laser source, where the fraction of coherent light is dominant with respect to the chaotic light component. The value of coherence factor k ranges from 0 for an ideal fully coherent light source to 1 for a totally incoherent light source. It is difficult to measure the k value. To limit the weight of the term multiplied by k in Equation 7.14, it is safer to work with small reconstructed charges and, therefore, to use low light intensity. This is the reason of the choice to use only high-gain laser calibration runs taken with the filter wheel in position 8 to evaluate the PMT gain with the statistical method. In these conditions, only 1% of the laser light is transmitted to the PMTs.

In order to calculate k the *covariance method* is used, where the same light source is measured with several PMTs. By definition $k = \frac{\mathrm{Var}[I]}{\langle I \rangle^2}$, and for any PMT pair i and j, the k parameter yields:

$$k = \frac{\mathrm{Cov}[q_i, q_j]}{\langle q_i \rangle \langle q_j \rangle} \tag{7.15}$$

Using Equation 7.14, the PMT gain G and the measured mean charge $\langle q \rangle$ can be written as:

$$G = \frac{1}{f \cdot e} \cdot \left(\frac{\mathrm{Var}[q]}{\langle q \rangle} - k \cdot \langle q \rangle \right) \tag{7.16}$$

Tests to validate the statistical method were done in the Pisa laboratory. Although the method has the important advantage of determining the actual PMT gain, it presents significant fluctuations and therefore was never employed standalone to determine the PMT calibration constants.

7.4 PMT calibration with the Combined method

The determination of the PMT response with the Direct method is based on the assumption that a sub-sample of cells exists with a stable response in time. These "stable" cells are used to evaluate the effects due to laser stability and inequalities on the transmission system. However, with the increase in luminosity since the beginning of Run-2, a measurable down-drift in the response was detected in all cells including the PMTs reading out the assumed "stable" cells. All the PMT responses are now drifting due to the larger amount of collected light.
The Combined method was developed to set aside these assumptions, using the Direct method as the basis to determine the PMT calibration constants, from Equation 7.4, but deriving the global and fibre corrections from the PMT gain determination with the statistical method. In this way, no a priori assumption is made on the PMT response stability. The relative gain of the PMT i ($x_{G,i}$) with respect to a reference is given by:

$$x_{G,i} = \frac{G_i}{G_i^{\text{ref}}} \tag{7.17}$$

where G_i is the gain of the PMT i and G_i^{ref} is the gain of that PMT determined with the laser reference run.
To overcome possible effects of fluctuations of the PMT gain measurements, the reference G_i^{ref} is averaged over the laser runs taken within ± 10 days with respect to the reference run. The laser runs used for averaging were taken in the period before the physics collision started.

The global correction is determined from the average ratio between the PMT relative gain ($x_{G,i}$) determined by the statistical method and the PMT relative response (x_i defined in Equation 7.2) determined with the Direct method, using PMTs reading the D-layer and the BC1, BC2, B13, B14, B15 cell.

$$\delta x_{\mathrm{G}} = \langle \frac{x}{x_G} \rangle_{\mathrm{D,B-cells}} \tag{7.18}$$

The geometric weighted average is computed iteratively, removing outlying channels. Additionally, the PMTs having bad status, saturated or $\Delta\mathrm{HV} > 10\mathrm{V}$ are discarded. It is highlighted that since this global correction is obtained from an average compared with the PMT gain measurement the relative scale between the barrels is not lost, as occurred for the Direct Method. Therefore there is no necessity for a further re-equalization between the LB/EB PMTs response.

The fibre corrections are determined in approximately the same way as the global correction except that the average runs over the channels connected to a common long fibre f, with the global correction taken into account to avoid double correcting:

$$\delta x_f = \langle \frac{x}{x_G} \delta x_{\mathrm{G}} \rangle_f \tag{7.19}$$

Since the statistical method works better at a lower light intensity, only high gain calibration runs with filter wheel position 8 are used in this calibration method.

Validation of the Combined method

The response of the TileCal PMT channels to the Laser II system, obtained with the Combined method, as compared to the response of the calorimeter obtained with the cesium calibration system. The response of the calorimeter scintillators and Wavelength shifting (WLS) fibres do not change substantially within a small period of time or within a period of low radiation exposure, i.e. of low delivered luminosity. Thus the response variation of PMTs measured by the Combined method should yield the same result as the one obtained with the cesium system assuming no scintillating tile degradation, providing a procedure to validate the laser algorithm itself.

During 2015 and 2016, three periods of low integrated luminosity were available within consecutive cesium scans. The response variation obtained with the cesium system is shown as a function of the response variation obtained with the laser in Figure 7.1 for the period from July 2015 to November 2015. The results are displayed at the channel level and

separating channels per layer A, B/BC and D. The great majority of channels have the same response variation for laser and for cesium.

The distribution of the ratio between the laser calibration constants (f_{Laser}) and the cesium constants (f_{Cs}) corresponding to Figure 7.1 is shown in Figure 7.2. This figure shows all the TileCal channels, separated by layer and Long/Extended barrel, for the time intervals from July 2015 to November 2015. Here, the calibration constants are specifically set to correct for the response evolution that occurred exclusively during the period of time being evaluated. Each distribution is fitted with a Gaussian function to measure its average and standard deviation. In general, differences observed between the Cs and the laser systems are more evident in the extended barrel and on the A layers. These regions of the calorimeter are less shielded and thus the effects of radiation damage to the scintillator and WLS fibre are faster. The average difference is below 0.1% and the standard deviation is 0.6%.

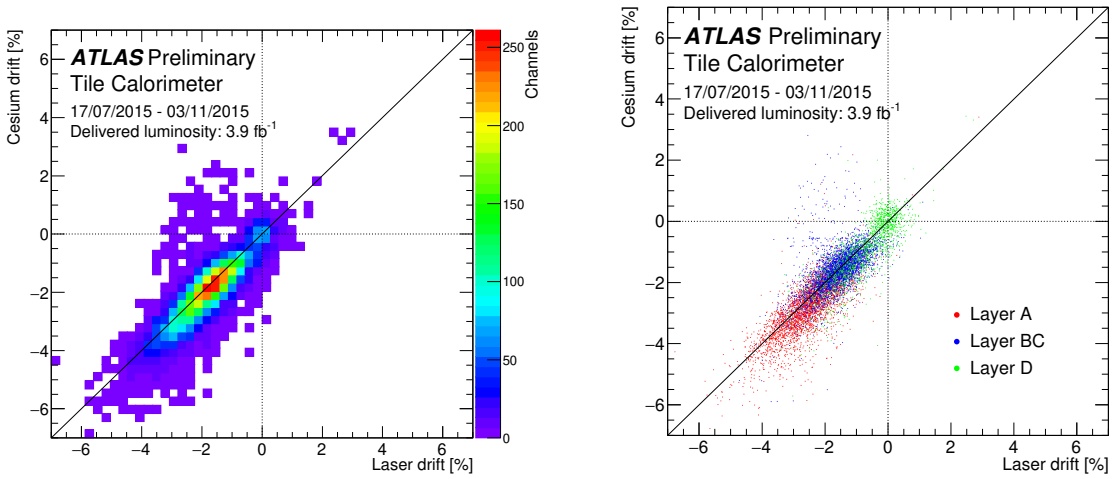

Figure 7.1: Response variation (in %) measured by the cesium calibration system (y-axis) and by the Laser II system with Combined method (x-axis) between July 17 and November 3, 2015, for TileCal channels that are calibrated by cesium system, i.e. special C10-, E-cells and MBTS are not included (left). The same response variation was reported per A-, B/BC, and D-layer (right).

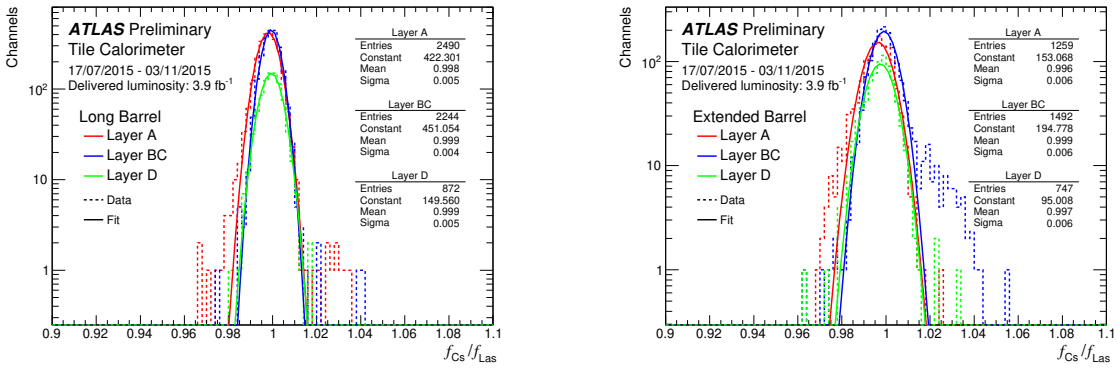

Figure 7.2: Ratio between the laser calibration constants calculated with Combined method (f_{Las}) and the cesium calibration constants (f_{Cs}) for channels in Layer A, B/BC, and D in the (left) Long Barrel and (right) Extended Barrel. Special C10-, E-cells, and MBTS are not included.

7.4.0.1 Evolution of optics correction

Figures 7.3 and 7.4 show the evolution of the optics global correction per year in Run-2, determined with the Combined method using laser runs taken in high gain. For all the years, the magnitude of the correction does not exceed 2.5%. For the years 2017 and 2018, the correction is more stable in time than for 2015 and 2016, for which the correction respectively increases and decreases in a nearly constant manner.

The global correction is a very important quantity since it dominates the scale of the PMT calibration. Its precision should match the global scale uncertainty on the PMT calibration assessed from laser and cesium comparisons presented in Section 7.4, and thus be better than 0.4%.

A large contribution to the global correction comes from the stability of the HG QDC of D6 in the direct method and combined method used for the normalization of PMT response.

7.5 Calibration of the calorimeter

7.5.1 Calibration procedure

Each year, the data recorded by the ATLAS detector is reprocessed. Data reprocessing consists of the update of the physics data set (proton-proton and heavy ion collision runs)

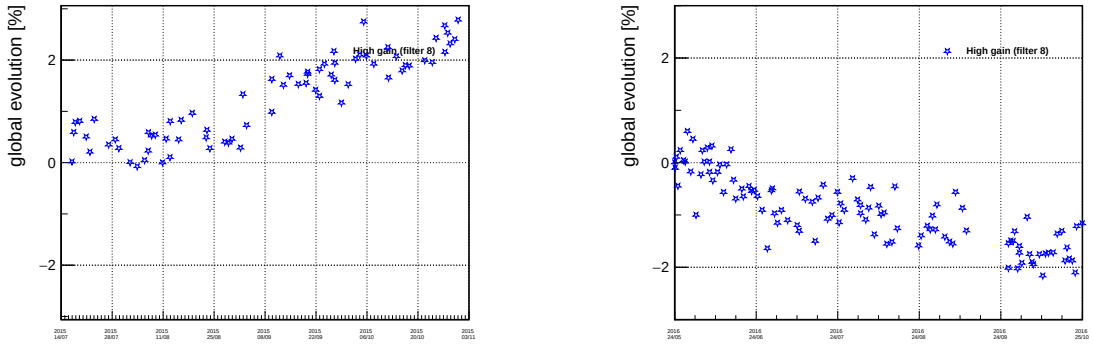

Figure 7.3: Global correction (in %) as a function of time for (left) 2015 and (right) 2016, determined using laser high gain runs and the Combined method. The global correction is calculated as a weighted geometric mean and the corresponding errors are included in the data points.

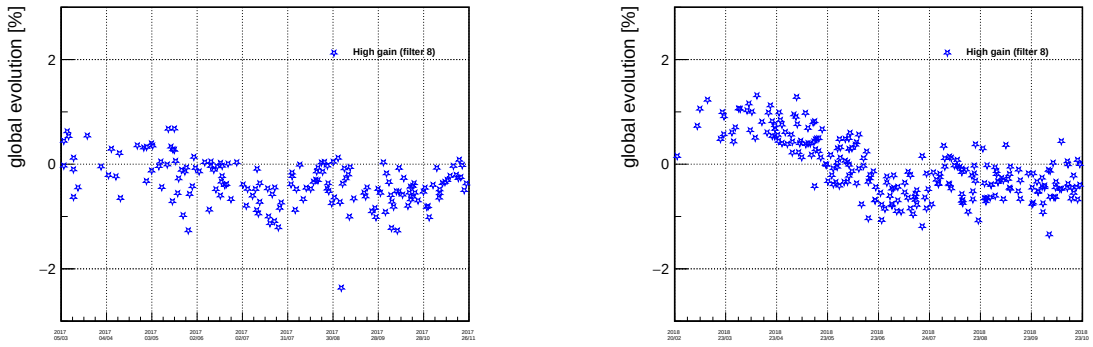

Figure 7.4: Global correction (in %) as a function of time for (left) 2017 and (right) 2018, determined using laser high gain runs and the Combined method. The global correction is calculated as a weighted geometric mean and the corresponding errors are included in the data points.

with updated conditions and calibration constants. Moreover, a reprocessing of a full Run-2 data set is performed during LHC Long Shutdown 2 (LS2). This step is necessary to apply new reconstruction and calibration algorithms as well as the corrections that were impossible to be done or missed during prompt data processing. The Intervals of Validity (IOVs) are readjusted and chosen to coincide with the data-taking periods. They occur every 1-2 weeks in order to smoothly follow the evolution of PMTs' response during the data-taking period.

The method to compute the laser constant f_{Laser} introduced in Equation 6.2 is based on the analysis of specific laser calibration runs, taken daily during the data-taking period, for which both the laser system photodiodes and the TileCal PMTs are readout. The laser calibration employs two types of successive laser runs:

- Low Gain run (labeled as LG), taken by setting the filter wheel in position 6, consists of ∼10,000 pulses with a constant amplitude and the filter attenuation factor equal to 3,
- High Gain run (labeled as HG), taken by setting the filter wheel in position 8, consists of 20,000–150,000 pulses with a constant amplitude and the filter attenuation factor equal to 330.

The laser calibration is a relative calibration with respect to a laser reference run taken right after each cesium scan. By definition, if the response of a channel to a given laser intensity is stable (the response of the PMT and of the associated readout electronics are stable), the laser constant f_{Laser} is 1. The reference runs used during LHC Run-2, for both prompt processing and reprocessing of data are taken from the following dates for each year:

The references for the PMT gain G_i^{ref} from Equation 7.17, used in the Combined method, significantly fluctuate run by run. The fluctuations are caused by laser light instability and statistical uncertainty. Therefore, they are averaged over the laser runs taken within ±10 days with respect to the reference runs. The laser runs used for averaging were taken in the period before the physics collision started.

The laser references and laser constants are stored in the ATLAS conditions database in the dedicated folders.

Year	Reference date
2015	2015-07-17
2016	2016-04-01
2017	2017-03-06
2018	2018-02-15

Table 7.1: This table enlists the years with respective dates of the reference runs used during LHC Run-2 used for prompt processing and reprocessing of data.

The laser calibration procedure evolved during Run-2. Due to increasing instantaneous luminosity and response variation observed in all PMTs, the methods to derive laser constants were adopted. The applied methods are described in detail in Section 7.1.2. In this section, the description of the procedure to produce the laser calibration constants f_{Laser} using these methods for prompt processing and reprocessing of data 2015–2018 is presented.

Calibration using Direct method

The Direct method described in Section 7.2 was used to produce the laser calibration constants f_{Laser} for the prompt processing of data 2015–2017. Moreover, it was used for data for 2015–2016 reprocessing.

In Equation 6.2, f_{Laser} represents the correction of the PMT response variation computed with the laser system. However, only channels that have undergone a significant deviation are corrected. It means that the previous value of f_{Laser} stored in the database is kept if the calculated deviation is smaller than a predetermined threshold of about three times the overall precision of the laser system measured in Run-1, thus a threshold of 1.5% for the long barrel and 2% for the extended barrels. In 2017, this threshold was lowered to 0.5% for both long and extended barrels. The LG data are more precise than the HG where the signal amplitude is much smaller than in the LG one (a factor of 100 between them for the same channel). Therefore, the LG laser runs are used to determine the laser calibration constants applied for both gains, while the HG runs were used for cross-checks. A readout electronics issue can be revealed by an incompatibility between the LG and the HG laser calibration constants.

The production of the laser calibration constants f_{Laser} follows this procedure:

- a laser calibration constant is computed for all channels with laser references available,
- a channel is corrected if its gain variation is larger than 1.5% (2%) in the LB (EB) and the observed deviation is understood. In 2017, this threshold was lowered to 0.5% for both long and extended barrels. The channel's deviation is considered as understood if it is compatible with the mean deviation of channels in a given TileCal layer or if it is compatible with the HV change,
- a channel is also corrected when its gain variation is below the thresholds defined in the previous point, if the observed deviation is understood and the channel was corrected since the last reference run, i.e. its calibration constant was different than 1 in the database,
- if a channel is known as bad, its laser calibration constant is not updated, and the previous constant stored in the database is kept, whatever the nature of the problem. Indeed, this flag is very often due to readout electronics, or corrupted data, and the laser system is not presumed to correct these cases.

In data 2015–2016 reprocessing the requirement on the goodness of channels was dropped. Thus, channels known as bad were also calibrated. The MBTS channels have reduced HV during the high average instantaneous luminosity $\langle\mu\rangle$ of the physics runs. Therefore, those channels are not calibrated by the laser system.

Calibration using Combined method

The Combined method was used to produce the laser calibration constants f_{Laser} for the prompt processing of data in 2018. Moreover, it was used for data from 2017–2018 reprocessing.

In the Combined method, described in Section 7.4, the HG laser runs are used in order to minimize the term multiplied by coherence factor k from Equation 7.14. The other gain is used for cross-checks. In 2017–2018, when the combined method was applied, the channel gain variations were larger and appeared faster than in 2015–2016 due to the large instantaneous luminosity. Also, the spread of the gain variations between the channels of a given TileCal layer was larger. Therefore, the requirements applied in the Direct method were dropped in the Combined method, and the laser constants f_{Laser} were calibrated for

all channels.

Similarly, as in the Direct method, the MBTS channels were not calibrated by the laser system, due to reduced HV during the high $\langle\mu\rangle$ physics runs, and MBTS is not used to provide energy measurements.

7.6 Study of the PMT response variation by Combined Method

PMT drift overview by laser system in Run-2

The laser system is used to measure the evolution of the PMT response. In this section, the average response variation of the PMTs as a function of time during the LHC Run-2 is presented. The Combined method, discussed in Section 7.4, is utilized to calculate the response variation with respect to a set of reference runs. In particular, Equation 7.5 is used to obtain the response for each channel. Channels with bad data quality status, problematic high voltage, or flagged as affected by any calibration system are discarded. For each cell type, the average response is obtained by a Gaussian fit to the distribution of PMT response variation. The χ^2 fit method is applied. The Gaussian approximation is used in order to obtain the average variation that is not affected by outliers.

The PMT response variation strongly depends on the delivered luminosity by the LHC. The total integrated delivered luminosity during Run-2 was 156 fb^{-1} (4.2 fb^{-1} in 2015, 38.5 fb^{-1} in 2016, 50.2 fb^{-1} in 2017, 63.3 fb^{-1} in 2018).
Figures showing the measured drift in the entire Run-2 are presented in this section. Due to the increase of the integrated luminosity during Run-2 with respect to Run-1, a significant down drift variation of the PMTs response is observed.

Figure 7.6 shows the average PMT response variation (in %) per TileCal cell type as a function of $|\eta|$ and radius, observed during the high $\langle\mu\rangle$ proton-proton collisions data taking period in 2018. It can be seen from Figure 7.6 that PMTs reading the cells in the inner layer A and E-cells located in the gap/crack region are mostly affected. Those cells are the most irradiated and their readout PMTs experience the largest anode current. PMTs reading the cells in the outer layer D are least affected, due to their location away from the interaction point.

Figure 7.5 show the average response variation of the channels as a function of polar

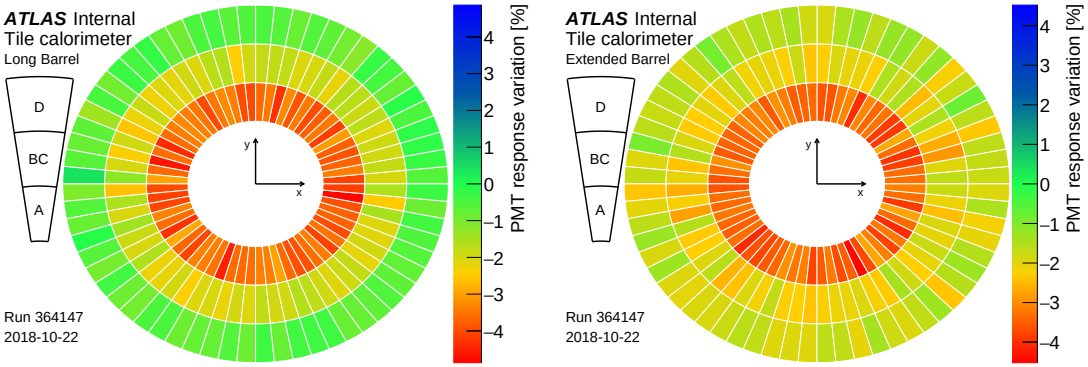

Figure 7.5: The average PMT response variation (in %) as a function of polar angle ϕ and layers for long barrel (left) and extended barrel (right), observed during the entire high $\langle\mu\rangle$ proton-proton collisions data taking period in 2017 (between April 18 and October 22, 2018). The plot is made using the Combined method.

angle ϕ and layers for the same period in 2018. In this figure, each ϕ bin corresponds to one module per partition. It can be seen that PMTs reading the cells in the layer closest to the beam axis, composed of A-cells, are mostly affected. The next layers, formed of the BC- and D-cells are significantly less affected. This map provides useful insight into the uniformity of the PMT variation over ϕ.

The Laser II system was not operational due to technical problems in the period September 10–27, 2016. Thus, no laser data can be seen in the time evolution plots for this time interval. In Figure 7.7, presenting the response in the entire Run-2, the vertical dashed lines show the start of proton-proton collisions in respective years. The observed PMTs response variation is the result of three competing factors:

- the constant up-drift observed when PMTs are at rest;
- the down-drift during a high instantaneous luminosity period when PMTs are under stress;
- the partial recovery during technical stops.

For the BC/B and layers D, the average PMT response degradation during proton-proton collisions was almost totally recovered in technical stops. It resulted in -1.25% accumulated PMT response variation at the end of Run-2 for the layer BC/B and even in +1.5% balance for the layer D. PMTs reading the layer A exhibit larger response gradients and reach the end of the Run-2 with an average -5.5% response drift. The Gaussian width for all

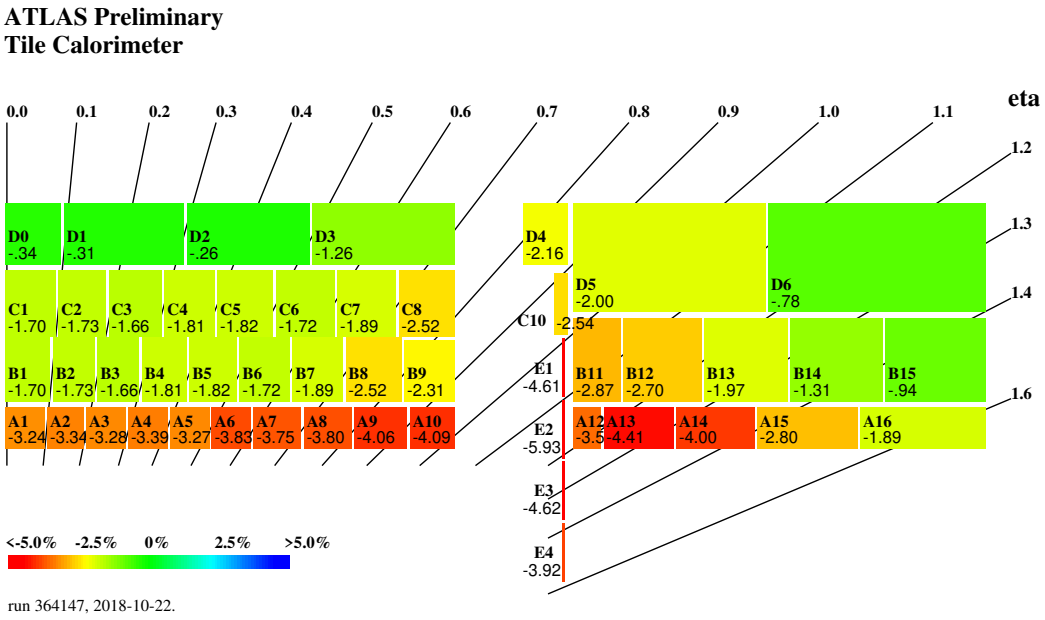

Figure 7.6: The average PMT response variation (in %) per TileCal cell type as a function of $|\eta|$ and radius, observed during the entire high $\langle\mu\rangle$ proton-proton collisions data taking period in 2018 (between April 18 and October 22, 2018) calculated using the Combined method.

layers increases with time during a high instantaneous luminosity period when PMTs are under stress. It is caused by the different behaviour of different PMTs over time which is at different $|\eta|$ positions. During technical stops, when PMTs are at rest, a quick decrease of Gaussian width is observed indicating the recovery of mostly affected PMTs to the average response in a given layer or cell type.

Figures 7.8 show the evolution of the average response variation (left) and Gaussian width distribution (right) as a function of time for A9, A10 cells from the long barrel (LB) region and A12, A13 cells from the extended barrel (EB) region in entire Run-2, respectively. The PMTs reading the A13 cells manifest the largest average down-drift as these cells are the more exposed to radiation with respect to the PMTs reading A9, A10, and A12 cells. Similarly, the Gaussian width increases with the luminosity accumulated over the years, affecting mostly the PMTs associated with A13 cells that have higher exposure.

Figures 7.9 show the evolution of the average response variation (left) and Gaussian width distribution (right) as a function of time for the BC2, BC8, and B9 of the long barrel of BC-cells in entire Run-2. The BC8 and B9 cells are more exposed to the beam-induced particles, hence their readout PMTs drift down more than PMTs reading the BC-cells of the LB region.

Figures 7.10 show the evolution of the average response variation (left) and Gaussian width distribution (right) as a function of time for B11, B14 and C10 cells from extended barrel region in entire Run-2. Special C10 cells made of a single scintillator are excluded from the analysis.

Figure 7.11 show the evolution of the average response variation (left) and Gaussian width distribution (right) as a function of time for D-cells in LB in entire Run-2. The D-cells from LB is the most stable cells as they have the smallest particle fluence for being located on the outer radius of TileCal. Their readout PMTs also present the most stable response of all TileCal PMTs.

Figure 7.12 show the D-cells in EB for 2015, 2016, 2017, 2018 and entire Run-2, respectively. As compared with the LB D-cells PMTs, the EB D-cells PMTs show larger down drift with the increase in luminosity, as expected from slightly larger anode currents.

In the Figure 7.13, the E-cells PMT response variation (left) and their gaussian width (right) are shown for entire Run-2. Special modules are excluded. The E-cells are located in the gap between the calorimeter barrel and end-cap sections. Those cells are the most exposed to radiation and for that reason, a much larger down-drift in their PMTs is observed. One would expect from the collected charge, the E3 degradation to be larger than E2, however,

the opposite is observed. This can be explained by the installation of active dividers for E3 and E4 cells, which was performed during Long Shutdown 1. In E1 and E2 cells the passive dividers remained in use. Although the system was designed to keep PMT response linearity at a high PMT current regime, it could affect PMT ageing. The only analyzed data from Run-1 (before active dividers) show E3 degrading more than E2 Ref [24]. On July 26, 2017, the high voltage (HV) of E3 and E4 PMTs was significantly decreased to avoid PMT integrator readout saturation. A summary of these HV changes is presented in Table 7.2. The PMT gain variation resulting from this HV change is corrected in order to determine the PMT response drift. Lowering the HV set to the PMTs reduced the rate of response degradation of E4 and E3, when compared to previous years, which resulted in E4 PMTs drifting less than E2 PMTs. This indicates the degradation is related to the anode current delivered by the PMT.

In entire Run-2 measurements of the PMT, drift is shown in Figure 7.13, the width of the distributions is larger when compared with the individual year measurements. Hence, in this case, the Gaussian fit is estimated by maximizing a likelihood function. For individual years the χ^2 fit method is used to estimate the average and width of the gaussian fit to the distributions. It is observed for all years that the E2 response degradation is larger than E1, as expected from integrated currents and simulated dose. Considering E3 and E4 cells, there are two clear regimes to distinguish: before and after HV change, better understood from single-year plots where the accumulated drift is not present. Before the HV change, E4 has always larger drift than E3, expected from the PMT collected charge. After the HV change, the degradation rate of the E4 PMTs becomes slightly smaller than the E3, justified by a smaller average HV set to E4 PMTs (≈650 V) than to E3 PMTs (≈700 V). The relation between the E2-3 responses was discussed previously.

Cell	No. of channels	HV before change (V)	HV after change (V)
E3	7	750	650
E3	115	750	700
E4	100	750	650
E4	20	750	700

Table 7.2: This table enlists the HV in volts (V) before and after changes in HV for the PMTs reading E3 and E4 cells.

In all those Figures, a correlation between PMT response drop (during LHC collisions

when PMTs are subject to larger currents) and width of the drift distribution of PMTs reading the same cells is observed. Conversely, when PMT recovers in technical stops, the width of the distribution improves. Whether the spread is due to the intrinsic properties of the PMT or to the different conditions they experience is an interesting question that should be furthered by comparing the data from the Minimum Bias system.

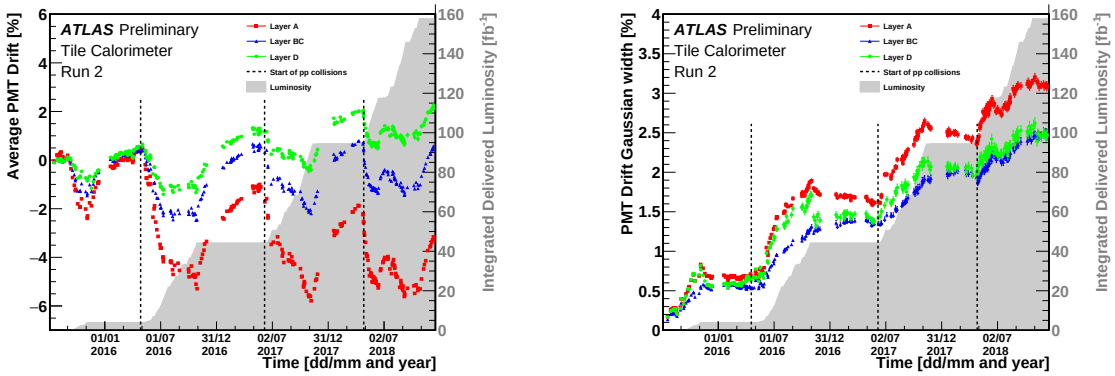

Figure 7.7: (Left) Average response variation (in %) and (right) Gaussian width per TileCal layer as a function of time in entire Run-2 calculated using the Combined method. For each layer, the average response is obtained by a Gaussian fit to the distribution of PMT response variation with respect to an average reference prior to the start of collisions (including all laser runs in the time period of ±10 days of July 17, 2015).

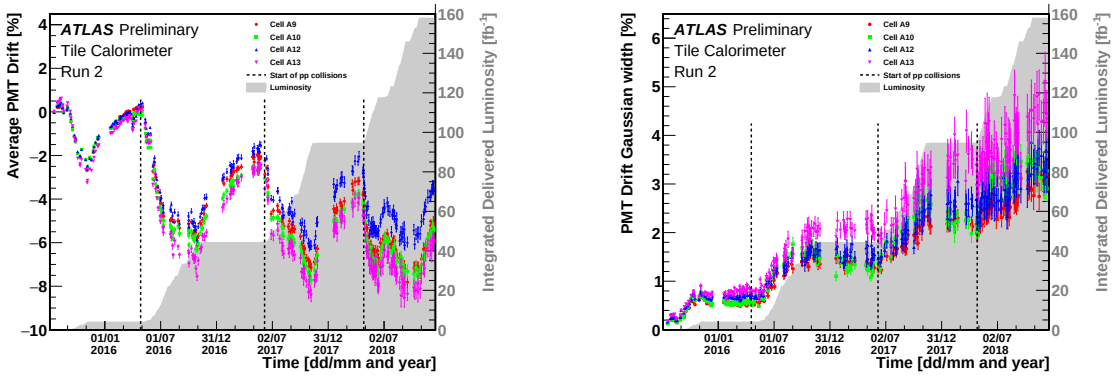

Figure 7.8: (Left) Average response variation (in %) and (right) Gaussian width per TileCal A-cell (A9, A10, A12, A13) as a function of time in entire Run-2 calculated using the Combined method. For each cell, the average response is obtained by a Gaussian fit to the distribution of PMT response variation with respect to an average reference prior to the start of collisions (including all laser runs in the time period of ±10 days of July 17, 2015).

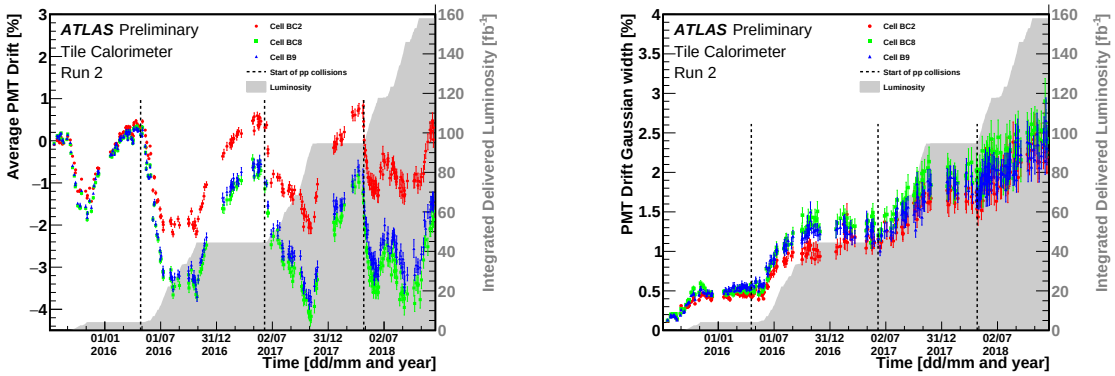

Figure 7.9: (Left) Average response variation (in %) and (right) Gaussian width per TileCal BC-cell from long barrel region as a function of time in entire Run-2 calculated using the Combined method. For each cell, the average response is obtained by a Gaussian fit to the distribution of PMT response variation with respect to an average reference prior to the start of collisions (including all laser runs in the time period of ±10 days of July 17, 2015).

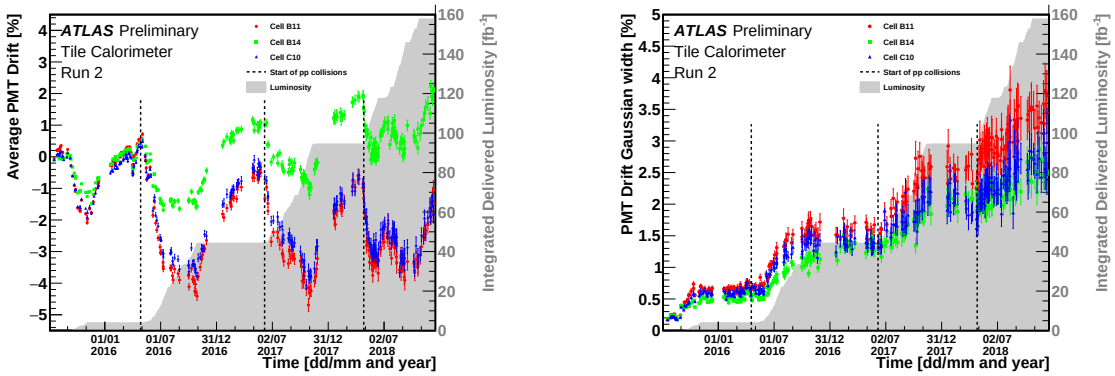

Figure 7.10: (Left) Average response variation (in %) and (right) Gaussian width per TileCal BC-cell from extended barrel region as a function of time in entire Run-2 calculated using the Combined method. For each cell, the average response is obtained by a Gaussian fit to the distribution of PMT response variation with respect to an average reference prior to the start of collisions (including all laser runs in the time period of ±10 days of July 17, 2015). Special C10 cells made of single scintillator are excluded from the analysis. The LHC delivered luminosity is shown for comparison.

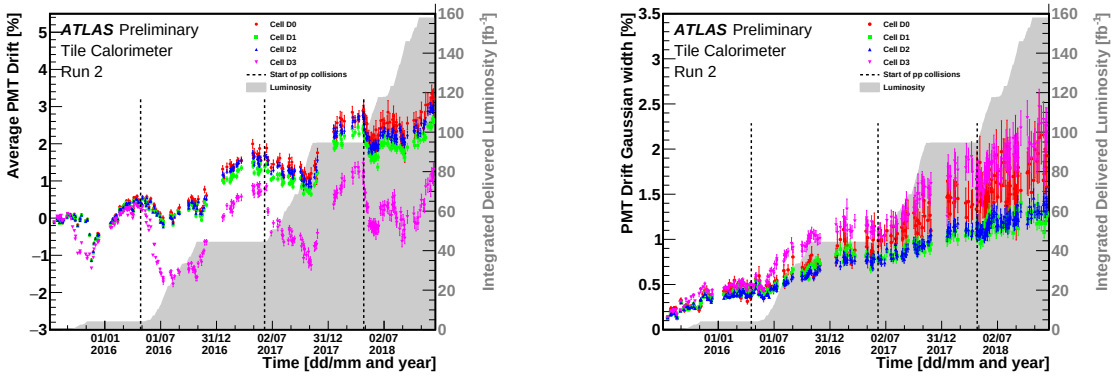

Figure 7.11: (Left) Average response variation (in %) and (right) Gaussian width per TileCal D-cell from long barrel region as a function of time in entire Run-2 calculated using the Combined method. For each cell, the average response is obtained by a Gaussian fit to the distribution of PMT response variation with respect to an average reference prior to the start of collisions (including all laser runs in the time period of ±10 days of July 17, 2015).

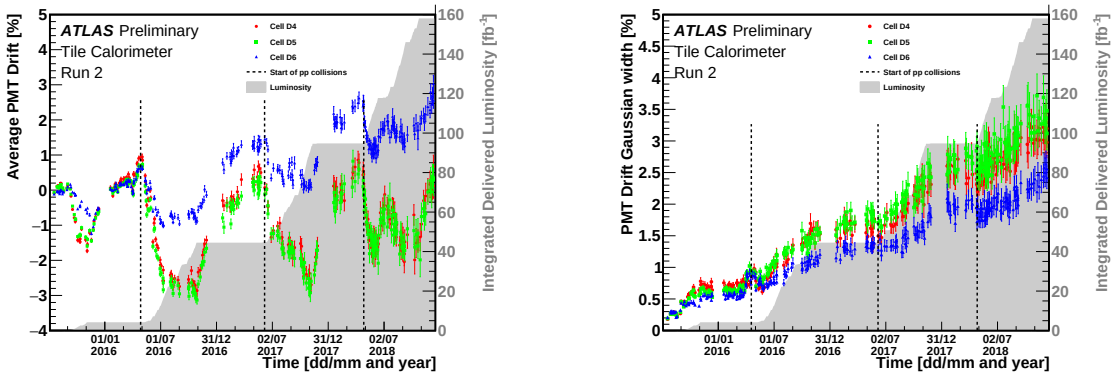

Figure 7.12: (Left) Average response variation (in %) and (right) Gaussian width per TileCal D-cell from extended barrel region as a function of time in entire Run-2 calculated using the Combined method. For each cell, the average response is obtained by a Gaussian fit to the distribution of PMT response variation with respect to an average reference prior to the start of collisions (including all laser runs in the time period of ±10 days of July 17, 2015).

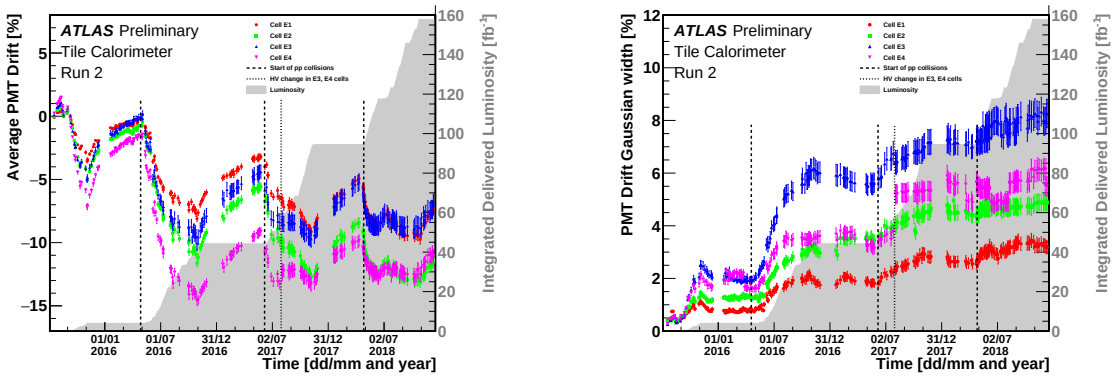

Figure 7.13: (Left) Average response variation (in %) and (right) Gaussian width per TileCal E-cell as a function of time in entire Run-2 calculated using the Combined method. For each layer, the average response is obtained by a Gaussian fit to the distribution of PMT response variation with respect to an average reference prior to the start of collisions (including all laser runs in the time period of ±10 days of July 17, 2015). Due to large width of the distribution, the gaussian fit is estimated by maximising a likelihood function.

Chapter 8

Modelling of Photomultiplier response evolution

The PMTs suffer from ageing effects i.e., the loss in their global response due to operation for a long time with large amounts of integrated anode charge. This chapter is divided into different sections starting from explaining some of the general characteristics of photomultiplier tubes to explaining different models studied to describe the response of PMTs over time and in the end projecting these results to predict the response of PMTs during Run-3 and Run-4 LHC operations.

8.1 Photomultiplier tubes

A photomultiplier tube operates under two fundamental phenomena:

- **photoemission** : incident photons on photocathode results in the emission of electrons known as *photoelectrons* through photo-electric effect.

- **secondary emission**: the accelerated *photoelectrons* under electric field strike the first dynode resulting in the emission of secondary electrons which strike the next dynode and emits more electrons. The process continues from dynode to dynode amplifying the signal up to the anode stage where all these electrons are finally collected.

Different essential elements of a PMT are listed below:

Photocathode

A photocathode of the PMT is a negatively charged electrode that converts light signals into electrical signals through *photoemision*. Normally the photocathodes are made of a deposited photoemissive semiconductor. To generate a high number of electron flux, the primary electrons generated at the PMT's photocathode are accelerated by a high-voltage potential.

Electron-optical input system

The electron-optical input system focuses the *photoelectrons* emitted by the photocathode onto the first dynode. This system must be able to keep the *collection efficiency* greater than 80% and to keep the transit time of emitted electrons between the photocathode and the first dynode to be independent of the point of origin and initial velocity. The *collection efficiency* is the ratio between photoelectrons striking the active area of the first dynode and the total number of primary electrons emitted by the photocathode.

Electron multiplier

The electron multiplier consists of stages of dynodes (maximum up to 14) which emit electrons through secondary emissions. The dynodes are arranged in such a way that the electric fields between them accelerate and focus the electrons emitted by each dynode and strike the next dynode thus producing the electron flux.
The structure of all dynodes (except the first one or two and the last) are usually identical to each other in an electron multiplier. The electrons are focused and accelerated between the dynodes by electric fields. Due to the high curvature of incoming electron paths, the space between the first and second dynode forms a critical coupling between the electron-optical input system and the iterative part of the multiplier. Hence a higher voltage is often applied between the first two or three dynodes than between the other dynodes. Figure 8.1 shows the voltage divider across the terminals of a high-voltage supply to create the potential gradients between the dynodes. The total number of electrons collected by anode n_a can be written in terms of primary electrons (n_k) that strike the first dynode as Equation 8.1

$$n_a = n_k \prod_{i=1}^{N} g_i \tag{8.1}$$

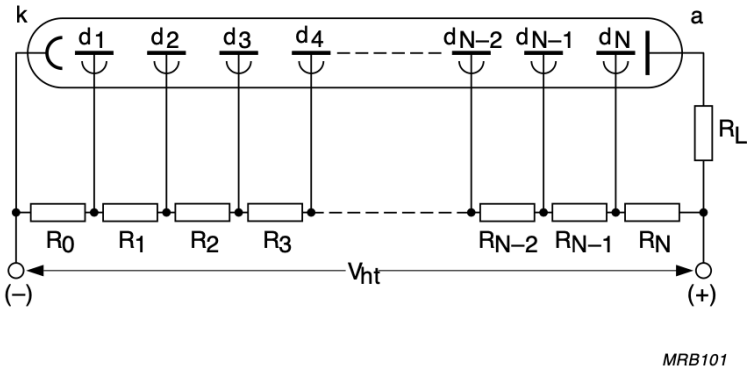

Figure 8.1: Voltage divider high-tension supply applied between the stages of dynodes of a PMT

where "N" is the total number of dynodes and "g" is the gain of each dynode "i"

Electron collector

The photocurrent accumulated after the last dynode forms an amplified signal and is collected by the electron collector known as an anode. The collector or anode is a grid placed close to the last dynode so that the electrons emitted by the last dynode can be collected.
The linearity and stability of the PMTs are very crucial terms for the study of the PMTs response evolution under high current operations.

8.1.1 PMT linearity

The linearity of a PMT is defined as the ratio of the number of electrons collected at the anode to the number of incident photons at the photocathode. In general, PMT linearity can be affected by both internal and external factors.

External factors affecting linearity

The main external factor affecting PMT linearity is the voltage change between the different successive dynodes. This change in voltage affects the gain by influencing the dynode secondary emission factors and the paths of emitted electrons.
The electrode voltages derived for stabilized power supply across the resistive divider, the anode current I_a decreases the potential between the last dynode and the anode. This creates a voltage difference between the different electrodes leading to an increase in the gain and thus affecting the linearity. The relative gain variation of an iterative divider (where $R_1 = R_2 ... = R_N$) can be written as the ratio of anode current I_a and nominal divider current at $I_a = 0$ Ref [21] as:

$$\frac{\Delta G}{G} \approx \alpha \frac{N}{N+1} \frac{I_a}{I_p} \tag{8.2}$$

where I_p is the divider current. The equation 8.2 holds only when the collection efficiency is independent of the voltage changes across the terminals of the last stage. Under these conditions, an increase in the anode current results in an increase of gain causing *overlinearity* in the PMT.
The equation 8.2 becomes invalid when the ratio $\frac{I_a}{I_p} \to 1$. In that case with the increase in anode current (I_a), the voltage greatly drops at the last dynode stage decreasing the collection efficiency which leads to an abrupt decrease in gain.
Thus the PMT linearity largely depends on the voltage across the tube as well as the affect on the voltage distribution among the first stages of dynodes due to the voltage drop between the anode and the last dynode.

Internal factors affecting linearity

The internal factors that affect linearity are space charge, cathode resistivity as well as gain drift. The space charge influences the electron paths at high currents causing collection losses. As the current increase, space charge causes some electrons to return to the surfaces from which they were emitted. This effect is more prominent between the last dynode and the anode due to the highest current density between them.
On the other hand cathode resistivity mostly affects the collection efficiency of the first dynode. The design of the electron-optical input system assumes that the photocathode is an equipotential surface and any deviation from this assumption leads to *non-linearity* of a PMT by altering the photoelectron trajectories. The linearity of a PMT can also be

affected by gain drift due to variations in the anode current. When the mean anode current varies, a gain of a PMT may undergo reversible variations leading to a linearity error. Many methods have been developed to calculate the linearity deviation Ref [21].

8.1.2 PMT stability

The term 'stability' of a PMT refers to the consistency of anode sensitivity over temperature, time, mean current, and other external as well as internal factors. The following are the most significant factors that affect the consistency of anode sensitivity:

- **short-term drift**: Fluctuations in the gain of a PMT in response to a change in mean current.
- **long-term drift**: Fluctuations in the gain of a PMT that occurs over time in the presence of constant illumination.

Short-term drift

When a photomultiplier is subjected to a flux that produces a mean anode current of less than 10μA, the gain is generally sufficiently stabilized after approximately 10 or 15 minutes and ignores the effects of long-term drift. However, if the input flux is changed abruptly, the anode current begins a new drift phase before stabilizing from the previous effect. As a result, the gain becomes a function (typically increasing) of the mean value of the anode current computed over a second or longer interval. For most types of photomultipliers, the time needed to stabilize the PMT gain after an abrupt change of average flux is roughly a second. However, in some circumstances, this quick shift in flux is supplemented by one with a significantly longer time constant (about an hour) Ref [21].

Long-term drift

The long-term drift of a PMT can occur when either the mean anode current is too high or too low. After a long period of non-operation, when a photomultiplier tube is operated under high mean anode currents, a large drift of gain is observed for the first few days of operation. After a few days of operation, the gain becomes relatively stable and then it slowly decreases as a function of the total accumulated charge. This effect is more or less irreversible at mean anode current greater than about 10μA ($I_a > 10\mu A$) Ref [21].
The operating life of a PMT can be defined as the time in which the anode sensitivity

becomes half of its initial value. This time is a function of the total delivered charge, which is typically 300 to 1000 coulombs. Figure 8.2 shows the relative gain variation of a PMT operating at 30μA of anode current after a long period of rest. Initially, the PMT drifts down very quickly (between 20% and 40%) which is called initial ageing. After some time, the anode sensitivity declines slowly. The slow ageing is observed as long as the mean anode current stays above 100nA Ref [21]. In the condition of low mean anode charge (only a

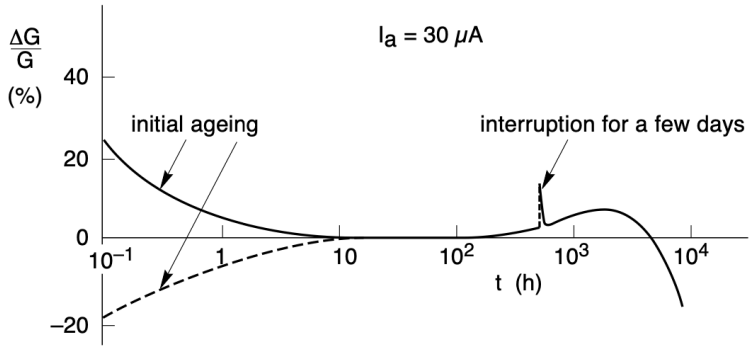

Figure 8.2: Relative gain variation of PMT operated at high average current. Figure taken from [21].

few μA), the variations of anode sensitivity depend on the changes in the surface state of dynodes. The gain variation in this case usually differs from PMT type to type and even from one PMT to another of the same type. Figure 8.3 illustrates that the PMT gain does not returns to its original value even when the input flux does return and the difference between the two gains is referred to as hysteresis. This hysteresis exhibit an interaction between short-term and long-term stability parameters. During long periods of operation, the higher the current, the faster the hysteresis dissipates.

The stability and linearity of PMT response evolution in the high irradiation environment of the LHC is crucial to be able to maintain the high performance of the Tile Calorimeter. The stability of the PMT response is continuously monitored using minimum bias events, cesium, and laser calibration systems. The PMT response drifts were studied in detail using laser calibration data taken during LHC Run-2 operation. The results of these studies are

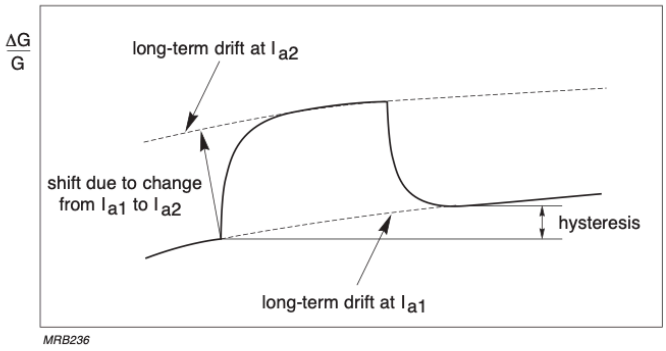

Figure 8.3: Gain variation of a photomultiplier tube indicating long-term gain drift and short-term shift due to change of operating conditions. a1 and a2 represent two different operating conditions. The figure is taken from Ref [21].

explained in detail in Section 7.6. In order to better understand the response evolution of the TileCal PMTs during LHC operation as well as the shutdown period different models were formalized. These models are listed and explained in chapter 8.

8.2 PMT recovery during Year End Technical Stops

TileCal monitored the PMT response along the detector operation during LHC Run-2 using laser calibration data. TileCal PMTs response loss (down-drift) was observed during normal operation with particle collisions in LHC, while a partial recovery (up-drift) of the response is observed when PMTs are powered OFF during each technical stop period as well as during **Y**ear **E**nd **T**echnical **S**top (YETS). This effect (up-drift) is clearly seen in all the Figures of Section 7.6 showing the average response variation of the PMTs over the entire Run-2.

Figure 8.4 shows the average response evolution of layers A, BC, and D during the entire Run-2 period. In this figure the response loss (down-drift) during each year corresponds to the proton-proton collision period while the response recovery (up-drift) at the end of each

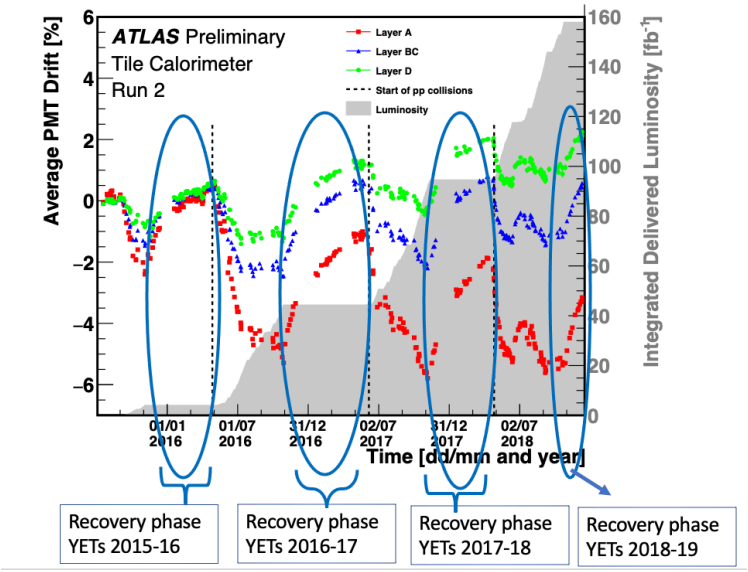

Figure 8.4: Average response evolution in all the three layers of TileCal during the entire Run-2 highlighting the response recovery of the PMTs reading all layers during Year End Technical Stops in 2015, 2016, 2017, and 2018. The reference is taken prior to the start of collisions in 2015.

year corresponds to the Year End Technical Stop of the corresponding year. However, it can be seen from this Figure 8.4 that the response recovery is different for PMTs reading different layers and during different years. For most PMTs the response does not return to its original (*"starting"*) value in the absence of pp − collisions. The difference between the original value and the value of PMT response after recovery is referred to as the "hysteresis" effect, which is explained in subsection 8.1.2. The hysteresis effect is more prominent in PMTs reading the cells of the A layer, as they are the most exposed PMTs with the highest accumulated anode charge. For PMT's reading D cells a positive drift is observed at the end of each year as they are the least exposed cells with the lowest accumulated anode charge.

Based on these observations, different statistical approaches were studied to quantify and to better understand the response recovery of all PMTs reading all the cells during YETS periods with the main goal to describe the up-drift of all the PMTs of different cells in a single **unified model**. The different models that were studied are explained in the following subsections. In all these models, the combined method explained in Section 7.4 is used to determine the PMT response variation during each year's YETS data with respect to a set

of reference runs of the respective year. For each year's YETS data the reference is taken around the start of pp − collisions period of the next year while the Interval Of Validity (IOV) is taken around the end of pp − collisions of that year. The ATLAS conditions database allows the storing of conditions data according to an interval of validity (IOV). The IOV has a start and end run identifier, between which the stored conditions are valid and applicable to the data. The fit in each YETS is applied between the IOV and the corresponding reference. The references and IOVs are taken from the following dates:

- YETS data **2015-2016** - Reference : 2016-03-25 - IOV: 2015-11-04
- YETS data **2016-2017** - Reference : 2017-05-20 - IOV: 2016-10-27
- YETS data **2017-2018** - Reference : 2018-04-18 - IOV: 2017-10-12
- YETS data **2018-2019** - Reference : 2019-02-18 - IOV: 2018-10-24

8.2.1 Single exponential model

Assuming that the PMT response variation has exponential dependencies, this model applies a single exponential fit function [8.3] to study the PMT response recovery during Year End Technical Stops. This model assumes that the response of the PMTs recovers exponentially with time giving a time constant (τ).

$$A - D \times \exp(\frac{-t}{\tau}) \tag{8.3}$$

where in Equation 8.3, "A" is the value of the function at $t = \infty$. At $t = 0$, the function becomes A + D, where "D" is the drift parameter which is related to the down-drift during the run that is expected to recover with time in the absence of collisions. "τ" gives the characteristic time of a PMT; the time after which the response has recovered by $1/e$ of its starting value. The value of "τ" parameter gives a quantitative estimate of how rapidly the PMT response recovers back to its initial value.

The single Exponential Fit model has been applied to all PMTs reading different cells during all YETS periods of Run-2. Figures 8.5, 8.6, 8.7 and 8.8 show examples of the single exponential fit model applied to most exposed E cells and least exposed D cells during YETS 2015-2016, 2016-2017, 2017-2018 and 2018-2019, respectively. The corresponding fit parameters are shown in tables 8.1 (characteristic time in days) and 8.2 (drift parameter in percent). Combined method 7.4 is used to evaluate the PMT response variation in all

YETS. In each YET the fit is applied from the end of *pp-collisions* of the previous year till the start of *pp-collisions* of the next year.

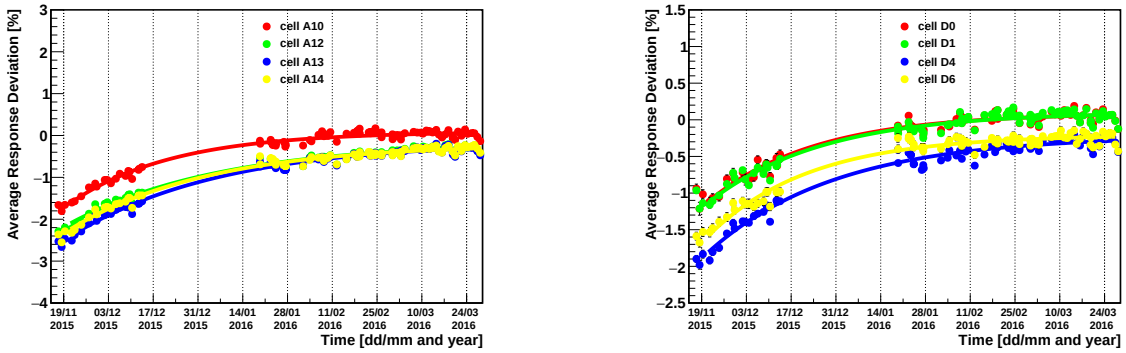

Figure 8.5: Single exponential fit applied to the 2015-2016 Year End Technical Stop laser data of PMTs reading A10, A12, A13, and A14 cells (Left) and D0, D1, D4, D6 cells (Right). Reference is taken around March 29, 2016.

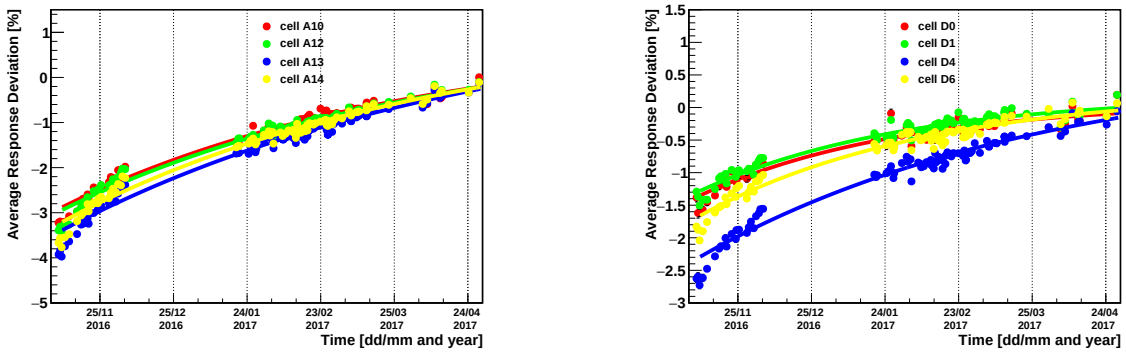

Figure 8.6: Single exponential fit applied to the 2016-2017 Year End Technical Stop laser data of PMTs reading A10, A12, A13, and A14 cells (Left) and D0, D1, D4, D6 cells (Right). Reference is taken around May 23, 2017.

Table 8.1 shows that with a single exponential fit the time taken by the PMTs to recover during YETS 2015-2016 is ≈ 47 days for E cells and ≈ 36 days for D cells. For YETS 2016-2017 the time constant is much higher for E cells with an average of about ≈ 155 days with an error of ≈ 6 days, for D cells the average is ≈ 100 days with an error of about 5 days. For YETS 2017-2018, the characteristic time-constant for E cells is ≈ 114 days

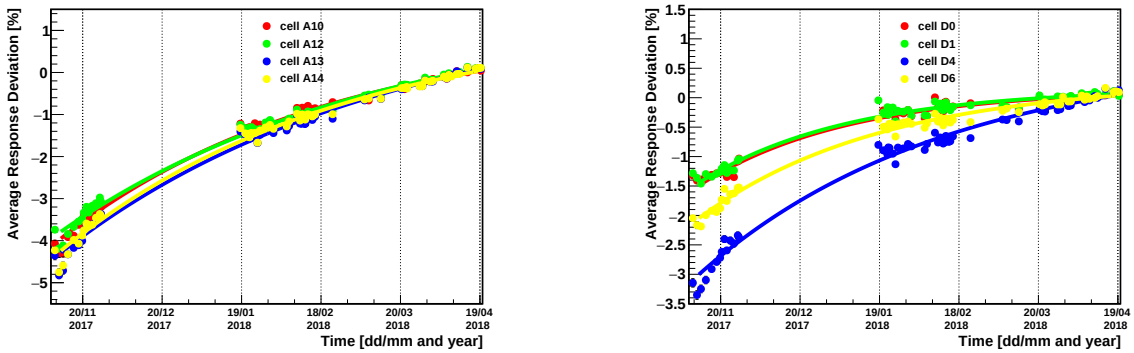

Figure 8.7: Single exponential fit applied to the 2017-2018 Year End Technical Stop laser data of PMTs reading A10, A12, A13, and A14 cells (Left) and D0, D1, D4, D6 cells (Right). Reference is taken around April 18, 2018.

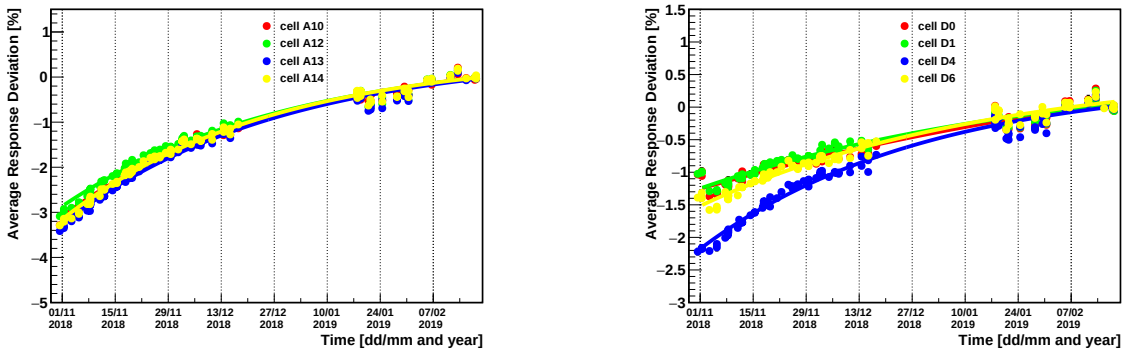

Figure 8.8: Single exponential fit applied to the 2018-2019 Year End Technical Stop laser data of PMTs reading A10, A12, A13, and A14 cells (Left) and D0, D1, D4, D6 cells (Right). Reference is taken around February 18, 2019.

Cell	2015-2016	2016-2017	2017-2018	2018-2019
A10	33 ± 1	140 ± 4	102 ± 2	60 ± 1
A12	47 ± 2	150 ± 6	119 ± 3	61 ± 2
A13	47 ± 1	173 ± 7	121 ± 3	58 ± 1
A14	44 ± 1	151 ± 6	106 ± 2	55 ± 1
D0	34 ± 2	82 ± 6	54 ± 2	121 ± 1
D1	36 ± 1	84 ± 4	54 ± 1	74 ± 3
D4	41 ± 2	142± 7	93 ± 2	59 ± 2
D6	32 ± 2	93 ± 5	68 ± 2	69 ± 3

Table 8.1: This table enlists the characteristic time in days for recovery of PMT response during YETS 2015-2016, 2016-2017, 2017-2018, and 2018-2019 using the single exponential fit model. The time constant is shown for PMTs reading the most exposed E cells and least exposed D cells.

Cell	2015-2016	2016-2017	2017-2018	2018-2019
A10	1.74 ± 0.02	3.83 ± 0.07	5.09 ± 0.03	3.65 ± 0.02
A12	1.97 ± 0.02	4.03 ± 0.09	5.31 ± 0.05	3.38 ± 0.02
A13	2.29 ± 0.02	5.03 ± 0.13	6.03 ± 0.06	3.78 ± 0.02
A14	2.07 ± 0.02	4.44 ± 0.09	5.58 ± 0.04	3.63 ± 0.02
D0	1.23 ± 0.02	1.46 ± 0.04	1.66 ± 0.02	2.53 ± 0.19
D1	1.26 ± 0.02	1.48 ± 0.02	1.62 ± 0.01	1.86 ± 0.02
D4	1.61 ± 0.02	3.07 ± 0.09	3.77 ± 0.03	2.59± 0.02
D6	1.40 ± 0.03	1.94 ± 0.04	2.35 ± 0.02	2.21 ± 0.03

Table 8.2: This table enlists the drift parameter in percent for recovery of PMT response during YETS 2015-2016, 2016-2017, 2017-2018, and 2018-2019 using the single exponential fit model. The drift parameter is shown for PMTs reading the most exposed E cells and least exposed D cells.

and for D cells are ≈ 67 days. While during 2018-2019 the time constant for E cells is ≈ 58 days and ≈ 90 days for D cells. Similarly, the value of the drift parameter shown in table 8.2 is widely spread for each cell type and for each year.
The single exponential model works well for all cells only in YETS 2015-2016 and 2018-2019. For all other YETS, the single exponential model is not enough to explain the PMT response recovery. Thus in order to find a unified model for all YETS, the Double-Exponential fit model is applied which is described in the following section.

8.2.2 Double-exponential model

Considering the fact that PMT response evolution is affected by several factors and that the previous "Single-Exponential Model" failed to describe the early recovery in a number of cases, a double exponential fit function [8.4] was applied to study the PMT response recovery during Year End Technical Stops. In this model one of the exponentials corresponds to the fast recovery and the other one to the slow recovery process.

$$A - D_1 \times \exp(\frac{-t}{\tau_1}) - D_2 \times \exp(\frac{-t}{\tau_2}) \tag{8.4}$$

where in Equation 8.4, D_1, D_2 corresponds to down-drifts during collisions and τ_1, τ_2 are their corresponding characteristic recovery time-constant introduced by different processes affecting PMT response variation over time.

In order to understand the PMT response recovery over time, the double exponential fit model is applied to YETS laser data for all PMTs reading different cells, and the corresponding parameters were studied. Following are some of the examples fit for the different YETS.

Figures 8.9, 8.10, 8.11, 8.12 show the double exponential fit applied to 2015-2016, 2016-2017, 2017-2018 and 2018-2019 YETS data, respectively for the most exposed E cells (left) and least exposed D cells (right).

For most of the cells, the fit function failed to fit the laser YETS data. The two time constants corresponding to two exponentials are enlisted in table 8.3 and 8.4 and the drift fraction in fast recovery process is given in table 8.5. The output parameters indicate three different cases for the different cells.
In one case for some cells the two exponentials gives almost similar values of fit parameters i.e $D_1 = D_2$ and $\tau_1 = \tau_2$ particularly during YETS 2018-2019 in all cells. This indicates that the YETs data can be better explained with a single exponential instead of two separate

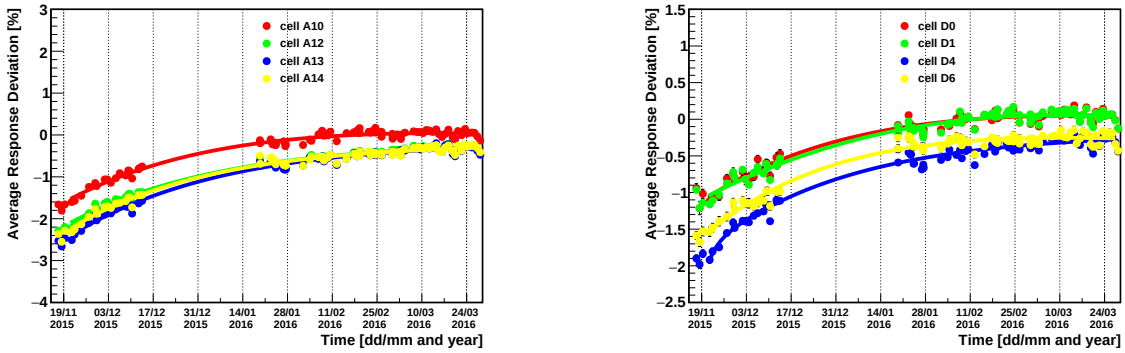

Figure 8.9: Double exponential fit applied to the 2015-2016 Year End Technical Stop laser data of PMTs reading A10, A12, A13, and A14 cells (Left) and D0, D1, D4, D6 cells (Right). Reference is taken around March 29, 2016.

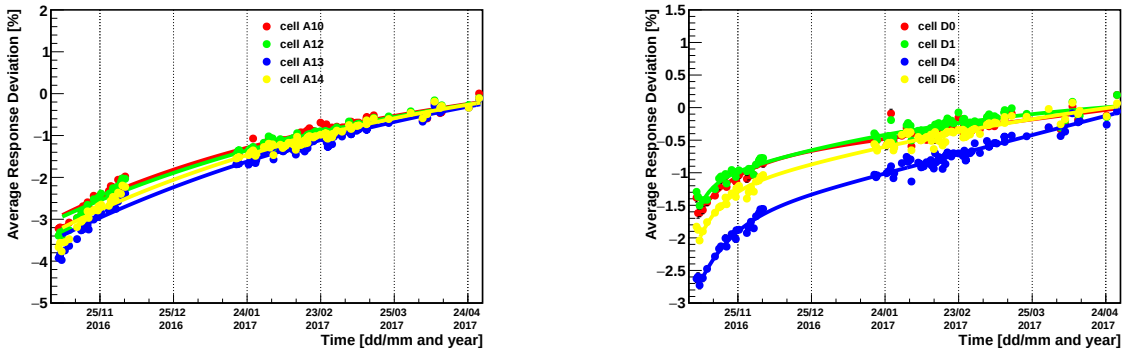

Figure 8.10: Double exponential fit applied to the 2016-2017 Year End Technical Stop laser data of PMTs reading A10, A12, A13, and A14 cells (Left) and D0, D1, D4, D6 cells (Right). Reference is taken around May 23, 2017.

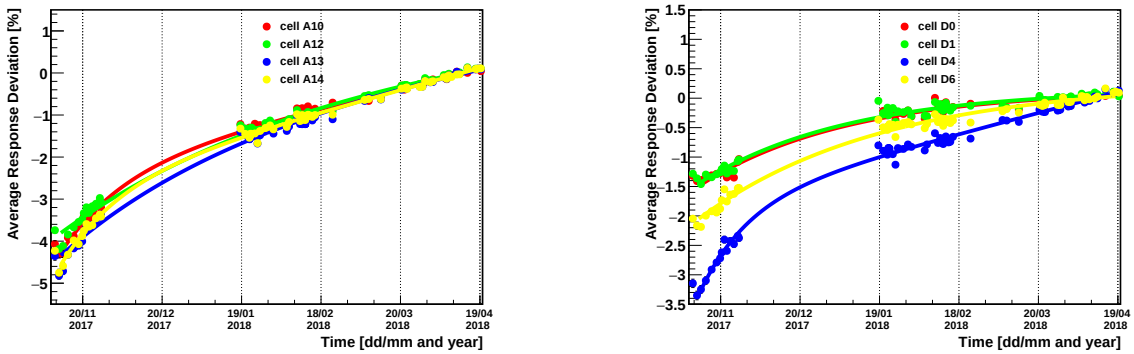

Figure 8.11: Double exponential fit applied to the 2017-2018 Year End Technical Stop laser data of PMTs reading A10, A12, A13, and A14 cells (Left) and D0, D1, D4, D6 cells (Right). Reference is taken around April 18, 2018.

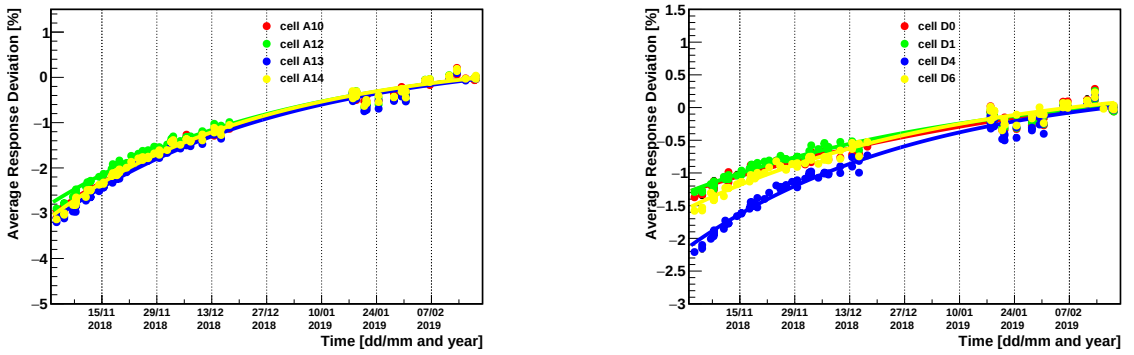

Figure 8.12: Double exponential fit applied to the 2018-2019 Year End Technical Stop laser data of PMTs reading A10, A12, A13, and A14 cells (Left) and D0, D1, D4, D6 cells (Right). Reference is taken around February 18, 2019.

Cell	τ_1 (2015-2016)	τ_1(2016-2017)	τ_1 (2017-2018)	τ_1 (2018-2019)
A10	56 ± 4	96 ± 3	24 ± 1	61 ± 4
A12	47 ± 8	150 ± 6	93 ± 2	61 ± 5
A13	48 ± 2	173 ± 7	68 ± 4	59 ± 4
A14	44 ± 3	151 ± 6	23 ± 1	55 ± 4
D0	57 ± 3	16 ± 2	57 ± 10	112 ± 17
D1	266 ± 19	6 ± 1	56 ± 9	74 ± 3
D4	3 ± 2	14± 1	18 ± 2	60 ± 6
D6	51± 10	9 ± 2	69 ± 9	69 ± 8

Table 8.3: This table enlists the time constant τ_1 parameter in days with their uncertainties corresponding to the fast recovery process of PMT response during YETS 2015-2016, 2016-2017, 2017-2018 and 2018-2019 using the double exponential fit model. The time constant is shown for PMTs reading the most exposed E cells and least exposed D cells.

Cell	τ_2 (2015-2016)	τ_2(2016-2017)	τ_2 (2017-2018)	τ_2 (2018-2019)
A10	$36\times10^5 \pm 26\times10^4$	$13\times10^5 \pm 28\times10^4$	$51\times10^5 \pm 61\times10^4$	61 ± 4
A12	47 ± 8	$15\times10^1 \pm 10$	$19\times10^5 \pm 15\times10^4$	61 ± 5
A13	$14\times10^2 \pm 20\times10^2$	$17.3\times10^1 \pm 7.6$	$30\times10^5 \pm 17\times10^4$	59 ± 4
A14	44 ± 3	$15.1\times10^1 \pm 9.1$	$14\times10^5 \pm 19\times10^3$	55 ± 4
D0	$42\times10^3 \pm 16\times10^5$	$90\times10^4 \pm 42\times10^3$	57 ± 10	$11\times10^1 \pm 17$
D1	$47\times10^1 \pm 35$	$11.1\times10^1 \pm 8$	56 ± 9	74 ± 3
D4	45 ± 2	$60\times10^5 \pm 94\times10^3$	$44\times10^5 \pm 63\times10^3$	60 ± 6
D6	$24.3\times10^1 \pm 64.5$	$19.7\times10^1 \pm 43$	69 ± 9	69 ± 8

Table 8.4: This table enlists the time constant τ_2 parameter in days with their uncertainties corresponding to the slow recovery process of PMT response during YETS 2015-2016, 2016-2017, 2017-2018 and 2018-2019 using the double exponential fit model. The time constant is shown for PMTs reading the most exposed E cells and least exposed D cells.

Cell	$\frac{D_1}{D_1+D_2}$ (2015-2016)	$\frac{D_1}{D_1+D_2}$(2016-2017)	$\frac{D_1}{D_1+D_2}$ (2017-2018)	$\frac{D_1}{D_1+D_2}$ (2018-2019)
A10	- 0.00012±0.00008	0.00038±0.0000002	0.00002±0.45105	0.5±0.5
A12	0.5±0.5	0.5±0.5	0.0004±0.0000004	0.5±0.5
A13	1.2±0.5	0.5±0.5	0.0001±0.6138	0.5±0.5
A14	0.5±0.5	0.5±0.5	0.00008±0.370648	0.5±0.5
D0	-0.01±0.00007	0.00017±0.4030	0.5±0.5	0.5±0.5
D1	-2.1±0.4	0.2±0.5	0.5±0.5	0.5±0.5
D4	0.16±0.79	0.00002±0.426367	0.00003±0.429832	0.5±0.5
D6	6.33±0.33	0.3±0.2	0.5±0.5	0.5±0.5

Table 8.5: This table enlists the drift fraction $\frac{D_1}{D_1+D_2}$ with corresponding uncertainties in fast recovery process in % during YETS 2015-2016, 2016-2017, 2017-2018 and 2018-2019 using double exponential fit model. The drift fraction is shown for PMTs reading the most exposed A cells and least exposed D cells.

Cell	(2015-2016)	(2016-2017)	(2017-2018)	(2018-2019)
A10	-1.55±0.27	-2.93±0.02	-4.34±0.03	-3.00±0.09
A12	-2.12±0.15	-2.96±0.09	-3.84±0.03	-2.78±0.08
A13	-2.43±0.06	-3.41±0.01	-4.38±0.13	-3.17±0.08
A14	-2.26±0.01	-3.23±0.09	-4.63±0.03	-3.07±0.08
D0	-1.08±0.09	-1.62±0.04	-1.51±0.27	-1.28±0.09
D1	-1.06±9.19	-1.56±0.03	-1.47±0.10	-1.28±0.01
D4	-2.04±0.09	-2.75±0.04	-3.41±0.04	-2.13±0.07
D6	-1.55±1.00	-2.05±0.01	-2.07±0.12	-1.53±0.09

Table 8.6: This table enlists the values of $(A - D_1 - D_2)$ with corresponding uncertainties during YETS 2015-2016, 2016-2017, 2017-2018, and 2018-2019 using the double exponential fit model. This term corresponds to the the initial point of fit for cells where $\tau_1 = \tau_2$.

exponentials and the value $A - D_1 - D_2$ gives the first point of a fit function of the linear term which is shown in Table 8.6.
In the second case, the fit failed to converge giving a very large drift parameter and corresponding time constants for the slow recovery process (i.e $\tau_2, D_2 \to \infty$). The value of τ_2 in such cases is greater than the total time period covered by the corresponding year's YETS data hence this case the double exponential function becomes almost equivalent to a linear recovery with a single exponential.
For few cells the fit output parameter indicate that for fast recovery process $\tau_1 < \tau_2$ the drift parameter is large i.e., $D_1 > D_2$. This indicates that the PMTs which have a fast down-drift at the beginning of the collisions also recover faster when the collisions stop. In this case, fit converges only for the cells whose τ_2 is less than the total time period of YETS data. For other cells, the fit does not converge.
The results corresponding to cases one and second indicate that the double exponential failed to explain the YETs data and leads to the next model to address the issues encountered in both cases which are explained in the following subsection.

8.2.3 Single-exponential with slope model

The results of the double exponential model point out that the PMT response recovery during YETS can be well explained with a linear component with a single exponential. In addition to this during Run-1, a linear deviation from the cesium source decay curve (2.3% per year) Ref [18] was observed with the cesium calibration system as shown in Figure 8.13. As seen in the figures the response of three longitudinal layers to the cesium source is almost linear until it reaches saturation. This linear response or slope was observed in all the PMTs during Run-1 and Run-2. While the deviation of the response of three layers from the expected cesium source decay curve is mainly introduced by PMTs hence it was decided to model the PMT recovery during YETS with a single exponential function with slope to see if this function better explains the response recovery of PMTs than the previously studied models.

In this model, a slope with a single exponential fit function [8.5] is applied to study the PMT response recovery during YETS.

$$A + S \times t + D \times \exp(\frac{-t}{\tau}) \tag{8.5}$$

In Equation 8.5, "S" is the slope parameter that corresponds to a fast recovery process

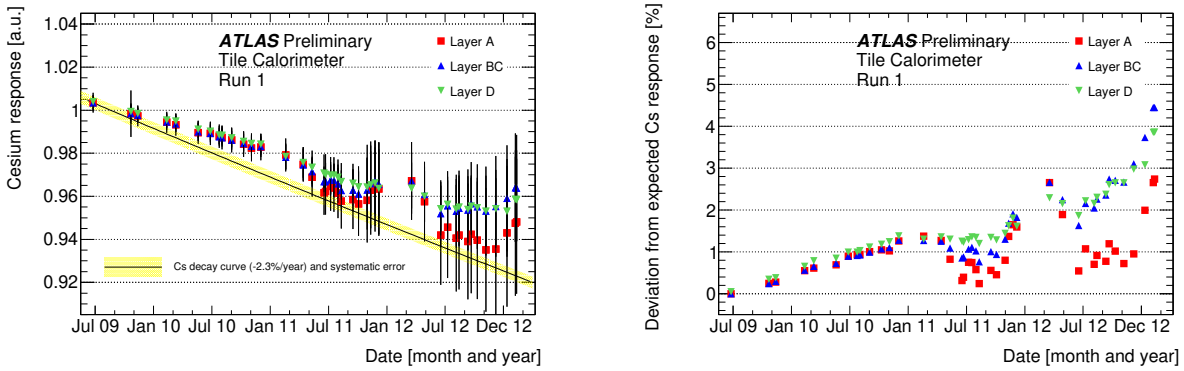

Figure 8.13: (Left) Response evolution of the three longitudinal layers of the Tile Calorimeter as a function of time to the cesium source. Error bars on the left figure corresponds to the RMS of the distribution of cesium integrals in the respective longitudinal layer. The black line is the cesium decay curve (2.3% per year) while the yellow band around this line indicates the precision of the cesium calibration system (0.3%). (Right) Deviation of measured response to cesium source from expected cesium decay curve. The figures are taken from Ref [18].

while the parameters "D" and "τ" corresponds to the overall observed down-drift during collisions of respective years and characteristic time, respectively. A graphical explanation of this function is given in Figure 8.14, where the "red line" represents the fit function while the "green" and "blue" line explains the slope and exponential parts of the function, respectively. The values of the slope and time-constant parameters are highly correlated with each other. It has been already seen that the PMTs reading cells which are more exposed to the beam have faster down-drift and faster recovery than the cells which are less exposed to the beam. Hence with this model, it is expected to see higher values of slope and consequently small characteristic time for PMTs reading more *"exposed cells"*. Similarly, for *"less exposed cells"*, higher values of characteristic time with small slope values are expected.

In order to get a better understanding of this model, the fit is applied to all the PMTs' response recovery laser data during all the YETS. This model provides relatively better results for all the cells in all YETS than the models described previously [Subsection 8.2.1 and 8.2.2]. Some of the example fits are shown for E and D cells for all YETS data.

Figures 8.15, 8.16, 8.17 and 8.18 show the slope with single exponential fit function applied to the 2015-2016, 2016-2017, 2017-2018 and 2018-2019 YETS data, respectively. As seen in these figures this model explains the data very well giving almost comparable

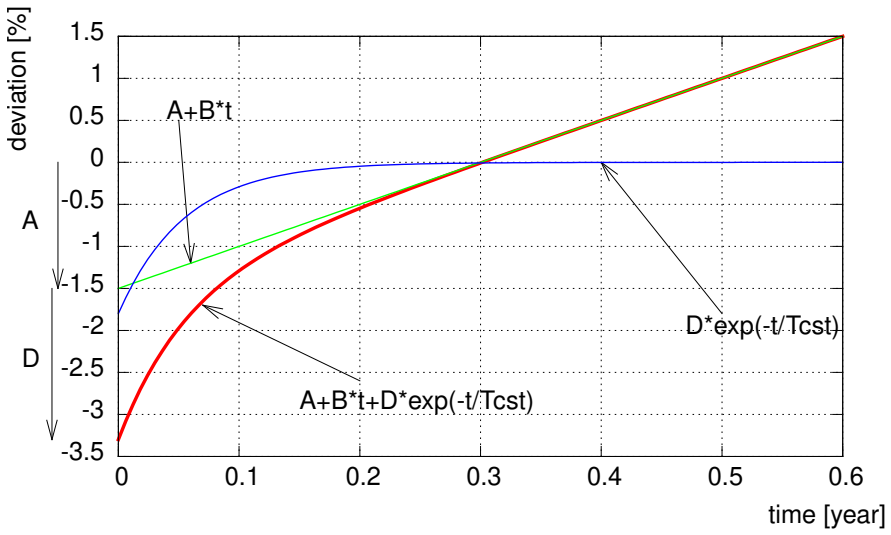

Figure 8.14: Single Exponential with Slope Fit model to study PMT response recovery during YETS

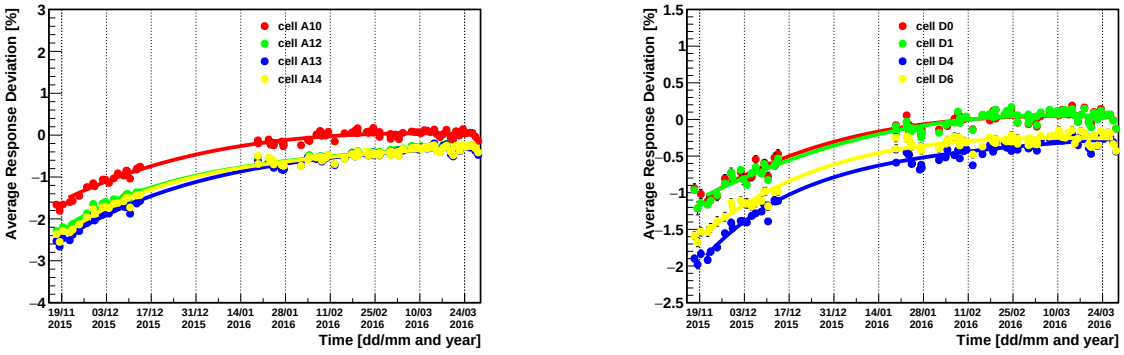

Figure 8.15: Single exponential fit with slope function applied to the 2015-2016 Year End Technical Stop laser data of PMTs reading A10, A12, A13 and A14 cells (Left) and D0, D1, D4, D6 cells (Right). Reference is taken around March 29, 2016.

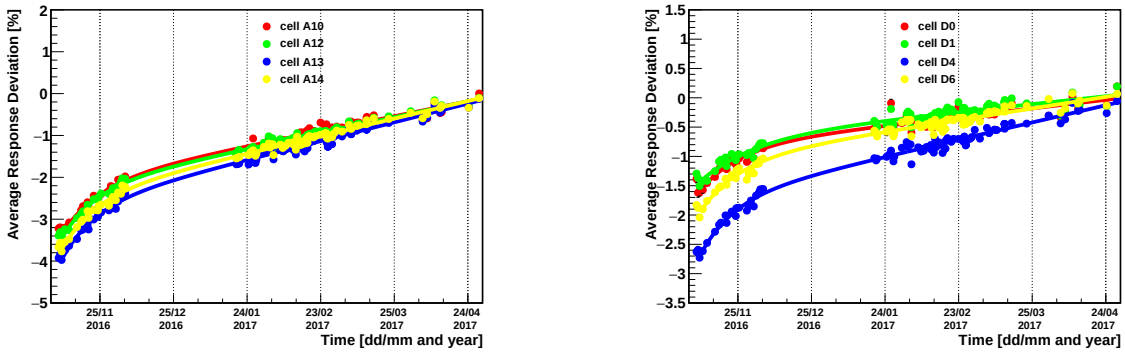

Figure 8.16: Single exponential fit with slope function applied to the 2016-2017 Year End Technical Stop laser data of PMTs reading A10, A12, A13 and A14 cells (Left) and D0, D1, D4, D6 cells (Right). Reference is taken around May 23, 2017.

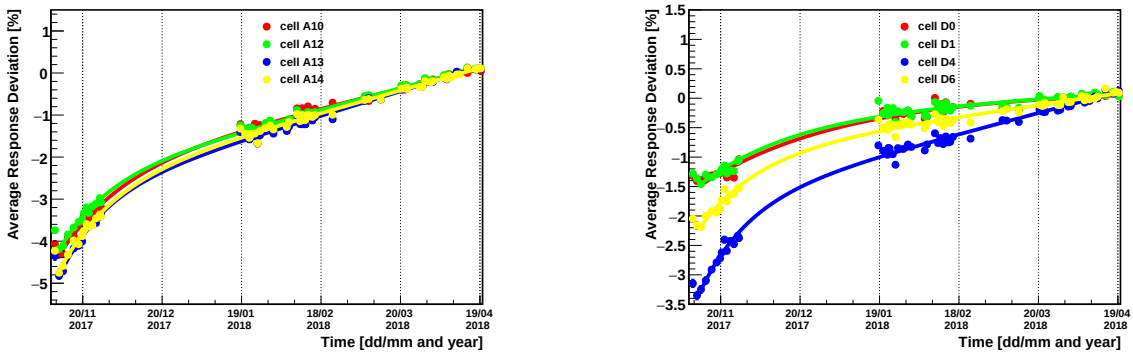

Figure 8.17: Single exponential fit with slope function applied to the 2017-2018 Year End Technical Stop laser data of PMTs reading A10, A12, A13 and A14 cells (Left) and D0, D1, D4, D6 cells (Right). Reference is taken around April 18, 2018.

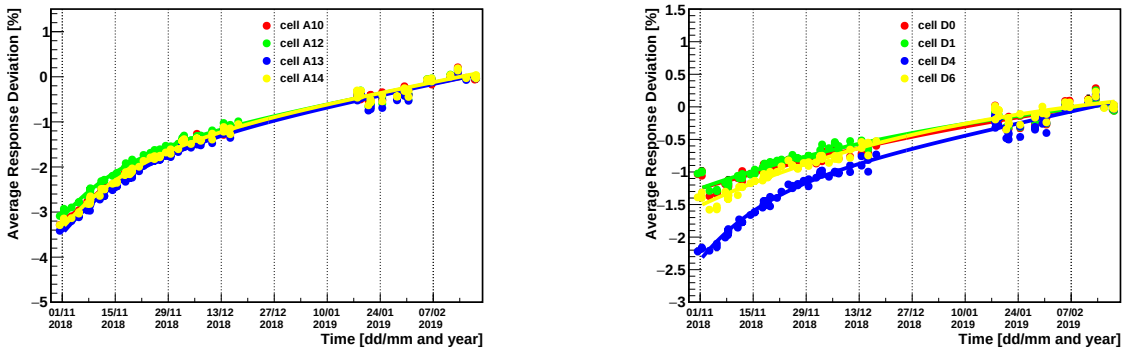

Figure 8.18: Single exponential fit with slope function applied to the 2018-2019 Year End Technical Stop laser data of PMTs reading A10, A12, A13 and A14 cells (Left) and D0, D1, D4, D6 cells (Right). Reference is taken around February 18, 2019.

parameters for different cells during different YETS. The response recovery of almost for all the PMTs reading different cells can be well-quantified with this model. The different output fit parameters are also plotted for all the YETS data.
Figures 8.19, 8.20 and 8.21 show the output parameters slope, time constant and drift respectively, for A, D and BC cells. Each point in these figures corresponds to a parameter value of a particular cell during corresponding YETS.

Figure 8.19 gives the slope parameter values for all the cells during different YETS. For A cells in the long barrel region (ALB-cells) the slope values are around ≈ 1.5 during YETS 2015-2016, ≈ 4 during YETS 2016-2017, ≈ 5 and ≈ 5.5 during YETS 2017-2018 and 2018-2019, respectively. Comparatively larger slope value is observed for A cells in extended barrel (AEB-cells) with the highest for A13 cell during all YETS. During 2015, the PMTs are exposed to less luminosity (less anode current) and thus less down-drift is observed during this period. Thus a small recovery is seen during the 2015-2016 YETS data, due to which smaller slope values are observed as compared to other YETS data. Similarly, for D cells the slope values are small as compared to other cells which are closer to the beam and accumulate for anode current.

Figure 8.20 gives the characteristic time for all the cells during different YETS. For YETS 2016-2017, 2017-2018, and 2018-2019, a characteristic time of about ≈ 20 days is observed to be taken by the PMTs reading A and BC and EB-D cells to recover. For the cells where the slope values are smaller, a large characteristic time is observed for the PMTs to up-drift. Hence for LB-D cells, the characteristic time is around ≈ 30 days. For

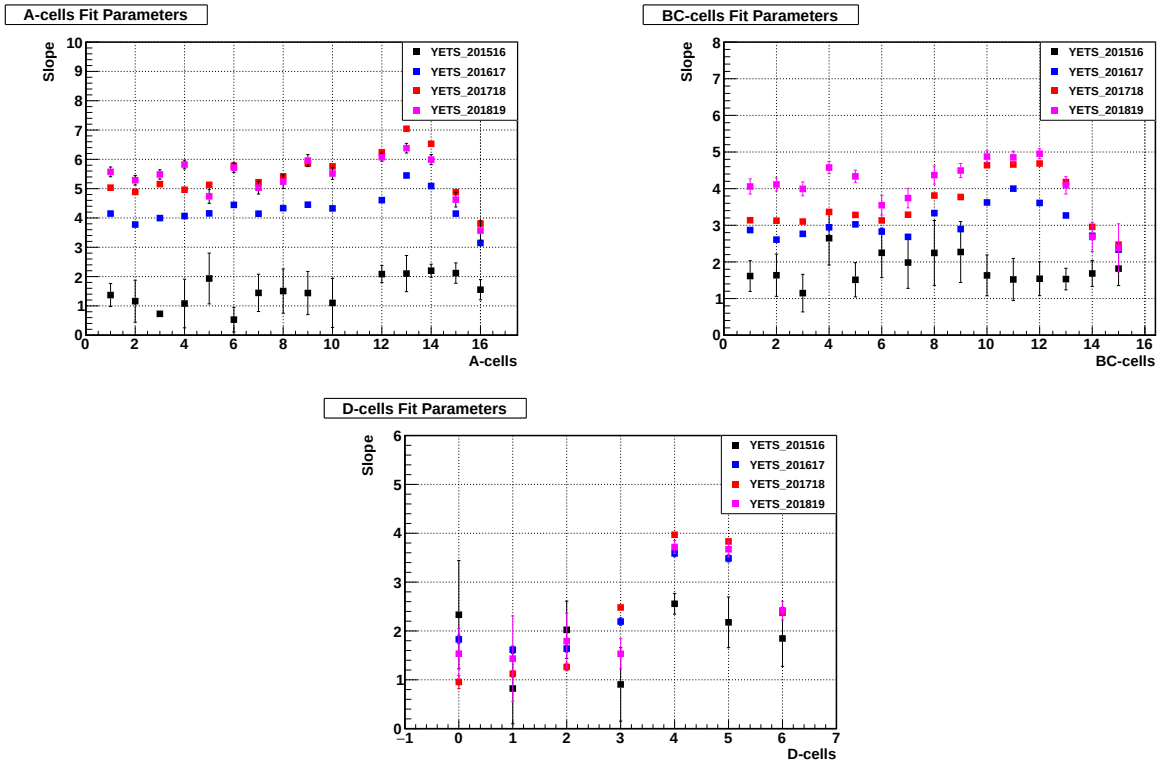

Figure 8.19: The output slope parameter of the Single Exponential with Slope model. The top left figure corresponds to the time constant for all PMTs reading the A cells, the top right figure shows the cells in the BC layer and the bottom figure corresponds to the PMTs reading cells of the D layer. The parameters are obtained from the fitting of all YETS laser data. For each cell, the error bars correspond to the uncertainties of the output fit parameter.

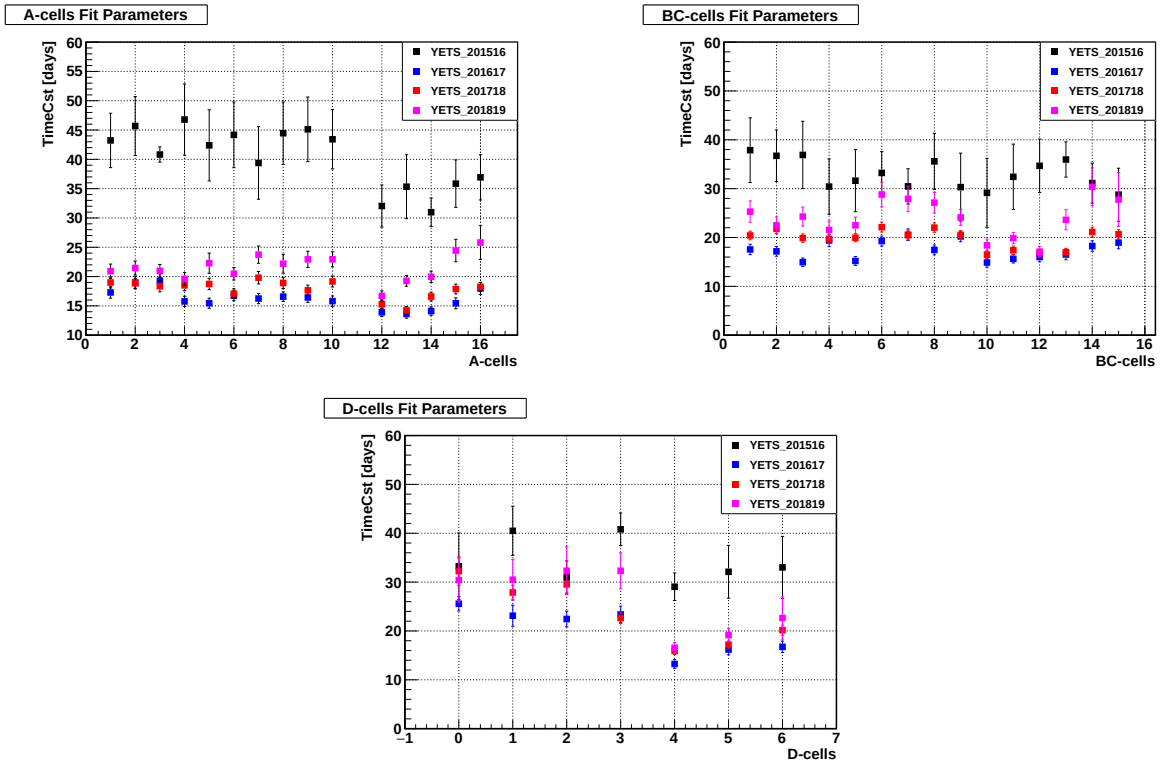

Figure 8.20: The output characteristic time [in days] parameter of the Single Exponential with Slope model. The top left figure corresponds to the characteristic time for all PMTs reading A cells, the top right figure shows the cells in the BC layer and the bottom figure corresponds to the PMTs reading cells of the D layer. The parameters are obtained from the fitting of all YETS laser data. For each cell, the error bars correspond to the uncertainties of the output fit parameter.

2015-2016 YETS data characteristic time of about ≈40-45 days is seen in all the cells.

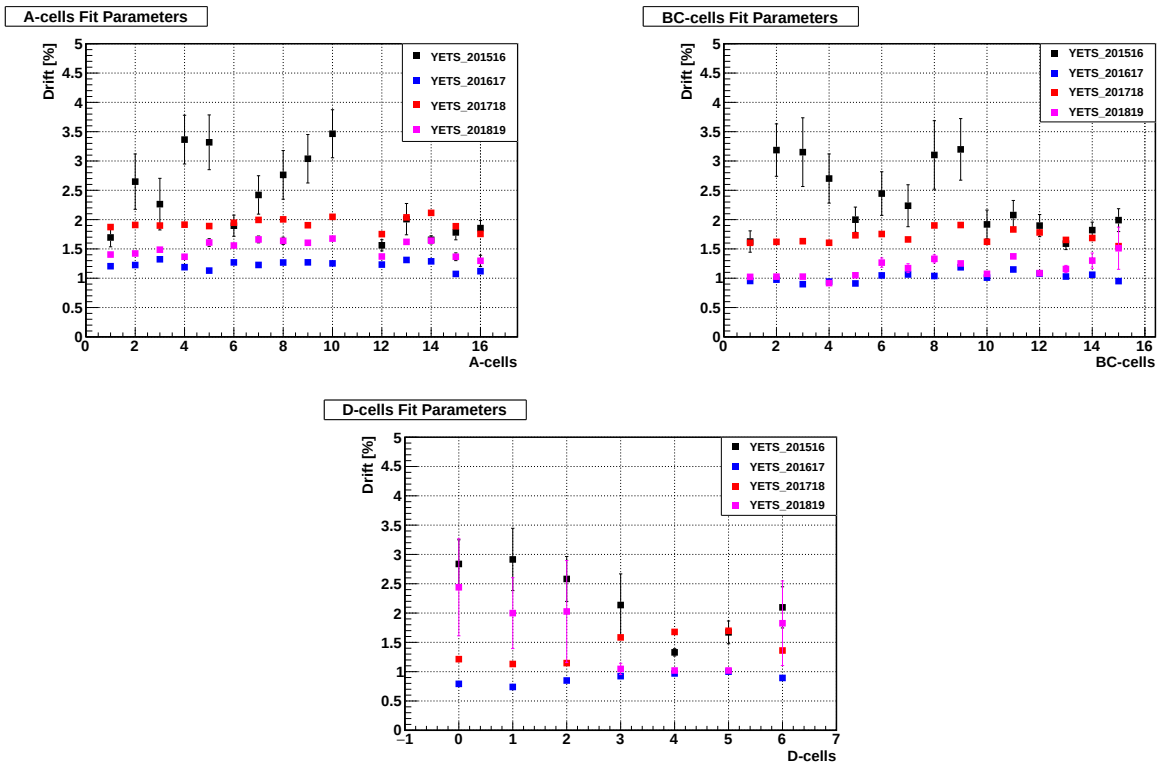

Figure 8.21: The output drift [in %] parameter of the Single Exponential with Slope model. The top left figure corresponds to the time constant for all PMTs reading the A cells, the top right figure shows the cells in the BC layer and bottom figure corresponds to the PMTs reading cells of the D layer. The parameters are obtained from the fitting of all YETS laser data. For each cell, the error bars correspond to the uncertainties of the output fit parameter.

Figure 8.21 gives the output drift parameter values for all the cells during different YETS. For E cells a drift of about ≈ 1.2% is observed during 2016-2017, ≈ 2% during 2017-2018, and ≈ 1.5% during 2018-2019 YETS. For BC cells ≈ 1% drift is seen during 2016-2017 and 2017-2018 YETS while during 2015-2016 ≈ 1.7% drift is observed with this model. For YETS 2015-2016 the drift parameter values are widely spread for the different cells.

Thus the PMTs response recovery during YETS data can be well explained with Single Exponential with Slope function for all the cells during all YETS. All the output parameters are comparable for the same cell type during different YETS. For YETS 2015-2016 some

discrepancies are observed for some cells since the luminosity in 2015 was very less, and the PMTs degraded less during the run hence the process with fast recovery is enough to describe the data.

8.3 Luminosity convoluted function

Different approaches have been discussed in Section 8.2 to understand the recovery or up-drift of the photomultiplier tubes during technical stops when there are no *pp*-collisions. But during *pp*-collisions all PMTs undergo response loss or down-drift which can be seen in Figure 8.4. The observed down-drifts mostly affect the PMTs reading out most exposed cells because the degradation of the PMT response depends mainly on the amount of integrated anode charge. Modelling of the PMT degradation is a very crucial element to make projections about the expected response loss of a PMT during the HL-LHC era which also helps to anticipate PMT replacements for the future when the PMTs will be exposed to more current. Modelling of the PMT response evolution could also be used to calibrate PMTs in the HL-LHC era where the drift might be so large and quick that it would not be possible to be corrected using Laser calibration data.
In past, a study was done by colleagues working at the Pisa laboratory to understand the response loss of a PMT as a function of integrated anode charge. A double exponential fit function as shown in Equation 8.6 was used to model the response loss of the PMTs.

$$R(Q) = p_0 . \exp^{(p_1 . Q)} + p_2 . \exp^{(p_3 . Q)} \tag{8.6}$$

where in Equation 8.6, p_0, p_1, p_2 and p_3 are the different output parameters and Q is the anode charge integrated by each PMT. Each PMT integrates different anode charges over the same time interval because of the different cell positions and activity during particle collisions.

Figure 8.22 shows the measurements of the global response loss of the PMTs reading the most exposed cells (A and E cells) at the end of LHC Run-2, regardless of the length of the collision and no-collision periods and regardless of the different anode current for PMTs reading-out different cells. The behaviour of the PMT response in the region where the integrated current is large is mostly affected by the PMTs reading out E2, E3, and E4 cells. Although this simple model explains well the average response loss of the PMTs which helped in anticipation of the PMTs' replacement for the future, but it does not include some important factors. These factors include the PMT response dependence over time as

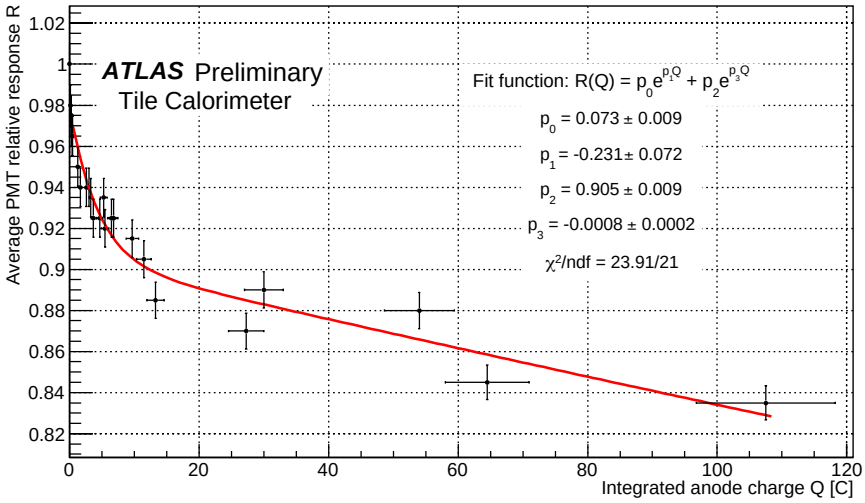

Figure 8.22: Average PMT response variation (in %) as a function of the integrated anode charge. The laser runs response is normalized to the run taken on July 17th, 2015. The points in this figure correspond to the average relative response loss of the most exposed cell types (A10, A12, A13, A14, E1, E2, E3, and E4) measured at the end of *pp*-collisions of each year during LHC Run-2. The figure is taken from Ref [22].

well as PMT recovery periods during heavy ion collisions and technical stops in between the Run-2 period.

A more refined approach is made to include the recovery period as well as the time dependence of the PMT response variation. As the integrated anode charge is proportional to integrated luminosity, this refined approach explains the PMT response variation over time as a convoluted function of luminosity. Several functions have been investigated to describe the response of PMTs as a function of convoluted machine luminosity. In this section, a brief overview of the different approaches and a detailed explanation of the approach that best fits the laser data of a PMT including the response loss as well as recovery period during the LHC Run-2 era is given.

8.3.1 Single-exponential fit function

Considering the fact that during the YETS recovery period single exponential fit with slope was the best model to describe the PMT response recovery, a similar attempt was made using the luminosity convoluted function. In this function down-drift per LHC luminosity

fill is assumed to be linear as a function of single exponential 8.7:

$$\Delta Lumi_{fill} = D \times Lumi_{fill} \tag{8.7}$$

where "D" is the *drift* parameter which corresponds to the total down-drift undergone by a PMT during the entire Run-2 collision period. The PMT response in terms of luminosity convoluted model is given by Equation 8.8:

$$PMT_{response}(t) = \sum_{fill(t_{fill}<t)} S \times t + \Delta Lumi_{fill} \times \exp(\frac{t_{fill} - t}{\tau_1}) \tag{8.8}$$

Where in Equation 8.8, S is the "slope" and τ is the "characteristic time" parameter. In this model, the fast PMT recovery process is accommodated by a slope function with a single exponential function while PMT response loss is linearly dependent on the single exponential function which can be seen graphically in Figure 8.23. In Figure 8.23 the

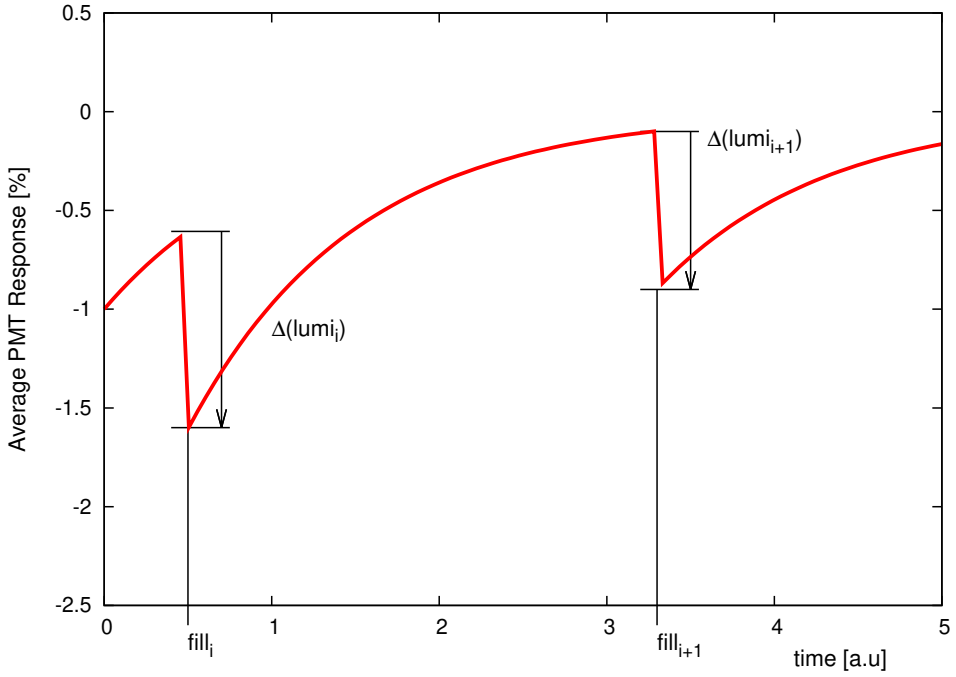

Figure 8.23: The PMT response evolution where down-drift per luminosity fill "i" is explained as linearly proportional to a single exponential function. In between the two luminosity fills $fill_i$ and $fill_{i+1}$, a PMT recovers single exponentially.

recovery phase between two luminosity fills "i" and "$i+1$" is given by single exponential function. This function is fitted to laser data of LHC's entire Run-2 period. Figure 8.24

gives an example of the luminosity convoluted single exponential model applied to 2018 laser data of A13 cell. This model gives residual values within a range of ±1.5% for A13

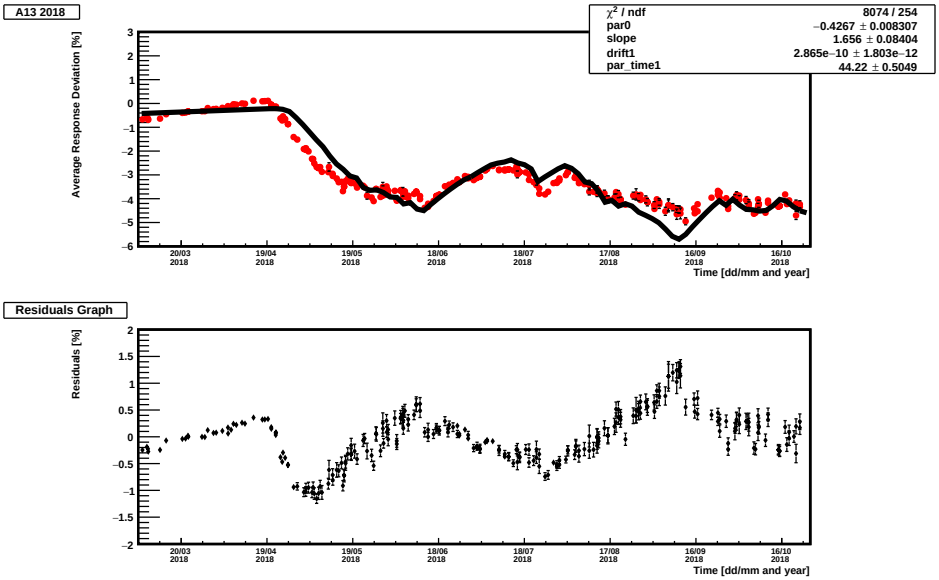

Figure 8.24: The top figure shows the average response evolution of the PMTs reading the A13 cell (red points) modelled by luminosity convoluted double-exponential with slope fit function (black line). The bottom figure shows the residual values i.e., the difference between the laser data points and the corresponding fit function value.

cell during 2018 data. The residuals are larger, particularly during the early down-drift period indicating that the model cannot properly describe the response loss of PMTs during collisions. Hence the PMT response evolution can not be well-described by the hypothesized model when down-drift per run is considered to be a linear function of the fill luminosity convoluted exponential function.

8.3.2 Power law function

Since the PMT response evolution cannot be explained by linearly dependent luminosity exponential function, a new attempt was made in which down-drift per run is defined by a power law of luminosity 8.9.

$$\Delta Lumi_{fill} = D \times (Lumi_{fill})^{\gamma} \tag{8.9}$$

Similar to 8.7, up-drift is given by a slope with single exponential function 8.10.

$$PMT_{response}(t) = \sum_{fill(t_{fill}<t)} S \times t + \Delta Lumi_{fill} \times \exp(\frac{t_{fill} - t}{\tau_1}) \tag{8.10}$$

where in Equation 8.10, S, γ and τ are the output fit parameters, "slope", "power" and "characteristic time", respectively. The fit function is applied to all PMTs laser data during the LHC Run-2 period. Figure 8.25 shows an example of a power law function applied to the PMTs reading the A13 cell during 2018 laser data. The results of this model are better

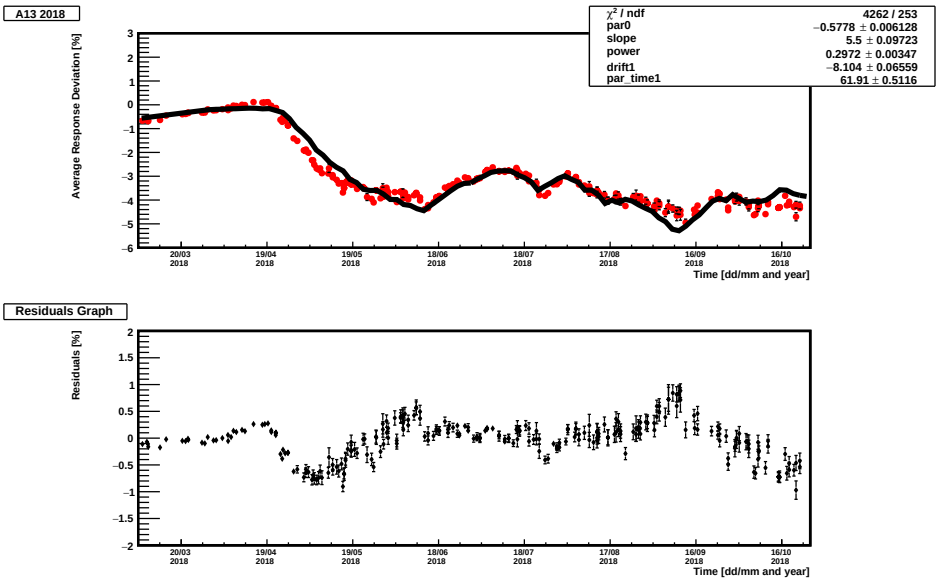

Figure 8.25: The top figure shows the PMT response evolution of A13 cell (red points) modelled by the power law of luminosity convoluted function (black line). The up-drift is given by a single exponential with slope fit function. The figure at the bottom shows the residual values i.e., the difference between the laser data points and the corresponding fit function value.

than the previously discussed model 8.3.1 however as shown in Figure 8.25 this fit function also gives larger residual values during the early down-drift period. Hence the fit function cannot well describe the immediate loss in the response of PMTs at the start of collisions. Additionally the value $\chi^2/ndf \approx 16$ is much larger than 1, thus the proposed model where down-drift per fill is defined as a function of the power law of luminosity cannot describe well the response evolution of PMTs during data-taking periods.

8.3.3 Luminosity convoluted superfunction

After fitting the laser data of the PMTs response evolution by linear as well as a power function of luminosity, an entirely new approach based on the "logistic function" was made. This approach is based on the typical behaviour of a PMT at the beginning of collisions the response of the PMT degrades very quickly and then it slows down until it reaches a plateau or saturation and after that the loss in the response of a PMT becomes constant. As the response of the PMT is affected mainly due to the integrated anode current, the more anode current the more rapid loss in the response of a PMT is observed. It is known that the integrated anode current is proportional to the instantaneous luminosity:

$$\begin{aligned} I &\propto Lumi_{inst} \\ I &= \beta \times Lumi_{inst} \end{aligned} \tag{8.11}$$

where β in equation 8.11 is the luminosity coefficient measured by the minimum bias system in the Tile Calorimeter. Figure 8.26 shows the luminosity coefficient β vs η calculated during 2018 proton-proton collision period. The luminosity coefficient is calculated by dividing the average currents of all PMTs belonging to a cell with the corresponding average instantaneous luminosity i.e, $I/Lumi_{inst}$. The error bars represent the standard deviation of measured for a given cell. In this luminosity convoluted superfunction model, PMT response evolution at a given time t is expressed as a function of effective luminosity $Lumi_{eff}$ during that interval:

$$PMT_{Response}(t) = f(Lumi_{eff}) \tag{8.12}$$

In equation 8.12, $Lumi_{eff}$ is equivalent to the total anode current to which a PMT has been exposed starting from the beginning of collisions at time $t = 0$ till the given time t. Effective luminosity is a function of efficiency which gives the down-drift of a PMT during specific luminosity fill and can be calculated at time t from the efficiency using an inverse hyperbolic tangent function as shown in equation 8.13:

$$Lumi_{eff}(t) = B \times \tanh^{-1}(\frac{1 - eff(t)}{A}) \tag{8.13}$$

where A and B are the output fit parameters. The parameter A defines the maximum loss of efficiency of a PMT whereas the parameter B is sensitive to the change in luminosity (or integrated current) of a particular PMT. Different PMTs accumulate different anode currents, thus the value of B is unique for each PMT.

After an LHC luminosity fill the effective luminosity is incremented by the luminosity of

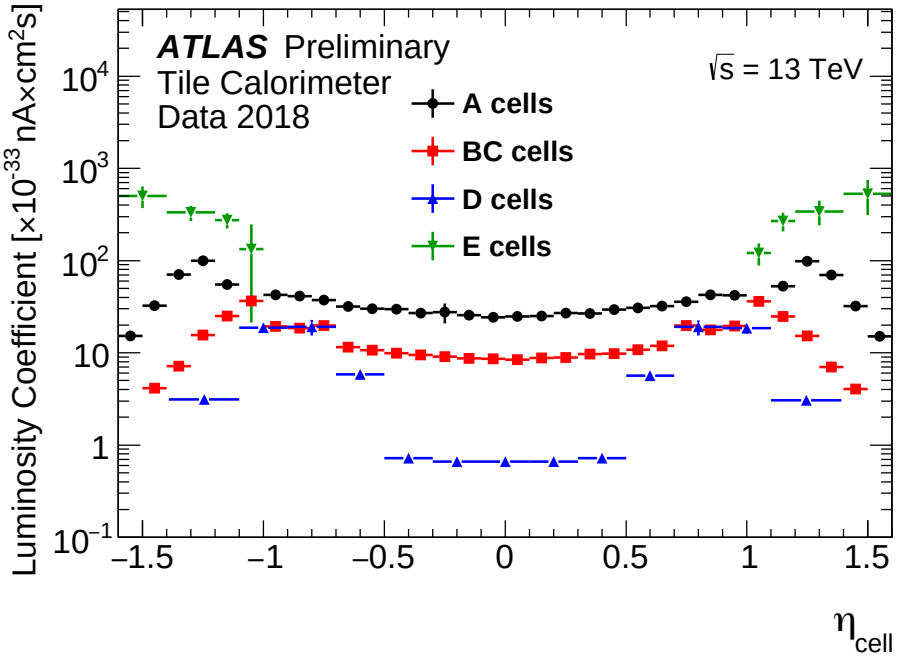

Figure 8.26: Luminosity coefficient β vs η measured by minimum bias system in p-p collision data collected during 2018 data period. A range of 20 consecutive lumiblocks (time interval) has been used. The average of the corresponding instantaneous luminosity is 1.7×1033 $cm^{-2}s^{-1}$. Each cell of the Tile Calorimeter covers a range in η and is read out by one or two PMTs. The figure is taken from Ref [20].

the fill, resulting in a decreased PMT efficiency given by equation 8.14:

$$eff(t) = 1 - A \times tanh(\frac{Lumi_{eff}(t) + Lumi_{fill}}{B}) \tag{8.14}$$

The function (" tanh ") linking the efficiency to the effective luminosity is a solution to the logistic equation. The logistic equation is a scaled and offset hyperbolic tangent function. It is a common sigmoid-shaped (S-shaped) curve as shown in Figure 8.27 and can be expressed in terms of the equation as 8.15:

$$f(x) = \frac{L}{1 + e^{-k(x-x_0)}} \tag{8.15}$$

where x_0 and L are the middle and maximum values of the curve and k is the growth rate of the logistic curve. A typical logistic equation is an equation when parameters mentioned in equation 8.15 are $k = 1$, $x_0 = 0$ and $L = 1$ and leads to:

$$f(x) = \frac{1}{2} + \frac{1}{2}tanh(\frac{x}{2}) \tag{8.16}$$

The logistic equation was initially introduced by Pierre François Verhulst Ref [49] in the mid-1830s by adjusting the exponential growth function to model population growth. In this model, the population growth is explained as initially, the growth follows the exponential curve (geometric) until the start of saturation. When saturation starts the growth becomes linear (arithmetic) and finally stops at maturity. Pierre François Verhulst in his studies used the term "logarithmic curve" for the exponential curve and hence is presumably named "logistic growth" by analogy.

In this modelling of the PMT evolution, the initial phase starts at the optimal secondary electron emission yield in the linear regime of the logistic equation, which gets reduced under the wear of current going through the PMT dynodes. Ultimately it reaches to minimum gain i.e., "saturation value". After the saturation, the PMTs stop down-drifting, and their response become almost constant with time. This behavior can be seen in Figure 8.28 which shows the evolution of an efficiency function with respect to increasing effective luminosity.

The efficiency ($eff(0)$) of a PMT at the beginning of collisions is considered as maximum i.e., 1 and as the effective luminosity increases with time during *pp*-collisions the efficiency starts decreasing until it reaches a saturation value. The time taken by the effective luminosity of a PMT to reach its saturation value depends upon several factors such as the difference in the photoelectron velocities, the dimensions, and positions of the collection electrodes, the incident flux as well as composition of a PMT. These factors are compensated

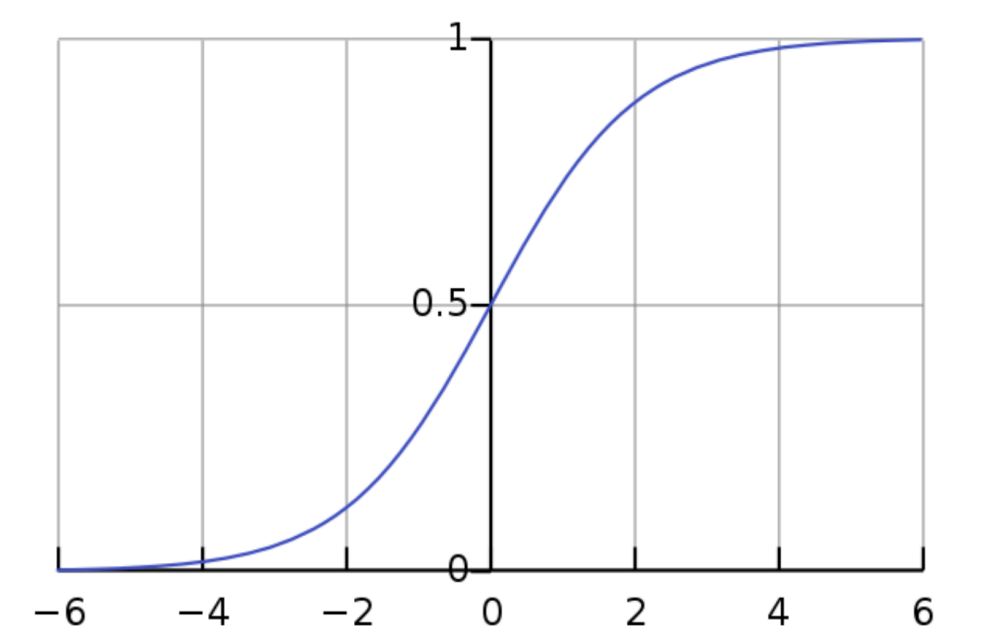

Figure 8.27: Standard logistic equation sigmoid (s-shape) curve within x-axis range ±6 when parameters are $k = 1$, $x_0 = 0$ and $L = 1$. The figure is taken from Ref [23].

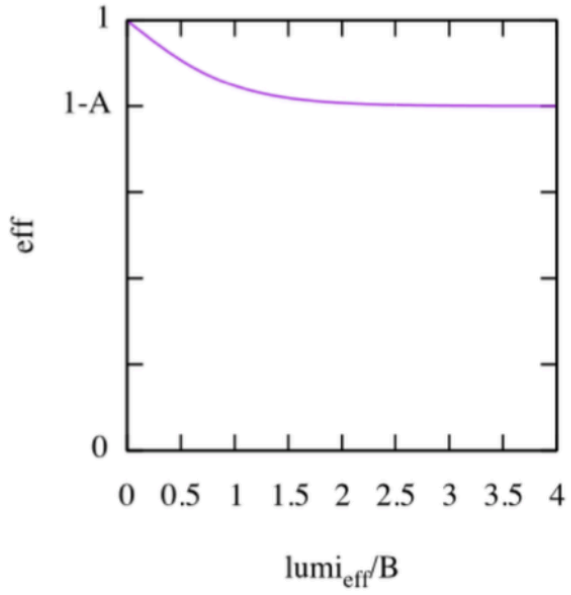

Figure 8.28: This figure shows the evolution of the efficiency function of a PMT with respect to effective luminosity/B. With the increase in luminosity, the efficiency of a PMT decreases until it reaches a saturation point. At saturation point, the loss in efficiency becomes nearly zero.

by the output fit parameter A. All the PMTs, due to their positions, accumulate different anode currents hence they are exposed to different effective luminosity. These differences are compensated by the fit parameter B. $Lumi_{fill}$ corresponds to a luminosity of a particular LHC physics run while the $Lumi_{eff}$ can also be referred as the effective exposure of a PMT at the current point in time.
In between the two luminosity fills the efficiency of a PMT recovers exponentially as shown in the Equation 8.17.

$$eff(t) = 1 - (1 - eff(t_0)) \times exp^{(\frac{-(t-t_0)}{\tau})} \tag{8.17}$$

Taking into account all the above equations, PMT response as given by equation 8.12 can also be expressed in terms of efficiency as equation 8.18:

$$PMT_{response}(t) = (PMT_{response}(0) + S \times (t) \times eff_1(t) \times eff_2(t) \tag{8.18}$$

where in Equation 8.18, eff_1 and eff_2 corresponds to the efficiency of a PMT describing different processes, affecting the gain of the PMT mostly at the last stages of amplification and S is the slope parameter to describe the total up-drift. The two efficiency functions also give two different A, B, and τ fit parameters, one corresponding to the last dynode and the other corresponding to all but not the last dynode.
The logistic luminosity convoluted fit model is applied to all the PMTs laser data for the entire Run-2 as well as individual years during Run2. Figures 8.29 and 8.30 show the luminosity convoluted super function fit applied to 2017 (a), 2018 (b) and entire Run2 laser data of the most exposed A13 cell.
Each laser data point (red points) in the following figures is estimated by including laser statistics as well as systematics as shown in equation 8.19:

$$Total_{Err} = \sqrt{(sys^2_{Err} + stat^2_{Err})} \tag{8.19}$$

where $stat_{Err}$ is calculated using *chi*-2 fit on gaussian distribution for each laser data point while sys_{Err} is evaluated by comparing the response of the PMTs to the cesium and laser system Ref [50]. An indirect comparison was performed between the responses of left and right PMTs reading the same cell with the cesium and laser systems for each year for Extended (EB) and Long Barrel (LB) regions. For the laser calibration system, the Combined method was used to evaluate the PMT response while for the cesium calibration

system, the PMT response is extracted from the TileCal optics response and cesium calibration constant factor as follows:

$$R(PMT) = \frac{R(Cs)}{R(tiles + fibres)} \tag{8.20}$$

The comparison was performed on 2018 data using available four cesium scans and nearest laser calibrations runs. Taking into account the uncertainties of the laser and cesium measurements the systematic errors calculated separately for LB and EB are given in equation 8.21 while the differences between the right and left wavelength shifting fibres are considered to be negligible.

$$\begin{aligned} syst_{Err}(LB) &= \sqrt{0.4^2 + (\frac{0.3 + 0.2 \times L}{\sqrt{N}})^2} \\ syst_{Err}(EB) &= \sqrt{0.4^2 + (\frac{0.3 + 0.1 \times L}{\sqrt{N}})^2} \end{aligned} \tag{8.21}$$

Here L is the total delivered luminosity during each year ($\approx$ 50.3 fb^{-1} for 2017, $\approx$ 63.3 fb^{-1} for 2018 and $\approx$ 156 fb^{-1} for entire Run-2), 0.4% is the global scale uncertainty on the laser calibration and N are the number of PMTs reading each cell type. By including the systematics into the model, the fit estimation becomes better giving χ^2/ndf<1.

As this function is being studied on all the cells Figures 8.31 and 8.32 show examples of least exposed D0 cell for 2017, 2018 and entire Run-2 laser data.

It can be seen from the figures that this model describes very well the response evolution of a PMT. The down-drift of a PMT can be well quantified with luminosity convoluted tangent hyperbola function and up-drift with a slope and single exponential function. The residuals for PMTs reading A13 cell during individual years 2017 and 2018 is within $\pm$0.4% and for entire Run-2 is within $\pm$0.9% while the residuals of D0 cell for individual years range within $\pm$0.1% and for entire Run-2 is $\pm$0.5%. For the A13 cell as well as the D0 cell the goodness of fit χ^2/ndf is <1 for individual 2017, and 2018 data as well as the entire Run-2 period indicating that this model describes well the PMT response evolution.

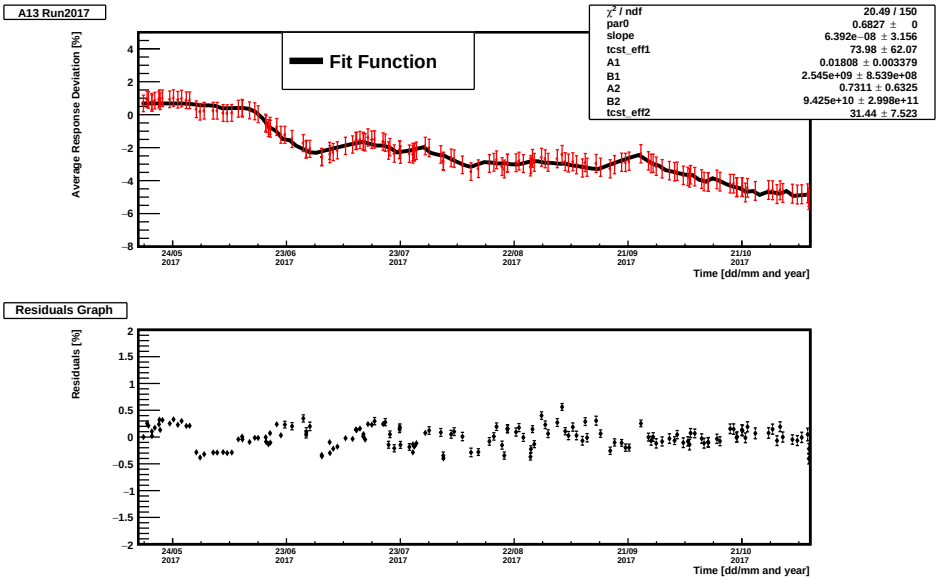

(a)

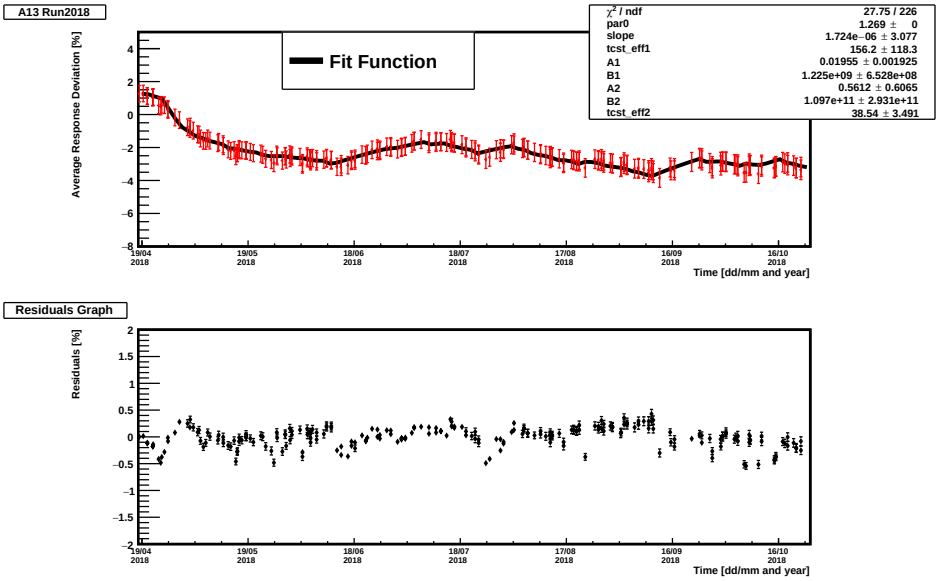

(b)

Figure 8.29: The figure shows the PMT response evolution of A13 cell modelled by luminosity convoluted function where down-drift per fill is defined as a function of tanh during the data-taking period of 2017(a) and 2018(b). The error bar on each data point corresponds to the total error including laser statistics as well as systematics for the corresponding calibration run. The figure at the bottom of (a) and (b) shows the residual values i.e., the difference between the laser data points and the corresponding fit function value.

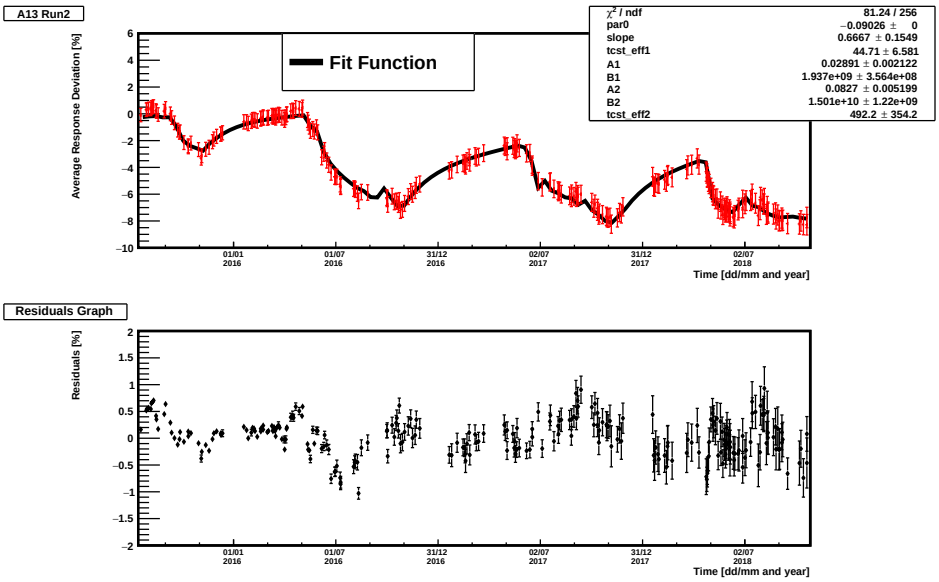

Figure 8.30: The top figure shows the PMT response evolution of A13 cell modelled by luminosity convoluted function where down-drift per fill is defined as a function of tanh. The error bar on each data point corresponds to the total error including laser statistics as well as systematics for the corresponding calibration run. The figure at the bottom shows the residual values i.e., the difference between the laser data points and the corresponding fit function value. This figure corresponds to the entire Run-2 data-taking period.

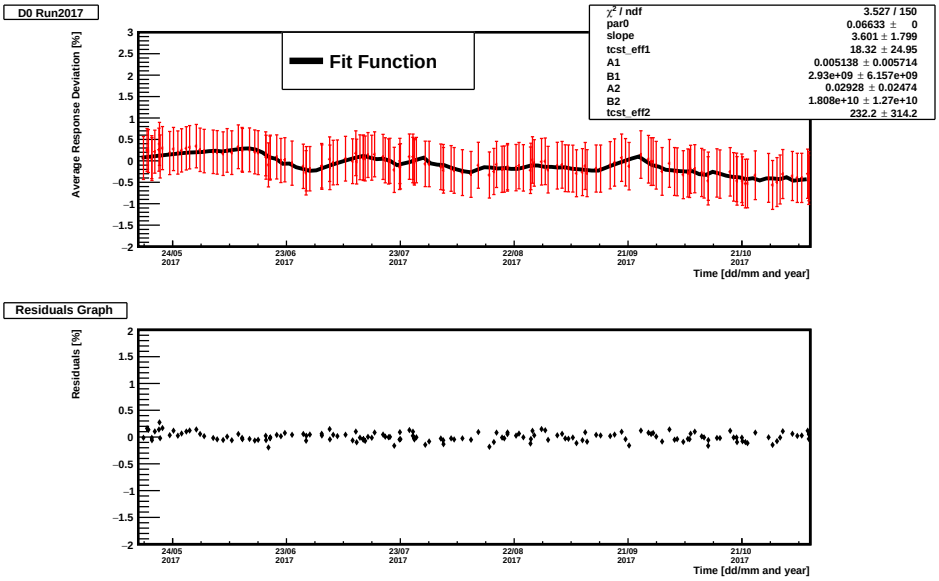

(a)

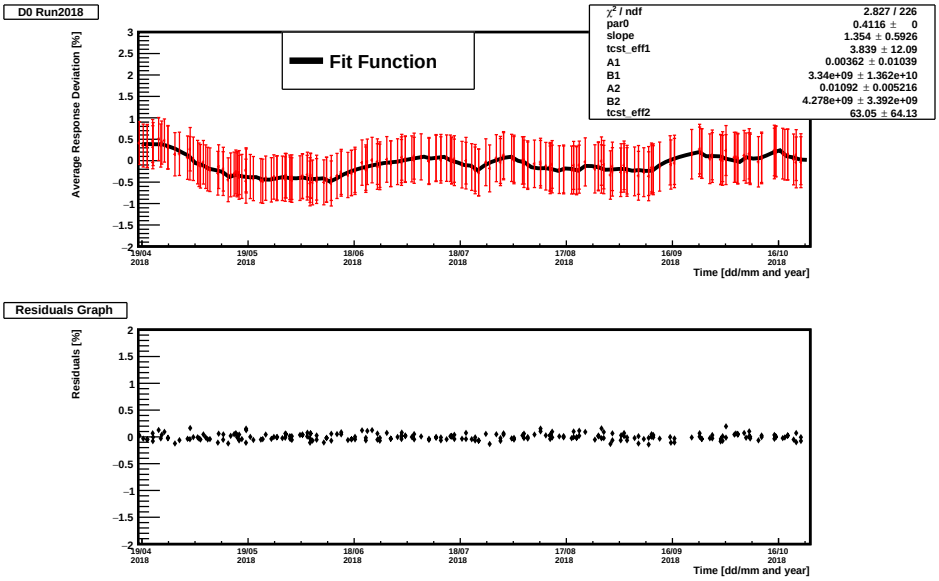

(b)

Figure 8.31: The figure shows the PMT response evolution of D0 cell modelled by luminosity convoluted function where down-drift per fill is defined as a function of tanh during the data-taking period of 2017(a) and 2018(b). The error bar on each data point corresponds to the total error including laser statistics as well as systematics for the corresponding calibration run. The figure at the bottom of (a) and (b) shows the residual values i.e., the difference between the laser data points and the corresponding fit function value.

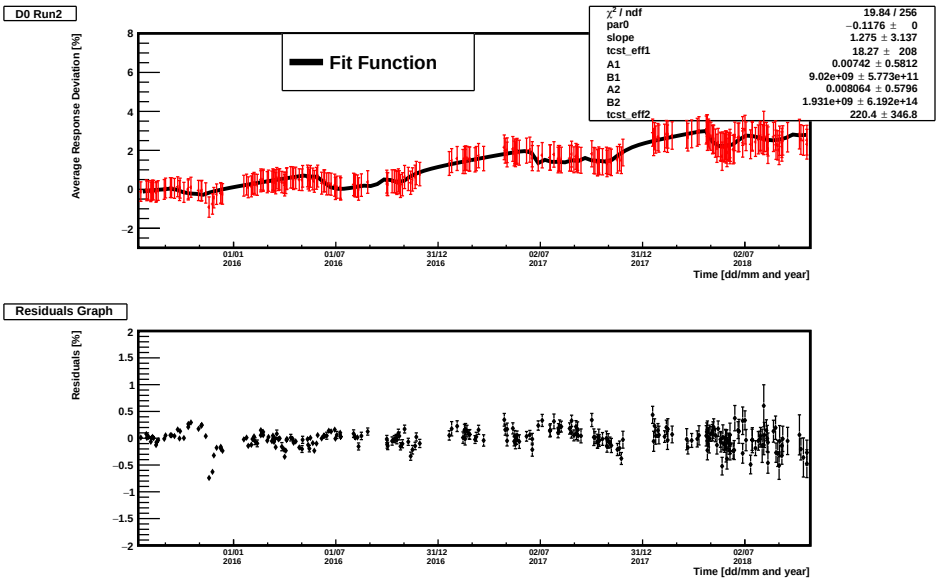

Figure 8.32: The top figure shows the PMT response evolution of D0 cell modelled by luminosity convoluted function where down-drift per fill is defined as a function of tanh. The error bar on each data point corresponds to the total error including laser statistics as well as systematics for the corresponding calibration run. The figure at the bottom shows the residual values i.e., the difference between the laser data points and the corresponding fit function value. This figure corresponds to the entire Run-2 data-taking period.

Fitting with minuit

The output fit parameters of eff_1 and eff_2 of the luminosity convoluted model, correspond to different processes. To allow more freedom to the fit parameters and the function, fit is also performed using Minuit (Function Minimization and Error Analysis) tool. Minuit is a tool that uses either chi-square or log-likelihood functions to compute the best values of output fit parameters and their uncertainties, including correlation between the parameters Ref [51]. Fit using luminosity convoluted superfunction as discussed in subsection 8.3.3 was performed with Minuit using chi-square minimization by the method of MIGRAD. MIGRAD is the most efficient and reliable method to perform the minimization of a function Ref [51]. The fitting was performed for all the cells during the entire Run-2 period. In this section, the fit results of the PMTs reading cells from each of the three longitudinal layers (A, BC, D) and E2-, E4-cells are shown using the Minuit tool.

Using the Minuit tool the quality of the fit gets better giving reasonable values of fit parameters. In general, the residuals for PMTs reading cells of the D layer, BC layer, and LB-A range less than $\pm 0.8\%$, while for PMTs reading cells of AEB is within $\pm 1\%$. For E cells which are the most exposed cells of TileCal and also they have less laser systematics (since each E cell is readout by only one PMT), they give larger residual values $\pm 1.5\%$ as compared with other cells.
In all the shown figures 8.33, 8.34, 8.35 and 8.36 during each luminosity fill a PMT down-drift resulting decrease in the efficiency of a PMT, where efficiency decrease of a PMT per luminosity fill is defined by luminosity convoluted tangent hyperbolic function 8.14. The efficiency function gives fit parameters A and B corresponding to two different efficiencies. In between the two luminosity fills when a PMT up-drifts, the efficiency of the PMT recovers exponentially 8.17 giving characteristic time parameter. The following figures show the different fit parameter values for each cell type during the entire Run-2 period.

Figure 8.37 shows the values of fit parameter slope on the y-axis (in % per year) for all the cells shown along the x-axis during the entire Run-2 period. As the slope parameter defines the up-drift of the PMTs, the D cells which are least exposed to the beam give a maximum value of slope ($\approx 0.9\%$ per year). While the slope is minimum for the most exposed cells (E cells and A13cell $\approx 0.1\%$ per year) with some discrepancies.

Figure 8.38 shows the exponential characteristic time parameters (τ_1 and τ_2) for the two efficiencies over entire Run-2 period. For E cells the characteristic time is larger ($\tau_1 \approx$ 70-85 days and $\tau_2 \approx$ 400-500 days). For other cells τ_1 range within $\approx 40 - 60$ days while

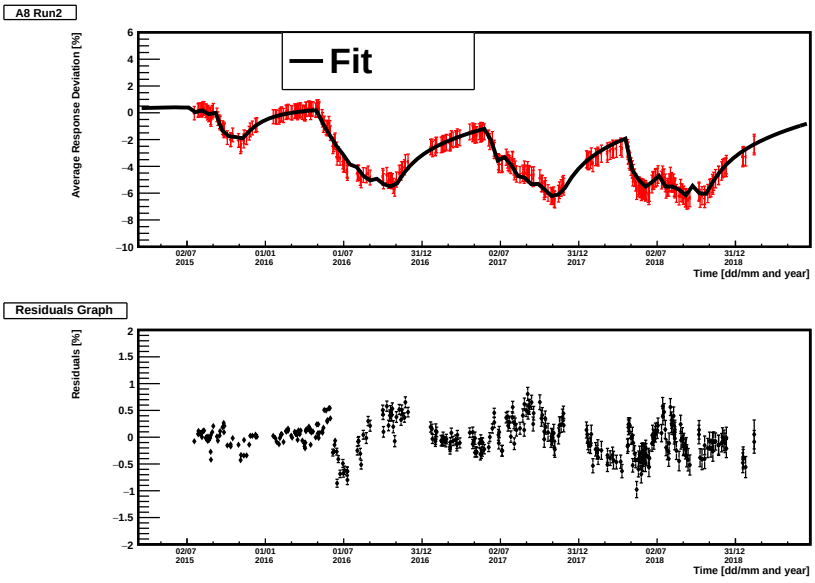

(a)

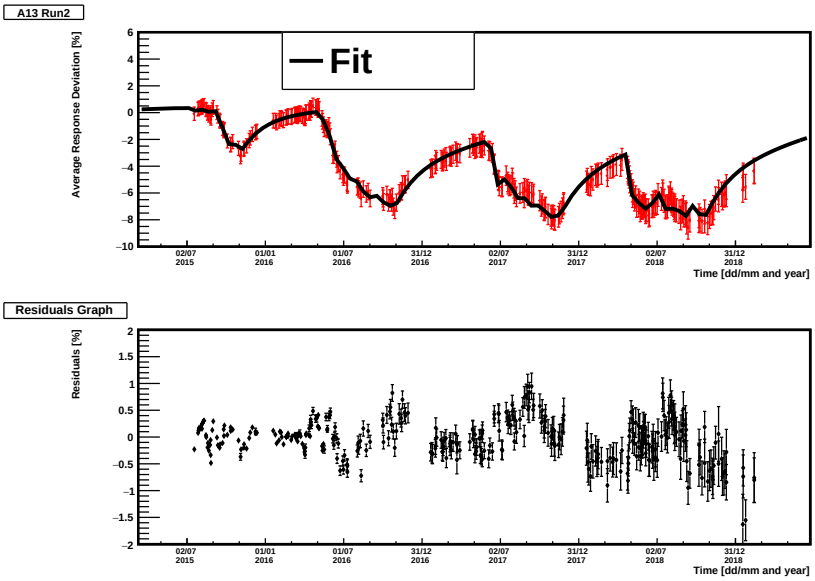

(b)

Figure 8.33: The luminosity convoluted fit function applied to the mean response variation in the PMTs reading (a) A8 cell and A13 cell(b) to the entire Run-2 laser data using miniut. Each red point corresponds to laser data that has been normalized to the beginning of $pp-$collisions in 2015 (around 17 July 2015). The error bar on each data point corresponds to the total error including laser statistics as well as systematics for the corresponding calibration run. The applied fit function is represented by the black line. Down-drift periods are defined by tangent hyperbola function while the PMTs recover exponentially with time. The bottom graph of both figures (a) and (b) show the residuals between the laser data point and the corresponding fit result.

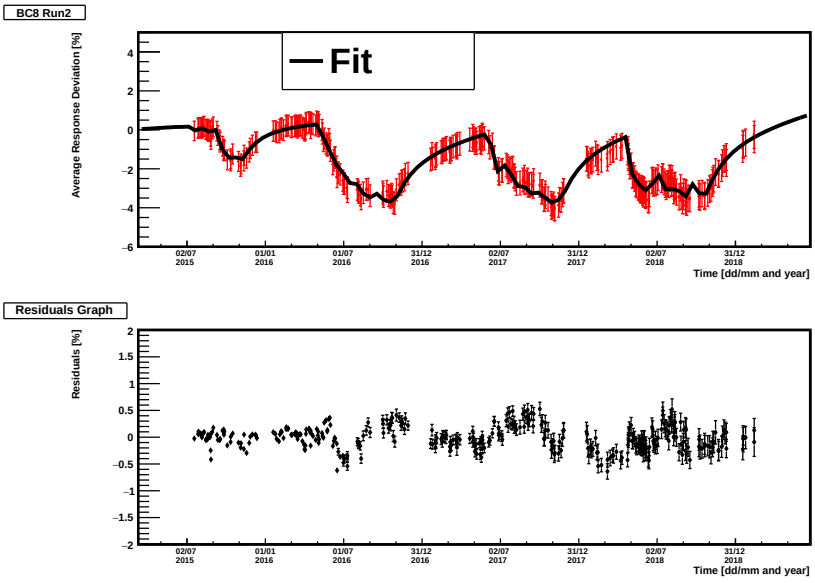

(a)

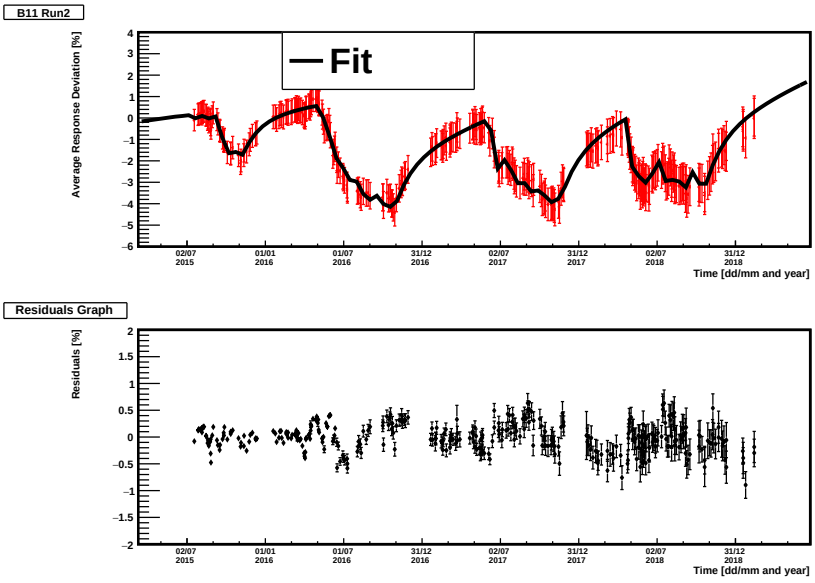

(b)

Figure 8.34: The luminosity convoluted fit function applied to the mean response variation in the PMTs reading (a) BC8 cell and B11 cell(b) to the entire Run-2 laser data using miniut. Each red point corresponds to laser data that has been normalized to the beginning of $pp-$collisions in 2015 (around 17 July 2015). The error bar on each data point corresponds to the total error including laser statistics as well as systematics for the corresponding calibration run. The applied fit function is represented by the black line. Down-drift periods are defined by tangent hyperbola function while the PMTs recover exponentially with time. The bottom graph of both figures (a) and (b) show the residuals between the laser data point and the corresponding fit result.

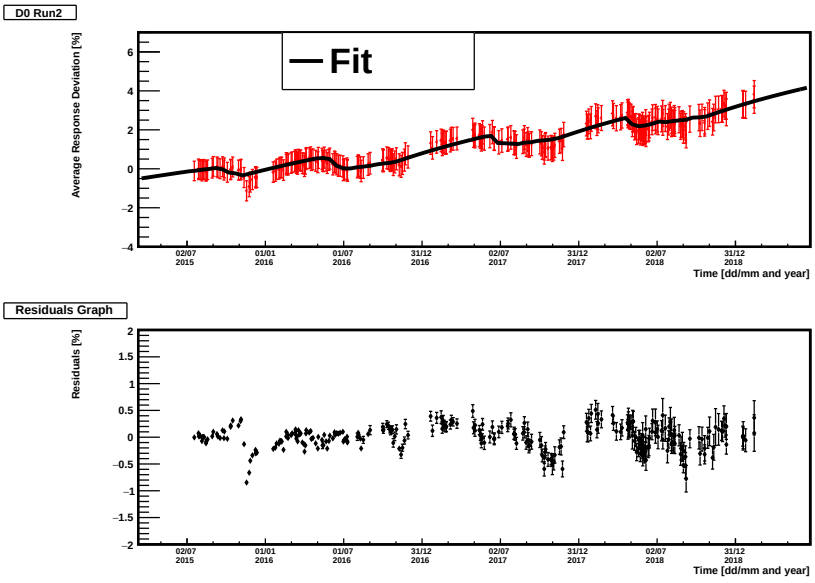

(a)

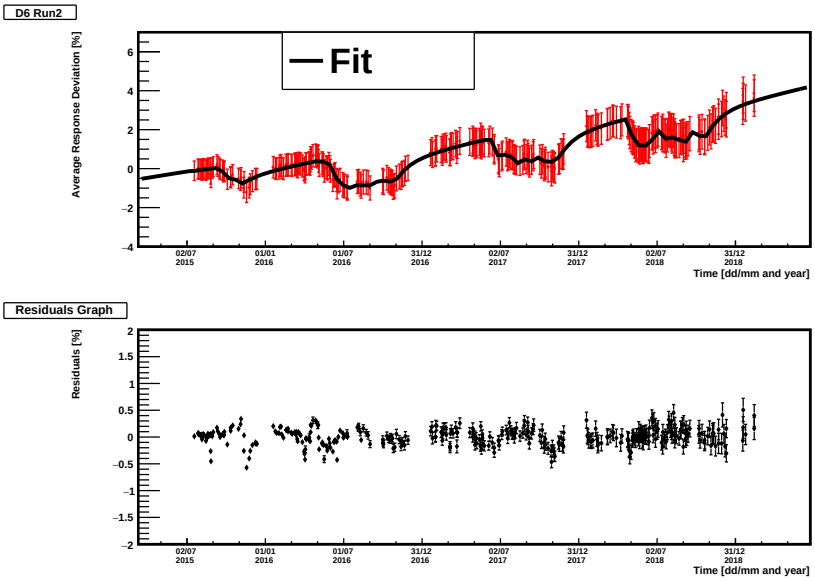

(b)

Figure 8.35: The luminosity convoluted fit function applied to the mean response variation in the PMTs reading (a) D0 cell and D6 cell(b) to the entire Run-2 laser data using miniut. Each red point corresponds to laser data that has been normalized to the beginning of $pp-$collisions in 2015 (around 17 July 2015). The error bar on each data point corresponds to the total error including laser statistics as well as systematics for the corresponding calibration run. The applied fit function is represented by the black line. Down-drift periods are defined by tangent hyperbola function while the PMTs recover exponentially with time. The bottom graph of both figures (a) and (b) show the residuals between the laser data point and the corresponding fit result.

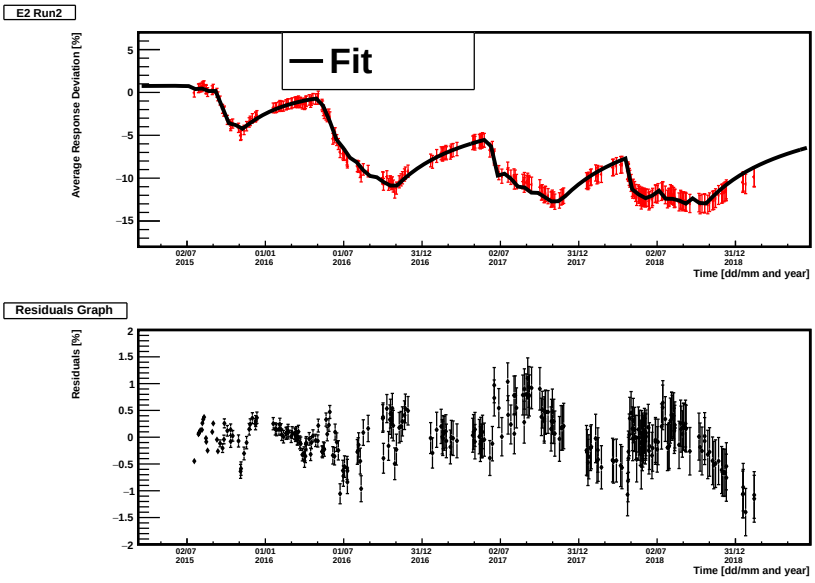

(a)

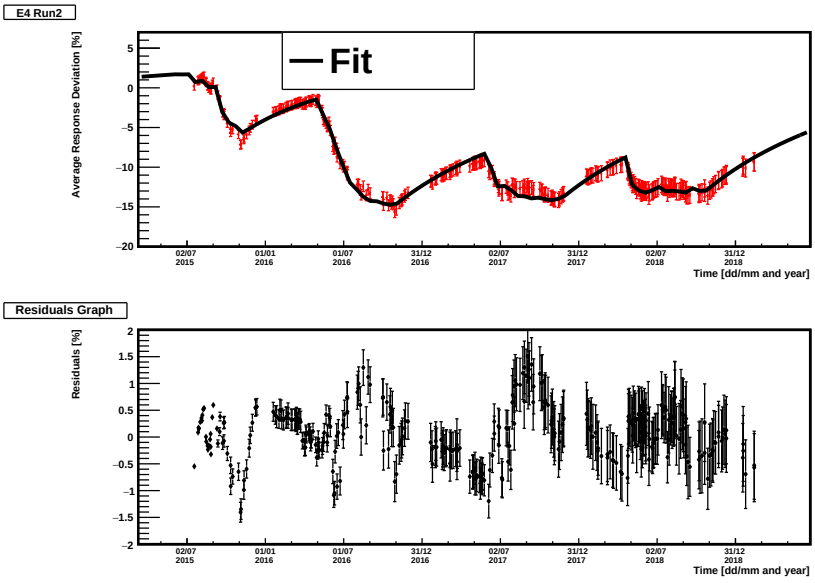

(b)

Figure 8.36: The luminosity convoluted fit function applied to the mean response variation in the PMTs reading (a) E2 cell and E4 cell(b) to the entire Run-2 laser data using miniut. Each red point corresponds to laser data that has been normalized to the beginning of $pp-$collisions in 2015 (around 17 July 2015). The error bar on each data point corresponds to the total error including laser statistics as well as systematics for the corresponding calibration run. The applied fit function is represented by the black line. Down-drift periods are defined by tangent hyperbola function while the PMTs recover exponentially with time. The bottom graph of both figures (a) and (b) show the residuals between the laser data point and the corresponding fit result.

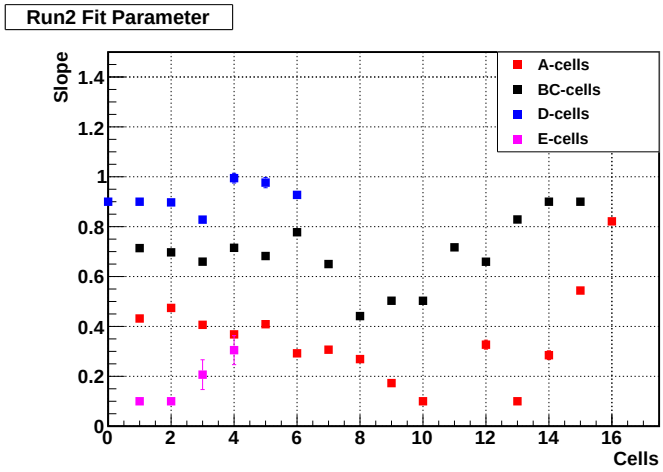

Figure 8.37: The output fit parameter slope per year [in %] for A cells (red), BC cells (black), D cells (blue) and E cells (magenta) using luminosity convoluted function over entire Run-2 data. For each cell, the error bars correspond to the uncertainties of the output fit parameter.

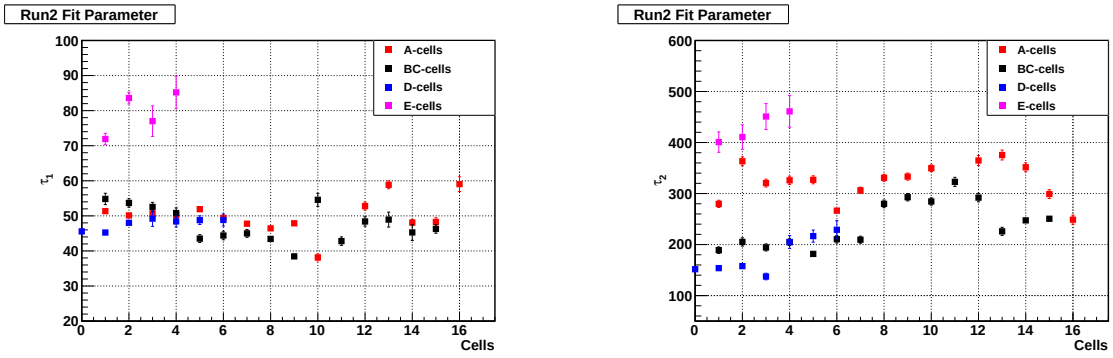

Figure 8.38: The output fit parameter time constant τ_1 (left) and τ_2 (right) [in days] for A cells (red), BC cells (black), D cells (blue) and E cells (magenta) using luminosity convoluted function over entire Run-2 data. For each cell, the error bars correspond to the uncertainties of the output fit parameter.

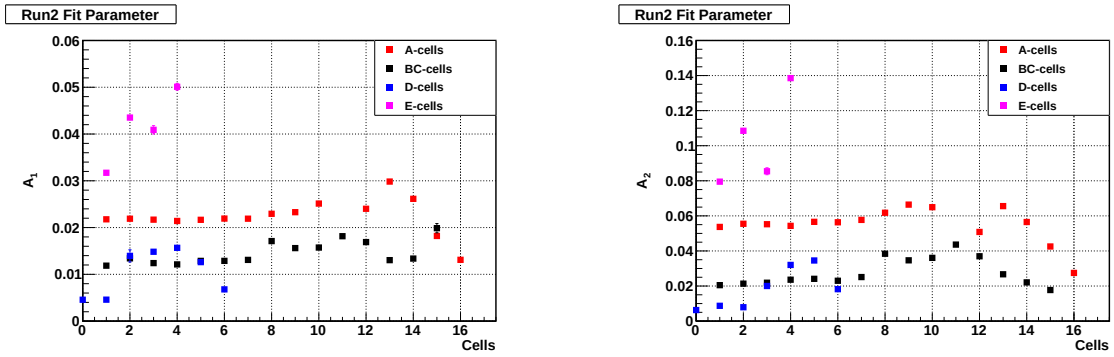

Figure 8.39: The output fit parameter A_1 (left) and A_2 (right) for A cells (red), BC cells (black), D cells (blue) and E cells (magenta) using luminosity convoluted function over entire Run-2 data. For each cell, the error bars correspond to the uncertainties of the output fit parameter.

the τ_2 values are randomly distributed.

Figure 8.39 shows the distribution of fit parameters A_1 and A_2 for each cell over entire Run-2 period. As already discussed the parameter A is sensitive to the loss in the efficiency of a PMT during pp-collision periods, the PMTs which are close to the beam interaction point are more prone to rapid efficiency loss than the other PMTs which are less exposed. Thus the loss in efficiency is least for the PMT's reading D cells (A_1 around 1% and A_2 around 2%) and maximum for the PMT's reading E cells and more exposed A cells. In E cells the maximum loss in efficiency is observed in E4-cell which has a loss of $\approx 5\%$ in A_1 and $\approx 14\%$ in A_2 parameter. For A cells, PMTs reading A13 cell loses more efficiency with values of $\approx 3\%$ in A_1 and $\approx 7\%$ in A_2 parameter.

Figure 8.40 shows the B_1 and B_2 parameters of all the cells during Run-2 period. The B parameter defines the sensitivity to the luminosity increment. In the figure showing the B_1 parameter, the parameter gives higher values for the cells which accumulate more anode current. But the B_2 parameter follows the opposite of this trend giving higher values for the PMTs which are less exposed to the beam. This indicates that with the increase in luminosity, the PMTs become less sensitive to the luminosity increment, and at some point, they stop drifting. However few discrepancies in the output parameters are observed for some cells.

In general, the luminosity convoluted superfunction works well in explaining the response

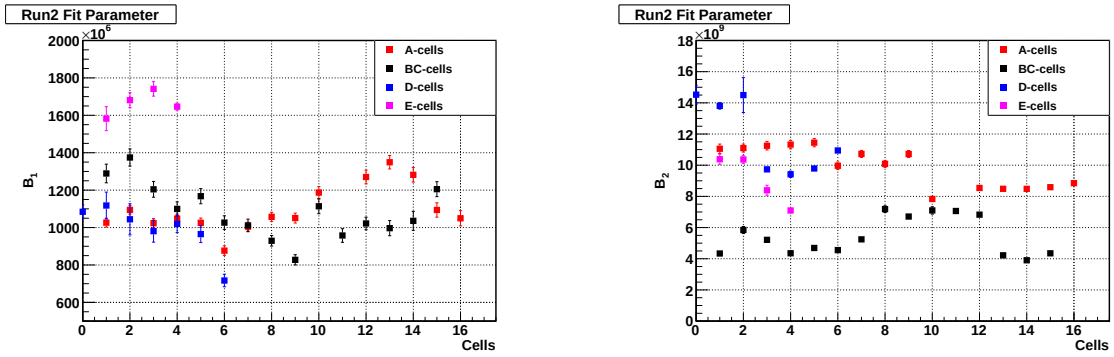

Figure 8.40: The output fit parameter B_1 (left) and B_2 (right) for A cells (red), BC cells (black), D cells (blue) and E cells (magenta) using luminosity convoluted function over entire Run-2 data. For each cell, the error bars correspond to the uncertainties of the output fit parameter.

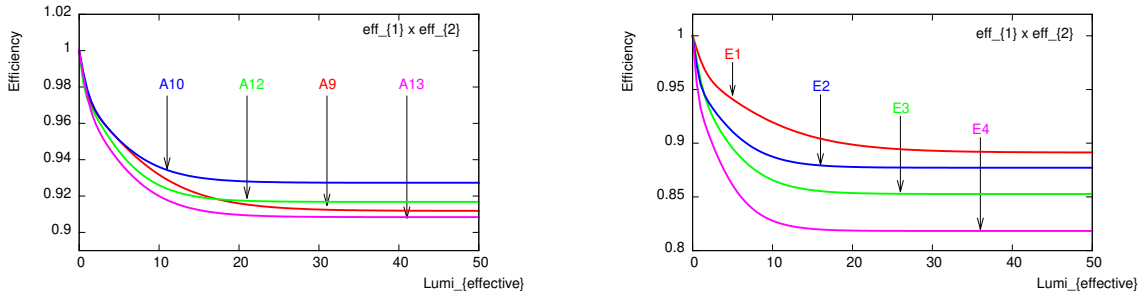

Figure 8.41: Loss in the efficiency of PMT versus effective luminosity during Run-2 of more exposed A cells (left) and E cells (right). Each line corresponds to the product of the two efficiency functions ($eff_1 \times eff_2$) of a particular cell.

loss of a PMT which is crucial in deciding the PMTs to replace in the future when LHC will deliver much higher integrated luminosity than Run-2. The maximum loss in the efficiency (or gain) of PMTs reading A cells and E cells observed with fit results is shown in Figure 8.41

From this Figure 8.41 it can be seen that during Run-2 E4 cell losses about $\approx 17\%$ of the efficiency of the PMT while the A13 cell losses about $\approx 10\%$. With the results of this model, it is also possible to predict the future PMT response during Run-3 and Run-4.

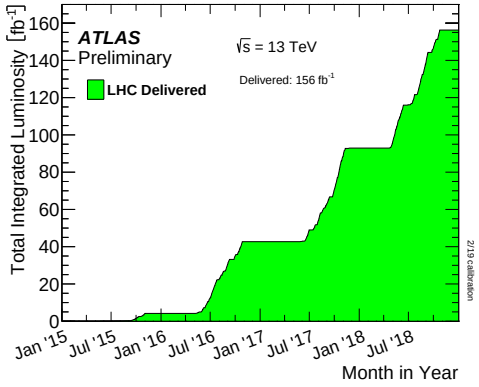

Figure 8.42: Total luminosity delivered to ATLAS versus time during stable beams for *pp* collisions periods of 2015-2018 at 13 TeV center-of-mass energy. Figure is taken from Ref [7].

8.4 Long term extrapolations from Run-2

All the results shown in Section 8.3.3 show that the PMT response over the entire Run-2 period can be well explained by luminosity convoluted superfunction. As discussed earlier in Section 8.3 one of the motivations to study PMT response evolution modelling is that it provides an important tool to predict the PMT response evolution in the future. The obtained results of Run-2 are projected to predict the PMT response during Run-3 and Run-4 periods.
During LHC Run-2 about $\approx 156 fb^{-1}$ is delivered 8.42 during stable beams for *pp* collisions at 13 TeV centre-of-mass energy Ref [7].

After the second long shutdown (LS2) period the long-term planning of LHC anticipates delivering about $\approx 275 fb^{-1}$ integrated luminosity during LHC Run-3 covering the collision period of 2022-2025. For Run-4 it is anticipated that LHC will deliver about 5 times $\approx 750 fb^{-1}$ the total delivered luminosity observed during LHC Run 2. Based on these predictions, a luminosity profile was made for Run-3 and Run-4. This profile contains a toy schedule with ramp-up, technical stops (TS), and EYETS. machine developments (MDs) and special physics run. Moreover, these profiles are created by assuming three runs per day during Run-3 and Run-4 stable beam periods. All these assumptions allow us to better compare the number of physics days and luminosity potential.

Figure 8.43 shows the predicted luminosity profiles of the ATLAS experiment during

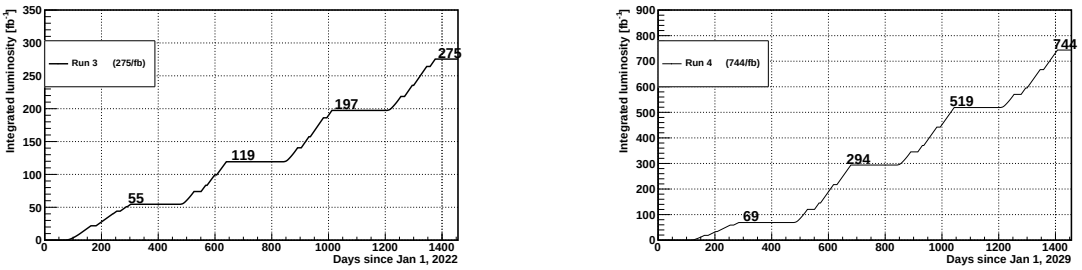

Figure 8.43: Total expected luminosity versus time to be delivered to ATLAS during Run-3 (left) and Run-4 (right) stable beams calculated using predicted luminosity profiles. Three runs per day are assumed in the predicted Run-3 and Run-4 profiles. For Run-3 60% efficiency is assumed for the year 2022 while for other years 100% efficiency is considered.

Run-3 and Run-4. As seen in the figures, during the first year of Run-3 total delivered luminosity is expected to be $\approx 55 fb^{-1}$ which is slightly less than the LHC delivered luminosity during 2018 ($\approx 63.3 fb^{-1}$). While during Run-4 it is anticipated to have more accumulated luminosity ($\approx 69 fb^{-1}$) than in 2018. As is already discussed that the change in luminosity affects the PMT response evolution. Based on these luminosity profiles the PMT response evolution is predicted for Run-3 and Run-4 using the fit results of luminosity convoluted superfunction.

8.4.1 Extrapolation from Run-2 to Run-3

The fit results of the entire Run-2 data using luminosity convoluted function were used to extrapolate the future PMT response during Run-3. The extrapolation was studied for all the PMTs reading all the cells of layers A, BC, D, and E. The extrapolated results of some TileCal cells are shown in this subsection. In all the figures down-drift corresponds to expected $pp-collision$ periods while the large up-drift corresponds to expected YETS. The quick up-drift periods can also be seen which occur during expected machine development and small technical stops within the same year.

Figure 8.44 shows the extrapolated results of PMTs reading A cells during Run-3 from Run-2 fit results. All the PMTs lose response during collision periods while they recover during technical stop periods. A13 cell is the most exposed and least stable cell of TileCal in the A layer and hence it experiences more loss in response than the rest of the cells. During Run-2 the observed maximum down-drift of A13 cell is $\approx 8.2\%$ while from Run-3

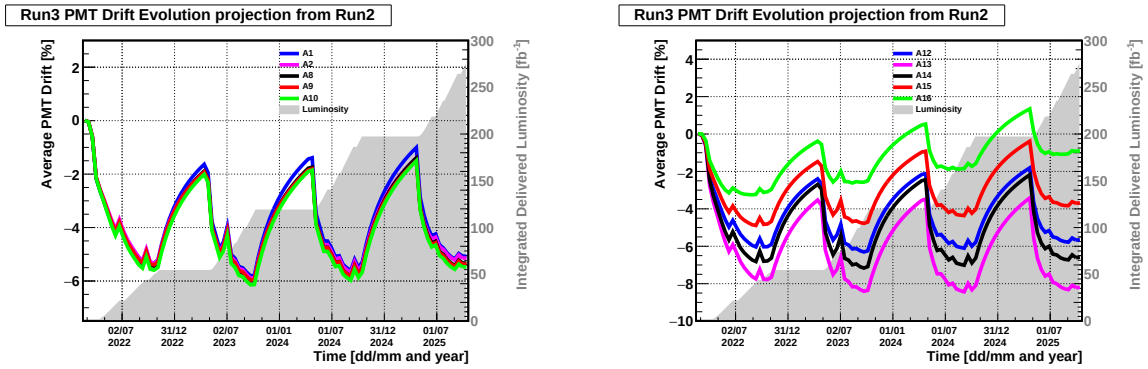

Figure 8.44: Expected average PMT response variation [%] versus time shown for the PMTs reading A1, A2, A8, A9 and A10 cell of ALB (left) and the PMT reading cells of AEB region (right) during anticipated Run-3 collision period. The response evolution of each PMT is normalized to the expected first day of data taking. Integrated delivered luminosity is shown for comparison.

extrapolated results it is $\approx 8.5\%$ with a difference of about 0.3%. The cells of the LB-A region are less exposed to the beam as compared to the cells of EB-A, hence less down-drift is expected in these cells with a maximum down-drift of $\approx 6.2\%$ in the A10 cell. For most of the A cells, the maximum down-drift is expected during the second year of data taking in Run-3 with an expected integrated luminosity of $\approx 119 fb^{-1}$. While during Run-2 the maximum down-drift in most of the A cells is observed in 2018 with an integrated luminosity of $\approx 63.3 fb^{-1}$. This indicates that the PMTs reading A cells start saturating after $\approx 63.3 fb^{-1}$ delivered luminosity.

Figure 8.45 shows the extrapolated results of PMTs reading BC cells during Run-3 from Run-2 fit results. As BC cells are sandwiched between A cells and D cells, they are relatively more stable than the A cells. During Run-2 for most of the BC cells, the maximum down-drift is seen during 2017 pp-collisions with integrated luminosity $\approx 50.2\% fb^{-1}$. While with extrapolated Run-3 drifts, the PMTs reading BC cells start saturating during the 2022 data-taking period with $\approx 55 fb^{-1}$ expected luminosity. From 2022 to 2023 a very small drift of about $\pm 0.1\%$ is expected. The expected maximum down-drift of BC8 and B11 cells during Run-3 is $\approx 4.2\%$ and $\approx 5\%$ respectively while during Run-2 the maximum observed down-drift for these cells is$\approx 4\%$ and $\approx 4.8\%$ respectively.

The Run-3 extrapolated results of the most stable cells i.e., D cells are shown in

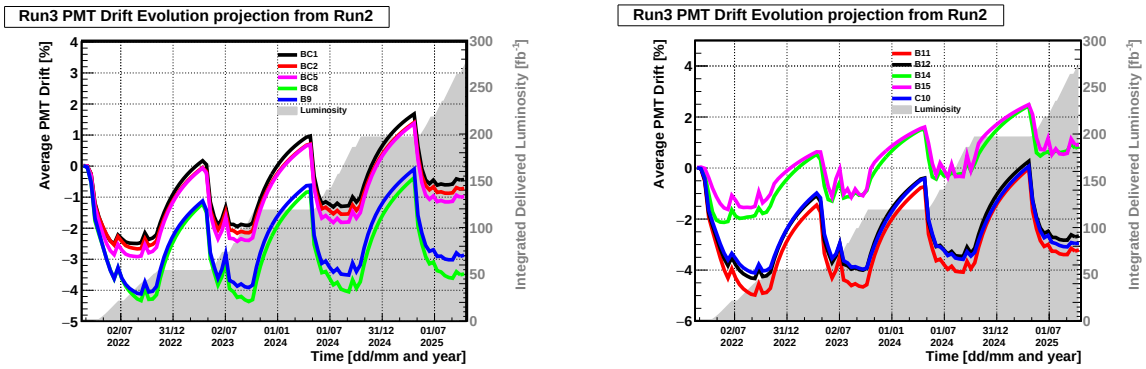

Figure 8.45: Expected average PMT response variation [%] versus time shown for the PMTs reading BC1, BC2, BC5, BC8 and B9 cell of LB-BC (left) and the PMT reading B11, B12, B14, B15 and C10 cells of EB-BC region (right) during anticipated Run-3 collision period. The response evolution of each PMT is normalized to the expected first day of data taking. Integrated delivered luminosity is shown for comparison.

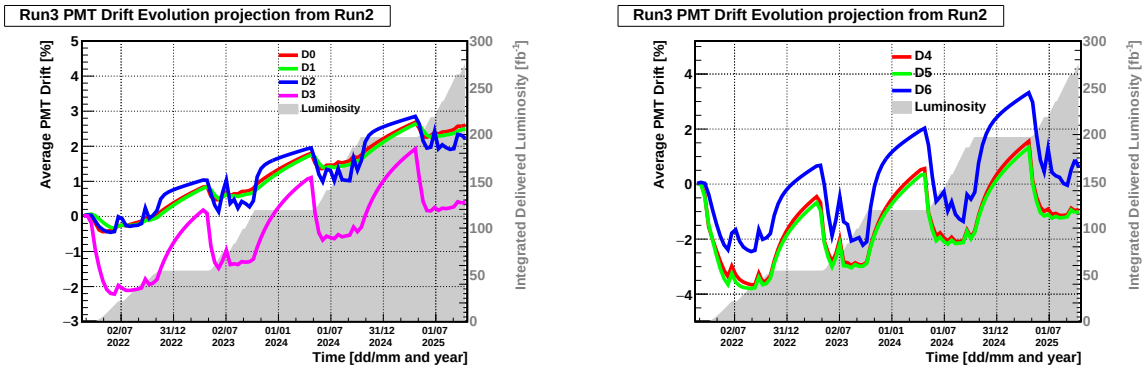

Figure 8.46: Expected average PMT response variation [%] versus time shown for the PMTs reading LB-D (left) and the PMT reading cells of EB-D region (right) during the anticipated Run-3 collision period. D cells are the most stable cells of TileCal. The response evolution of each cell is normalized to the expected first day of data taking. Integrated delivered luminosity is shown for comparison.

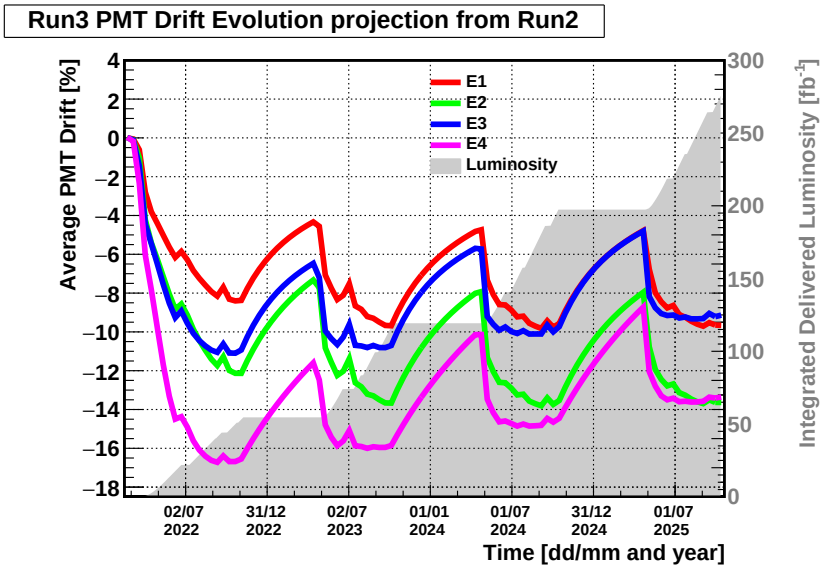

Figure 8.47: Expected average PMT response variation [%] versus time shown for the PMTs reading the E cells during the anticipated Run-3 collision period. E cells are the most unstable cells of TileCal. The response evolution of each cell is normalized to the expected first day of data taking. Integrated delivered luminosity is shown for comparison.

Figure 8.46. At the end of Run-2, an up-drift of about $\approx 2.2\%$ and $\approx 2\%$ is observed for D0 and D6 cells while at the end of Run-3 an up-drift of $\approx 2.5\%$ and $\approx 1\%$ is expected for the same cell types.

8.47 shows the Run-3 extrapolation of E cells which are the most exposed and hence the least stable cells of the TileCal. For E4 cell a maximum down-drift of about $\approx 17\%$ is expected during the first year of Run-3 data taking which is almost the same as observed during the Run-2 period.

8.4.2 Extrapolation from Run-2 to Run-4

The Run-2 fit results of luminosity convoluted superfunction are also projected to predict the behaviour of PMTs during the expected Run-4 data-taking period. The expected integrated luminosity during Run-4 is almost five times more than the delivered luminosity during Run-2. Due to such higher integrated luminosity, the predicted PMTs' response reaches their saturation point very early and stays there for the rest of the Run-4 period. Figures 8.48, 8.49, 8.50 and 8.51 are the extrapolated average PMT response variation over

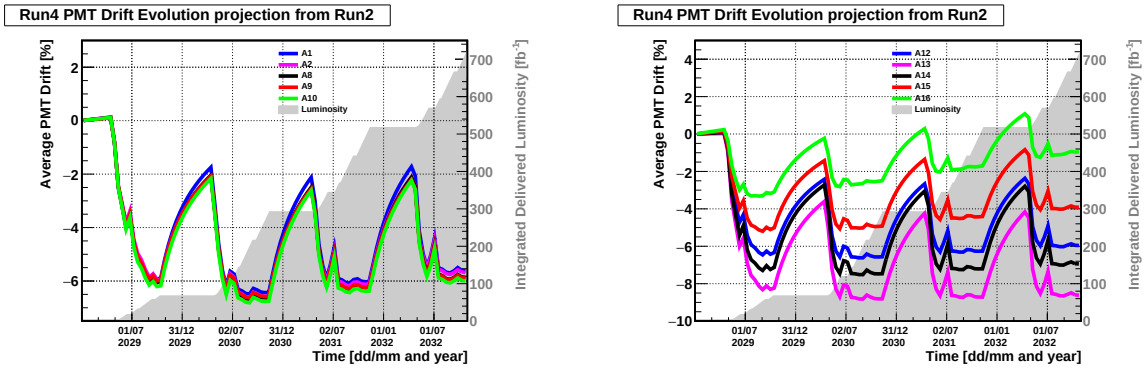

Figure 8.48: Expected average PMT response variation [%] versus time shown for the PMTs reading A1, A2, A8, A9 and A10 cell of LB-A (left) and the PMT reading cells of EB-A region (right) during anticipated Run-4 collision period. The response evolution of each PMT is normalized to the expected first day of data taking. Integrated delivered luminosity is shown for comparison.

entire Run-4 $pp-collision$ period for A , BC, D and E cells respectively.

During the Run-4 period, for A cells maximum down-drift is expected to achieve during the second year of data taking at an integrated luminosity of $\approx 294 fb^{-1}$, while for BC cells and E cells the maximum down-drift is expected during the first year of data taking at an integrated luminosity of $\approx 69 fb^{-1}$.
The observed maximum down-drift of the most stable and least stable PMTs during Run-2 and the expected maximum drift during Run-3 and Run-4 are shown in the table 8.7.

The extrapolation of fit results to predict the average PMT drift for all cells during Run-3 and Run-4 are compatible with observed PMT behaviour during the Run-2 period.

8.4.3 Extrapolation from Run 2015-2017 to entire Run-2

In order to cross-check the luminosity convoluted fit function and reliability of extrapolated results obtained for Run-3 and Run-4, a cross-check was performed. For cross-checking, a backtest has been performed using the luminosity convoluted fit function applied to the 2015-2017 data of the Run-2 period. The obtained fit results of 2015-2017 data are used to extrapolate the average PMT drift during the entire Run-2 (2015-2018) period. The extrapolated results are then compared with the laser Run-2 data.

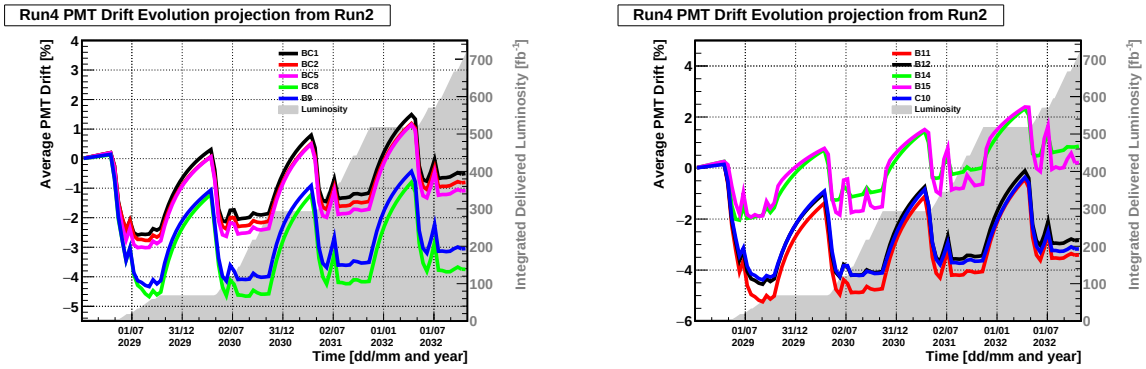

Figure 8.49: Expected average PMT response variation [%] versus time shown for the PMTs reading BC1, BC2, BC5, BC8 and B9 cell of LB-BC (left) and the PMT reading B11, B12, B14, B15 and C10 cells of EB-BC region (right) during anticipated Run-4 collision period. The response evolution of each PMT is normalized to the expected first day of data taking. Integrated delivered luminosity is shown for comparison.

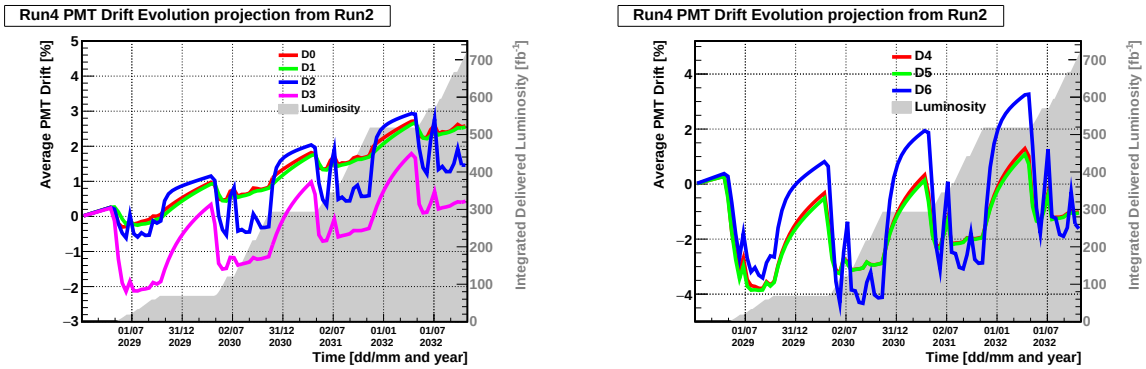

Figure 8.50: Expected average PMT response variation [%] versus time shown for the PMTs reading LB-D (left) and the PMT reading cells of EB-D region (right) during the anticipated Run-4 collision period. D cells are the most stable cells of TileCal. The response evolution of each cell is normalized to the expected first day of data taking. Integrated delivered luminosity is shown for comparison.

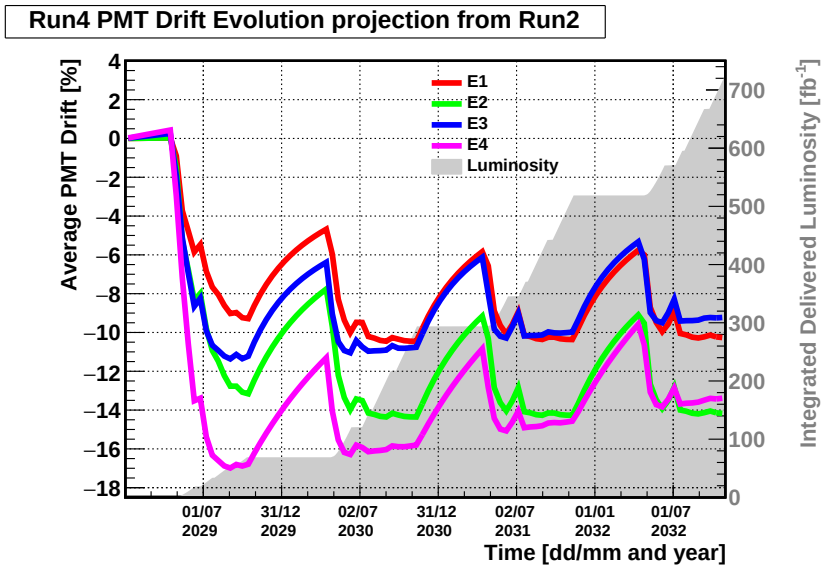

Figure 8.51: Expected average PMT response variation [%] versus time shown for the PMTs reading the E cells during the anticipated Run-4 collision period. E cells are the most unstable cells of TileCal. The response evolution of each cell is normalized to the expected first day of data taking. Integrated delivered luminosity is shown for comparison.

Cell	Run-2	Run-3	Run-4
A8	5.7%	6%	6.8%
A13	8.2%	8.5%	9%
BC8	3.8%	4.3%	4.9%
B11	4%	5%	5.3%
D0	0.5%	0.5%	0.4%
D6	0.7%	2%	4.5%
E2	13.8%	14%	14.4%
E4	16%	17%	17%

Table 8.7: This table enlists the approximate values of maximum down-drift (in %) for some cells observed during the Run-2 collision period and expected during Run-3 and Run-4 collisions. The Run-3 and Run-4 expected values are extrapolated results obtained from Run-2 fit results.

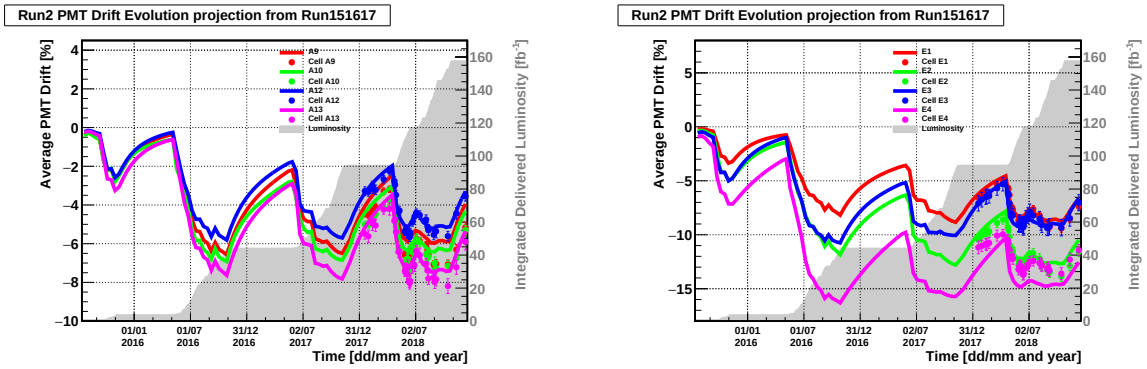

Figure 8.52: Average PMT response variation [%] versus time shown for the PMTs reading most exposed A cells (left) and the PMT reading cells of E cells (right) during the entire Run-2 period extrapolated from 2015-2017 fit data. The response evolution of each cell is normalized to an expected first laser data point. Each point shows the laser calibration data of a particular cell during 2018. Integrated delivered luminosity is shown for comparison.

Figures 8.52 shows the Run-2 extrapolation from fit results of 2015-2017 data. The observed maximum down-drift and the predicted maximum down-drift for all cells are consistent. For each cell, the 2018 laser calibration data is shown for comparison. For most cells, the calibration data and extrapolated data of 2018 agree within ±1%. This comparison can be clearly seen in Figures 8.53 and 8.54 for A and E cells, respectively.

Figures 8.53 and 8.54 shows the comparison of extrapolated function of A10, A13 and E2, E4 cells with laser calibration data. The residuals for all cells range within ±1%. Thus the prediction for 2018 using fit results of 2015-2017 agrees with measured drift within ±1%. This indicates that the luminosity convoluted fit function works well to explain the PMT response evolution.

The extrapolated results are also helpful in determining the PMTs which should be replaced for High luminosity LHC (HL-LHC). Further details about the replacement and testing of the PMTs are discussed in the next Chapter 9.

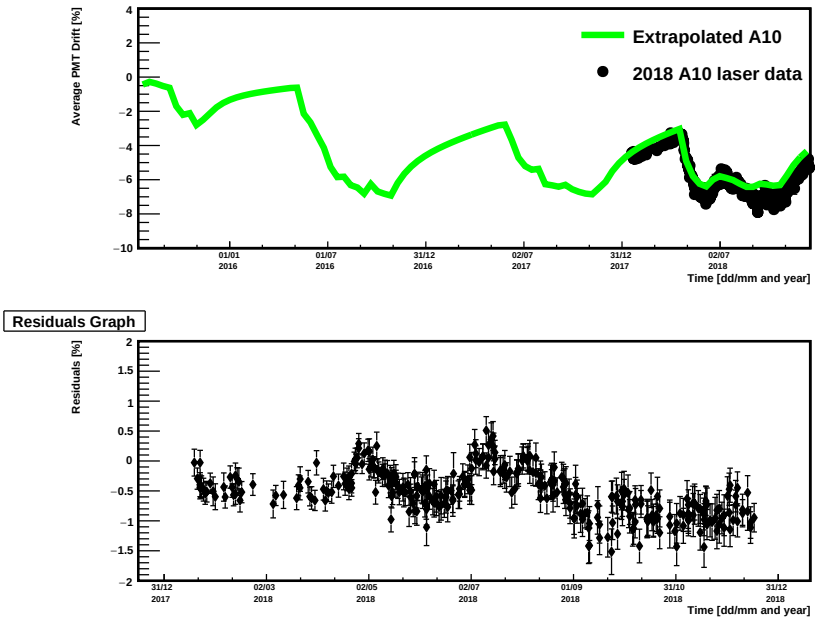

(a)

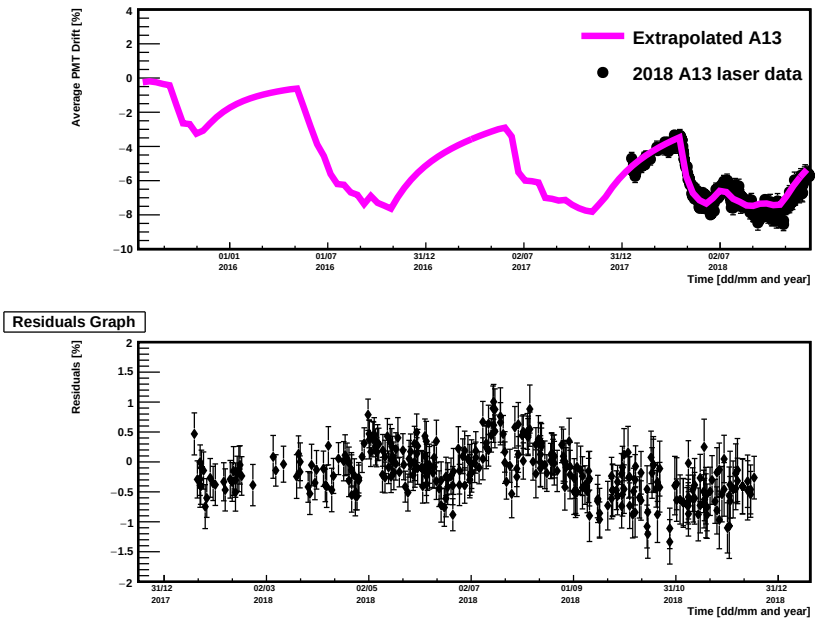

(b)

Figure 8.53: Extrapolation of the luminosity convoluted fit function applied to the mean response variation in the PMTs reading (a) A10 cell and A13 cell (b) to the entire 2015-2017 laser data using miniut. Each point has been normalized to the beginning of $pp-$collisions in 2015 (around 17 July 2015). The black points correspond to the 2018 laser calibration data and are shown for comparison with the extrapolated function. The bottom graph of both figures (a) and (b) show the residuals between the 2018 laser data point and the corresponding extrapolated function.

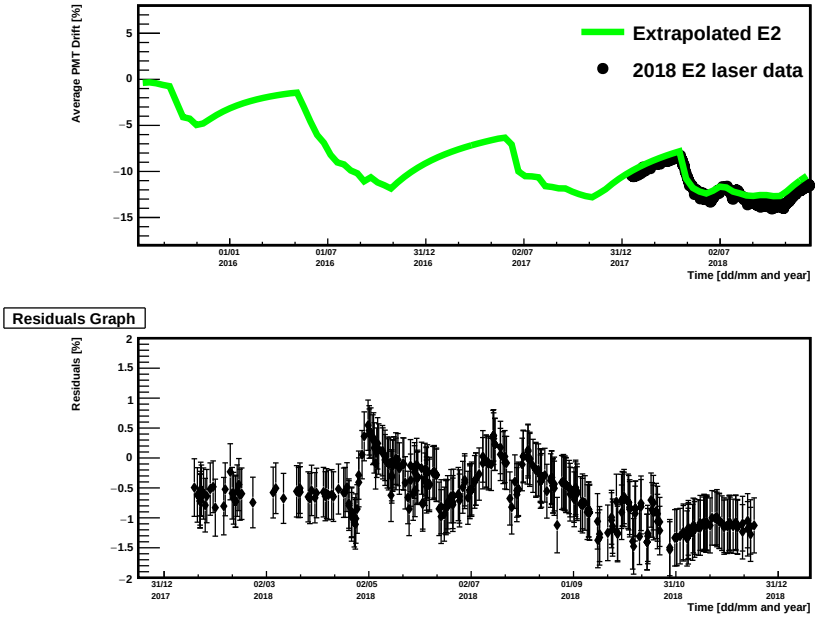

(a)

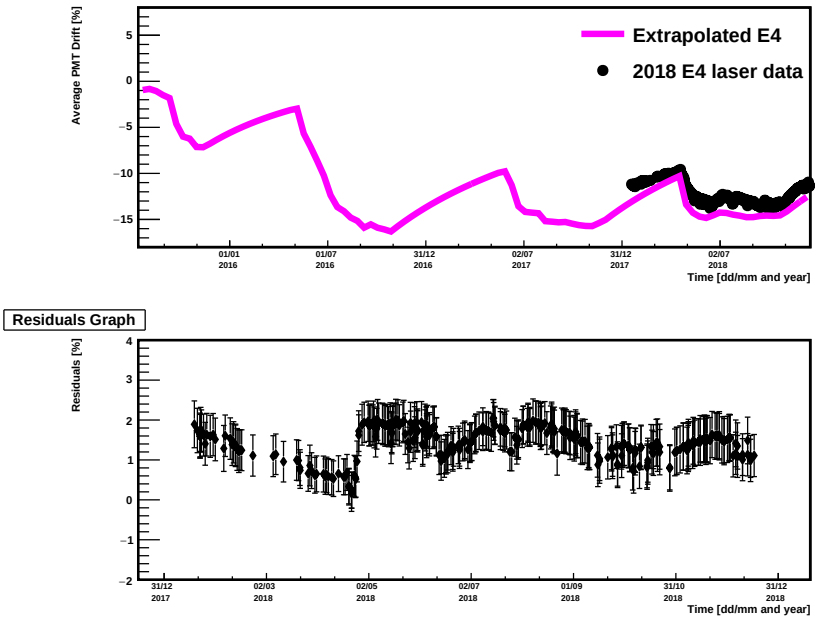

(b)

Figure 8.54: Extrapolation of the luminosity convoluted fit function applied to the mean response variation in the PMTs reading (a) E2 cell and E4 cell (b) to the entire 2015-2017 laser data using miniut. Each point has been normalized to the beginning of $pp-$collisions in 2015 (around 17 July 2015). The black points correspond to the 2018 laser calibration data and are shown for comparison with the extrapolated function. The bottom graph of both figures (a) and (b) show the residuals between the 2018 laser data point and the corresponding extrapolated function.

Chapter 9

TileCal photomultipliers test bench

9.1 Introduction

The ATLAS Tile Calorimeter is equipped with 9,852 photomultiplier tubes (PMTs) of type R7877 from HAMAMATSU PHOTONICS [38]. 10,140 PMTs were produced and delivered from 2000-2002, have been mounted in the TileCal detector during the preparation of the ATLAS detector for the LHC Run-1 from 2004-2008, and have been operating for the ATLAS data taking during LHC Run-1 and Run-2 until 2018.
The experience gained in operating the TileCal detector during Run-1 and Run-2 and the results of monitoring procedures made it possible to model the time evolution of the PMT response as described in Chapter 9. An estimation of the response loss at the end of High Luminosity LHC (HL-LHC) was derived as a function of PMT integrated anode charge and extrapolation results shown in Sec 8.4. Based on the estimation it was decided to replace ≈1024 most exposed PMTs reading the A-cells (A10, A12, A13, and A14) before the beginning of the Run-4 operation. Both new and old PMTs have to be tested against standard characteristics to eliminate those that do not qualify for the standard requirements. In the past test benches for the PMT, qualifications have been operational in Clermont-Ferrand, Dubna, Lisbon, Pisa, Valencia, and the University of Illinois. In order to test these photomultiplier tubes, three identical and fully automatic test benches are set up at CERN, Bratislava, and Pisa laboratories. In this chapter, the test bench setup at CERN, which is created at the building 175 laboratory and assembled using the part of the Valencia and University of Illinois test benches, is described in detail. A special thanks to Goncalo Ritto who did most of the hard work to make the CERN test bench work and ready for future testing. The general description of the setup and results are shown in the

following sections.

9.2 General description of the setup

The purpose of the test bench at CERN is the re-qualification of the dismounted PMTs which were used during Run-1 and Run-2. As mentioned earlier we took some parts of the legacy PMT test bench components from Valencia and the University of Illinois and refurbished them to make them operational for future testing. The legacy software package was migrated to LabVIEW version 18. Figure 9.1 shows the flow chart of the general setup of the test bench at CERN. This section contains some information about the electronics of the CERN test bench which is divided in three main parts. A LabVIEW (version 2018) based software framework is used to communicate with electronics.

- **the PMT box**, with position to test 24 PMTs simultaneously,
- **the light box** containing filter wheels for pulsed as well as DC light,
- **the data acquisition and control system**.

9.2.1 Electronic equipment

The electronic equipment of the test bench consists of VME and NIM electronics. The CERN test bench has all the electronic equipment fitted into a rack as shown in figure 9.2.

VME electronics

The CERN test bench uses the CAEN v1718 USB to VME bridge which sends and receives signals from the computer. The detailed description of the CAEN v1718 VME bridge can be found in Ref [52]. The VME crate consists of different electronic boards to perform different functions. The boards include a digital input/output circuit (DIO), a slow ADC containing 64 channels and four LeCroy 1182 charge ADCs. In addition, there is a patch panel in the VME crate. Three of the LeCroy ADCs are for PMTs in the PMT box to be tested and one is for the photodiodes. Figure 9.3 shows a diagram of the VME crate with its electronics used in the test bench. A brief summary of the functions of VME electronics is given below:

- **The DIO circuit**
  A VMI/VME 2510B DIO (digital input/output) circuit sends signals to the patch

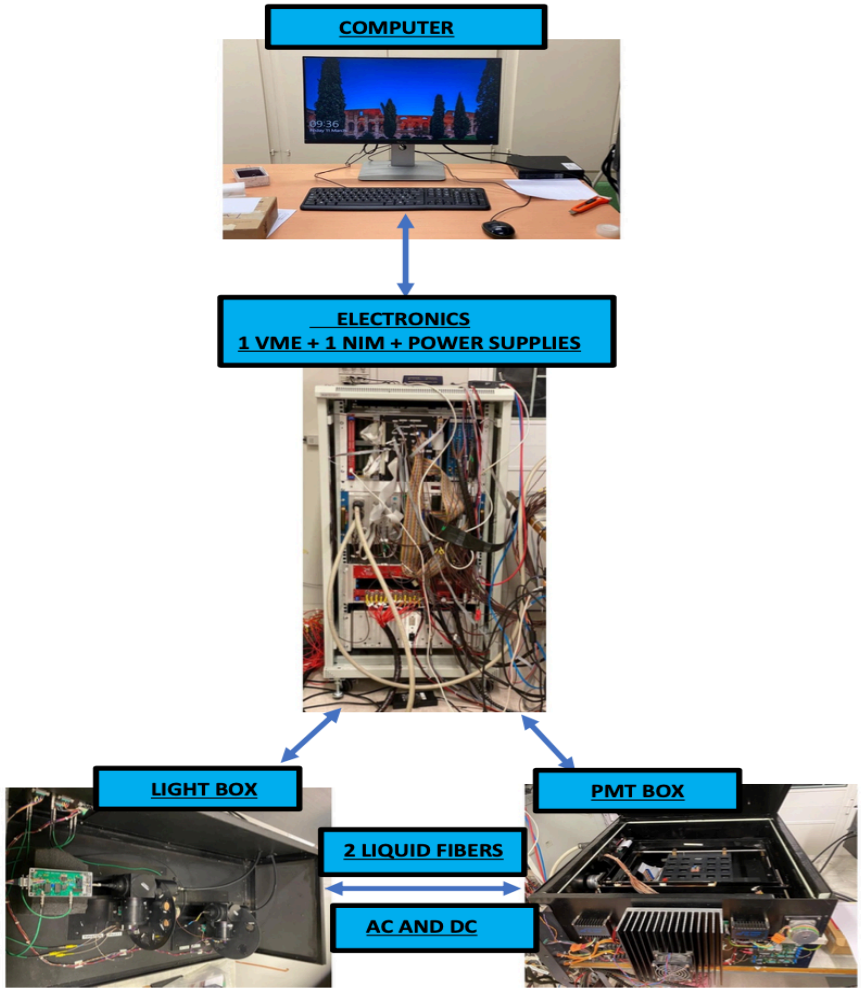

Figure 9.1: General setup of the test bench at CERN laboratory in building 175

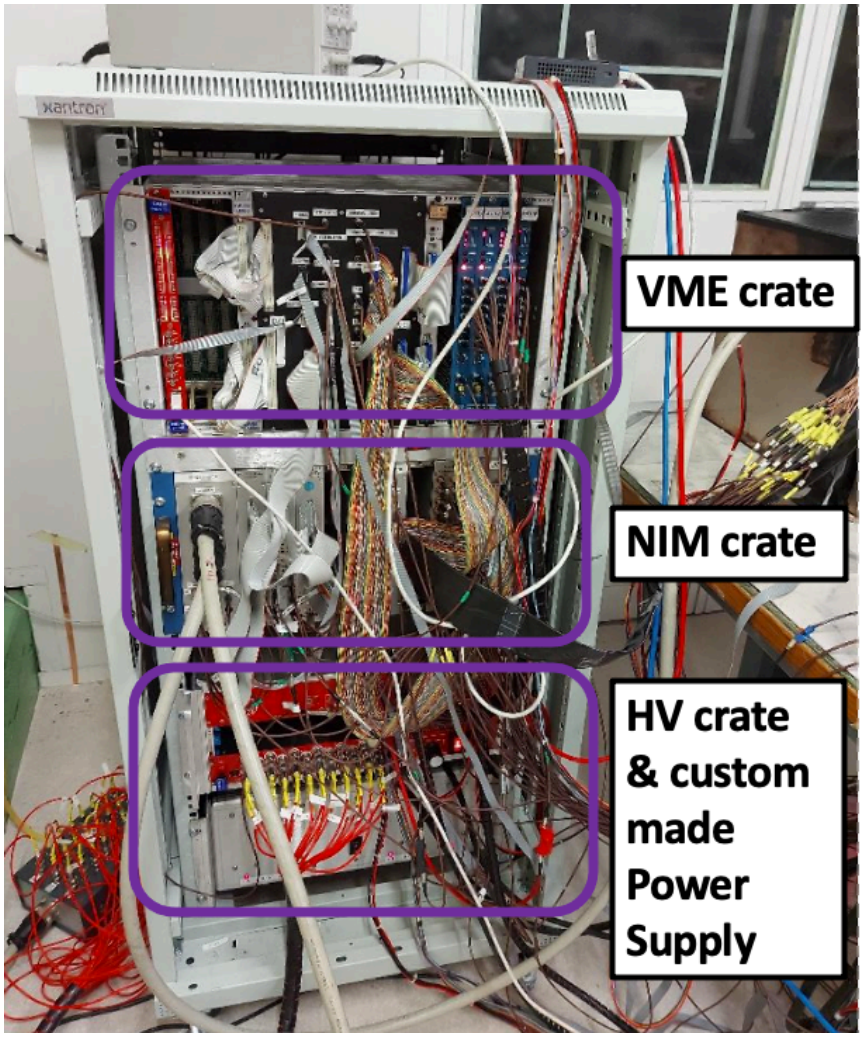

Figure 9.2: Rack with electronic equipment boards at CERN test stand

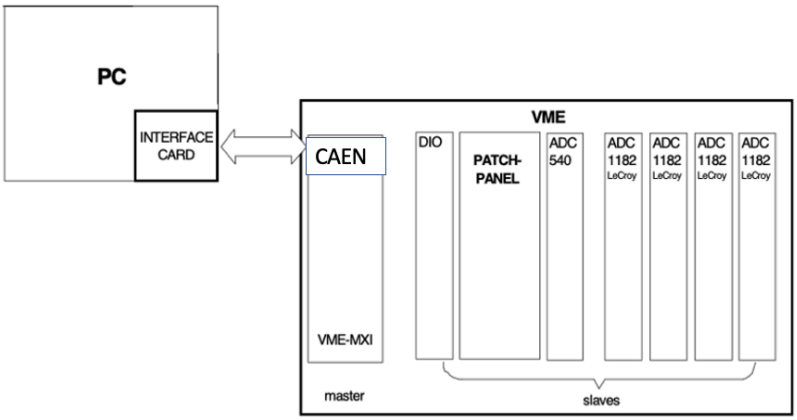

Figure 9.3: VME crate containing 4 charges and one slow ADC with a digital input/output circuit

panel to control many components of the test bench such as it control the movement of the XY table in the PMT box and filter wheels in the light box. The DIO circuit also controls the attenuation (switching between the pulse and DC mode) before the fast ADCs to cover a sufficiently large dynamic range while measuring the gain of PMT versus HV. Besides these functions, DIO circuit is also involved in controlling the modes of working of the special dividers in STEP1 as well as programming the different voltages needed for STEP1 and STEP2.

- **The slow ADC**
  The slow ADC module in the VME crate can perform 12-bit resolution of the analog to digital conversions on up to 64 channels in three different modes. The different modes include conversion of a single channel, repeated conversion of one channel, and conversions on sequential channels. It is used during the tests with DC light.

- **The fast ADCs**
  From the legacy PMT test stands at the University of Illinois, CERN received four LeCroy 1182 charge Analog to Digital Converters (ADCs). These ADCs offer 12-bit resolution with a sensitivity of 50 fC count on 8 channels. These ADCs digitize PMTs and photodiodes analog signals. Three LeCroy ADCs are used for the 24 PMTs and

the fourth one for the two pulsed photodiodes (the photodiode near the pulsed LED and the one inside the PMT box monitoring the light coming out of the liquid fibre). The Pisa and Bratislava test benches use QDC V792 CAEN ADCs.

NIM electronics

The different modules of the NIM electronics crate is shown in Fig 9.4. Brief detail about these circuits is given below

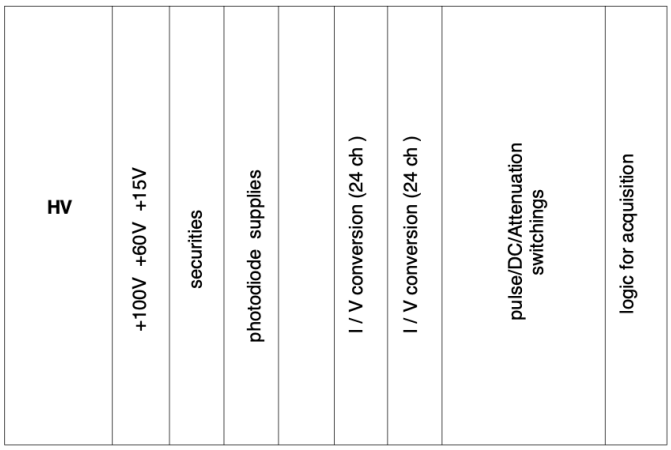

Figure 9.4: NIM crate showing the different circuits

- **Programmable voltages**
  The programmable voltages module receives the DAC values from the software and programs the three voltages i.e, +100 V of voltage to apply between the photocathode and the first dynode in STEP1, +60 V for the pulsed LED and +15 V for the DC LED. An external power supply supplies the required voltage which is then delivered to the security board. +100 V and +60 V are attained from a +120 V supply and the +15 V is made from the +24 V of the NIM crate. The circuit takes up one NIM unit.

- **Securities on the voltages**
  The securities module provides the possibility to turn ON or OFF the voltages through the program to avoid accidents during testing. Securities are mainly used to able/disable the high voltage for the PMTs, the voltage for the LEDs, and the

voltage between the photocathode and the first dynode of the PMTs. It is part of the safety interlocking.

- **I/V conversion**
  The I/V conversion module is used to measure the DC output of 24 PMTs and the photodiodes in STEP1 (Sec: 9.3.1) and STEP2 (Sec: 9.3.2). The current of the PMTs and photodiodes is then converted into voltage by the I/V conversion circuit. The obtained voltages are digitized by the DIO board in the VME crate. The conversion gain of I/V conversion can be switched between two values of resistors to measure in different current ranges. In a single NIM module, the conversion circuits are grouped into 24 channels. The currents go from the PMT box to the I/V conversion circuit via 50 lemo-cables (each cable is 4 meters long) and a flat cable (25 twisted pairs). The corresponding voltages are then sent to the patch panel via a similar 50 cm long flat cable of 25 twisted pairs.

- **Pulse/DC/Attenuation**
  The pulse/DC/attenuation module attenuates the signals from the PMTs and sends those signals to the charge ADCs. Attenuation switchings are mainly used in STEP2 in order to switch between DC and pulse mode to measure dark current and to avoid saturation of charge ADCs. Additionally, in pulse mode, it is useful to be able to change the attenuation before the charge ADC to increase the range of the measurements.

- **Logic of acquisition**
  The logic of the acquisition module receives the DAC values from the software and can change the frequency of the pulsed LED. It provides four ranges of frequencies (10 Hz, 100 Hz, 1 kHz, and 10 kHz). The module can operate in four different modes which are Pedestal, LED, Alpha, and PPG modes. The different modes allow different functionalities such as in pedestal mode acquisition of the pedestals of the ADCs is performed. In LED mode the circuit generates the trigger pulses for the light-emitting diode in pulsed mode. Alpha mode accounts for the signals coming from alpha sources only and PPG mode sends the calibration signals simultaneously to the preamplifiers and the corresponding ADC.

- **Supplies** The supplies module provides the voltage needed to change from photocathode to anode mode, to the LED driver, and to the preamplifier for the diodes of

the PMT and light box. The 3 photodiodes inside the PMT box are supplied with $+-12$ V through the supplies circuit.

High voltage crate

The legacy test bench used LeCroy 4032 HV power supply but at CERN a power supply SY5527LC with modules A7030SN 24 channels based on modules from CAEN is used. The details about the power supply can be found here Ref [53]. The HV supply communicates with the computer through an ethernet cable. Its function is to send the HV to the security board which will send it to the PMTs.

Power supply crate

The CERN test bench uses custom-made power which is driven by a custom VME I/O unit. It provides the required voltage to the peltiers, the motors of the PMT box, and the filter wheels from the light box. It was modified to use 240V AC input. However, the Pisa test bench uses a power supply of 3 ITT MX series units which is driven by the host PC via USB. The CERN setup should be upgraded to newer supplies too.

9.2.2 The PMT box

The PMT box is a light-tight and thermo-regulated box that could contain up to 24 photomultiplier tubes to test. Figure 9.5 shows an inside picture of the PMT box with its different components. These 24 PMTs are placed inside two different types of grids (one for each STEP) in the form of a 5×5 matrix in front of corresponding light mixers. A photodiode is placed at the centre of the matrix. On each light-mixer pulsed and DC light is brought through two plastic fibres. All these fibres are grouped in two bundles leading to optical connectors. A PMT box uses two different grids one for each of the two STEPs. A brief introduction of the two grids and other parts of the PMT box is given below.

- **Grid for STEP1**
  The continuous light operation in STEP1 requires the operation of the photomultiplier tubes in two modes: anode mode and photocathode mode. In order to be able to switch between the two modes of configuration, special dividers are used in STEP1. The anode mode in STEP1 corresponds to the classic operation of the photomultiplier while the photocathode mode provides the possibility to evaluate the performance of the photocathode (quantum efficiency) and optical input (collection of electrons

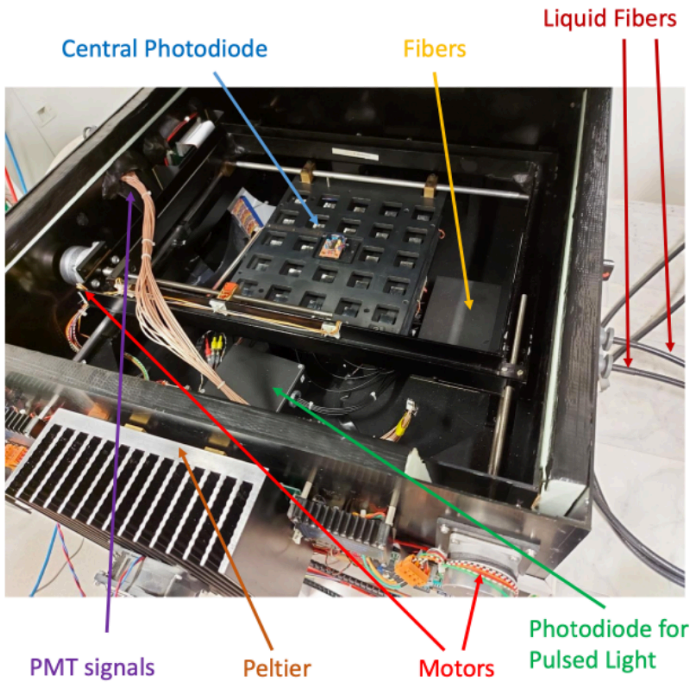

Figure 9.5: The PMT box with its different components.

by the first dynode). The switching between the two modes is done through the use of relays. The dividers are supplied with a voltage varying from 0 V to +100 V and +5 V to control the relays. A twisted flat cable with 50 pins connector is used to extract the PMTs currents. Another 20 pins connector flat cable is used for the special dividers command. Figure 9.6 shows the STEP1 grid with active dividers.

- **Grid for STEP2**
  The main purpose of STEP2 is the pulse measurements which use the grid with standard passive dividers. Signals from 24 PMTs go out of the PMT box through coaxial cables. The cables are then connected to Lemo connectors outside of the PMT box. Figure 9.7 shows the STEP2 grid with standard passive dividers.

- **Central photodiode and the monitoring Photodiodes**
  The photodiode in the centre of the matrix is used to calibrate every position of the grid and to apply corrective coefficients to compensate for the discrepancies coming from the curvature, length, and polishing of the plastic fibres. It can be moved above each light mixer with a system of stepper motors.
  In addition to the central photodiode, there are additional two monitoring photodiodes

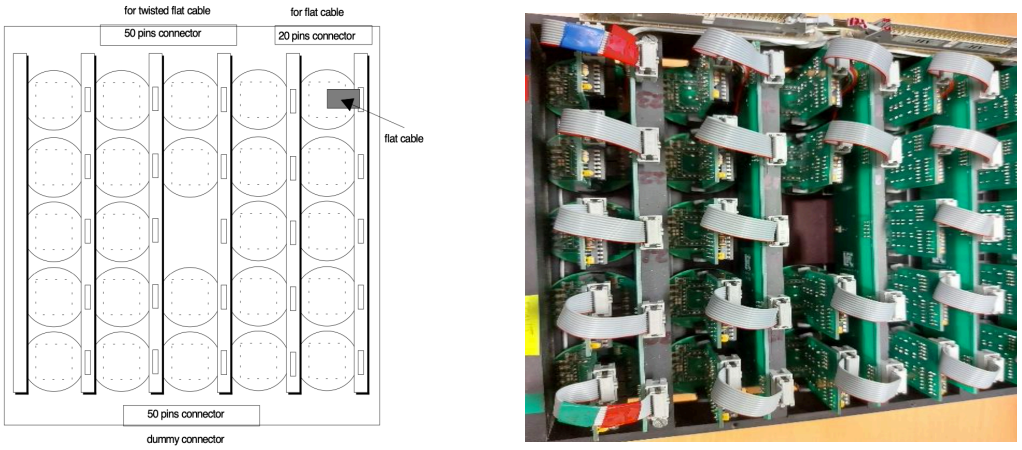

Figure 9.6: Diagram of Grid for STEP1(left) and a picture taken of STEP1 grid with special dividers at CERN test bench (right). The special divider enables to put of 100 V on the photocathode or high voltage on the anode.

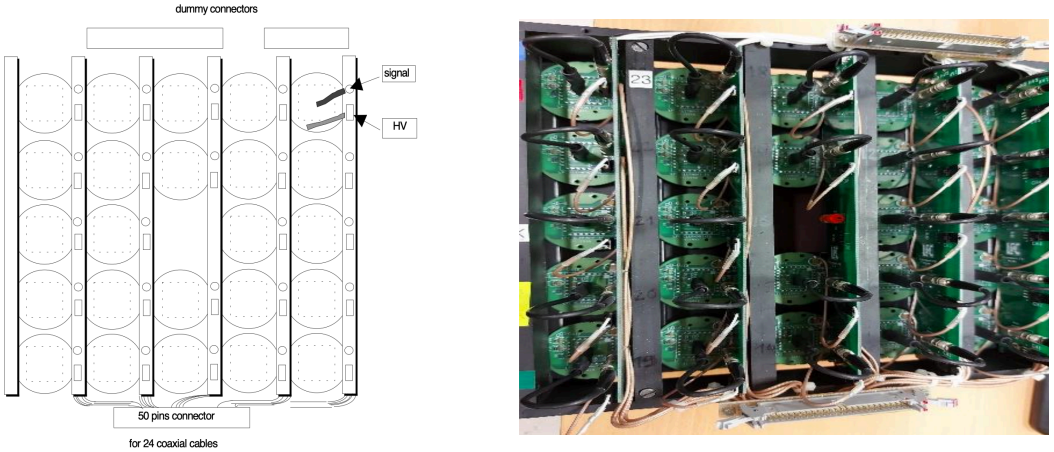

Figure 9.7: Diagram of Grid for STEP2 (left) and a picture taken of STEP2 grid with passive dividers (right) at CERN test bench.

that monitor the light coming from the light generators. Inside the PMT box, the liquid fibre coming from the light box is directed to a light mixer. From the light mixer, a total of about 36 fibres leave. 24 of these 36 fibres are for 24 PMTs while 12 fibres (in the form of 6×6) are for the photodiodes. Out of 12, two of the fibres are for the central photodiode and the remaining (10) are for the monitoring photodiodes to increase the sensitivity of the pulsed light.

- **Temperature regulation inside the PMT box**
  The temperature of the box containing photomultiplier tubes is regulated around 25^oC using Peltier elements. Four Peltier elements are used to increase or decrease the temperature depending on the direction of the current. Inside the box, the temperature is measured by a semiconductor probe whose current is proportional to the temperature. A few temperature sensors are placed at different places at the level of PMTs to verify homogeneity. Two fans are also placed to improve the homogeneity in the temperature when the box is open.

- **XY table inside the PMT box**
  The XY table of the PMT box houses the PMT grid for STEP1 and STEP2. The table can move inside the PMT box to allow the inter-calibration of the different channels. The movements of the XY table are controlled by two stepper motors and their drivers. Two switches X0 and Y0 provide a reference position. Four other switches are also placed for material safety by cutting off the steps of the motor if the XY table exceeds the imposed limits.

9.2.3 The light box

The light box contains two blue Light Emitting Diodes (LEDs) from Ledtronics for the generation of the pulsed light and DC light. The light from the LEDs of the light box is sent to the PMTs, one from a DC LED and another from a pulsed LED. The different components inside the light box are shown in Figure 9.8.

- **Pulsed Light**
  The LED which generates pulsed light is driven by a pulse, the amplitude of which is programmable up to 60 Volts. The beam coming from the LED passes through a first lens and is split into two parts by a beam splitter. A small amount of light is monitored by a photodiode while the main part is focused on a liquid fibre via

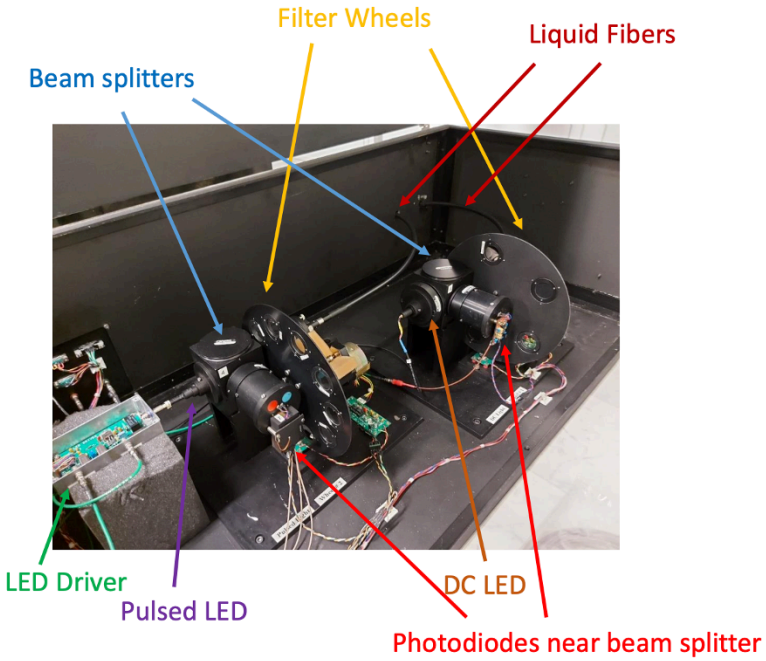

Figure 9.8: The light box with its different components.

another lens.
After the beam splitter, there is a filter wheel with 10 different attenuations that are driven by a motor. Each attenuation factor is calibrated by switching from pulse to DC mode on the LED to perform precise calibration with the DC central photodiode. All 24 pulsed light channels are also intercalibrated in the same way.

- **DC Light**
  The DC light system has the same configuration as the pulsed light except the number of filters is only five. The five filters include one with no filter, one black filter, and three filters to superimpose DC light in STEP2. One filter has an attenuation of about 1000 for the gain measurements in STEP1.

9.3 PMT qualification procedure

For the complete qualification of photomultiplier tubes, two types of measurements are defined. They are referred to as STEP1 and STEP2 and are shown in Figure 9.9.
Many parameters of both steps are checked through an Autotest procedure before actually

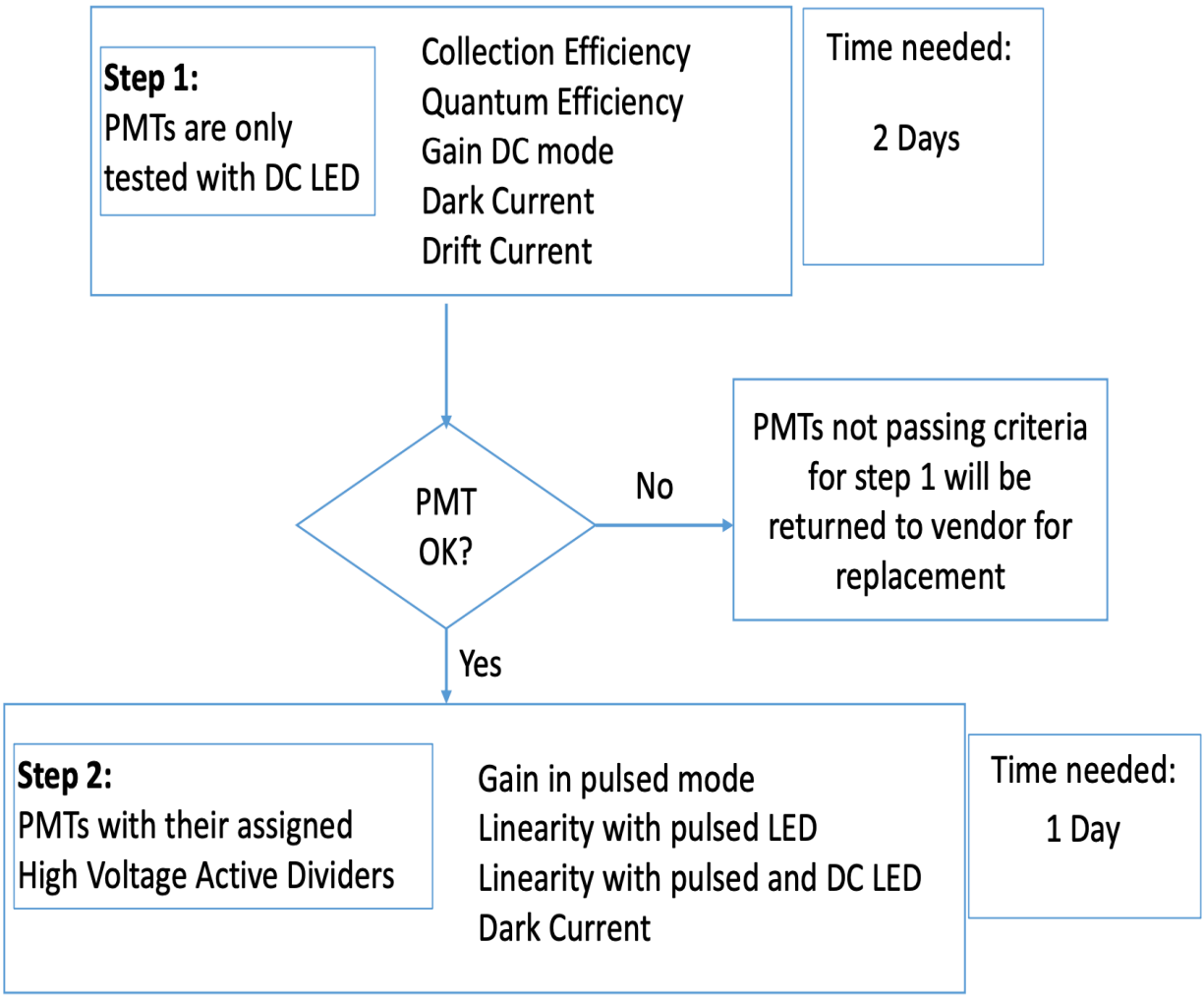

Figure 9.9: Complete procedure of the two STEPs and the respective time required for the full qualification of a PMT.

performing the two STEPS. The purpose of the Autotests is to check if every component of the test bench is in good condition to be able to do a full run to measure every desired characteristic of the PMTs. A brief description of STEP1 and STEP2 and their Autotests are following:

9.3.1 STEP1

Before running STEP1 an autotest is performed to make sure that every component of the test bench is working properly.

Autotest-STEP1

Many parameters of STEP1 are tested during Autotest-STEP1. The Autotest-STEP1 is divided into two parts. The first part is performed without a grid or PMTs inside the PMT box while part 2 requires PMTs inside the box.
During Autotest-STEP1 part 1 following different components are tested:

- Interlock is checked to test if the PMT Box is well closed or not.
- The voltage of the DC LED is measured while applying a DAC Value from 0 to 4000 with an interval of 200. A linear fit is done between DAC Value and the Voltage and the slope and the intercept of it will be compared with the expected results.
- Photodiode next to the DC LED is checked which measures the expected current obtained from the light from the LED.
- Central Photodiode inside PMT Box is checked which measures the expected current obtained from the light from the LED.
- The attenuation of the filter wheels is measured on wheel 1.
- The temperature inside the PMT box is checked. It should be between 25 and 30 degrees Celsius.
- The calibration factors are obtained by moving the central photodiode by two motors in two different axis over every different grid position. The lower the light received from the central photodiode in a certain position, the higher will be the calibration factor.

After successfully performing all the steps of autotest-STEP1 part 1, the procedure moves to autotest-STEP1 part 2. This step is performed with PMTs inside the grid in the PMT box. During this part, the voltage between the photocathode and the first dynode is measured by applying +100 V. For channel 0 PMT, a DAC value is measured for 10 nA current. Also, PMTs are tested by applying a HV of 550 V and the obtained high voltage is stored in the output file.

STEP1 measurements

In STEP1, the photomultiplier tubes are operated with DC light to measure the following quantities.

- **Photocathode efficiency**
  A voltage is applied between the photocathode and the first dynode and measures the photocathode current. The corresponding curve allows to detection of abnormal behavior in the first stage of the PMT. If the current is stable after a certain voltage it means that the photocathode is in good condition.

- **Quantum efficiency**
  Quantum efficiency is the measurement of the ratio of the incident photons and the electrons produced by the photocathode. Quantum efficiency of the PMTs is calculated by equation 9.1:

$$\frac{Q.e_{ph}}{I_{ph}} = \frac{Q.e_{pmt}}{I_{pmt}} \tag{9.1}$$

  where $Q.e_{ph}$, $Q.e_{pmt}$ and I_{ph}, I_{pmt} are the quantum efficiency and current of the photodiodes and the PMTs, respectively. The value of $Q.e_{ph}$ is known. The current and the pedestal value of PMTs and photodiodes are measured and subtracted from each other. The resulting value is multiplied by the calibration factors obtained in the Autotest-STEP1 part1 to calculate the quantum efficiency of the PMTs.

- **Gain**
  The ratio of the anode current with the photocathode current gives the gain of a PMT. To measure the currents initially filter wheel is positioned to black filter to measure the dark currents of the photocathode and anode. To measure anode current the filter with the higher attenuation is used while to measure photocathode current

no filter is used. The dark currents are subtracted from the obtained currents and then the calculated gain anode current is divided by the photocathode current. the voltage needed to obtain a gain of 10^5 is called the nominal high voltage.

- **Dark current**
  Photomultiplier tubes produce signals even in the absence of light due to a dark current. Dark current is generated due to a number of reasons such as the thermal emissions of electrons from the photocathode, leakage current between dynodes, and stray high-energy radiation. Electronic noise also contributes to the dark current and is included in the dark current value. The Dark Current is measured when applying high voltage without any incident light to the PMTs. The high voltage is applied from 500V to 900V with an interval of 50V.

- **Drift current**
  The drift current is obtained by comparing the initial anode current of the PMTs with the highest variation of the anode current of the PMTs after 25 hours. To measure the drift current, the DC LED DAC value is changed so that an average current of $3\mu A$ is applied to all the PMTs. The DC LED stays on for 7 hours and then it goes off for 3 hours and then it stays on for another 3 hours. This whole procedure is repeated twice. The current of the PMTs acquired when the light is on is divided by the current of the central photodiode and a coefficient is obtained. The obtained coefficient is normalized by dividing every row by the 1st row. A polynomial fit is applied to all the normalized coefficient values. The highest value of the polynomial fit is considered to be the drift value for every PMT.

9.3.2 STEP-2

In STEP2, a pulsed light is used to perform all the measurements. Similar to STEP1, an autotest-STEP2 is performed before running the STEP2 procedure.

Autotest-STEP2

During Autotest-Step2 many parameters from Step 2 are tested. Following are the different steps performed during autotest-Step2:

- Interlock of the PMT Box is tested.

- The response of the pulsed LED is determined using a scan of the applied voltage with DAC values 0 to 4000 $+60V$ in intervals of 200. A linear fit is applied between DAC Value and the voltage. The slope and the intercept of fit are compared with the expected results.
- The light of the pulsed LED inside the Light Box is measured with a photodiode near the beam splitter. The DAC value obtained is compared with an expected value.
- The light from the Pulsed LED obtained by a photodiode inside PMT Box is measured.
- The attenuation factor of every filter of the wheel is calculated by dividing the DAC value of the light obtained by the photodiode without filter by the DAC value of the light obtained by the photodiode with every other filter. The average of the attenuation factor is done after 3 measurements of the filters.
- The pedestal values of the Photodiodes and PMTs are measured by turning off the pulsed LED.
- Every PMT from the grid is checked by applying a high voltage of 500V. The high voltage obtained is stored in an output file.

STEP2 measurements

In STEP2, the photomultiplier tubes are operated with pulsed light and measure various quantities to fully qualify a PMT.

- **Pulsed gain**
  The value of pulsed gain is calculated by dividing the charge of each PMT by the number of photoelectrons as given by equation 9.2

$$Gain = \frac{Q}{N_{pe}} \times \frac{attenuation - coefficient}{1.6 \times 10^{-19}} \tag{9.2}$$

  where Q is the charge given by equation 9.3 and N_{pe} are the number of photoelectrons.

$$Q = Signal_{channel} \times ADC_{slope} \tag{9.3}$$

  where $ADC_{slope} = 50fC$ per channel and $Signal_{channel}$ is:

$$Signal_{channel} = mean - pedestal \tag{9.4}$$

- **Linearity with pulsed LED**
  Pulsed light with fixed is applied to every PMT in the grid and to a photodiode inside the PMT box. The non-linearity is measured by doing a linear regression between the PMTs and the Photodiode by measuring the ADC values obtained with the different filters.

- **Linearity with pulsed + DC LED**
  Linearity with Pulsed + DC LED is calculated in the same way as the Linearity with Pulsed LED, the only difference is that a DC LED light is superimposed to the applied constant value of pulsed LED light to obtain an average of an anode current of $3\mu A$ on PMTs.

- **Dark current**
  Dark current in STEP2 is calculated the same way as it is calculated in STEP1.

9.4 PMT characteristics and performances specifications

The PMT must fulfill all the characteristics and performance criteria to be accepted by TileCal. These requirements are enlisted below:

- The Quantum Efficiency (QE) of each PMT should be above 15%,

- the maximum dark current must be less than 2 nA and 8 nA at 800 V and 900 V, respectively,

- the ratio of dark current at 800 V and 900 V should be not more than 10,

- the value of the coefficient β must be between six and eight for each PMT. It is defined in the gain-to-voltage equation as:

$$\frac{G_1}{G_2} = \alpha + (\frac{V_1}{V_2})^{\beta} \tag{9.5}$$

- For pulses of 20 ns width and 50 mA peak current the non-linearity over the full dynamic range must be less than 2 %,

- the PMTs must provide a gain of 10^5. This gain value must be reached in a voltage range between 600 V - 800 V.

9.5 Results

The full qualification procedure was repeated several times with the same set of legacy PMTs at CERN to check the consistency and stability of the test bench. Data from individual tests is stored in an output file with acquired parameters. These output files can be used for further investigations and performing different cross-checks.
Data from testing the same set of PMTs is CERN and is analyzed to check the stability of the test bench. Figures 9.10, 9.11, 9.12 shows the output results of STEP1 performed over the same set of PMTs. Similarly the figures 9.13, 9.14, 9.15 shows the stability of STEP2 output parameters for the same set of PMTs.

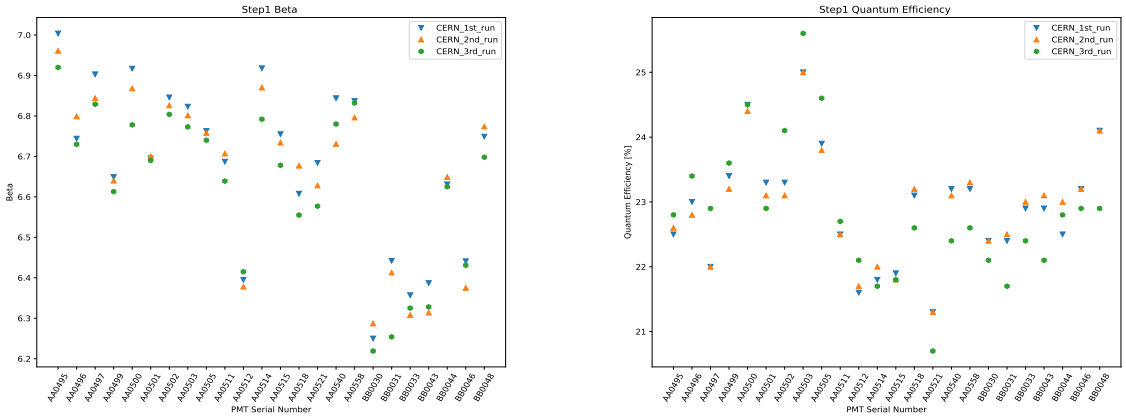

Figure 9.10: The beta (left) and quantum efficiency (right) of 24 legacy PMTs obtained using STEP1 with CERN test bench.

All the data from the CERN test bench is stable which indicates that the CERN test bench is ready to perform qualification and/or re-qualification tests of PMTs. All the PMTs shown in the results figures fulfill the required characteristics and performance criteria of the PMTs to be accepted.
In addition to this, sets of PMTs were exchanged between three laboratories to cross-check the consistency of the measurements and their compatibility. Typical differences between the three labs are below 2.5% and the maximum is below 5% which indicates a good agreement between the three test benches.

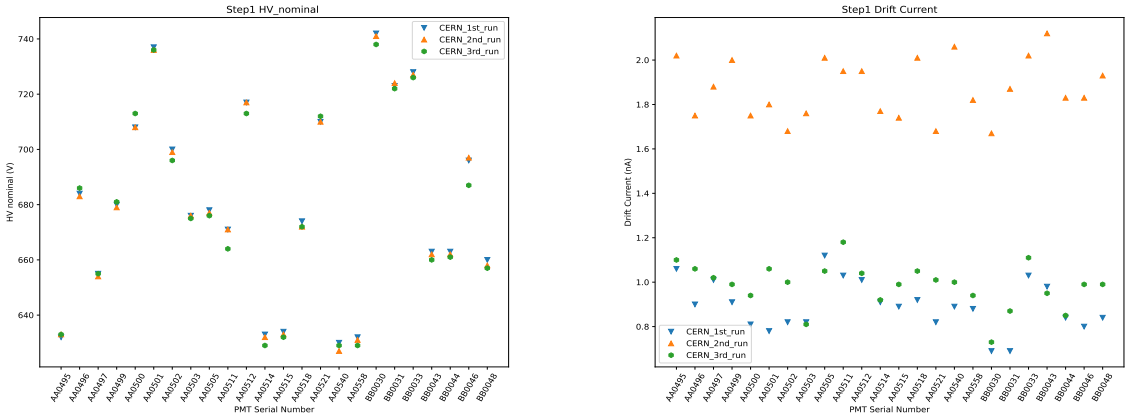

Figure 9.11: The nominal HV (gain 10^5) (right) and drift current (left) of 24 legacy PMTs obtained using STEP1 with CERN test bench.

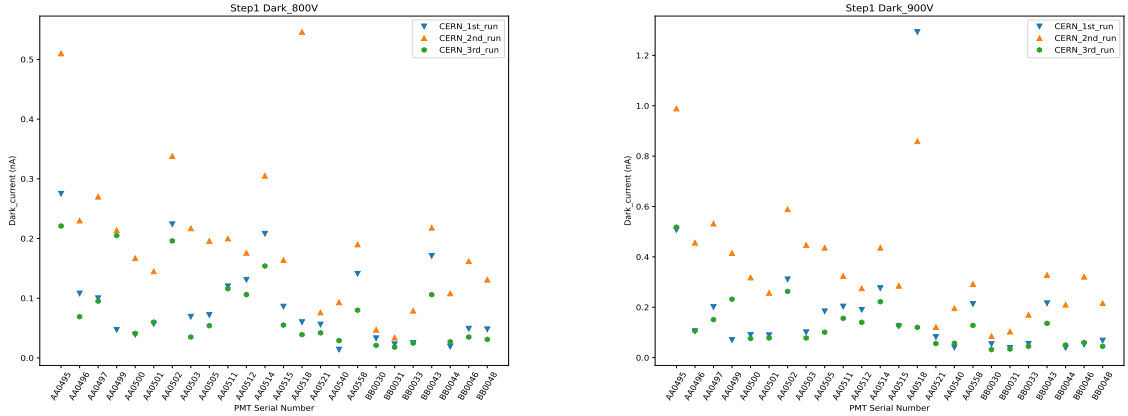

Figure 9.12: The dark current at 800V (right) and 900V (left) of 24 legacy PMTs obtained using STEP1 with CERN test bench.

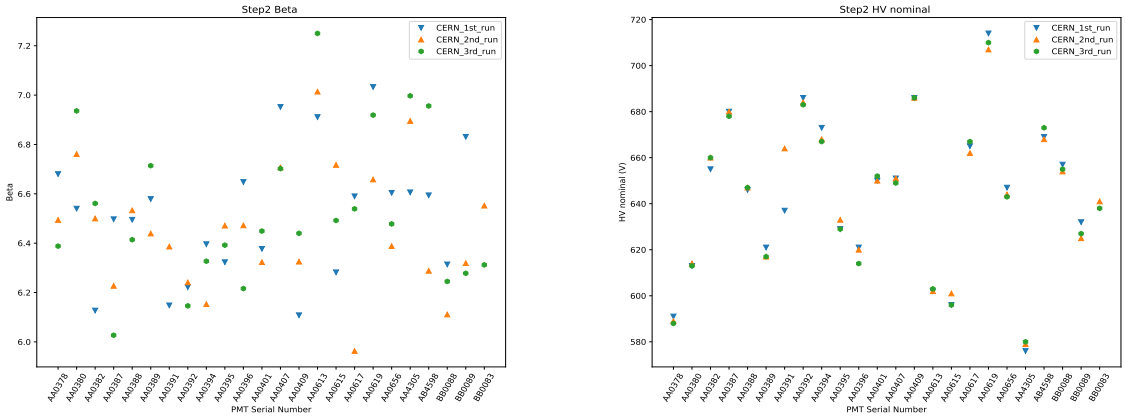

Figure 9.13: The beta (right) and nominal HV (gain 10^5) (left) of 24 legacy PMTs obtained using STEP2 with CERN test bench.

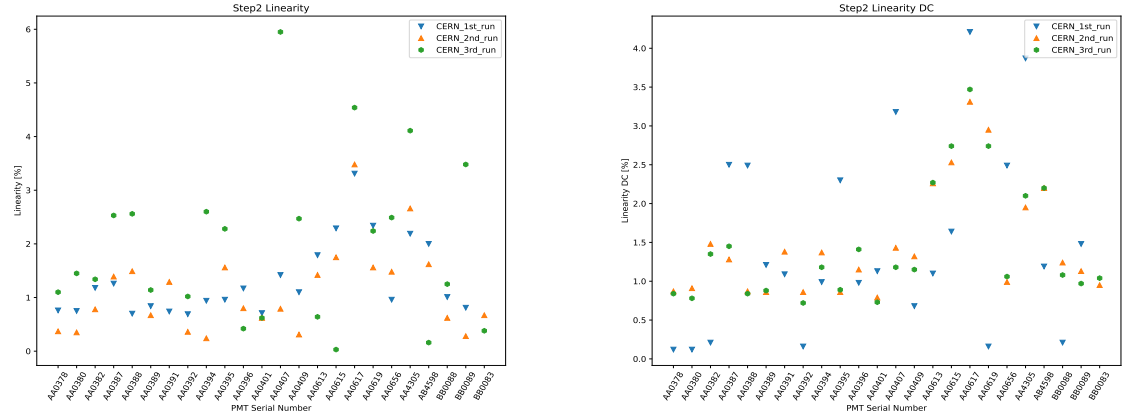

Figure 9.14: The linearity (right) and linearity DC (left) of 24 legacy PMTs obtained using STEP1 with CERN test bench.

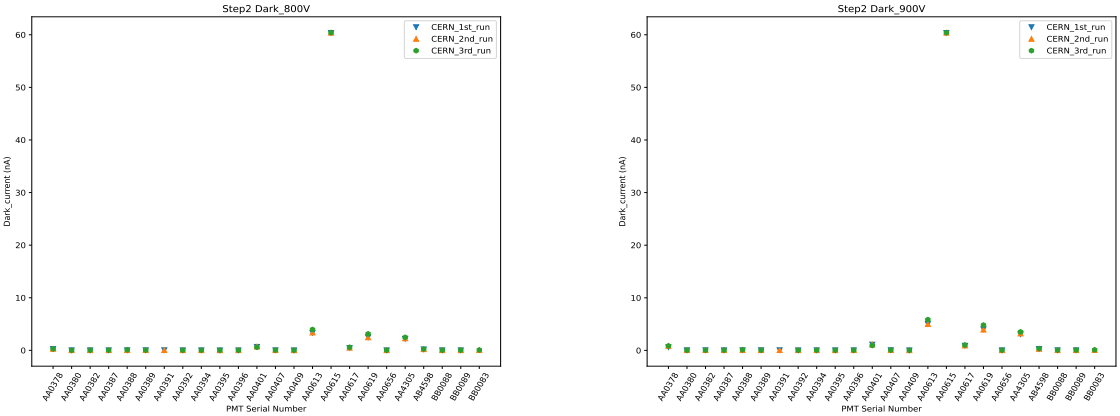

Figure 9.15: The dark current at 800V (right) and 900V (left) of 24 legacy PMTs obtained using STEP2 with CERN test bench.

Chapter 10

Conclusion

This thesis presents a description of the calorimetry, Laser II calibration system, and modelling of the response evolution of the photomultiplier tubes of the ATLAS Tile Calorimeter during the Run-2 data-taking period of the LHC. The Laser II calibration system is one of the three dedicated systems to ensure the calibration of the entire calorimeter response. This system probes individually the 9852 photomultiplier tubes of the detector, together with the readout electronics of each channel. During the LHC Run-2, the Laser II was providential for calibrating TileCal due to compromised operation of the Cesium system, with laser constants being weekly updated to keep uniform the energy response of the calorimeter between sparse cesium constants updates.

Three methods for laser data analysis were involved in the monitoring/calibration of PMT channels during the Run-2: the Direct method, the Statistical method, and the Combined method. They differ on the determination of the corrections that compensate for bias in the PMT response evaluation due to instabilities of the light source and monitoring (bias up to 2.5%) and inhomogeneities in the light dispatching to the PMTs (bias up to 1%). The Direct method relies on stable PMT references (reading D-cells) to derive these corrections and was used for calibration during 2015 and 2016. For the years 2017 and 2018, the reference PMTs were no longer stable enough due to the dependence of the PMT response on the delivered integrated luminosity and the increase of luminosity during this period. The Combined method, independent of reference PMTs, was then used in calibrations of 2017 and 2018 collision data. The Combined method was validated by comparing the measured PMT response evolution to the response evolution of the associated calorimeter cell, determined with Cs scans, for periods of low delivered luminosity where small optics degradation is expected and thus the two quantities should be equal. The average difference

is 0.1% and the standard deviation is 0.8%. The Laser calibration factors were derived and applied in the entire Run-2 for both prompt calibrations during data taking and for yearly data reprocessing campaigns. They address drifts in the PMT response exhibiting a strong dependence on the PMT collected charge, which increases with the delivered luminosity and with the exposure of the cell read by the PMT to the particle flux. Inner cells, in the A layer, E cells, and the forward region are more affected. The accumulated response drift for an entire collision year period ranged from 0.9% (D cell PMTs) to around 3% (E cell PMTs) in 2015 at 4.2 fb^{-1} and from -0.1% (D cell PMTs) to around -6% (E cell PMTs) in 2018 at 63.3 fb^{-1}.

Three different models have been studied to understand and quantify the PMT response recovery during Year End Technical Stops (YETS) during Run-2: single exponential, double exponential, and single exponential with slope fit method to find a unified model. The fit function is applied to all the PMTs during each YETS period. The single and double exponential fit model does not work well for all PMTs during all YETS. Single exponential with slope function provides a unified model of the PMT response recovery during all YETS for all cells with few discrepancies in 2015-2016 YETS. For all other YETS, all the output fit parameters are comparable for the same cell type during different YETS with the characteristic time constant of about $\approx$ 20 days for the PMTs reading A and BC and EB-D cells.

In order to be able to fully understand the response evolution of PMTs during pp-collisions as well as technical stops, the modelling of response loss (down-drift) along with the up-drift (recovery) is crucial. Different approaches were made to find a model which can explain the PMT response over time as a function of luminosity which could also be used to predict the future PMT response in Run 3 and Run 4. The PMT response evolution of the entire Run 2 can be well quantified with a double efficiency model when the luminosity convoluted fit function is applied to the average response variation of the PMTs where down-drift per luminosity fill is defined by tangent hyperbola function. In between the two luminosity fills the PMTs recover exponentially with time. The two efficiencies correspond to different processes which give two different sets of output parameters corresponding to slow and fast recovery processes. Systematic effects due to the model and the interplay of down-drift and recovery are very difficult to be estimated. Using this model it has been estimated that E4 which is the most exposed cell losses about $\approx$17% while the PMTs reading

A13 lose about ≈10% of their response during the entire Run 2 period. Hence the results of the fit model are qualitatively consistent, the two efficiency model seems to apply in almost all cases during the entire Run 2 period. However, the Results are quantitatively different for different PMTs reading different cells. Using the results of the luminosity convoluted fit function, projections to the HL-LHC era are drawn with a big uncertainty (both statistical and systematic). A cross-check was also performed to check the reliability of the extrapolation. For this, backtesting was performed using the fit results of 2015-2017 data to extrapolate the entire Run 2 period. The extrapolated results agree with the laser data within ± 1%.

TileCal expects a large response loss ($\geq$ 25%) of the PMTs reading out the most exposed cells during operation at High Luminosity LHC (HL-LHC). Hence studies were made and based on those studies, it was decided to replace 1024 of the total 9852 TileCal photomultiplier tubes. In order to replace about 10% of the TileCal PMTs, it was decided to qualify all replacement PMTs and to re-qualify a fraction of legacy PMTs with renewed three qualification test benches (at CERN, PISA, and Bratislava) used in the past for initial qualification of the original TileCal PMTs. The test bench at CERN is refurbished and in fully working condition. The test bench at CERN can measure the quantum efficiency, dark current at 800 and 900 V, short-term drift as well as the linearity of 24 PMTs at the same time. The test bench has good stability and reproducibility of measurements. A cross-check of measurements between the three test benches verified the consistency of the qualification results at the percent level for the most important parameters.

Bibliography

[1] K. Olive, *Review of Particle Physics*, Chinese Physics C **38** no. 9, (2014) 090001. https://doi.org/10.1088/1674-1137/38/9/090001.

[2] S. Lee, *On the limits of the hadronic energy resolution of calorimeters*, Journal of Physics: Conference Series **1162** (2019) 012043. https://doi.org/10.1088/1742-6596/1162/1/012043.

[3] *Calorimetry I Electromagnetic Calorimeters*,. https://www.physik.uni-hamburg.de/en/iexp/gruppe-schleper/lehre/detectors-methods-ss18/documents/detectors-and-analysis-methods-ss-18-notes-09.pdf.

[4] E. Mobs, *The CERN accelerator complex in 2019.*,. https://cds.cern.ch/record/2684277. General Photo.

[5] A. Team, "Computer-generated diagram of an LHC dipole. Schéma d'un dipôle du LHC." Sep, 1998.

[6] Xabier Cid Vidal, Ramon Cid Manzano, *LHC layout*,. https://www.lhc-closer.es/taking_a_closer_look_at_lhc/0.lhc_layout.

[7] Luminosity webpage, *Public ATLAS Luminosity Results for Run-2 of the LHC*,. https://twiki.cern.ch/twiki/bin/view/AtlasPublic/LuminosityPublicResultsRun2.

[8] J. Wenninger, *LHC Accelerator Complex (I). 2007 CERN-Fermilab HCP Summer School*,. https://cds.cern.ch/record/1565601.

[9] *ATLAS experiment overview*,. https://mediaarchive.cern.ch/MediaArchive/Photo/Public/1998/9803026/9803026/9803026-A5-at-72-dpi.jpg.

[10] J. Pequenao and P. Schaffner, "How ATLAS detects particles: diagram of particle paths in the detector." Jan, 2013.

[11] ATLAS Collaboration, G. e. a. Aad, *The ATLAS Inner Detector commissioning and calibration.*, Eur. Phys. J. C **70** (2010) 787–821. 34 p, arXiv:1004.5293. https://cds.cern.ch/record/1262789. Comments: 34 pages, 25 figures.

[12] ATLAS website:. https://atlas.cern.

[13] L. Rossi, G. Apollinari, M. Lamont, O. Bruning, and I. Bejar, *High-Luminosity Large Hadron Collider (HL-LHC) : Preliminary Design Report*. 12, 2015.

[14] S. Kaiser, H. Kroha, S. Horvat, and O. Kortner, *Search for the Higgs Boson in the Process $pp \to Hqq$, $H \to WW$ with the ATLAS Detector*,.

[15] ATLAS Collaboration, *Performance of the ATLAS Trigger System in 2015*, Eur. Phys. J. C **77** no. 5, (2017) 317.

[16] TileCal webpage:, *Published Tilecal Figures*,. https://twiki.cern.ch/twiki/bin/view/AtlasPublic/PublishedTilecalFigures.

[17] Matsusada Precision, *Photomultiplier Tube (PMT)*,. https://www.matsusada.com/application/ps/photomultiplier_tubes/.

[18] Cesium webpage:, *Approved Plots TileCalibration Cesium*,. https://twiki.cern.ch/twiki/bin/view/AtlasPublic/ApprovedPlotsTileCalibrationCesium.

[19] CIS webpage:, *Approved Plots TileCalibration CIS*,. https://twiki.cern.ch/twiki/bin/view/AtlasPublic/ApprovedPlotsTileCalibrationCIS.

[20] Minimum bias system webpage:, *Approved PlotsTileMinimumBiasSystem*,. https://twiki.cern.ch/twiki/bin/view/AtlasPublic/ApprovedPlotsTileMinimumBiasSystem.

[21] S-O Flyckt and Carolde Marmonier, "Photomultiplier tubes principles and applications.". https://www2.pv.infn.it/~debari/doc/Flyckt_Marmonier.pdf.

[22] G. Di Gregorio, *Plots for approval on PMT robustness studies*, tech. rep., CERN, Geneva, May, 2018. https://cds.cern.ch/record/2317070.

[23] Wikipedia, *Logistic*,. https://en.wikipedia.org/wiki/Logistic_function.

[24] Laser webpage:, *Approved Plots TileCalibrationLaser*,. https://twiki.cern.ch/twiki/bin/view/AtlasPublic/ApprovedPlotsTileCalibrationLaser.

[25] Ammara AHMAD, *The ATLAS Tile Calorimeter Performance and Its Upgrade towards the High-Luminosity LHC*,. https://rdcu.be/cViKS.

[26] Richard Wigmans, *Calorimetry: Energy Measurement in Particle Physics*. Oxford University Press, second ed., 2017.

[27] C. W. Fabjan and F. Gianotti, *Calorimetry for Particle Physics*, Rev. Mod. Phys. **75** (2003) 1243–1286. 96 p. https://cds.cern.ch/record/692252.

[28] Rossi, Bruno Benedetto, *High-energy particles*. Prentice-Hall physics series. Prentice-Hall, New York, NY, 1952. https://cds.cern.ch/record/99081.

[29] T. Gabriel, D. Groom, P. Job, N. Mokhov, and G. Stevenson, *Energy dependence of hadronic activity*, Nuclear Instruments and Methods in Physics Research **338** no. 2, (1994) 336–347.

[30] Groom, D.E, *Energy flow in a hadronic cascade*, Nuclear Instruments and Methods **A572** (2007) 633.

[31] F. Ariztizabal et al, *Construction and performance of an iron-scintillator hadron calorimeter with longitudinal tile configuration*, Nuclear Instruments and Methods in Physics Research **349** no. 2, (1994) 384–397.

[32] K.Pinkau, *Errors in Electromagnetic Cascade Measurements Due to the Transition Effect*, Phys. Rev. **139B** (1965) 1548.

[33] CERN website:. https://home.cern/science/accelerators/linear-accelerator-2.

[34] CERN website:, *The Proton Synchrotron Booster*,. https://home.cern/science/accelerators/proton-synchrotron-booster.

[35] CERN website:, *The Proton Synchrotron*, 2019. https://home.cern/science/accelerators/proton-synchrotron.

[36] CERN website:, *The Super Proton Synchrotron Booster*,. https://home.cern/science/accelerators/super-proton-synchrotron.

[37] ATLAS Collaboration Collaboration, *ATLAS tile calorimeter: Technical Design Report*. Technical design report. ATLAS. CERN, Geneva, 1996. https://cds.cern.ch/record/331062.

[38] Hamamatsu Photonics K.K, *Photomultiplier Tubes*, 2010.

[39] Cleland, W.E. and Stern, E.G., *Signal processing considerations for liquid ionization calorimeters in a high rate environment*, Nucl. Instrum. Meth. A **338** no. 2-3, (1994) 467–497.

[40] Fullana,E et al., *Optimal Filtering in the ATLAS Hadronic Tile Calorimeter*, tech. rep., CERN, Geneva, 2005. https://cds.cern.ch/record/816152.

[41] P. Adragna et al., *Testbeam studies of production modules of the ATLAS tile calorimeter*, Nucl. Instrum. Meth. **A606** (2009) 362–394. CITATION = NUIMA,A606,362;.

[42] G. Blanchot, et al, *The cesium source calibration and monitoring system of the atlas tile calorimeter: design, construction and results*, Journal of Instrumentation **15(03):P03017** (2020).

[43] ATLAS Collaboration, O. Solovyanov, *Performance of the ATLAS hadronic Tile Calorimeter in Run-2 and its upgrade for the High Luminosity LHC*, tech. rep., CERN, Geneva, Sep, 2017. https://cds.cern.ch/record/2285795.

[44] ATLAS Tile Calorimeter system Collaboration, Abdallah, J. et al., *The Laser calibration of the ATLAS Tile Calorimeter during the LHC run 1. The Laser calibration of the Atlas Tile Calorimeter during the LHC run 1*, JINST **11** (2016) T10005. 31 p, arXiv:1608.02791. http://cds.cern.ch/record/2206626.

[45] Spectra Physics, "Navigator laser.". http://www.spectra-physics.jp/member/admin/document_upload/Data_Sheet_-_Navigator_FamilyAugust_2009.pdf.

[46] Blanco Castro, Alberto et al., *Performance of the upgraded Laser calibration system of the ATLAS Tile Calorimeter*, Tech. Rep. ATL-COM-TILECAL-2017-061, CERN, Geneva, Oct, 2017. https://cds.cern.ch/record/2290200.

[47] J. Bures J. Opt. Soc. Am. **64** no. 12, (1974) 1598–1605.

[48] Arisaka, K.s, *New trends in vacuum-based photon detectors*, vol. A442. Nucl. Instrum. Meth., 2000.

[49] P.-F. Verhulst, *"Notice sur la loi que la population poursuit dans son accroissement."*,. https://books.google.fr/books?id=8GsEAAAAYAAJ&redir_esc=y. Retrieved 3 December 2014.

[50] B. C. Pinheiro Pereira, *Radiation damage of the optical components of the ATLAS TileCal calorimeter at the High-Luminosity LHC*, Dec, 2020. https://cds.cern.ch/record/2764597. Presented 18 Jan 2021.

[51] F.James, *MINUIT Function Minimization and Error Analysis*, March 1994. https://root.cern.ch/download/minuit.pdf.

[52] CAEN, *Technical Information Manual*, July, 2018. https://twiki.cern.ch/twiki/pub/Atlas/PMTTestBench/V1718_rev10.pdf. Revision n.10.

[53] International Power, *International Power DC Power Supplies*,. https://www.mouser.ch/datasheet/2/199/InternationalPower_IHD15-6-1286616.pdf.